Design and analysis of current stress minimalisation controllers in multi-active bridge DC-DC converters.

HEBALA, O.M.

2020

Design and Analysis of Current Stress Minimisation Controllers in Multi Active Bridge DC-DC Converters

Osama Mohamed Hebala

PhD **2020**

Design and Analysis of Current Stress Minimisation Controllers in Multi Active Bridge DC-DC Converters

Osama Mohamed Hebala

A thesis presented in partial fulfilment of the

requirements of the

Robert Gordon University

for the Degree of Doctor of Philosophy

In Electrical Engineering

February 2020

Declaration

I hereby declare that this submission is my own work and that, to the best of my knowledge and belief, it contains no material previously published or written by another person nor material which to a substantial extent has been accepted for the award of any other degree or diploma of the university or other institute of higher learning, except where due acknowledgment has been made in the text.

……
Osama Mohamed Hebala

Acknowledgements

All praise and thanks are to almighty Allah for enabling me to complete this work. I would like to express my gratitude to my supervisors Dr. Sam Burgess and Dr. Radhakrishna Prabhu for impeccable guidance and invaluable support throughout this challenging period. I would also like to thank the rest of my supervisory team Dr. Ahmed Aboushady and Dr. Khaled Ahmed for offering valuable technical comments and enthusiastic support during the research period. Sincere gratitude are also due to Dr. Ibrahim Abdelsalam for helpful discussions. Thanks are also due to school administration manager Dr. Rosslyn Shanks for her help throughout the PhD three-year period. I am also grateful to the Electric Engineering Department's staff members of the Arab Academy for Science, Technology and Maritime Transport in Alexandria (AASTMT),Egypt — particularly: Prof. Mostafa Saad, Prof. Samah El-Safty, Prof. Amany El-Zonkoly, Prof. Hamdy Ashour and Dr. Moustafa Abdelgelil— for encouraging me along the way. Mr. Ahmed Shaaban – secretary of Electrical Engineering Department in AASTMT, Egypt – has also offered much appreciated support during the last three years.

I would like to convey my sincere thanks and gratitude to my parents for their great support and encouragement that really helped me to overcome challenges and to complete this research. Finally, I am extremely thankful to my wife and little daughter for their patience and support during the entire PhD journey. Without the support of my parents, my family and my friends, it would have not been possible to complete this work.

Abstract

Multi active bridge (MAB) DC-DC converters have attracted significant research attention in power conversion applications within DC microgrids, medium voltage DC and high voltage DC transmission systems. This is encouraged by MAB's several functionalities such as DC voltage stepping/matching, bidirectional power flow regulation and DC fault isolation. In that sense this family of DC-DC converters are similar to AC transformers in AC grids and are hence called DC transformers. However, DC transformers are generally less efficient compared to AC transformers due to the introduction of power electronics. Moreover, the control scheme design is challenging in DC transformers due to its nonlinear characteristics and multi degrees of freedom introduced by the phase shift control technique of the converter bridges. The main purpose of this research is to devise control techniques that enhance the conversion efficiency of DC transformers via the minimisation of current stresses. This is achieved in this work by designing two new generalised controllers which minimise current stresses in MAB DC transformers.

The first developed controller is for dual active bridge (DAB). This is the simplest form of MAB, where particle swarm optimisation (PSO) is implemented offline to obtain optimal triple phase shift (TPS) parameters for minimising the RMS current. This is achieved by applying PSO on DAB steady state model with generic per unit expressions of converter AC RMS current and transferred power under all possible switching modes. Analysing the generic data pool generated by the offline PSO algorithm enabled the design of a generic real-time closed-loop PI-based controller. The proposed control scheme achieves bidirectional active power regulation in DAB over the 1 to -1 pu power range with minimum-RMS-current for

buck/boost/unity modes without the need for online optimisation or memory-consuming look-up tables. Extending the same controller design procedure for MAB was deemed not feasible as it will involve a highly complex PSO exercise that is difficult to generalise for N number of bridges and would generate a massive data pool that is quite cumbersome to analyse and generalise.

For this reason a second controller is developed for MAB converter, without using a converter-based model, where current stress is minimised and active power is regulated. This is achieved through a new real time minimum current point tracking (MCPT) algorithm that realises iterative-based optimisation search using adaptive-step perturb and observe (P&O) method. Active power is regulated in each converter bridge using a new power decoupler algorithm. The proposed controller is generalised to MAB regardless of the number of ports, power level and values of DC voltage ratios between the different ports. Therefore, it does not require an extensive look-up table for implementation, the need for complex non-linear converter modelling and it is not circuit parameter-dependent. The main disadvantages of this proposed controller are the somehow sluggish transient response and the number of sensors it requires.

Index Terms: RMS Current stress, multi active bridge (MAB), dual active bridge (DAB), particle swarm optimization (PSO), triple phase shift (TPS), Perturb and Observe (P&O), Minimum Current Point Tracking (MCPT).

Contents

List of Abbreviations

BDC	Bidirectional DC–DC converters
COMM	Communication Network
CPS	Conventional Phase Shift
DAB	Dual Active Bridge
DG	Distributed Generation
DPS	Dual Phase Shift
EPS	Extended Phase Shift
ESS	Energy Storage System
EV	Electric Vehicles
FHA	Fundamental Harmonic Approximation
FID	Fault Identification Device
HFL-PCS	High Frequency Link Power Conversion Systems
HVAC	High Voltage Alternating Current
HVDC	High Voltage Direct Current
KKT	Karush Kahn Tucker
LMM	Lagrange Multiplier Method
MAB	Multi Active Bridge
MCP	Minimum current Point
MCPT	Minimum current Point tracking
MPP	Maximum Power Point
MPS	Multi Phase Shift
MVDC	Medium Voltage Direct Current
P&O	Perturb and Observe
PCS	Power Conversion Systems
PSO	Particle Swarm Optimisation
PSSW	Phase Shifted Square Wave
PV	Photo Voltaic
PWM	Pulse Width Modulation
QAB	Quad Active Bridge
SPS	Single Phase Shift
SST	Solid State Transformer
TAB	Triple Active Bridge
TPS	Triple Phase Shift
UDC	Unidirectional DC-DC converters
ZVS	Zero Voltage Switching

List of Symbols

D_i	Duty ratio of bridge's i voltage in MAB/DAB
D_{ij}	Phase shift angle between AC-side voltages of bridges i and j in MAB/DAB
f_s	Switching frequency
i_i	Instantaneous AC-side current of bridge i in MAB/DAB
$i_L(t_i)$	Instantaneous AC-side inductor current in DAB at switching instant t_i
$I_{dc\,i}$	DC-side current of bridge i in MAB/DAB
I_{RMS}	Resultant of AC side RMS currents in MAB
$I_{i\,RMS}$	AC-side RMS current of bridge i in MAB
$I_{L\,RMS}$	AC-side RMS current in DAB
$I_{L\,RMS(1)}$	AC-side RMS fundamental-harmonic current in DAB
k	Current sampling instant (in a digital controller)
K_{ij}	DC voltage ratio of bridge i with respect to bridge j
L_{base}	Base Inductance
L_i	AC side inductance at bridge i in MAB
m	Number of sampling instants (in a digital controller)
n	Number of active bridge module in a MAB converter
P	Transferred active power in DAB
$P_{(1)}$	Transferred fundamental-harmonic active power in DAB
P_e	Active power error (difference between measured and desired power)
P_i	Active power measured at terminal of bridge i
P_i*	Desired active power level at bridge i in MAB/DAB
P_{re}	Active power measured at the receiving end in DAB
P_{se}	Active power measured at the sending end in DAB
P_{Tol}	Tolerance of active power error
Q_i	Reactive power measured at terminal of bridge i
R_{ac}	Parasitic resistance of AC side inductor
T_h	Half switching period (cycle)
T_s	Full switching period (cycle)
V_{base}	Base voltage
$V_{dc\,i}$	DC-side voltage of bridge i in MAB/DAB
v_i	Instantaneous AC-side voltage of bridge i in MAB/DAB
$V_{L\,RMS}$	Inductor RMS voltage in DAB

D_r	Perturbation duty ratio where ***r*** stands for reference bridge
$(\Delta D_r)_I$	Perturb value generated with respect to RMS current variation
$(\Delta D_r)_P$	Perturb value generated with respect to active power error variation
Z_{base}	Base Impedance
δ_{ij}	Phase shift angle between AC-side fundamental-harmonic voltages of bridges ***i*** and ***j*** in MAB/DAB

List of Figures

List of Tables

Chapter 1. Introduction

1.1. Background

Across the world electrical power generation and distribution is currently witnessing rapid and unprecedented challenges. This is mainly because many types of clean sustainable renewable energy sources have been widely utilised as distributed energy resources into the grid [1]–[3], as a result of environmental, social, economical aspects as well as political interests. At the moment nearly 36% of UK electrical energy is from renewable sources with about 12% increase compared to renewables portion in Q1 2015 UK energy statistics — as depicted in Fig 1.1 — and this is expected to keep increasing in the next years [1], [2].

Fig. 1.1: Sources of electricity generation in UK [1], [2].

Relying on natural phenomenon, such as sunshine or wind, these renewable energy systems are of stochastic nature [4], [5] and therefore it is difficult to accurately predict their output power. In addition, their generation peaks do not necessarily match power demand peaks, which adds further complexity in system design. Besides, the voltage-current characteristics of loads are usually different than those of energy sources and storage devices. Consequently, the need to supply small-scale loads (e.g.: local generation, buildings or electric vehicles.) in an uninterruptible fashion, and the fact that the existing power system

infrastructure cannot handle high penetration of renewables, have given rise to technologies such as energy storage systems (ESS) and micro-girds. ESSs such as super-capacitors, batteries and flywheels can maintain a smooth and continuous power flow and compensate the fluctuations [3], [6]. Micro-grids are proposed to help transform the centralised energy production and unidirectional flow in the conventional distribution grids, to de-centralised energy production and bidirectional flow [7], [8]. Therefore, flexible energy management systems are needed to facilitate intelligent energy capturing from diverse energy sources, and interface them with energy storage elements in a multi-directional power flow manner. In this context, there is a growing attractiveness of power conversion systems (PCSs) and solid state transformers (SST) as efficient interface key components [9]–[13]. Fig. 1.2 shows the SST interfacing ESS, photovoltaic (PV) generation, plug-in electric vehicles (EV) as well as DC and AC loads [14]. Furthermore, SST can enable distributed intelligence via implementing a communication network (COMM) and protection via implementing a fault identification device (FID). This can greatly improve the stability and achieve optimal operation of the distribution system [15].

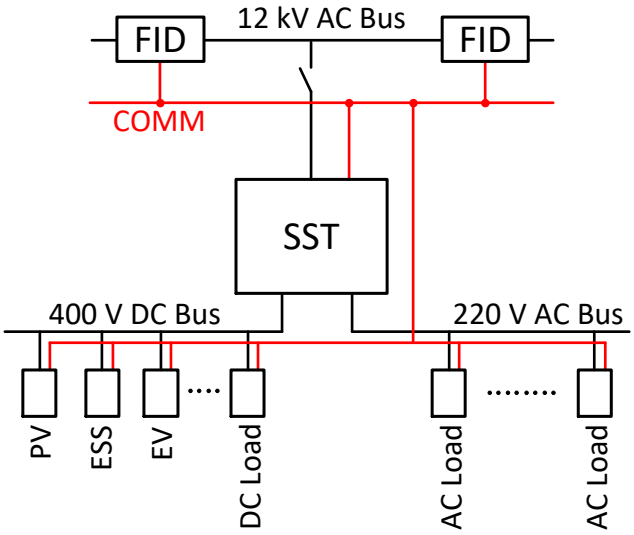

Fig. 1.2: Solid state transformer for Integration of Renewables, ESSs and AC/DC loads [14].

Bidirectional DC–DC converters (BDCs) have been proposed as an essential building block of SSTs in micro-grids. An example of a relevant application is shown in Fig. 1.3 [16] where a BDC-based SST can enable the interfacing of distributed energy resources and distributed storage systems that can be conjugated and integrated into grid. In this case, the BDC interfaces a low-voltage bus, where an energy storage system such as a super capacitor or a battery is usually installed, and a high-voltage bus, where an energy generation system such as a fuel cell stack or a photovoltaic array is implemented. In fact, a bidirectional DC-DC converter with an installed transformer (as shown in Fig. 1.3) is often referred to as DC transformer due to similar functionalities to the transformer in AC grid such as voltage matching and galvanic isolation. In this regard, modern power conversion systems employ high frequency transformers, which offer various advantages over conversion systems with line-frequency transformers [17], [18], such as: lower physical footprint (lower volume), lighter weight, lower noise and lower cost [19].

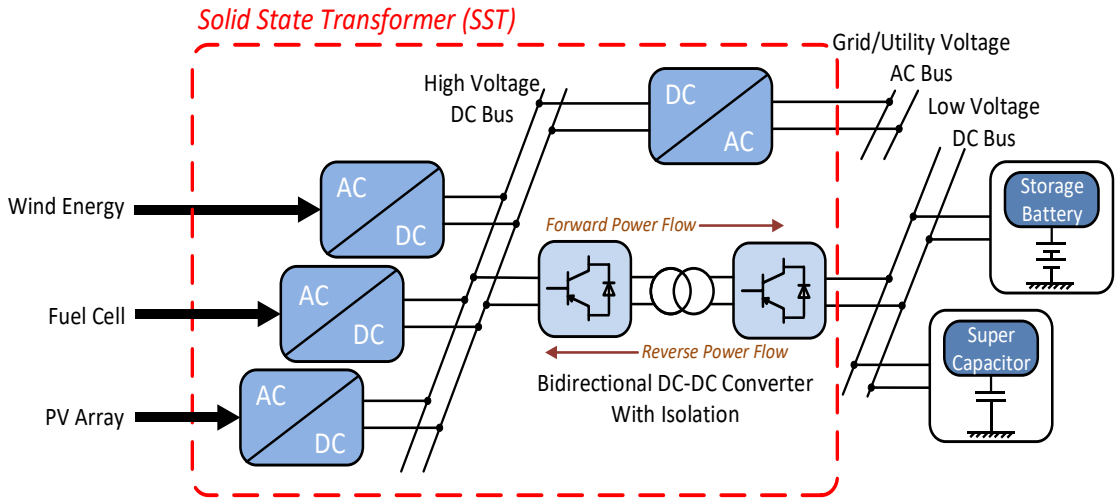

Fig. 1.3: Typical application of BDC in SST for power distribution in microgrid[16].

On the other hand, aging AC networks and increased consumer demand for electrical energy requires a means to strengthen and increase bulk power

transmission to main distribution grids [20]. Connecting large scale offshore wind energy to a distant onshore power grid has become a challenge: especially with recent trends to locate large offshore wind farms in deeper waters to take advantage of high average wind speeds and reduce constraints imposed by local planning regulations [21], [22]. However, long distance and/or bulk power AC transmission is inefficient compared with DC transmission as shown in Fig 1.4. This triggers the need to replace high voltage alternating current (HVAC) transmission with high voltage DC (HVDC) transmission. Potential functions of DC transmission can include asynchronous or grid integration of isolated power systems (i.e.: like oil industry, offshore renewables and international power links [23].).

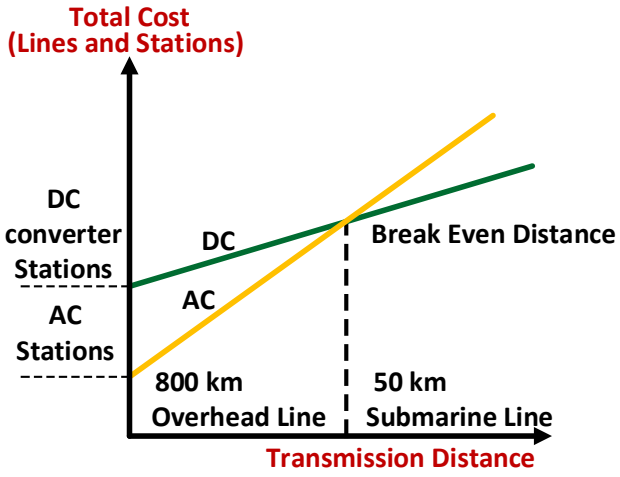

Fig. 1.4: Break even analysis of DC vs. AC transmission [24].

Bidirectional DC-DC converters have been proposed as a multi-functional interface component within the large scale HVDC grids given its fault-isolation capability (in isolated version), voltage stepping and power regulation functionalities within the grid [25]–[27]. Fig. 1.5 illustrates some of the converter expected functionalities in a four terminal VSC-HVDC grid. The interface between offshore wind farms (WF1 and WF2) and the grid, operating at different voltage levels, is carried out using DC-DC conversion. Moreover, DC-DC converters should

be able to limit and isolate the DC fault when it occurs at the offshore DC cable (location highlighted in the Fig 1.5); thus eliminating the need to install DC circuit breakers, which are not yet commercially ubiquitous at high voltage/power due to their high cost and high on state losses. Alternatively, affordable mechanical circuit breakers can be used to isolate the fault permanently.

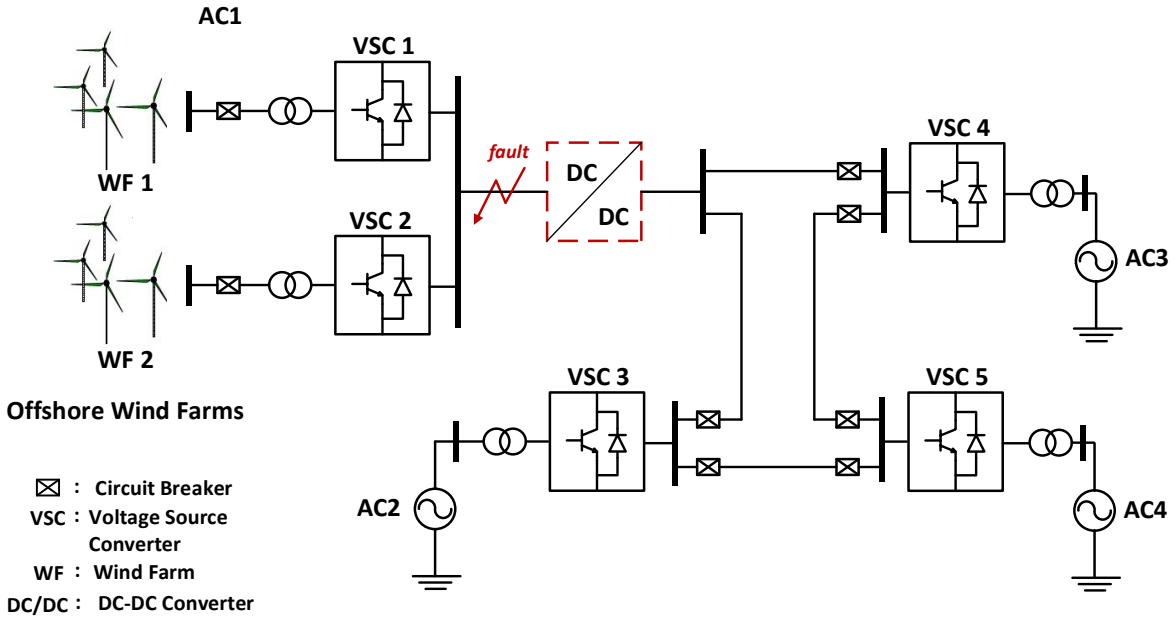

Fig. 1.5: A four terminal VSC-HVDC [28].

Bidirectional DC-DC converters can also help minimising the number of conversion stages for both small-scale and large-scale DC power transmission, which directly increases the investment benefit and transmission efficiency. This will ultimately increase the use of 'DC-based' power transmission and distribution in the future: thus reducing the overall energy losses resulting from the conversion of electrical power [29]. Therefore, the research and development of DC-DC converters – capable of efficiently operating in a DC grid environment – is gaining great interest in both academia and industry. One of the main challenges facing the implementation of DC transformers compared to AC transformers is making them operate with similar high efficiencies, as AC transformers are well known with.

1.2. Research Motivation

The main motivation of this thesis is to enhance the conversion efficiency of DC transformers via minimising current stresses, and this is the primary research focus in this work. The current stresses in this thesis refer to the effective root mean square (RMS) value of the AC-side current in Dual/Multi Active Bridge converters (i.e.: the DC transformers which will be the focus of this thesis.). RMS current stress has a direct impact on conduction losses (in the widely used MOSFET power switches) which are considered to be the dominant portion of converter's total losses [30], [31], beside the fact that the copper losses are proportional to the square of the RMS current [32]. The AC-side current in Dual/Multi Active Bridge converters usually incorporates a reverse current portion that transmits power backwards [33]. In this case, the forwarding power portion will not be sufficient to maintain the desired power transfer level, and as a result AC-side current has to increase its forwarding portion; causing high peak (and high RMS) current value and thus increased total losses (decreased converter efficiency). This phenomenon is called circulating current and is best described by the analogy with a similar phenomenon in AC grid, where the circulating current (reactive current) does not contribute to any energy transfer but yields power device conduction losses and transformer copper losses. Detailed description of the circulating current phenomenon is provided in section 2.1.1 while the mathematical definition of the RMS current is provided in section 3.1.2.

Minimising these current stresses can help toward the development of existing grids to enable small-scale (i.e.: microgrids, electric vehicles and UPS.) and large-scale (i.e.: HVDC and MVDC grids.). However, before the development and widespread roll-out of DC grids happens there needs to be significant advances in

DC-DC converters. The existing efficiency enhancement techniques lack the following:

- Unified implement standard.
- Standardised high-efficiency power flow controller.
- Scalable power flow analysis for multi-port networks.
- Efficiently interconnecting lines with different DC voltage levels.

The devised techniques in this work will look at providing standardised solutions to tackle the above-mentioned aspects. This will facilitate deployment of multi-terminal networks and improving operational efficiency of low voltage/low power DC grids (e.g.: UPS systems, aircraft power distribution system [34], electric vehicles [35] and traction applications [36].). Additionally, advances in these fields will help HVDC grids replace HVAC transmission networks or at least become a preferable solution. Efficient HVDC transmission grids will facilitate transmission of bulk renewable energy [28], [37] which is one of the main challenges facing the HVDC grid.

Overcoming the aforementioned challenges is expected to have positive impact on many aspects, such as:

Economic Impact – Reducing the operational losses and hence the cooling requirement in DC transformers, as well as minimising the voltage and current stresses on devices and components, which will increase the working life and operational performance of DC grids. It will be more economical to operate and manage DC grids.

National Impact – The research project will facilitate solutions to current issues facing the implementation of multi-terminal DC grids in the UK. The expected advancement in knowledge in this field may contribute toward enabling multi-point connection of UK offshore renewable parks: hence contributing towards

government 2050 energy plans [38]. This will also support UK compliance with reduced carbon footprint as internationally agreed in the Paris agreement.

Social Impact – Society will benefit from lower energy costs and increased security of domestic energy supply. Moreover, high skilled employment roles in the UK renewable sector will be created in the future.

1.3. Research Aim and Objectives

The work in this thesis focuses on the design of high-efficiency power flow controllers for DC-DC converters via minimising current stresses. The targeted DC-DC converters are the Dual Active Bridge (DAB) and the Multi Active Bridge (MAB). A key design goal is to develop a generic control scheme that achieves efficient power flow control while concurrently maintaining minimum current stress hence improved efficiency. In keeping with the research aim, the objectives of this study are **–**

Objective 1. Review state-of-the-art bidirectional DAB and MAB DC-DC converters in power conversion systems and identify the operational challenges and shortcomings regarding the following aspects:

a) Steady state modelling, switching mode classification and basic characterisation.
b) Efficiency improving techniques, particularly in situations of unmatched DC side voltages and light loading.
c) Control schemes for MAB converters and related challenges such as the need for offline calculation and non-universality.

Objective 2. Steady state modelling and simulation of DAB and MAB DC-DC converters:

a) Modelling of Dual Active Bridge (DAB).
b) Modelling of Multi Active Bridge (MAB).
c) Analysing different AC link topologies in non-isolated MAB converters and identification of optimal topology.
d) Power flow analysis for MAB converters with N number of ports.
e) Verification of (a)-(d) via simulation in MATLAB/Simulink.

Objective 3. Develop a new control scheme for power flow regulation in DAB:

a) Offline application of particle swarm optimisation (PSO) method to minimise AC-side RMS current.
b) Calculation of optimal control parameters and identification optimal operating modes under different DC voltage stepping/matching conditions.
c) Verification of both (a) and (b) and the proposed control scheme via simulation in MATLAB/Simullink along with an experimental prototype.
d) Identify the limitations considering application of this design approach on MAB converter with N number of ports.

Objective 4. Develop a generic control design approach for MAB converter that includes:

a) New minimum current point tracking (MCPT) technique that iteratively search for the minimum RMS current in real time based on an adaptive-step perturb and observe (P&O) method.
b) New phase shift decoupling analysis which leads to new decoupled power controller for MAB with any number of ports.
c) Verification of both (a) and (b) and the proposed control scheme via simulation in MATLAB/Simullink.

1.4. Methodology

The research methods applied to achieve the research objectives included mathematical modelling using piecewise time domain analysis in addition to harmonic analysis using Fourier series expansion. These methods were mainly used for steady state modelling of the investigated DC-DC converters. In addition, simulation using MATLAB (Simulink and m-file) was used to verify the correctness of the derived models and designed controllers. Part of the work involved sensitivity analysis to verify the robustness of the designed controller to different system parameters. Two methods were investigated for optimisation in MAB converters: offline particle swarm optimisation (PSO) technique and online perturb and observe (P&O) method. An experimental prototype has been developed for dual active bridge DAB converter to confirm the derived model and controller.

1.5. Contributions

Main contributions to knowledge in this work are:

- New mathematical expression derived for the AC-side RMS current in DAB any operating point.
- Implementation of PSO method to calculate optimum modulation parameters for current stress minimisation in DAB. The results from the PSO

application are non-specific to converter rating, which makes the results generic to any DAB.

- Investigation of new AC link topologies for non-isolated MAB converter based on pure-inductive AC link and identification of the optimal topology in terms of minimum AC inductance and RMS currents. Active/reactive power and RMS current expressions were derived for all topologies along with developing a method to calculate the inductance that ensure maximum power transfer in all investigated topologies.
- New algorithm for tracking minimum RMS current in MAB converter, namely minimum current point tracking (MCPT) technique. This proposed technique is based on a new developed version of the adaptive-step perturb and observe (P&O) method.
- New decoupled power controller for active power regulation in MAB converter regardless of number of ports.
- Two new active-power-flow controllers with minimum current stress were developed for DAB and MAB converters. The proposed control schemes are generic as they both cover bi-directional power flow regardless of DC voltage ratios. Plus they are simple to implement and do not involve any offline calculation or look-up tables.

1.6. Published Work

Conference Papers

1. O. M. Hebala, A. A. Aboushady and K. H. Ahmed, "Analysis of AC link topologies in non-isolated DC/DC triple active bridge converter for current stress minimization," *2017 IEEE 6th International Conference on Renewable Energy Research and Applications (ICRERA)*, San Diego, CA, 2017, pp. 608-613.

2. O. M. Hebala, A. A. Aboushady, K. H. Ahmed, S. Burgess and R. Prabhu, "Generalized Small-Signal Modelling of Dual Active Bridge DC/DC Converter," *2018 7th International Conference on Renewable Energy Research and Applications (ICRERA)*, Paris, 2018, pp. 914-919.
3. O. M. Hebala, A. A. Aboushady, K. H. Ahmed and S. Burgess, "Active Power Regulation in Dual Active Bridge DC-DC Converter with a Minimum-Current-Point-Tracking Technique,"*IECON 2019 45th Annual Conference of the IEEE Industrial Electronics Society*, Lisbon, 2019 (accepted for publication).

Journal Papers

1. O. M. Hebala, A. A. Aboushady, K. H. Ahmed and I. Abdelsalam, "Generic Closed-Loop Controller for Power Regulation in Dual Active Bridge DC–DC Converter With Current Stress Minimization," in *IEEE Transactions on Industrial Electronics*, vol. 66, no. 6, pp. 4468-4478, June 2019.
2. O. M. Hebala, A. A. Aboushady, K. H. Ahmed, and S. Burgess, " A New Active Power Flow Controller for Multi Active Bridge Converters with Adaptive P&O Minimum Current Point Tracking," (prepared and ready for submission to IEEE transaction).

1.7. Thesis Outline

Chapter 2 provides a detailed overview of DAB and MAB DC-DC converters in view of the following aspects: basic characterisation, phase shift control strategies, power flow control schemes and efficiency improvement techniques.

Chapter 3 focuses on the steady state analysis of dual active bridge DC-DC converter under triple phase shift (TPS) modulation having been identified from Chapter 2 as the most commonly used DC-DC converter in DC grids/microgrids. A

detailed, analytical, per unit steady state analysis of all identified switching and operating modes of a dual active bridge DC-DC converter under TPS modulation is presented as this will represent the base for the proposed controllers.

Chapter 4 discusses the steady state analysis of multi active bridge converter under multi-phase shift (MPS) modulation. A new steady state approximate model of the MAB converter under different AC link topologies is investigated in detail and optimal AC link topology, in terms of minimum RMS current and inductor value, is identified. Analysis of the derived model has led to a generic design of a new phase shift decoupler and a proposed PI-based power flow controller for MAB.

Chapter 5 examines a new per unit AC link current minimisation algorithm for dual active bridge DC-DC converter based on a simple PI-closed loop scheme. The method has been developed by analysing a data pool produced offline by applying an artificial-intelligence-based optimisation method (PSO). The proposed optimised control scheme is generic covering all possible conversion ratios/converter voltage gains (i.e.: Buck/Boost/Unity.) and the entire loading range: however, extending this control scheme to multi active bridge converters is not feasible as it gets mathematically highly complicated when trying to follow the same design procedure.

Chapter 6 presents a unified, current-stress optimised, power flow controller for MAB converters; including the case of a DAB converter. A key feature of the proposed control scheme is that it can perform online current-stress minimisation (i.e.: in real-time.) based on a new adaptation of P&O technique in a minimum current point search algorithm. There is no need for complex converter modelling given the scheme is converter-parameter independent.

Chapter 7 provides a general summary of the main work findings, contributions to knowledge and suggested areas for future research.

Chapter 2. Literature Review

This chapter presents a comprehensive literature survey on the dual active bridge (DAB) bidirectional DC-DC converter (BDC) which serve as the key circuits in high-frequency-link power conversion systems (HFL-PCSs). Overall, isolated BDC topologies for HFL-PCSs are diverse and numerous. However, isolated BDCs generally emerge from traditional isolated unidirectional DC-DC converters (UDCs), such that:

- Flyback UDC can compose dual-flyback BDC.
- Half-bridge or push–pull UDC can compose dual-half-bridge or dual-push–pull BDC.
- Full-bridge UDC can compose dual-active-bridge BDC.

In addition, the BDCs can be composed of UDCs with the different types, such that half-bridge UDC and push–pull UDC can compose a half-bridge-push-pull BDC for applications requiring a bidirectional power flow and a wide voltage range. This is because the half-bridge topology can withstand high voltage while push pull topology suits applications involving low-source voltages. Classification of BDC topologies based on the number of switches is outlined in Table 2.1 such that –

- Dual-switch structure is the simplest BDC topology, such as: dual-flyback, dual-Cuk and Zeta-Sepic BDCs [39][40][41].
- Forward-flyback BDC is the typical model of three-switch topology [42].
- Topologies utilising four switches mainly include dual-push-pull, push-pull-forward, pushpull-flyback and dual-half-bridge BDCs [43]–[50].
- The full-bridge-forward BDC represents a typical model of the five-switch topology [51], whereas the half-full-bridge BDC represents the typical model for six-switch topology [52].

- Eight-switch topology is mainly DAB [53],[54] & [55].

Table 2.1 Classification of IBDC topologies according to number of switches.

Number of switches	Typical topology
Dual-switch	dual-flyback dual-Cuk Zeta-Sepic
Three-switch	Forward-flyback
Four-switch	dual-push-pull push-pull-forward pushpull-flyback dual-half- bridge
Five-switch	full-bridge-forward
Six-switch	half-full-bridge
Eight-switch	dual-active-bridge

In general, the transmission power (power capacity) of BDC is proportional to the number of switches having the same rated voltage and current. For example, the rated transmission power a four-switch BDC is half that of eight-switch BDC and twice that of dual-switch BDC [19]. In this context, the DAB has the maximum power capacity in addition to offering numerous functionalities [56]–[60]:

- Bidirectional power handing capability.
- High power density.
- High reliability.
- Galvanic isolation in transformer-based versions.
- Ease to implement soft switching control.
- Symmetric structure and evenly shared currents in the switches.
- Possibility of cascaded or modular configuration to enable higher power/higher voltage designs.

Due to these advantages, DAB DC-DC converters have attracted more attention in power energy conversion applications within DC microgrids, medium voltage DC (MVDC) and high voltage DC (HVDC) transmission systems [61]–[63]. That is why DAB was considered to serve as the core circuit for next-generation HFL-PCSs [64]

&[30]. Potential functionalities of DAB converters include: voltage matching/stepping in distributed generating systems incorporating variable-nature energy resources such as PV or wind in addition to accommodating power regulation between energy storage systems, energy sources and load demands [16], [65]–[67]. In addition, modular based dual active bridge DAB DC-DC converters have been used in MVDC and HVDC applications [63], [68].

The DAB was originally proposed in the 1990s [69]. However, back then DAB suffered from the high losses and poor efficiency due to the performance limitations of power devices. This has restricted the development of DAB converters until the advances in power devices and magnetic materials in recent years by eliminating heavy and bulky low frequency transformers [70] & [71]. Examples of such advances are the development of gallium-nitride (GaN)-based and silicon carbide (SiC) power devices along with iron-based nanocrystalline soft magnetic. Thus, DAB has regained the attention of researchers, especially when compared to the other bidirectional DC-DC converters.

2.1. Dual Active Bridge (DAB) DC-DC Converter

The typical topology of the single-phase DAB converter consists of two opposed H-bridges where bidirectional active switch devices are utilised as shown in Fig.2.1. The symmetric H-bridges topology (i.e.: connected in 'H' configuration.) creates an alternating output voltage pattern across an inductive storage element. If a large step-up conversion or a galvanic isolation between the two DC ports is required, a transformer can be utilised between converter bridges. Such isolated converter structures are typically operated using Phase Shifted Square Wave (PSSW) Modulation rather than Pulse Width Modulation (PWM) control. The cross-connected switch pairs in both full bridges are switched in turn to generate phase-

shifted square waves with 50% duty ratio across the transformer's primary and secondary sides. The power flow is essentially controlled through phase shift modulation of the square-wave voltages generated by their corresponding active bridge modules.

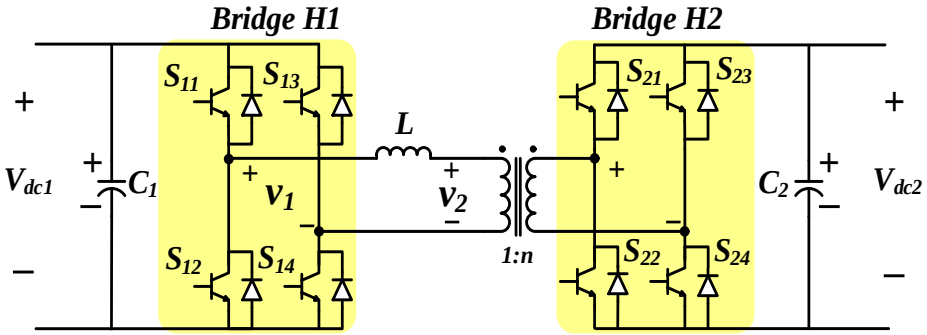

Fig. 2.1: Dual Active Bridge topology.

The presented single phase bidirectional DAB converter in Fig. 2.1 comprises of two active H-bridges, an external series inductor (L), an AC transformer and two DC link filter capacitors. As can be observed in Fig. 2.1, bridges H1 and H2 consist of four switches, S_{11}-S_{14} and S_{21}-S_{24} with integrated anti-parallel diodes. v_1 is the AC voltage of the first bridge and v_2 is the AC voltage of the second bridge after referring to primary side. At fixed values of DC voltage levels, AC link inductance and switching frequency, the amount of power transferred between the two bridges is essentially determined by the magnitude of the external phase shift between S_{11} and S_{21} while the polarity of this phase shift governs direction of power flow. Power flow direction and DC voltage levels V_{dc1} and V_{dc2} determine the DAB operating modes, which are: unity gain, buck and boost. The unity gain mode describes power transfer in DAB at equal DC voltage levels (i.e.: $V_{dc1}=V_{dc2}$.), while buck/boost operating modes occurs at different DC voltage levels (i.e.: $V_{dc1}\neq V_{dc2}$.). For instance, if $V_{dc2}<V_{dc1}$, bi-directional power inherently includes buck mode for operation in forward power flow (power flow from port 1 to port 2) and boost mode for operation in reverse power flow (power flow from port 2 to port 1). In this

regard, the ratio of DC voltage levels is usually referred to as voltage conversion ratio/gain [72]–[75] in output-voltage control schemes in DAB or stepping ratio in [76]. In this thesis, a factor K_{12} is used to represent the DC voltage ratio where K_{12}=nV_{dc2}/V_{dc1} such that n is the transformer's turns ratio and n is unity (n=1) in non-isolated (transformer-less) DAB converters.

As a potential building block in power conversion systems within HVDC, MVDC and microgrids, many existing DAB converter studies investigate modeling, control schemes, efficiency and operational performance improvements. So far, studies on DAB DC-DC converters mainly focus on the following aspects: basic characterisation, phase shift control strategies, power flow control, efficiency-improving control schemes and multi-port Active-Bridge-based DC-DC converters. This chapter will give an overview of active bridge DC-DC converters in view of this research situation.

2.1.1. Phase shift control and basic characterisation

Phase shift control techniques are the most commonly used modulation schemes in the literature due to their implementation simplicity, fundamental frequency operation (which reduces switching losses), uniform conduction of switching devices, enabling of zero voltage switching (ZVS) operation and non-active power circulation control within converter [19], [63] & [67]. The conventional phase shift (CPS), or single phase shift (SPS), was the first proposed technique [69]. The cross connected switches (S_{11} and S_{14}, S_{21} and S_{24}) are switched simultaneously in CPS modulation, which results in DAB waveforms shown in Fig. 2.2 across the transformer primary and secondary terminals. The amount and direction of the transferred power is regulated by the phase shift (D) between AC-side voltages v_1

and v_2. CPS modulation scheme is simple to implement, since only a single parameter (the phase shift angle) is required to control the power flow.

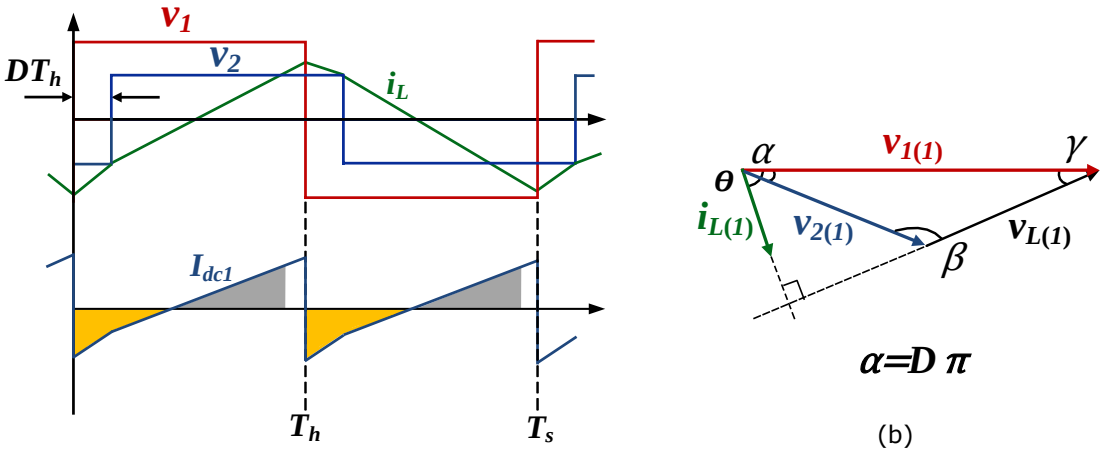

Fig. 2.2: DAB modulated using CPS: (a) AC link voltage/current waveforms (b) fundamental phasor diagram of AC link voltage/current waveforms [33].

However, when DAB is operated using CPS the inductor current i_L incorporates a reverse current portion, orange shaded area in Fig. 2.2(a), that transmits power backwards [33]. In this case, the forwarding portion (gray shaded area) will not be sufficient to maintain the desired power transfer level, and as a result i_L has to increase its forwarding portion. This phenomenon, specifically the orange and gray shaded portions, is called circulating current (or reactive current) in a DAB. There is a similar phenomenon in AC grid, where the circulating current (reactive current) does not contribute to any energy transfer but yields power device conduction losses and transformer copper losses. In addition, the circulating current will increase further as DC voltage ratio K_{12} decreases [33]. In order to explain this, the phasor diagram Fig. 2.2 (b) is employed, where the phasors $\bar{v}_{L(1)}$, $\bar{v}_{1(1)}$, $\bar{v}_{2(1)}$, $\bar{\imath}_{L(1)}$ represent fundamental harmonic components of the DAB's AC link voltages and current waveforms. These phasors satisfy:

$$\begin{aligned} \bar{v}_{L(1)} &= \bar{v}_{1(1)} - \bar{v}_{2(1)}. \\ \bar{\imath}_{L(1)} &= \bar{v}_{L(1)}/jwL\,. \end{aligned} \tag{2.1}$$

The angles between theses phasors satisfy the law of sines:

$$\begin{gathered}\beta+\gamma=\pi-\alpha \\ \frac{\sin\gamma}{\sin\beta}=\frac{|\bar{v}_{2(1)}|}{|\bar{v}_{1(1)}|}=K_{12} \\ \theta=\frac{\pi}{2}-\gamma\end{gathered} \tag{2.2}$$

According to (2.2) and Fig. 2.2(b), a small K_{12} (K_{12} < 1) results a small γ and a large θ (the angle between $\bar{v}_{1(f)}$ and $\bar{\imath}_{L(f)}$) for a given α. Therefore, a large θ, which reflects small K_{12}, leads to higher reactive power (circulating current).

Following this, dual phase shift (DPS) modulation technique was introduced [77] to overcome the phenomenon of backflow power that appeared when using CPS. This is achieved by utilising equal inner phase shift between both the converter switch pairs S_{11}-S_{13} and S_{21}-S_{23} (legs 1 and 2 of bridge H1, and legs 1 and 2 of bridge H2). The resulting waveforms are shown in Fig. 2.3 where D_1 is the inner phase shift for both H-bridges and D_2 is the external phase shift (D_2=D in CPS control).

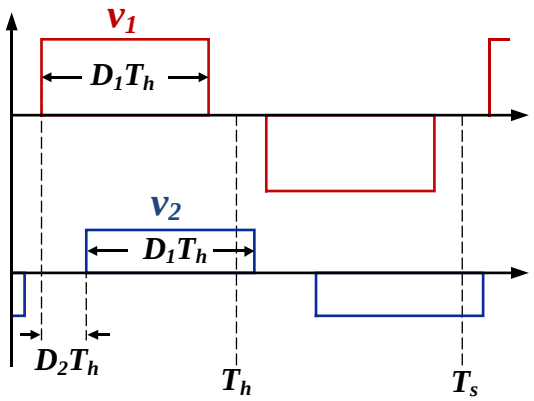

Fig. 2.3: Typical AC-link Voltages at DPS.

Extended phase shift (EPS) was further proposed [72], in order to extend the soft switching region and improve overall efficiency of the converter by minimising the losses (reactive power circulating within the converter bridges). An additional

inner parameter 'D_1' is utilised, in EPS control, which is the phase shift between the legs of one H-bridge; while the cross connected switches are switched simultaneously in the second H-bridge. This results in a quasi-square AC output waveform for the bridge where inner shift D_1 is used and a full AC square waveform for the second H-bridge as Fig. 2.4 depicts. The outer phase shift angle 'D_2' controls the power flow magnitude and direction, which is equivalent to 'D' in CPS modulation, whereas D_1 is introduced to extend the ZVS and reduce the reactive power.

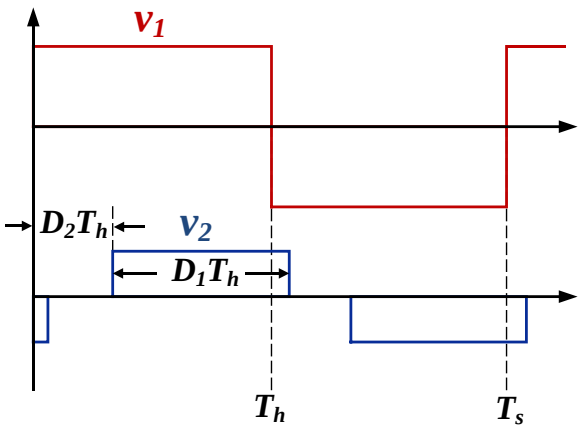

Fig. 2.4: Typical AC-link Voltages at EPS.

While all the above mentioned modulation techniques (CPS, DPS and EPS) do work they share a common drawback – partial exploitation of the available degrees of freedom (control variables), which leads to sub-optimal (poor) operational efficiency of DAB in situations of high stepping (high DC voltage ratios) and/or light loads. In this regard, triple phase shift (TPS) [73], [78], [79] introduces an additional control variable which can lead to further improvement of ZVS range; thus reducing the overall converter losses and increasing efficiency figures. TPS control employs three control parameters:

- D_1 is the inner phase shift between switches S_{11} & S_{14}.
- D_2 is the inner phase shift between the switches S_{21} & S_{24}.

- D_{12} is the outer/external phase shift between S_{11} & S_{21}.

This makes TPS the most general modulation control such that any other modulation scheme is a special case of TPS [80]. Utilisation of these three parameters results in the output voltage waveforms across primary and secondary transformer sides to be as depicted by Fig. 2.5. Phase shift D_{12} between the two H-bridges voltages is utilised to control the magnitude and direction of power flow, while the duty ratios D_1 and D_2 (inner phase shifts) are mainly introduced to improve the DAB operation.

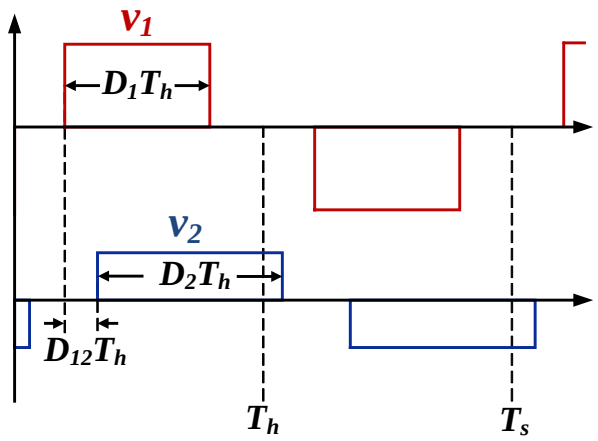

Fig. 2.5: Typical AC-link Voltages at TPS.

With the increase of phase shift degrees of freedom in TPS, there are infinite varieties of switch sequence combinations (when D_1, D_2, D_{12} take any values). The AC link inductor current waveform is usually analysed piece by piece to derive the analytic formulations of RMS current and transferred power [32], [73], [74], [80], [81]. Developing DAB steady state model and deriving the mathematical expressions for relevant parameters such as power transferred, RMS inductor current, and reactive power for DAB under any switching combination generated by TPS are considerably difficult due to multiple operation (switching) modes [73], [81]. In this regard, identification of switching modes in DAB under TPS has been extensively addressed in literature. Four switching modes were identified in [82]

using TPS to increase the converter efficiency and extend zero voltage switching (ZVS) operating range. Three converter switching modes were proposed in [83]. However, the model proposed cannot be considered as universal as it does not cover the entire bidirectional power range but only covers operation from -0.5 to -1 pu. A study of a multiphase shift scheme including DPS and TPS was investigated in [84] to identify optimal sub modes from the waveform features. DAB converter under TPS control has to be divided into twelve switching modes according to different conditions among three modulation parameters (phase shift variables), which are illustrated in [32], [85], [74], [80], [86]. In [32], [85] the twelve switching modes were characterised and fundamental component approximation was used to perform partial analysis for some of the modes. Detailed analytical derivations of transmission power and RMS current along with operational constraints for all possible switching modes DAB under TPS control were presented in [80], [86]. However the DC voltage ratio is not included in the proposed model in [80], which is a major drawback; in addition to lack of unified current stress characterisation and partial per unit analysis. On the other hand, the accuracy and design difficulty of control schemes are closely related to the mathematical model of the TPS method represented as piecewise time domain functions for different operation conditions and time intervals. That is why the efficiency-optimised and current-stress-optimised control schemes in [87] and [88] need to be divided into separate optimised sections in terms of DC voltage ratio and different loading condition.

On the other hand, Fourier analysis has been proposed an effective method of developing the steady-state DAB model [89], [90]. In fact, the fundamental harmonic component analysis represents the majority of active and reactive power values in the DAB converter [33], [90]. Using Fourier analysis can actually simplify

the analysis of operation status and the design of control systems of DAB under TPS. This is due to eliminating the need to derive the complicated mathematical model based on piecewise time domain functions for different operation condition and time intervals [80]. However, the major disadvantage of the control schemes based on Fourier analysis is the trade-off between the large amount of calculation and accuracy.

In reviewing the previous literature it is apparent that further advances in TPS control of DAB converter is required to address the concerns and unresolved issues pointed in [19] that include –

- TPS as a challenging modulation scheme to analyse and implement.
- Lack of uniformity in TPS analysis.
- The inclusion of DC voltage ratio to allow classification and analysing of all possible DAB operating modes: buck, boost and unity gain modes.
- Unified RMS current characterisation of DAB under TPS modulation scheme.

2.1.2. High-Efficiency Operation of DAB

Power transmission is the DAB's fundamental function in a power conversion unit, and to transport a desired power, there are an infinite variety of switching driving signal combinations with different system performances in terms of soft-switching range, current stress, reactive power and efficiency. Therefore, utilising the unique optimal combination of driving signal sequences, making certain performance indexes optimal in order to meet certain transmission power, is the main challenge and basic requirement to achieve high-efficiency operation of DAB [81]. This explains the recent trend toward improving the operational efficiency of DAB DC-DC converter when operated for power flow control.

There are mainly two aspects regarding DAB control schemes and performance studies: transient issues and steady-state issues. The main drive of investigating the transient issues is to eliminate the impact of non-ideal factors and improve the dynamic behavior in terms of the overshoot and the response speed. In this regard, many innovative control schemes such as feed forward control [91], [92], natural switching surface control [93], and virtual direct power control [94] have been proposed to improve dynamic performance in case of current/voltage reference changes or load disturbances. Different from the studies of transient issues, the steady-state studies are mainly conducted to explore the potential of improving overall system performance as much as possible. Steady-state studies will be the focus of this thesis and hence the upcoming reported literature review.

In this regard, there is a wide range of technical aspects that have been used in literature considering optimisation in DAB converter:

- Total power losses [88], [95].
- Back-flow power (or sometimes referred to as non-active power or reactive power) [72], [73], [75], [96]–[98].
- RMS value of inductor current [32], [74], [99].
- Current stress (often refers to peak value of inductor current) [72], [73], [83], [87].

Minimisation of any of these technical aspects is generally viable as the circuiting current is closely related with total power losses, reverse power, inductor RMS current and current stress. The current stress is the best choice in terms of simplicity as all other technical aspects require complicated calculation [33].

The phenomenon of backflow power in DAB converter and its effects on circulating current stress is extensively analysed in [72], where the authors

proposed a control scheme based on EPS for power distribution in microgrid. Non-active power loss minimisation was tackled in [96] for a DAB converter by analysing the inductor current to obtain an operating range where phase shifts achieving minimum non-active power loss for light and heavy loads were found in boost operation. However, the model was based on the EPS modulation technique, which results in local optimal operating points at light loads. A Neural Network NN-based algorithm has been proposed in [97], as shown in Fig 2.6, to search for TPS control variables that satisfy the desired active power flow while achieving minimum reactive power consumption. The proposed controller works in an open loop approach with no feedback information on whether the actual desired power level is achieved or not. In addition, the method is not generalised for buck and boost DAB operating modes.

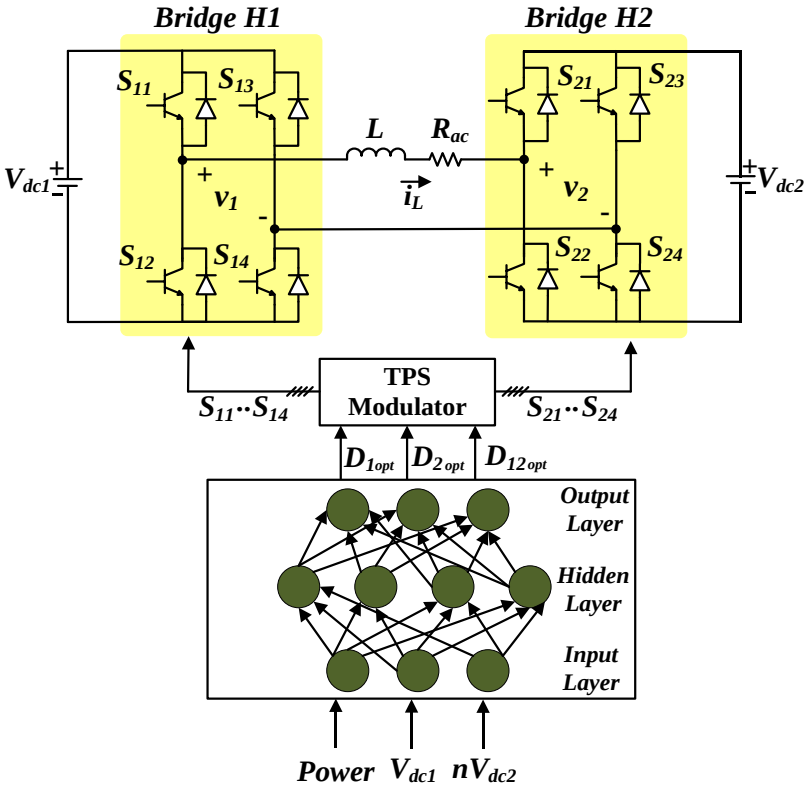

Fig. 2.6: NN-based Open-Loop Controller for Reactive Power Minimisation in DAB [97].

Authors in [83] used a Lagrange Multiplier method to calculate the optimal phase shift ratios for any given power level by targeting the minimum current stresses defined as peak inductor current. Nevertheless, the proposed converter switching modes in do not entirely cover the bidirectional power range which jeopardies the correctness of the derived controller. In addition, the peak inductor current was used as the minimisation objective however the major DAB loss is the conduction loss which it is related to the RMS current [100]. Lagrange multiplier (LMM) with Karush-Kahn-Tucker (KKT) method was used in [73] to minimise DAB current stress (described as the peak current) under TPS modulation scheme. However, it is too complicated to use KKT conditions for minimizing current and determining the ZVS boundary conditions as four order algebraic equations have to be solved. Besides, LMM lacks sufficiency due to the non-convex feasible region of this optimal problem [74].

In [32], a power flow control scheme was developed based on a hybrid phase shift technique composed of TPS and EPS to achieve the minimum inductor RMS current at a given transfer power point. However, the proposed work includes large amount of case-specific offline calculations. Such that when the parameters of DAB converter are changed, the whole offline calculations have to be computed again. A similar drawback exists in [101], [102] where a numerical method/solver was used to develop the modulation schemes to achieve the maximum efficiency. However, a case-specific offline calculation (numeric table) was required in advance as the numerical method cannot be implemented in real time for the embedded controller, hence the realisation of a practical controller is highly challenging. Reactive power minimisation was tackled in [75] using particle swarm optimisation (PSO) considering a harmonics-based DAB model such that the harmonics components are limited up to the 7^{th} harmonic as higher orders have

lower contribution. In terms of control design, a look-up table is implemented based on the optimal solutions obtained by PSO, which is a major drawback as it means that the control scheme is not generic. In addition, using a look table involve difficulties in practical implementation as for every run of the text rig, the implemented DSP needs to be loaded with the look up table at the initialization, which in turn, depends on the operating conditions (i.e.: DC voltage ratio and power levels.).

A control scheme based on the fundamental harmonic approximation (FHA) was tackled in [89], [90] & [98]. Based on these FHA methods, the optimal D_1, D_2, D_{12} are obtained by minimising peak values of fundamental component inductor current [89], maximising fundamental power factor [90] or minimizing fundamental reactive power [98]. The controller proposed by [90], shown in Fig 2.7, is based on a Fundament Optimal Phase Shift (FOBS) method that calculates TPS parameters for maximum power factor (hence minimised reactive power). In general, the FHA methods are straightforward and simple in terms of derivation and implementation, which can greatly improve the DAB efficiency. However, resultant phase shift ratios are not actually the global optimal solution in terms of circulating current minimisation [33] & [90]. This is due to neglecting the effect of higher harmonics. In fact the FHA equivalent of square voltages, inductor current or output power introduce large errors when either D_1 or D_2 is close 0 [33].

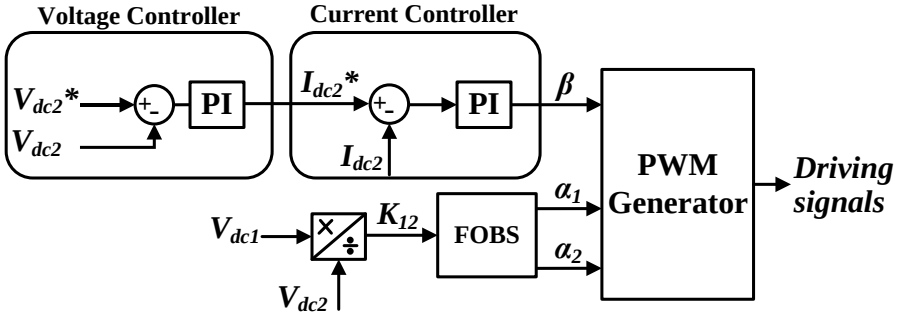

Fig. 2.7: Closed-Loop DAB Control based on Fundament Optimal Phase Shift (FOBS) method [90].

In reviewing the aforementioned literature, different minimisation objectives have been considered, however, it is believed that RMS inductor current is the most effective parameter for analysing converter performance: more so non-active power loss, peak current as minimisation objectives. This is due to the fact that RMS current stresses have a direct impact on conduction losses, which are considered to be the dominant portion of converter's total losses [30], [31]. In addition, conduction losses (in the widely used MOSFET power switches) and copper losses are proportional to the square of the RMS current [32]. In addition, reported literature in the area of efficiency-improving control schemes of DAB show various shortcomings that can be summarised as follows –

- Achieving local minimal solutions in some cases due to restricting optimisation to a specific control technique (i.e.: using EPS and/or DPS thus not utilising all possible degrees of freedom in phase shift control.).
- Control design approach that rely on a converter model which does not cover all possible switching modes or does not incorporate the effect of voltage conversion ratio, i.e.: whether converter is operating in unity gain or buck/boost modes.
- Lack of universality and existence of case-specific control design.
- The need for offline calculation, pre-set values or look up tables for implementation which is computationally exhaustive and requires complex inter/extrapolation.
- Sub-optimal TPS solutions due to using FHA-based control scheme (i.e.: ignoring the effect of higher order harmonics on RMS current.).
- Cumbersome analysis and impracticality of some derived controllers for real time implementation.

2.2. Multi Active Bridge (MAB) DC-DC Converters

The increasing penetration of renewables, the deployment of distributed generation (DG) at the consumer side and growth in load are the drivers for a technology that enables integrating DGs and storage into the distribution. This technology can work as an interface between diverse energy sources, storage elements and loads in a multi-directional power flow manner [14], [36], [103], [104]. The three-stage configuration based on a DAB converter has been proposed as a potential low-voltage-dc (LVDC) link for PV and storage integration [105]. Fig.2.8 shows a configuration of SST to achieve this via separate non-isolated DC–DC converters. In this case, separate controllers are required for each DC–DC converter; furthermore, their interaction may need to be investigated in order to ensure overall stability. In addition, if isolation is required for grounding and/or unmatched voltages exist, then additional HF transformers may be needed, thus increasing the size of the system.

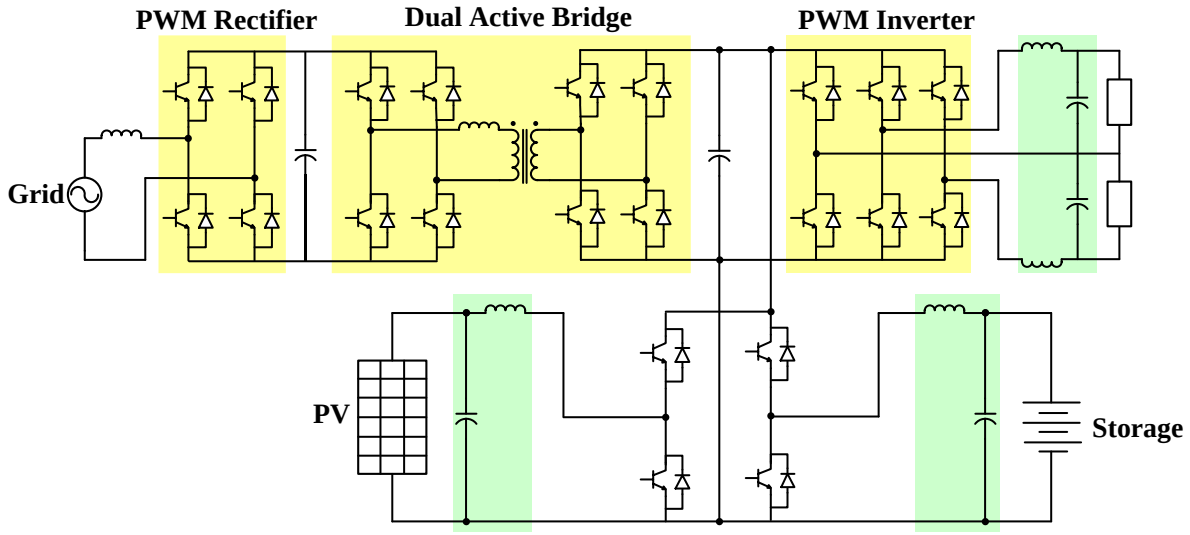

Fig. 2.8: DAB-based SST with storage and PV integrated via separate converters [14].

The fact that a DAB DC-DC converter can connect two separate ports formed the concept of multiport interfacing by using multi-individual DC-DC conversion

stages that share a common link where energy from all ports is exchanged. Various versions of the multi-port DC-DC converter have been presented in literature, such as the: current-fed multiport type, three-phase multiport type and half-bridge multiport type [106]–[109]. However, this thesis focuses on the active-bridge-based multi-port converter, which is usually referred to as multi active bridge (MAB) converter [110] and has been proposed by [109]. MAB DC-DC converters offers various functionalities and advantages compared to other versions of the multi-port DC-DC converter, which is the same case as DAB when compared to other bidirectional two port DC-DC converters [19]. MAB is a generic converter that can contain any number of active bridges (H-bridge) to increase the number of power ports [110]–[112]. Fig. 2.9 shows a circuit diagram of an *n*-port MAB converter that is comprised of *n*-active-bridge modules magnetically coupled through an *n*-winding HF transformer.

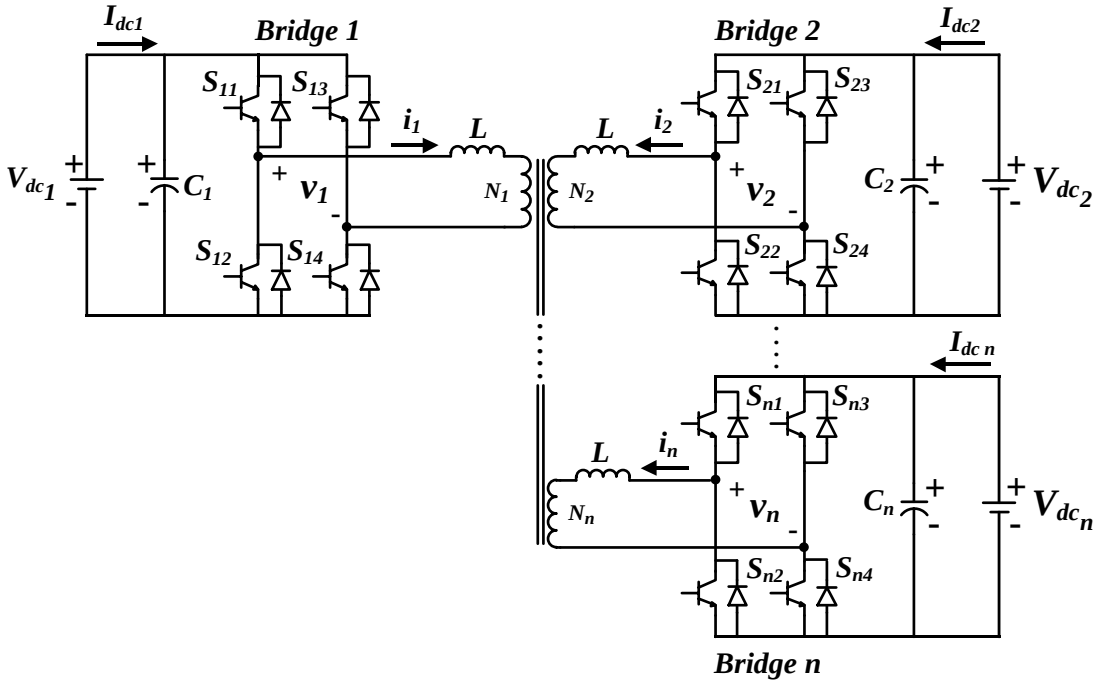

Fig. 2.9: Schematic of the MAB converter.

The main advantages of MAB are: interconnection of several sources with different voltage ratings by adjusting the HF transformer turn ratios, ZVS capability and reduced DC-DC conversion stages which yields a higher power density [57]–[60], [63]. MAB also offers cascaded or modular configuration capability in case of higher power/voltage requirements. Moreover utilising MAB converter can offer integrated control design with reduced number of controllers needed in multiple-stage configurations based on DAB – Fig. 2.4 – which ensures more stability and eliminates the need to study the interaction between controllers [14]. Fig 2.10 shows an example of SST based on a four-port MAB converter (quad-active-bridge (QAB)) that includes the grid, the load, the PV system, plus the storage through a single four-winding HF transformer providing isolation for DG and storage. This means minimum DC–DC conversion stages and a higher power density when compared to DAB-based SST configuration (Fig 2.4).

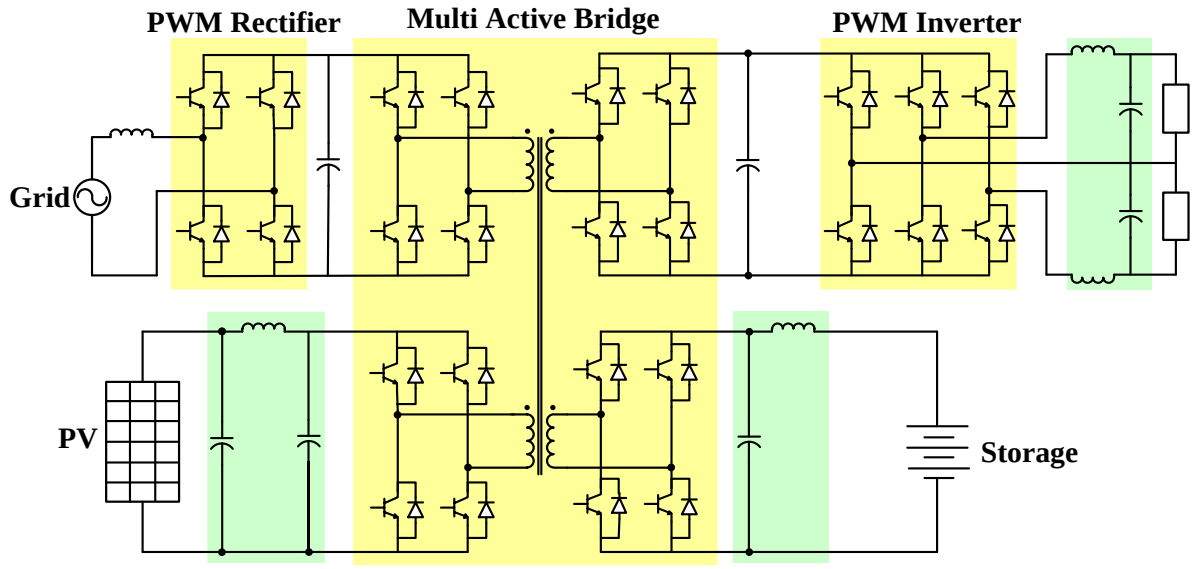

Fig. 2.10:MAB-based SST with storage and PV integrated via HF transformer [14].

Isolated MAB converters based on an AC-link topology that utilise multi-winding transformer interfaces are presented in [34], [35], [103], [104], [111]–[116]. The transformer handles integration and exchanging of energy between all

ports. In addition, the transformer provides full port-to-port isolation and matching of different port voltage levels. The equivalent circuit of a multi-winding transformer is given by star or delta connected inductive AC-link which is usually used to simplify modeling and steady state analysis [14], [103].

2.2.1. Steady state modelling and control

Given the fact that MAB DC-DC converters are derived from DAB, phase shift modulation control has been widely used for multiport DC-DC converters where square-wave gate signals, with 50% duty ratio, are implemented to enable control of power transfer and/or performance improvement. Power flow and voltage control schemes based on phase shifting modulation have been extensively addressed in literature for MAB converters. A study based on fundamental analysis and duty-changed modulation was proposed in [35] for isolated triple active bridge (TAB). Another study proposed a duty ratio modulation to extend ZVS for the isolated TAB in [114]. Furthermore, a control technique was designed to achieve power flow management with soft switching for TAB converter in a fuel cell and super capacitor system. However the proposed model in both [35] and [114] is not generalised as the duty ratio of one of the bridge voltages was assumed to be constant. A modelling and power flow scheme for triple active bridge was presented in [103], however the proposed model is cumbersome and non-scalable (i.e.: only applicable on three-port MAB converter.). Authors in [111], [112] proposed a case-specific (i.e.: 10 kW, 400 V, 20 kHz.) power flow control system for TAB. Another power flow management scheme, for a TAB converter implemented in Aircraft network, was proposed in [34] along with a procedure to restore the system back to normal operation in the event of a DC fault. A voltage control scheme was proposed in [14] for a quad active bridge based an average model. Regardless, control schemes in [14], [34], [111], [112] are not universal

for *n*-port MAB converter and utilise fixed duty ratios which leads to poor efficiency in light loads and/or non-unity DC voltage ratios. Power flow regulation in MAB incorporates has nonlinear relationship (coupled relationship) with phase shifts, unlike power transfer in DAB that depends on a single control parameter (i.e.: single phase-shift between the voltages across the terminals of the two H-bridges.). Power flow decoupling has been explored in [103] for a TAB converter with a case study assuming port 1 is connected to a voltage source, port 2 is connected to an RC Load and port 3 is connected to an RC load parallel to a voltage source. This case study is not universal as it does not treat ports as sources/sinks of power enabling bi-directional power flow at any port: the same drawback exists in [106].

On the other hand, more advanced control schemes have been proposed for the MAB converter with two ports (dual active bridge DAB) which is considered as the simplest form of MAB converter [32], [75], [83], [117]. Predictive control and/or optimal TPS relations obtained by particle swarm optimisation (PSO), Lagrange Multiplier and/or utilising look-up tables are implemented in DAB studies to operate the DAB under most suitable (optimal) switching states to improve the converter efficiency. However, the conventional methods, which are used to develop control strategies for the two-port (DAB) converter, become very complicated to design – and implement – as they require complicated modeling and/or huge amount of data points. As an example, in a four-port active bridge converter there are 256 switching states – for each additional active bridge the number of operating modes increases with a factor four [118]. In the presence of such a high number of states the normally applied piecewise-linear methods, used when developing control strategies, do not provide sufficient insight into the operation of the converter and are problematic to use.

Regarding the aforementioned literature, scalability is overlooked given that reported control schemes are often case-specific with regard to either number of ports, voltage-power rating and/or unidirectional power flow assumption at certain ports. Hence, studying MAB in this thesis will consider a generic use case, which includes multi fixed or variable DC side voltages (e.g.: batteries or controlled DC busses in a DC grid.). This use case guarantees universality as it treats ports as sources/sinks of power enabling bi-directional power flow at any port, whereas cases including a DC source and passive loads are more specific (i.e.: unidirectional power flow.) [103], [106], [107]. Shortcomings in reviewed literature regarding MAB DC-DC converters are summarised as follows:

- Lack of an implement standard of multi phase shifting in MAB converters as reported control schemes often utilise fixed duty ratio when applying multi phase shifting. This leads to high current stresses and sub-optimum operation of converter; particularly under light load or unmatched voltage amplitudes across the transformer sides (AC link).
- Control schemes developed for MAB are often case-specific with regard to either number of ports, voltage-power rating and/or unidirectional power flow assumption at certain ports.
- The heavy dependency of the controllers on complex converter modelling, non-linear equations and circuit parameters.
- Lack of a generic active power flow representation in MAB converters.
- Lack of a scalable phase shift decoupler for MAB converters with any number of ports. This is vital to decouple the power from phase shifts hence facilitating the use of conventional controller, such as PI controllers, for power flow regulation in MAB.

- Lack of per unit steady state modelling of the non-isolated DC-DC MAB converters under various purely inductor-based AC link topologies.

2.2.2. Non-isolated MAB converter

Considering the aforementioned literature, it is quite apparent that the study of non-isolated multi-port DC-DC converters, under purely inductive AC-link topologies, has not been fully investigated. Fig 2.11 shows a schematic of non-isolated MAB converter under inductive AC link with AC-side terminals (a_1:a_n and b_1:b_n) allowing for multiple AC link topologies that need investigating.

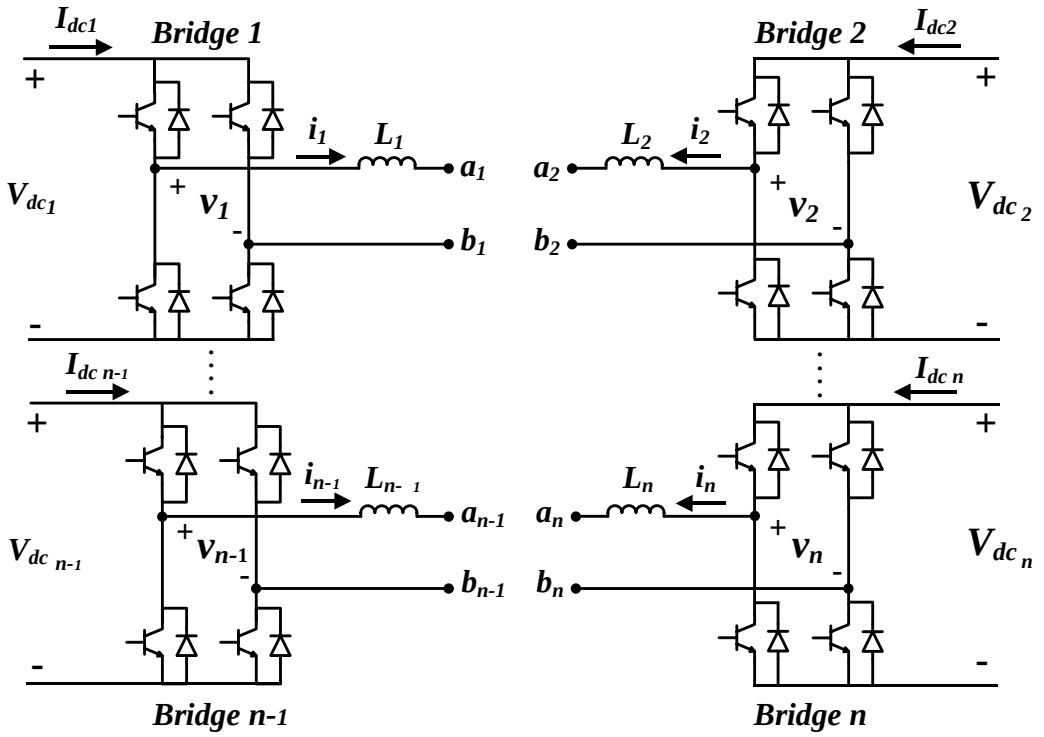

Fig. 2.11: Schematic of a Non-Isolated MAB converter under inductive AC link with possibility for multiple AC link topologies.

Despite the advantages offered by using a transformer (i.e.: such as voltage matching and isolation.), the use of the multi-winding transformer in MAB often leads to higher copper and switching losses. For example, in the case of a TAB, if two sources providing AC voltages are not in phase then their resulting flux will

oppose each other which, in turn, reduces the resultant flux [119]. This will decrease the induced voltages in the transformer windings – high inrush currents will also flow through the converter as well as the transformer winding. Moreover, in some low-power applications, absence of an interface transformer in the converter can significantly reduce the converter weight and footprint. In fact, since inductors can be air-core based their use can help avoid magnetic saturation and also mitigate the high frequency constraints imposed by high losses in magnetic cores. Additionally, studying the purely-inductive AC-link can significantly simplify analysis and controller design procedure for the multi-port active bridge converters. This is due to accepting that the AC inductor is fundamentally an equivalent model of a transformer's leakage inductance; besides, the transformer and its equivalent star/delta inductive circuit have almost the same performance in steady state. Based on the identified research gap this thesis will investigate the following:

- Modelling and analysis of the inductive-based AC-link non-isolated MAB DC-DC converter.
- Identifying the optimal topology of the inductive-based AC link non-isolated MAB in terms of minimum value of interface inductors (i.e.: lowest footprint.) as well as minimum current stresses.

2.3. Summary

An overview of literature in both DAB and MAB converters has been presented focusing on steady state modeling, control scheme design and efficiency improvement techniques. The reported literature shows various shortcomings, mainly: lack of universality and case-specific control design, offline calculation, sub-optimal solution due to using FHA-based control scheme and complexity in

implementation due to using look-up table. In addition, there is a lack of an implement standard of phase shift control in MAB (i.e.: using EPS and/or DPS in DAB or utilise fixed duty ratio in MAB.). This leads to high current stresses and sub-optimum operation of the converter; particularly under light load or unmatched voltage amplitudes across the transformer sides (AC link). Furthermore, control schemes developed for MAB are often case-specific regarding either number of ports, voltage-power rating and/or unidirectional power flow assumption at certain ports. Moreover, there is a lack of a generic power flow analysis which is valid for a MAB converter with any number of ports.

This explains the need of further advances in the modelling and control scheme design for MAB converters. In fact, to the best of the author's knowledge, no work has fully attempted to engage with all the above challenges. In the attempts made, there was a compromise on the level of control complexity and reduced ability to implement optimisation in real time. The work contained in this thesis identifies this research gap and therefore proposes a comprehensive set of solutions to the aforementioned shortcomings.

Chapter 3. Modelling and Analysis of DAB DC-DC Converter

This chapter presents a comprehensive and generalised steady state analysis in the use of TPS control for the bidirectional Dual Active Bridge (DAB) DC-DC converter with the circuit diagram shown in Fig.3.1. A complete switching mode classification method is adopted in this chapter based on the voltage decoupling of primary and secondary H-bridges method in [80]. A detailed steady state model of DAB is presented where per unit expressions for power transferred are derived under all switching modes. In addition, the model includes a new single equation representing AC link RMS current. All expressions are presented as function of TPS modulation parameters and DC voltage ratio. On this basis, a clear classification of the operating modes of DAB (i.e.: unity-gain and buck/boost modes.) under different conversion ratios is developed.

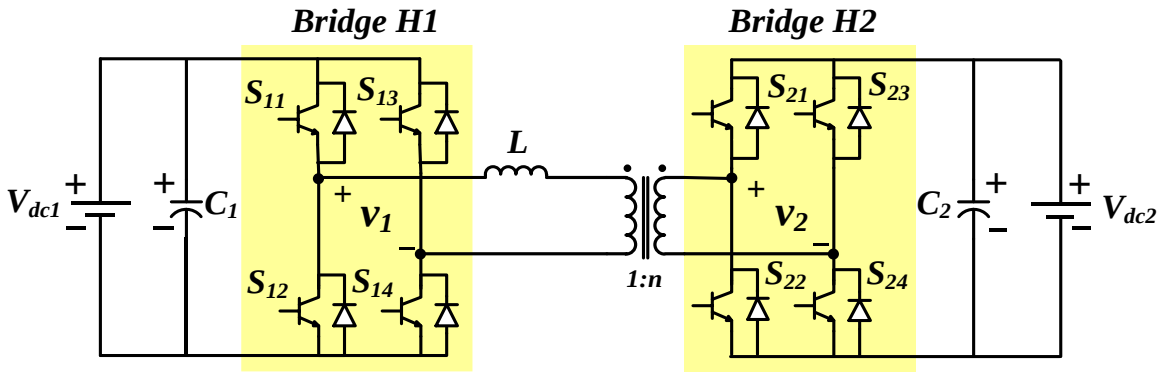

Fig. 3.1: Circuit Diagram of Dual Active Bridge converter.

After the analysis, SIMULINK-based switching DAB circuit is used to verify the correctness of the derived detailed model. In addition, an approximate DAB model is derived based on fundamental harmonic approximation. A model comparison is then held between both the detailed and approximate models to evaluate the effectiveness of fundamental-harmonic-based model as an approximate tool (free

from switching mode classification) in representing the main DAB parameters. A key chapter theme is the advanced treatment of TPS control of DAB by addressing the following concerns and unresolved issues:

- Non-standardised presentation of TPS modulation scheme.
- Lack of a generalised power flow analysis that incorporates DC voltage ratios (i.e.: Buck/Boost/Unity-gain operating modes.).
- Lack of a unified per unit analytical expression for DAB's AC RMS current.

3.1. Detailed Steady State Model

This section covers the development of an exact steady state model of DAB. This involves three parts: identification of all possible switching modes of DAB under TPS modulation scheme, AC link inductor analysis and power flow characteristics. TPS offers three degrees of freedom, particularly: duty ratios of AC-side voltages D_1, D_2 and phase shift D_{12}, such that in $0 \leq D_1 \leq 1$, $0 \leq D_2 \leq 1$ and $0 \leq D_{12} \leq 1$ where modulation parameters (D_1, D_2, D_{12}) are normalised with respect to half the switching cycle (T_h). The ratio D_1 represents the pulse width of the AC voltage waveform of first bridge (v_1), and similarly, ratio D_2 represents the pulse width of the second bridge voltage waveform (v_2). D_1, D_2 and D_{12} are obtained, as depicted in Fig 3.2 (a), by phase shifting the gate signals of switching devices S_{11}-S_{14} and S_{21}-S_{24}. Fig 3.2 parts(a) and (b) illustrate examples of AC-side current and voltages waveforms in DAB under TPS control representing bidirectional power flow [80], [120]. However, the definition of the phase shift D_{12} in [80], [120] is not unified, as it represents the phase angle between the positive edge of bridge voltages in forward power flow while, in the reverse power flow, D_{12} is defined as the phase angle between the positive edge of bridge 1 voltage and the negative edge of bridge 2 voltage. This definition also does not allow the phase shift D_{12} to

represent the actual performance converter in reverse power flow. Accordingly, phase shift D_{12} is re-defined in this thesis to represent the phase angle between the positive edge of bridge voltage v_1 and v_2 as this guarantees consistency in analysis, accordingly the operating range of D_{12} becomes $-1 \leq D_{12} \leq 1$.

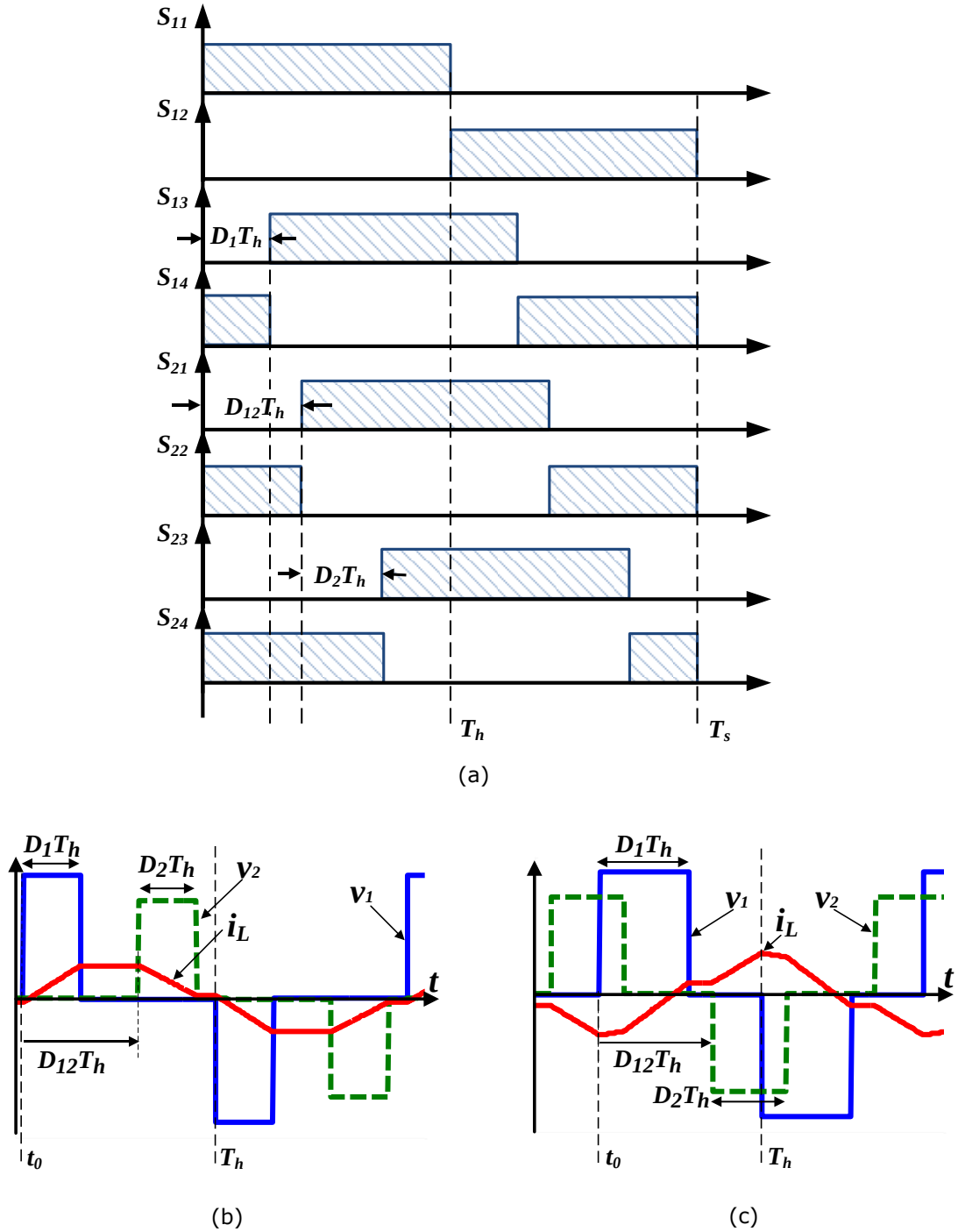

Fig. 3.2: Waveforms in DAB under TPS control in [80], [120]. (a) Switching Signals, and AC link Voltage and current in (b) Forward (+ve) power flow, (c) Reverse (-ve) power flow.

3.1.1. Switching modes classification

Considering all possible combinations of D_1, D_2 and D_{12} – with full, partial and no overlaps of both AC-side voltage waveforms – results in twelve switching modes for the bidirectional power flow. The twelve operating modes and their operational constraints (i.e.: boundary conditions.) are identified in [80][120]; which are adopted in this thesis as they represent all switching modes and whole operating power range of DAB [33]. After applying the new definition of phase shift D_{12} proposed in this thesis, typical AC link voltage and current waveforms of each switching modes with their operational constraints are outlined in Table 3.1. The operational constraints maintain the unique characteristics of each switching mode. For example, boundary conditions in mode 1 maintain full overlap of both bridge AC voltages, which is the unique characteristic that identifies switching mode 1. In the analysis of this chapter, the following assumptions are considered:

- Lossless DAB converter, the second H-bridge is referred to the primary side, while the transformer leakage inductance is added to an external inductor, resulting in inductance L. In a transformer-less DAB, L will be the interface inductor and the only energy storage element. Fig.3.3 shows the equivalent lossless DAB circuit after referring to the primary.
- Fixed DC side voltages V_{dc1} & V_{dc2}.
- The transformer magnetising inductance is neglected.
- It is assumed that parasitic resistances of passive components are neglected.
- Short time scale factors are neglected such as switching dynamics and dead band effects, which is widely accepted approach in steady state modelling [32], [72], [73], [80], [97], [121].
- For the sake of per unit analysis, (3.1) defines the base values.

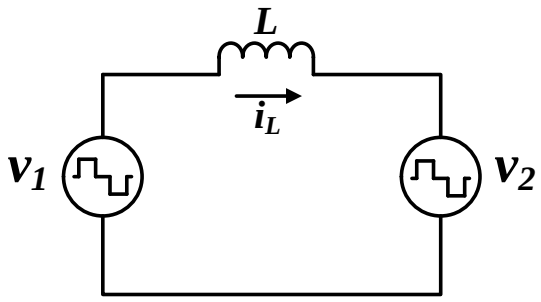

Fig. 3.3: Equivalent circuit of Dual Active Bridge.

$$V_{base} = V_{dc1}$$
$$Z_{base} = 8f_sL$$
$$P_{base} = \frac{{V_{base}}^2}{Z_{base}} = \frac{{V_{dc1}}^2}{8f_sL} \quad (3.1)$$

Where f_s *is the* switching frequency and $f_s = \frac{1}{2T_h}$ where T_h is half switching period.

Table 3.1: Switching Modes of DAB with Operational Constraints Under TPS control.

	Mode 1	**Mode 1'**
Waveforms	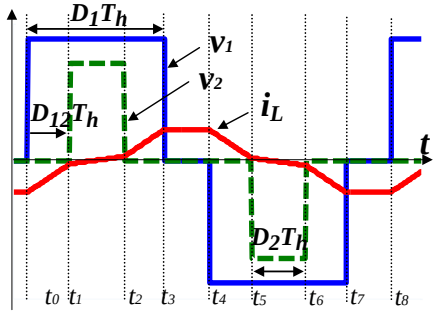	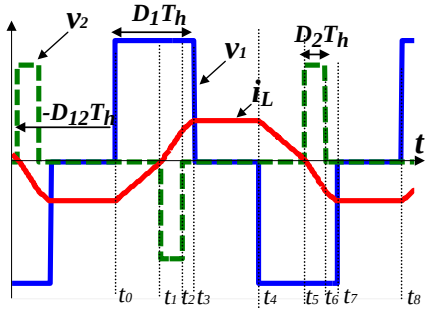
Normalised time instants to T_h	$t_0 = 0, t_1 = D_{12}, t_2 = D_2 + D_{12}$ $t_3 = D_1, t_4 = 1$	$t_0 = 0, t_1 = D_{12} + 1, t_2 = D_2 + D_{12} + 1$ $t_3 = D_1, t_4 = 1$
Operational Constraints	$D_1 \geq D_2$ $0 \leq D_{12} \leq D_1 - D_2$	$D_1 \geq D_2$ $0 \leq D_{12} + 1 \leq D_1 - D_2$
	Mode 2	**Mode 2'**
Waveforms	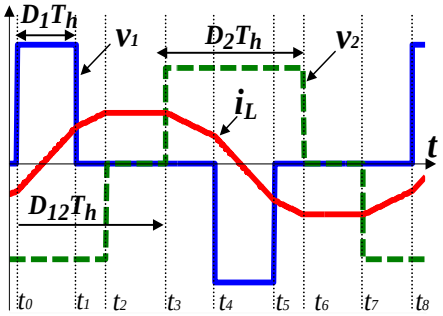	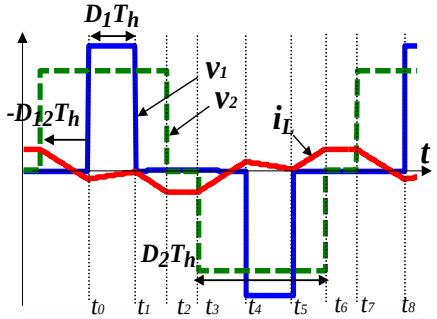

Normalised time instants to T_h	$t_0 = 0, t_1 = D_1, t_2 = D_2 + D_{12} - 1$ $t_3 = D_3, t_4 = 1$	$t_0 = 0, t_1 = D_1, t_2 = D_2 + D_{12}$ $t_3 = D_{12} + 1,\ t_4 = 1$
Operational Constraints	$D_2 \geq D_1$ $(1 + D_1 - D_2) \leq D_{12} \leq 1$	$D_2 \geq D_1$ $(1 + D_1 - D_2) \leq D_{12} + 1 \leq 1$
	Mode 3	**Mode 3'**
Waveforms	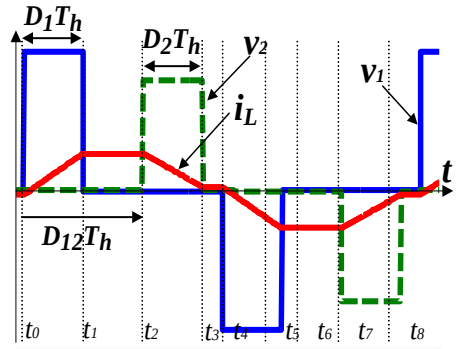	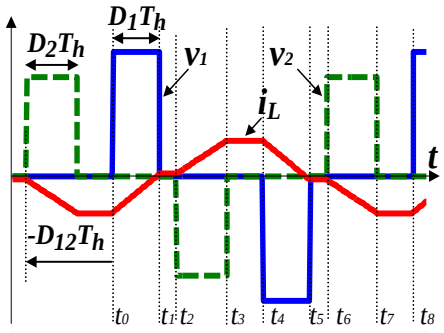
Normalised time instants to T_h	$t_0 = 0, t_1 = D_1, t_2 = D_3$ $t_3 = D_2 + D_{12}, t_4 = 1$	$t_0 = 0, t_1 = D_1, t_2 = D_{12} + 1$ $t_3 = D_2 + D_{12} + 1, t_4 = 1$
Operational Constraints	$D_2 \leq 1 - D_1$ $D_1 \leq D_{12} \leq 1 - D_2$	$D_2 \leq 1 - D_1$ $D_1 \leq D_{12} + 1 \leq 1 - D_2$
	Mode 4	**Mode 4'**
Waveforms	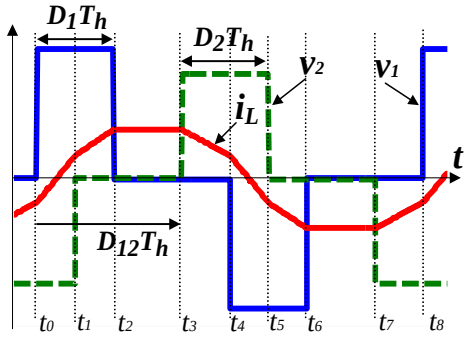	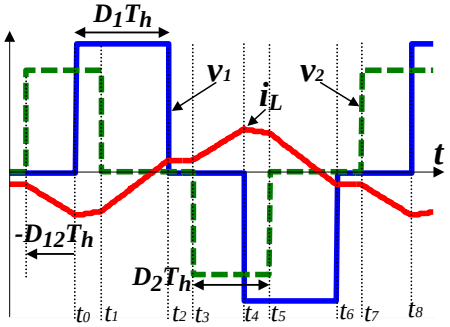
Normalised time instants to T_h	$t_0 = 0, t_1 = D_2 + D_{12} - 1, t_2 = D_1$ $t_3 = D_{12}, t_4 = 1$	$t_0 = 0, t_1 = D_2 + D_{12}, t_2 = D_1$ $t_3 = D_{12} + 1, t_4 = 1$
Operational Constraints	$D_1 \leq D_{12} \leq 1$ $1 - D_{12} \leq D_2 \leq 1 - D_{12} + D_1$	$D_1 \leq D_{12} + 1 \leq 1$ $-D_{12} \leq D_2 \leq -D_{12} + D_1$
	Mode 5	**Mode 5'**
Waveforms	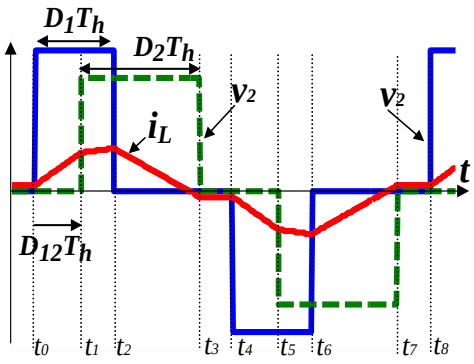	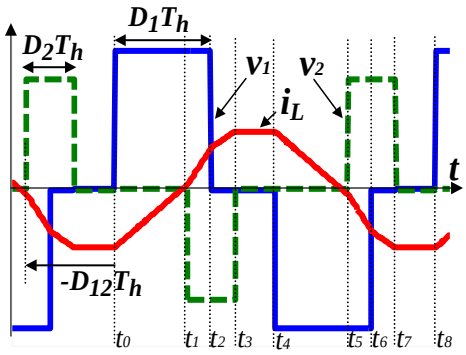
Normalised time instants to T_h	$t_0 = 0, t_1 = D_{12}, t_2 = D_1$ $t_3 = D_2 + D_{12}, t_4 = 1$	$t_0 = 0, t_1 = D_{12} + 1, t_2 = D_1$ $t_3 = D_2 + D_{12} + 1, t_4 = 1$

Operational Constraints	$D_1 - D_{12} \leq D_2 \leq 1 - D_{12}$ $0 \leq D_{12} \leq D_1$	$D_1 - D_{12} - 1 \leq D_2 \leq -D_{12}$ $0 \leq D_{12} + 1 \leq D_1$
	Mode 6	**Mode 6'**
Waveforms	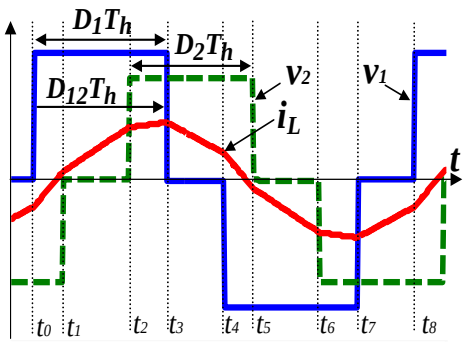	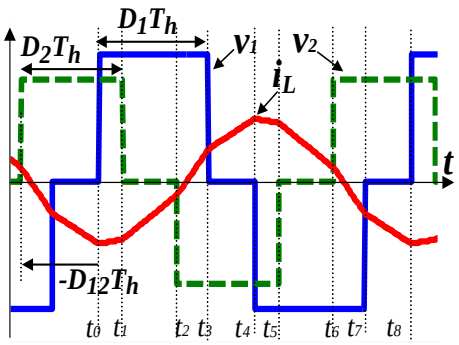
Normalised time instants to T_h	$t_0 = 0, t_1 = D_2 + D_{12} - 1, t_2 = D_{12}$ $t_3 = D_1, t_4 = 1$	$t_0 = 0, t_1 = D_2 + D_{12}, t_2 = D_{12} + 1$ $t_3 = D_1, t_4 = 1$
Operational Constraints	$1 - D_2 \leq D_1$ $1 - D_2 \leq D_{12} \leq D_1$	$1 - D_2 \leq D_1$ $1 - D_2 \leq D_{12} + 1 \leq D_1$

3.1.2. AC Link inductor current

This subsection covers the derivation of AC link inductor RMS current, which is critical for active and reactive power calculations. Authors in [80] derived an RMS current equation for every switching mode. The objective of this section is to derive a single per unit equation that is generalised for all switching modes of DAB; besides, this equation should be a function only of TPS control parameters D_1, D_2, D_{12} and voltage conversion ratio K_{12}. The AC link inductor current of a DAB is analysed using a half-wave-symmetrical approach as shown in Fig. 3.4. Using this approach, the AC-link current is segmented into $i_{L_1}(t)$, $i_{L_2}(t)$, $i_{L_3}(t)$ and $i_{L_4}(t)$ across the half wave. These current segments can be derived as function of switching instants (t_0, t_1, t_2, t_3, t_4) and associated current values ($i_L(t_0)$, $i_L(t_1)$, $i_L(t_2)$, $i_L(t_3)$, $i_L(t_4)$).

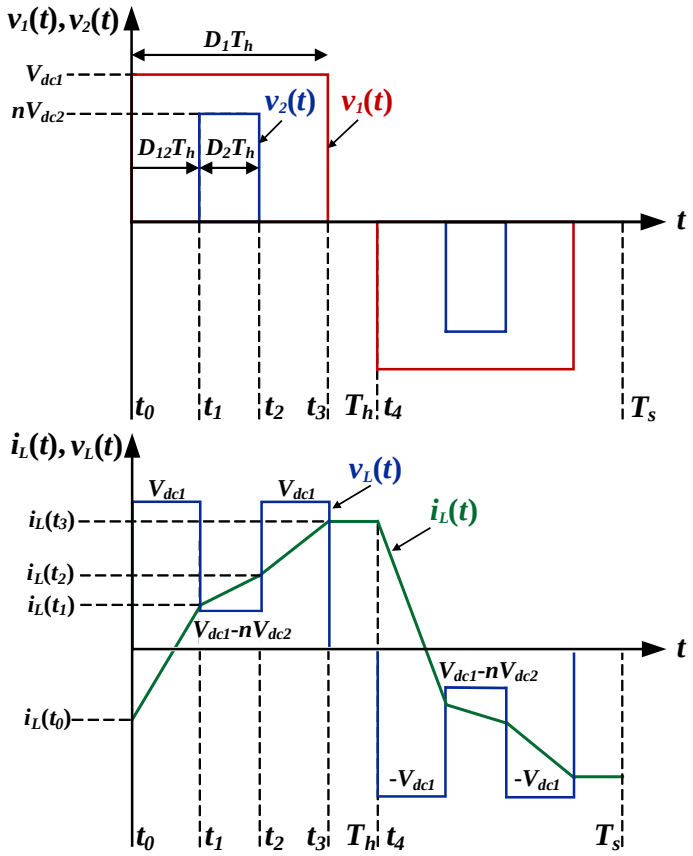

Fig. 3.4: Steady state AC voltage/current waveforms of DAB for mode 1.

For example, the two x-y coordinates (0, $i_L(t_0)$) and (t_1, $i_L(t_1)$) are utilised to derive $i_{L_1}(t)$. Since it is assumed it's a lossless DAB with neglected parasitic resistance as shown in Fig 3.3, then it is possible to substitute these coordinates in the linear equation (3.2) to obtain $i_{L_1}(t)$ as outlined by (3.3). Similarly, the remaining current segments are derived as given by (3.4) to (3.6) where current segments are expressed as function of switching instants and current instants.

$$\frac{y - y_1}{x - x_1} = \frac{y_2 - y_1}{x_2 - x_1} \tag{3.2}$$

$$i_{L_1}(t) = \left(\frac{i_L(t_1) - i_L(t_0)}{t_1}\right) t + i_L(t_0) \tag{3.3}$$

$$i_{L_2}(t) = \left(\frac{i_L(t_2) - i_L(t_1)}{t_2 - t_1}\right) t + i_L(t_1) \tag{3.4}$$

$$i_{L_3}(t) = \left(\frac{i_L(t_3) - i_L(t_2)}{t_3 - t_2}\right) t + i_L(t_2) \tag{3.5}$$

$$i_{L_4}(t) = \left(\frac{i_L(t_0) - i_L(t_3)}{t_0 - t_3}\right) t + i_L(t_3) \tag{3.6}$$

A generalised expression for squared RMS inductor current $({I_{L\,RMS}}^2)$ can be developed by examining the waveforms of inductor currents in the twelve switching modes shown in Table 3.1. Considering the inductor current half-wave symmetry as shown in Fig. 3.4, then a general expression of ${I_{L\,RMS}}^2$ can be derived using (3.7).

$${I_{L\,RMS}}^2 = \frac{1}{T_h}\int_0^{T_h} {i_L}^2(t)\ dt. \tag{3.7}$$

Firstly, (3.7) is expanded by piecewise consideration of the current waveforms over half the period as follows:

$${I_{L\,RMS}}^2 = \frac{1}{T_h}\left\{\int_0^{t_1} {i_{L_1}}^2(t)\ dt + \int_{t_1}^{t_2} {i_{L_2}}^2(t)\ dt\ + \int_{t_2}^{t_3} {i_{L_3}}^2(t)\ dt + \int_{t_3}^{t_4} {i_{L_4}}^2(t)\ dt\right\}. \tag{3.8}$$

By substituting equations (3.3) through to (3.6) into (3.8), a **single** per unit RMS current expression can be derived as shown by (3.9): this has not been presented before in the literature. In this way, calculation of RMS inductor current — using single equation — is simpler compared to the conventional tedious method that utilises many equations to calculate the inductor current stress ([80], [120] use twelve equations and [73] use five equations) depending on the TPS combination (i.e.: switching mode). Also, this facilitates programming structure by eliminating the need of conditions (used to differentiate between switching modes) and thus reduce run time. Last but not least, this equation does not compromise the accuracy of calculating the RMS current compared to the conventional methods, verification of the derived current and active power equations (i.e.: steady sate model.) will be presented later in this chapter.

$$I_{L\,RMS}{}^2(K_{12}, D_1, D_2, D_{12}) = \frac{1}{3}\{i_L(t_0)^2.(t_1 + 1 - t_3) + i_L(t_1)^2.(t_2) + i_L(t_2)^2.(-t_1 + t_3) + i_L(t_3)^2.(-t_2 + 1) + i_L(t_0).i_L(t_1).(t_1) + i_L(t_1).i_L(t_2).(t_2 - t_1) + i_L(t_2).i_L(t_3).(t_3 - t_2) + i_L(t_0).i_L(t_3).(-1 + t_3)\}$$

(3.9)

Consequently, RMS current can be calculated by substituting the switching instants t_1, t_2, t_3 and t_4 from Table 3.1 and current values at the switching instants, which is derived in this section.

The current values for the half wave switching instants for all modes have been derived in [120]. The same derivation method is used for all modes due to half wave symmetry of inductor current for all modes, therefore the derivation for only mode 1 is provided here. Considering the AC link's voltage and current waveforms of mode 1 depicted in Fig.3.4, due to half wave symmetry, only four different switching intervals will need to be analysed. By piecewise consideration the inductor current of each interval can be derived by applying Kirchhoff voltage law (KVL) according to:

$$i_L(t) = \frac{1}{L}\int_{t_n}^{t}\left(v_1(t) - v'_2(t)\right)dt + i_L(t_n) \qquad t_n \le t \le t_{n+1}. \tag{3.10}$$

Where $v_1(t)$ and $v_2(t)$ are the AC-side voltages and t_n represents n^{th} switching instant.

- ***Interval t_0 - t_1.*** The voltage across inductor is fixed at V_{dc1}. Therefore, according to (3.10), the current is obtained by −

$$i_L(t) = \frac{V_{dc1}}{L}(t - t_0) + i_L(t_0). \tag{3.11}$$

- ***Interval t_1 - t_2.*** The resultant inductor voltage is V_{dc1}-nV_{dc2}, thus, the inductor current is given by −

$$i_L(t) = \frac{V_{dc1} - nV_{dc2}}{L}(t - t_1) + i_L(t_1). \tag{3.12}$$

- ***Interval t_2 - t_3.*** The voltage imposed across inductor is V_{dc1}, thus, inductor current can be obtained as –

$$i_L(t) = \frac{V_{dc1}}{L}(t - t_2) + i_L(t_2). \tag{3.13}$$

- ***Interval t_3 - t_4.*** The inductor voltage is zero and thus, the current through L is –

$$i_L(t) = i_L(t_3). \tag{3.14}$$

Initial inductor current $i_L(t_o)$ can be derived from equations (3.11) to (3.14) considering the volts-second balance of the inductor current. This requires the following steps –

- Substitute by $t=t_1$ in (3.11). This will give $i_L(t_1)$ as a function of $i_L(t_0)$.
- Substitute for $i_L(t_1)$ in (3.12) and $t=t_2$. This will produce $i_L(t_2)$ as a function of the original $i_L(t_0)$.
- Substitute for $i_L(t_2)$ in (3.13) and $t=t_3$. This will give $i_L(t_3)$ as a function of the original $i_L(t_0)$.
- According to (3.14), $i_L(t_4)=i_L(t_3)$. Therefore, $i_L(t_4)$ is obtained as a function of the original $i_L(t_0)$.
- Since $i_L(t_4)$ is at half the period and $i_L(t_4)=-i_L(t_0)$ due to waveform symmetry, therefore by substituting $i_L(t_4)=-i_L(t_0)$ into the equation from the previous step, $i_L(t_0)$ is expressed as:

$$-2i_L(t_0) = \frac{V_{dc1}}{L}(t_3 - t_2) + \frac{V_{dc1} - nV_{dc2}}{L}(t_2 - t_1) + \frac{V_{dc1}}{L}(t_1 - t_0). \tag{3.15}$$

But switching instants t_n values can be expressed in terms of TPS parameters from Table 3.1 such that $t_0=0$, $t_1=D_{12}T_h$, $t_2=(D_{12}+ D_2)T_h$, $t_3=D_1T_h$ and $t_4=T_h$ Where $T_h=T_s/2$. Substituting values of t_n in (3.15), $i_L(t_0)$ can be obtained.

$$i_L(t_0) = -\left[\frac{V_{dc1}D_1 - nV_{dc2}D_2}{4f_sL}\right] \tag{3.16}$$

Substituting (3.16) into (3.11) to (3.14), the currents considering the half wave switching instants for mode 1 are as follows:

$$\begin{aligned} i_L(t_0) &= \frac{-(V_{dc1}D_1 - nV_{dc2}D_2)}{4f_sL} \\ i_L(t_1) &= \frac{(-V_{dc1}D_1 + 2V_{dc1}D_{12} + nV_{dc2}D_2)}{4f_sL} \\ i_L(t_2) &= \frac{(-V_{dc1}D_1 + 2V_{dc1}D_2 + 2V_{dc1}D_{12} - nV_{dc2}D_2)}{4f_sL} \\ i_L(t_3) &= \frac{(V_{dc1}D_1 - nV_{dc2}D_2)}{4f_sL} \end{aligned} \tag{3.17}$$

However, current values should be expressed as function of only TPS parameters and DC voltage ratio (i.e.: remove V_{dc1} and nV_{dc2} from the equation), which can be done by normalising with respect to V_{base} where $V_{base}= V_{dc1}$ and substituting by $K_{12}=nV_{dc2}$. Accordingly, the generalised format of (3.17) is given as follows:

$$\begin{aligned} i_L(t_0) &= -(D_1 - K_{12}D_2) \\ i_L(t_1) &= (-D_1 + 2D_{12} + K_{12}D_2) \\ i_L(t_2) &= (-D_1 + 2D_2 + 2D_{12} - K_{12}D_2) \\ i_L(t_3) &= (D_1 - K_{12}D_2) \end{aligned} \tag{3.18}$$

The same normalisation method will be applied to the currents at all switching instants for all modes of DAB converter under TPS control. In addition, D_{12} will be replaced by (D_{12}+1) in modes (1', 2', 3', 4', 5' and 6') to account for the proposed definition of D_{12} in this thesis. The per unit current values at the switching instants for operating modes of DAB are outlined in Table. 3.2. This new representation of the currents guarantees universality being only function of TPS modulation parameters (D_1, D_2, D_{12}) and DC voltage ratio (K_{12}); besides, it is consistent with the proposed definition of D_{12}. Consequently, the dependent RMS current represented in (3.9) is also function of D_1, D_2, D_{12} and K_{12}.

Table 3.2: Per Unit Inductor Current Values for Positive Half Cycle Switching Intervals.

Mode 1	$i_L(t_0)$	$-(D_1 - K_{12}D_2)$	$i_L(t_2)$	$(-D_1 + 2D_2 + 2D_{12} - K_{12}D_2)$
	$i_L(t_1)$	$(-D_1 + 2D_{12} + K_{12}D_2)$	$i_L(t_3)$	$(D_1 - K_{12}D_2)$
Mode 1'	$i_L(t_0)$	$-(D_1 + K_{12}D_2)$	$i_L(t_2)$	$(-D_1 + 2(D_{12} + 1) - K_{12}D_2)$
	$i_L(t_1)$	$(-D_1 + 2D_2 + 2(D_{12} + 1) + K_{12}D_2)$	$i_L(t_3)$	$(D_1 + K_{12}D_2)$
Mode 2	$i_L(t_0)$	$-(D_1 - 2K_{12} + KD_2 + 2KD_{12})$	$i_L(t_2)$	$(D_1 + K_{12}D_2)$
	$i_L(t_1)$	$(D_1 + 2K_{12}D_1 - K_{12}D_2 + 2K_{12} - 2K_{12}D_{12})$	$i_L(t_3)$	$(D_1 + K_{12}D_2)$
Mode 2'	$i_L(t_0)$	$-(D_1 + 2K_{12} - K_{12}D_2 - 2K(D_{12} + 1))$	$i_L(t_2)$	$(D_1 - 2K_{12} - 2K_{12}D_1 + K_{12}D_2 + 2K_{12}(D_{12} + 1))$
	$i_L(t_1)$	$(D_1 - K_{12}D_2)$	$i_L(t_3)$	$(D_1 - K_{12}D_2)$
Mode 3	$i_L(t_0)$	$-(D_1 - K_{12}D_2)$	$i_L(t_2)$	$(D_1 + K_{12}D_2)$
	$i_L(t_1)$	$(D_1 + K_{12}D_2)$	$i_L(t_3)$	$(D_1 - K_{12}D_2)$
Mode 3'	$i_L(t_0)$	$-(D_1 + K_{12}D_2)$	$i_L(t_2)$	$(D_1 - K_{12}D_2)$
	$i_L(t_1)$	$(D_1 - K_{12}D_2)$	$i_L(t_3)$	$(D_1 + K_{12}D_2)$
Mode 4	$i_L(t_0)$	$-(D_1 - 2K_{12} + K_{12}D_2 + 2K_{12}D_{12})$	$i_L(t_2)$	$(-D_1 - 2 + 2D_2 + K_{12}D_2 + 2D_{12})$
	$i_L(t_1)$	$(D_1 + K_{12}D_2)$	$i_L(t_3)$	$(D_1 + K_{12}D_2)$
Mode 4'	$i_L(t_0)$	$-(D_1 + 2K_{12} - K_{12}D_2 - 2K_{12}(D_{12} + 1))$	$i_L(t_2)$	$(-D_1 - 2 + 2D_2 + 2(D_{12} + 1) - K_{12}D_2)$
	$i_L(t_1)$	$(D_1 - K_{12}D_2)$	$i_L(t_3)$	$(D_1 - K_{12}D_2)$
Mode 5	$i_L(t_0)$	$-(D_1 - K_{12}D_2)$	$i_L(t_2)$	$(-D_1 + 2D_{12} + K_{12}D_2)$
	$i_L(t_1)$	$(D_1 - 2K_{12}D_1 + K_{12}D_2 + 2K_{12}D_{12})$	$i_L(t_3)$	$(D_1 - K_{12}D_2)$
Mode 5'	$i_L(t_0)$	$-(D_1 + K_{12}D_2)$	$i_L(t_2)$	$(-D_1 + 2(D_{12} + 1) - K_{12}D_2)$
	$i_L(t_1)$	$(D_1 + 2K_{12}D_1 - K_{12}D_2 - 2K_{12}(D_{12} + 1))$	$i_L(t_3)$	$(D_1 + K_{12}D_2)$
Mode 6	$i_L(t_0)$	$-(D_1 + K_{12}D_2 + 2K_{12}D_{12} - 2K_{12})$	$i_L(t_2)$	$(-D_1 + 2D_{12} + K_{12}D_2)$
	$i_L(t_1)$	$(-D_1 + 2D_2 + 2D_{12} + K_{12}D_2 - 2)$	$i_L(t_3)$	$(D_1 - 2K_{12}D_1 + K_{12}D_2 + 2K_{12}D_{12})$
Mode 6'	$i_L(t_0)$	$-(D_1 - K_{12}D_2 - 2K_{12}(D_{12} + 1) + 2K_{12})$	$i_L(t_2)$	$(-D_1 + 2D_2 + 2(D_{12} + 1) - K_{12}D_2 - 2)$
	$i_L(t_1)$	$(-D_1 + 2(D_{12} + 1) - K_{12}D_2)$	$i_L(t_3)$	$(D_1 + 2K_{12}D_1 - K_{12}D_2 - 2K_{12}(D_{12} + 1))$

dd

3.1.3. Power transfer characteristic

The average power transferred by the DAB converter can be calculated at either bridge by assuming a lossless inductor in the DAB converter's equivalent circuit model as shown in Fig. 3.3. Per unit power for each mode can be obtained from (3.19) with piecewise consideration of the voltage and current waveforms over half the period. For example, considering mode 1, power transferred can be derived as outlined by (3.20).

$$P = \frac{1}{T_h}\int_0^{T_h} v_{br1}(t).\, i_L(t)dt \tag{3.19}$$

$$P = \frac{V_{dc1}}{T_h}\left\{\int_0^{t_1}\left[\frac{i_L(t_1)-i_L(t_0)}{t_1}t + i_L(t_0)\right]dt + \int_{t_1}^{t_2}\left[\frac{i_L(t_2)-i_L(t_1)}{t_2-t_1}t + i_L(t_1)\right]dt + \int_{t_2}^{t_3}\left[\frac{i_L(t_3)-i_L(t_2)}{t_3-t_2}t + i_L(t_2)\right]dt\right\} \tag{3.20}$$

This reduces to:

$$P = \frac{V_{dc1}}{2T_h}\left[t_1\big(i_L(t_1)+i_L(t_0)\big) + (t_2-t_1)\big(i_L(t_2)+i_L(t_1)\big) + (t_3-t_2)\big(i_L(t_3)+i_L(t_2)\big)\right]$$

Substituting the time and current instants of mode 1 into (3.20), then dividing by base power, per unit power for mode 1 is obtained as follows:

$$P = 2K_{12}({D_2}^2 - D_1D_2 + 2D_2D_{12}). \tag{3.21}$$

Similarly, the transferred power for each of the twelve modes can be obtained using this approach. The derived power equations for all switching modes and the associated power ranges are therefore outlined in Table 3.3.

Table 3.3: Per Unit Power Transferred for Each Switching Mode with Power Range.

Switching Mode	Power Transferred	Power Range
Mode 1	$P = 2K_{12}({D_2}^2 - D_1D_2 + 2D_2D_{12})$	$P_{max} = 0.5K_{12}$ pu , $P_{min} = -0.5K_{12}$ pu
Mode 1’	$P = -2K_{12}({D_2}^2 - D_1D_2 + 2D_2(D_{12}+1))$	$P_{max} = 0.5K_{12}$ pu , $P_{min} = -0.5K_{12}$ pu
Mode 2	$P = 2K_{12}({D_1}^2 - D_1D_2 + 2D_1 - 2D_1D_{12})$	$P_{max} = 0.5K_{12}$ pu , $P_{min} = -0.5K_{12}$ pu
Mode 2’	$P = -2K_{12}({D_1}^2 - D_1D_2 - 2D_1D_{12})$	$P_{max} = 0.5K_{12}$ pu , $P_{min} = -0.5K_{12}$ pu
Mode 3	$P = 2K_{12}(D_1D_2)$	$P_{max} = 0.5K_{12}$ pu , $P_{min} = 0.0$ pu
Mode 3’	$P = -2K_{12}(D_1D_2)$	$P_{max} = 0.0$ pu , $P_{min} = -0.5K_{12}$ pu
Mode 4	$P = 2K_{12}(-{D_2}^2 - D_{12}^2 + 2D_2 + 2D_{12} - 2D_2D_{12} + D_1D_2 - 1)$	$P_{max} = 0.667K_{12}$ pu , $P_{min} = 0.0$ pu
Mode 4’	$P = -2K_{12}(-{D_2}^2 - (D_3+1)^2 + 2D_{12} - 2D_2D_{12} + D_1D_2 + 1)$	$P_{max} = 0.0$ pu , $P_{min} = -0.667K_{12}$ pu
Mode 5	$P = 2K_{12}(-{D_1}^2 - D_{12}^2 + D_1D_2 + 2D_1D_{12})$	$P_{max} = 0.667K_{12}$ pu , $P_{min} = 0.0$ pu
Mode 5’	$P = -2K_{12}(-{D_1}^2 - (D_{12}+1)^2 + D_1D_2 + 2D_1(D_{12}+1))$	$P_{max} = 0.0$ pu , $P_{min} = -0.667K_{12}$ pu
Mode 6	$P = 2K_{12}(-{D_1}^2 - {D_2}^2 - 2D_{12}^2 + 2D_{12} - 2D_2D_{12} + D_1D_2 + 2D_1D_{12} + 2D_2 - 1)$	$P_{max} = K_{12}$ pu , $P_{min} = 0.0$ pu
Mode 6’	$P = -2K_{12}(-{D_1}^2 - {D_2}^2 - 2(D_{12}+1)^2 + 2D_{12} - 2D_2D_{12} + D_1D_2 + 2D_1(D_{12}+1) + 1)$	$P_{max} = 0.0$ pu , $P_{min} = -K_{12}$ pu

On the other hand, (3.22) gives reactive power consumed by the inductance in DAB. This is based on the fact that inductors do not absorb active power, therefore, apparent power S_L calculated at the inductor is equivalent to reactive power consumed by the inductor.

$$Q = S_L = V_{L_{RMS}} I_{L_{RMS}} \tag{3.22}$$

Such that $I_{L_{RMS}}$ is calculated from (3.9) and $V_{L_{RMS}}$ is calculated from (3.23).

$$V_{L_{RMS}} = \sqrt{\frac{1}{T_h}\int_0^{T_h} {V_L}^2(t)dt} \tag{3.23}$$

For example, to calculate RMS value of inductor voltage for mode 1, integration in (3.23) gives:

$$V_{L_{RMS}} = \frac{1}{T_h}\left[{V_{dc1}}^2(t_1 - t_0) + (V_{dc1} - nV_{dc2})^2(t_2 - t_1) + {V_{dc1}}^2(t_3 - t_2)\right]^{1/2}. \tag{3.24}$$

Substituting t_n values of mode 1 into (3.24), and normalising (3.24) with respect to the base values defined in (3.1) such that:

$$(V_{dc1})_{pu} = \frac{V_{dc1}}{V_{base}} = 1\,,\ (nV_{dc2})_{pu} = \frac{nV_{dc2}}{V_{base}} = K_{12}.$$

This gives the per unit RMS value of inductor voltage for switching mode:

$$\left(V_{L_{RMS}}\right)_{mode1} = \left(D_1 + {K_{12}}^2 D_2 - 2K_{12}D_2\right)^{1/2}. \tag{3.25}$$

Similarly, RMS value of inductor voltage for all switching modes can be obtained.

3.1.4. Model comparison and validation

This subsection mainly investigates and evaluates the correctness of the detailed DAB model. This is achieved by a model comparison between the detailed model and the Simulink-based DAB switching model shown in Fig 3.5. The difference (error) between the transferred active power and the AC link's RMS current in both detailed model and SIMULINK model are calculated by (3.26). This is done over the entire range of duty ratios D_1 and D_2 ($0 \leq D_1 \leq 1$ and $0 \leq D_2 \leq 1$) at a fixed D_{12} and K_{12} to enable 3D plotting of active power and RMS AC link's current.

$$\Delta I = |I_{L_{RMS}} - I_{L_{RMS(Sim)}}|$$
$$\Delta P = |P - P_{(Sim)}| \quad (3.26)$$

Where:

- $I_{L_{RMS}}$ is the calculated RMS value of inductor current from the derived detailed DAB model.
- $I_{L_{RMS(Sim)}}$ is RMS value of inductor current from the SIMULINK DAB model.
- P is the calculated transferred active power using the derived detailed DAB.
- $P_{(Sim)}$ is the RMS value of inductor current from the SIMULINK DAB model.

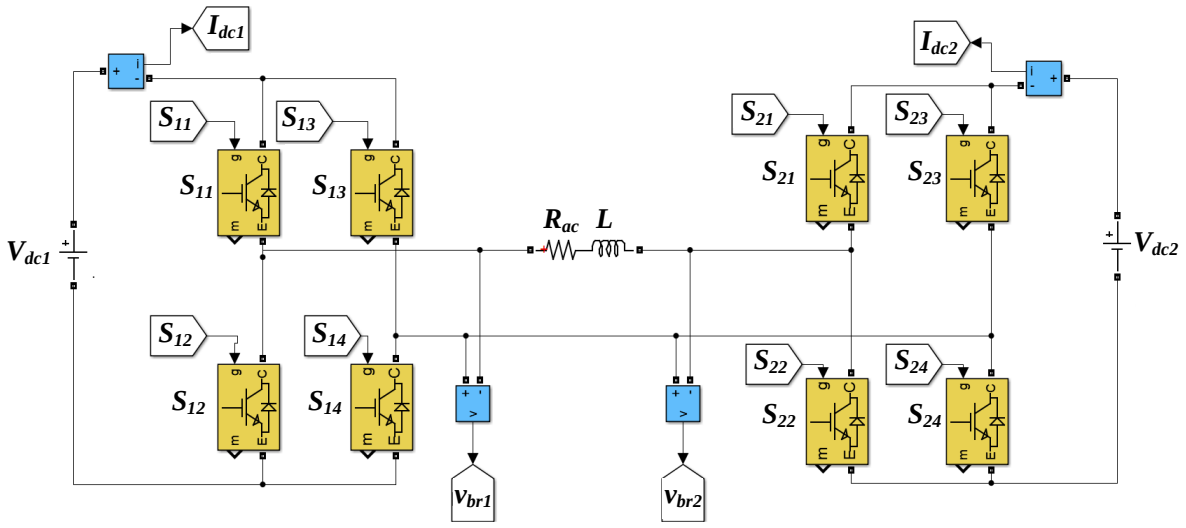

Fig. 3.5: SIMULINK-based DAB DC-DC Converter Model.

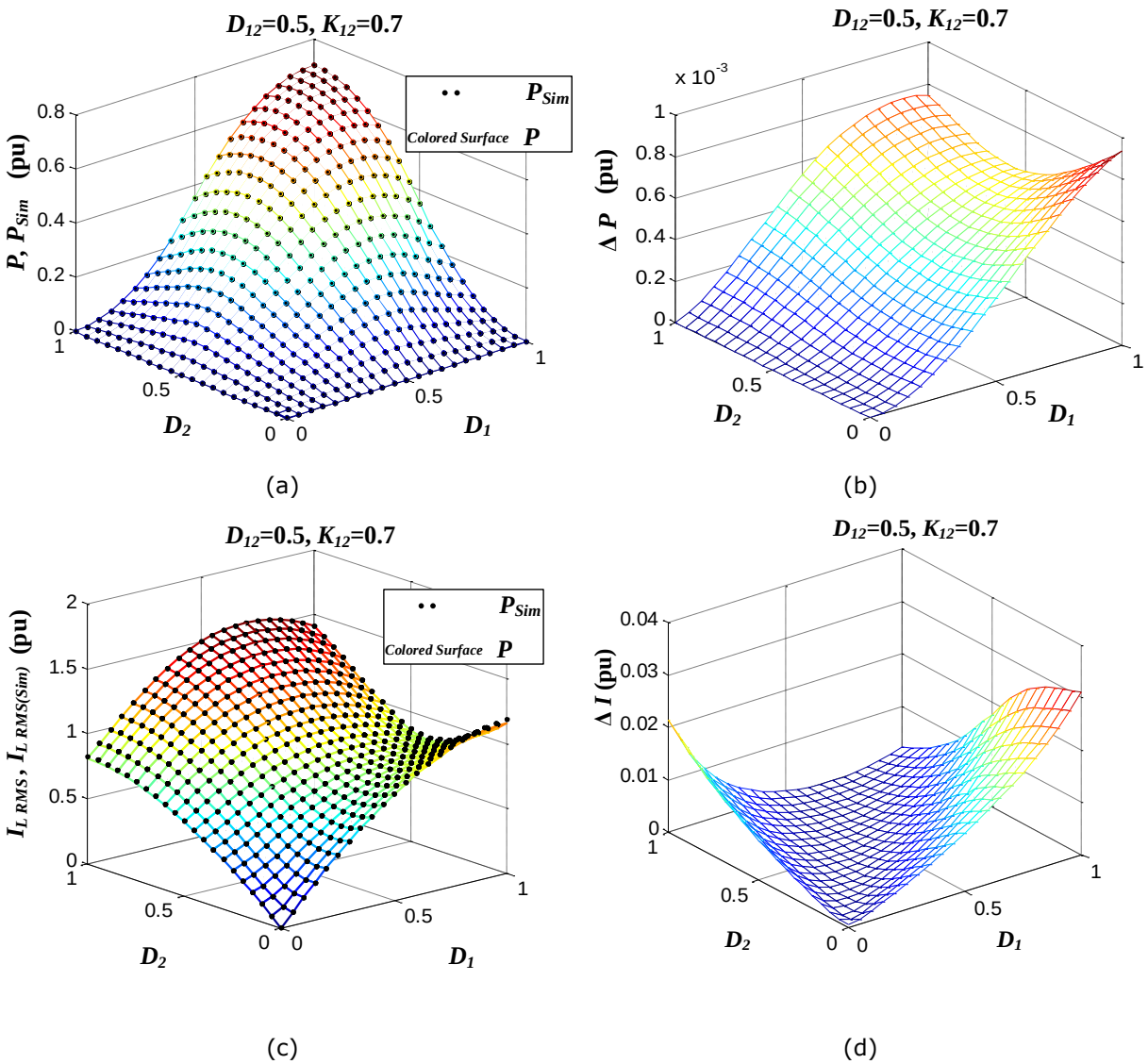

Fig. 3.6: Relative difference in active power and AC link's RMS current between exact model and approximate (FHA) model at K_{12}=1, D_{12}=0.5.

The comparison shown in Fig 3.6 proves the correctness of the derived detailed DAB model, which means that this derived model is valid for predicting the value of active power and RMS AC link's current at any combination of TPS values. Accordingly, this model will be used as the basis for controller design later in this thesis. It should also be stated that in order to calculate value of the active power and/or RMS current, the switching mode must be identified first based on the operational constraints previously shown in Table 3.1. On the contrary, frequency domain analysis does not involve complex switching mode classification [29], [90]

thus can simplify modelling compared to conventional time-domain modelling. That's why in the next section DAB modelling based on the fundamental harmonic is investigated to identify its potential and accuracy in representing the main DAB parameters (active power transfer and RMS AC link's current). In fact, this can be beneficial when it comes to high number of ports in a multi active bridge converter that involve very high number of switching modes and hence difficult to analyse and derive the time-domain based model.

3.2. Fundamental Harmonic Model

In this section, AC link RMS current, active and reactive power in fundamental harmonic under TPS is derived and will be referred as FHA model. The correctness of the FHA model will be verified by comparing power and current values (calculated using the FHA model) with the detailed model (derived in pervious section) over the full range of TPS parameters.

3.2.1. Power and current characterisation

DAB's equivalent circuit assuming fundamental harmonic analysis is depicted in Fig 3.7. The exact (quasi square) and fundamental harmonic bridge voltages with the TPS parameters are shown in Fig 3.8. Fundamental harmonic components of bridge voltages as function of (D_1, D_2, D_{12}) are outlined by (3.27).

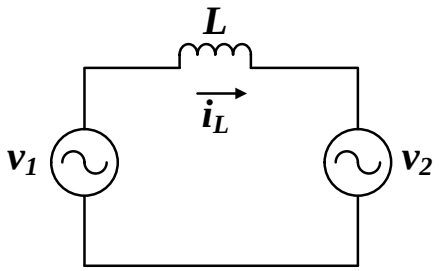

Fig. 3.7: Equivalent of DAB circuit in fundamental harmonic.

$$\begin{aligned} v_1(t) &= V_{1\,max}\, sin(\omega t). \\ v_2(t) &= V_{2\,max}\, sin(\omega t - \delta). \end{aligned} \tag{3.27}$$

Where $V_{1\,max} = \frac{4V_{dc1}}{\pi} sin\left(\frac{D_1\pi}{2}\right), V_{2\,max} = \frac{4nV_{dc2}}{\pi} sin\left(\frac{D_2\pi}{2}\right), \delta = \pi\left(D_{12} + \frac{D_2 - D_1}{2}\right)$

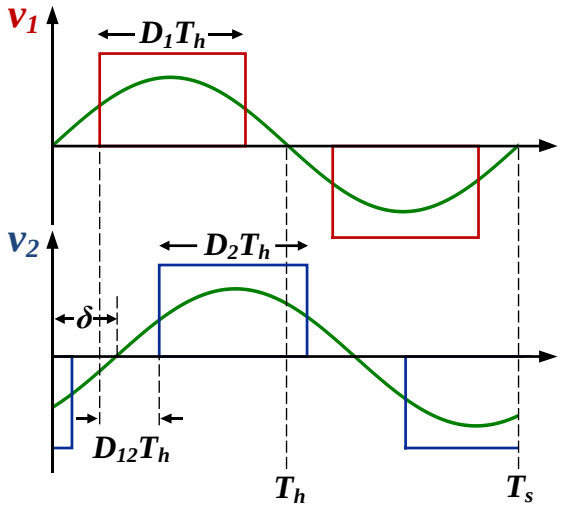

Fig. 3.8: Definition of triple phase shift in DAB with exact square wave along with fundamental harmonic.

The voltage across the inductor can be derived from:

$$\overrightarrow{V_L} = \overrightarrow{V_1} - \overrightarrow{V_2} = \frac{4V_{dc1}}{\pi} sin\left(\frac{D_1\pi}{2}\right)\angle 0 - \frac{4nV_{dc2}}{\pi} sin\left(\frac{D_2\pi}{2}\right)\angle -\delta \tag{3.28}$$

Dividing (3.27) by $\sqrt{2}$ (to get RMS) and changing to rectangular form

$$\begin{aligned}\overrightarrow{V_L} &= \frac{4V_{dc1}}{\sqrt{2}\pi} sin\left(\frac{D_1\pi}{2}\right) - \left[\frac{4nV_{dc2}}{\sqrt{2}\pi} sin\left(\frac{D_2\pi}{2}\right)\cos(-\delta) + j\frac{4nV_{dc2}}{\sqrt{2}\pi} sin\left(\frac{D_2\pi}{2}\right)\sin(-\delta)\right] \\ &= \frac{4}{\sqrt{2}\pi}\left[\left(V_{dc1} sin\left(\frac{D_1\pi}{2}\right) - nV_{dc2}\, sin\left(\frac{D_2\pi}{2}\right)\cos(\delta)\right) + jnV_{dc2}\, sin\left(\frac{D_2\pi}{2}\right)\sin(\delta)\right]\end{aligned} \tag{3.29}$$

Then RMS value of inductor voltage can be obtained as

$$\begin{aligned}{V_{L_{RMS}}}^2 &= \frac{8}{\pi^2}\left[\left(V_{dc1} sin\left(\frac{D_1\pi}{2}\right) - nV_{dc2}\, sin\left(\frac{D_2\pi}{2}\right)\cos(\delta)\right)^2 + \left(nV_{dc2}\, sin\left(\frac{D_2\pi}{2}\right)\sin(\delta)\right)^2\right] \\ &= \frac{8}{\pi^2}\left[{V_{dc1}}^2 sin^2\left(\frac{D_1\pi}{2}\right) + n^2{V_{dc2}}^2\, sin^2\left(\frac{D_2\pi}{2}\right) - 2nV_{dc1}V_{dc2}\, sin\left(\frac{D_1\pi}{2}\right) sin\left(\frac{D_2\pi}{2}\right)\cos(\delta)\right]\end{aligned} \tag{3.30}$$

Accordingly, AC link's RMS current can be calculated from

$${I_{L_{RMS}}}^2 = \frac{{V_{L_{RMS}}}^2}{X^2} = \frac{{V_{L_{RMS}}}^2}{(2\pi f_s L)^2} \tag{3.31}$$

Normalising (3.31) with respect to the base values defined in (3.1) such that

$$(V_{dc1})_{pu} = \frac{V_{dc1}}{V_{base}} = 1\,,\ \ (nV_{dc2})_{pu} = \frac{nV_{dc2}}{V_{base}} = K_{12},\ (X)_{pu} = \frac{2\pi f_s L}{8 f_s L} = \frac{\pi}{4}$$

Thus, per unit RMS value of AC link current is rewritten as

$$I_{L_{RMS}}{}^2 = \frac{128}{\pi^4}\left[sin^2\left(\frac{D_1\pi}{2}\right) + K_{12}{}^2\, sin^2\left(\frac{D_2\pi}{2}\right) - 2K_{12}\, sin\left(\frac{D_1\pi}{2}\right) sin\left(\frac{D_2\pi}{2}\right)\cos\left(\pi D_{12} + \pi\left(\frac{D_2 - D_1}{2}\right)\right)\right] \tag{3.32}$$

Regarding the active power flow, it can be obtained from:

$$P = \frac{(V_{1\,RMS})_{pu}(V_{2\,RMS})_{pu}}{X}\sin(\delta). \tag{3.33}$$

Normalising (3.33) with respect to the base values defined in (3.1), this gives the per unit RMS value of active power in DAB, rewritten as:

$$P = \frac{32}{\pi^3} K_{12}\, sin\left(\frac{D_1\pi}{2}\right) sin\left(\frac{D_2\pi}{2}\right)\sin\left(\pi D_{12} + \pi\left(\frac{D_2 - D_1}{2}\right)\right). \tag{3.34}$$

While reactive power can be determined from:

$$Q = V_{L\,RMS}\ I_{L\,RMS}\ . \tag{3.35}$$

Alternatively, converter reactive power can be represented by the summation of reactive powers calculated at bridge terminals such that:

$$Q = Q_1 + Q_2\,. \tag{3.36}$$

Where:

- $Q_i = V_{i\,RMS}\ I_{L\,RMS}\ \sin(\theta_{v_i} - \theta_{I_L}) \qquad i = 1, 2.$
- θ_{v_i} is the angle of bridge 1 or 2 voltage ($\overrightarrow{v_1}, \overrightarrow{v_2}$).
- θ_{I_L} is the angle of the inductor current $\overrightarrow{I_L}$.

The major advantage of the fundamental harmonic model is that it's free from switching mode classification which highly facilitates the representation of DAB. However, the effectiveness of this model (i.e.: fundamental harmonic model.) needs further investigation which will be discussed in next section.

3.2.2. Model comparison and validation

The objective from this section is to evaluate the effectiveness of the fundamental harmonic model in representing the main DAB parameters. To do this, a model comparison is held between the detailed model and the fundamental harmonic model. The difference (error) between the transferred active power and the AC link's RMS current in both exact and approximate models are calculated by (3.37).

$$\begin{aligned} \Delta I &= |I_{L_{RMS}} - I_{L_{RMS_{(1)}}}| \\ \Delta I\% &= \frac{|I_{L_{RMS}} - I_{L_{RMS_{(1)}}}|}{I_{L_{RMS}}} \\ \Delta P &= |P - P_{(1)}| \\ \Delta P\% &= \frac{|P - P_{(1)}|}{P} \end{aligned} \tag{3.37}$$

Where:

- $I_{L_{RMS}}$ is RMS value of inductor current.
- $I_{L_{RMS_{(1)}}}$ is RMS value of inductor current in fundamental harmonic.
- P is transferred active power.
- $P_{(1)}$ is fundamental harmonic active power transferred.

Results shown in Fig.3.9 and Fig. 3.10 confirm the following:

- Relative difference is negligible (especially at high values of D_1 and D_2) such that it does not exceed of 0.05 pu which verifies the correctness of the exact model. A high value of error is observed in active power — in Fig 3.9 (d) and Fig 3.10(d) — at areas near D_1=0 or D_2=0 or D_1=D_2=0 as these values of duty ratios produce very small value of P and hence P is at the denominator of ΔP — outlined by (3.37) — the value of error is high.
- Percentage difference is relatively high at small values of D_1 and D_2 which supports the claim from literature [33]&[90].

- The fundamental harmonic components represent the majority of the power and current in DAB, which means the approximate model can be used as a simplified tool for performing preliminary steady state analysis.

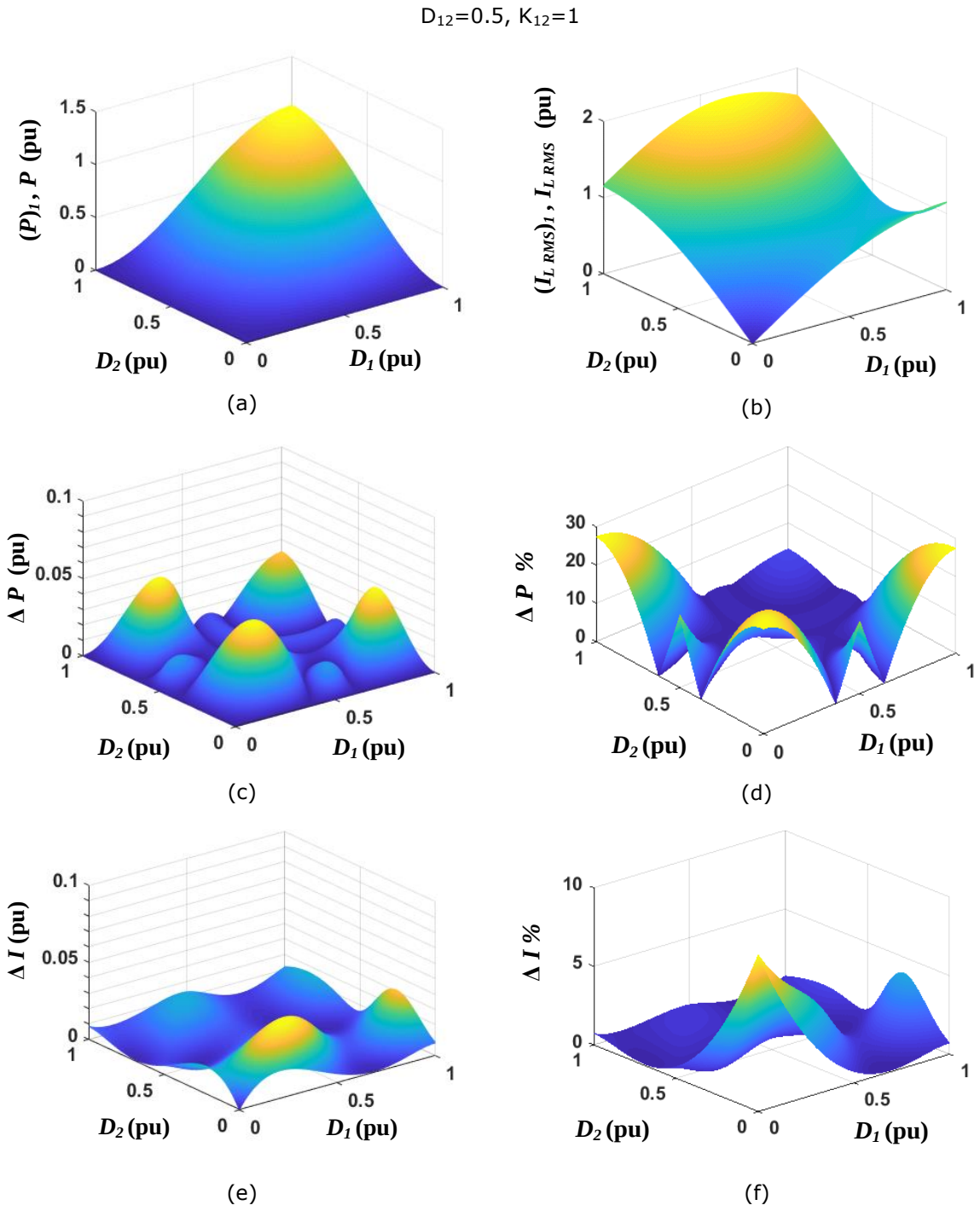

Fig. 3.9: Relative difference in active power and AC link's RMS current between exact model and approximate (FHA) model at K_{12}=1, D_{12}=0.5.

D_{12}=-0.5, K_{12}=0.5

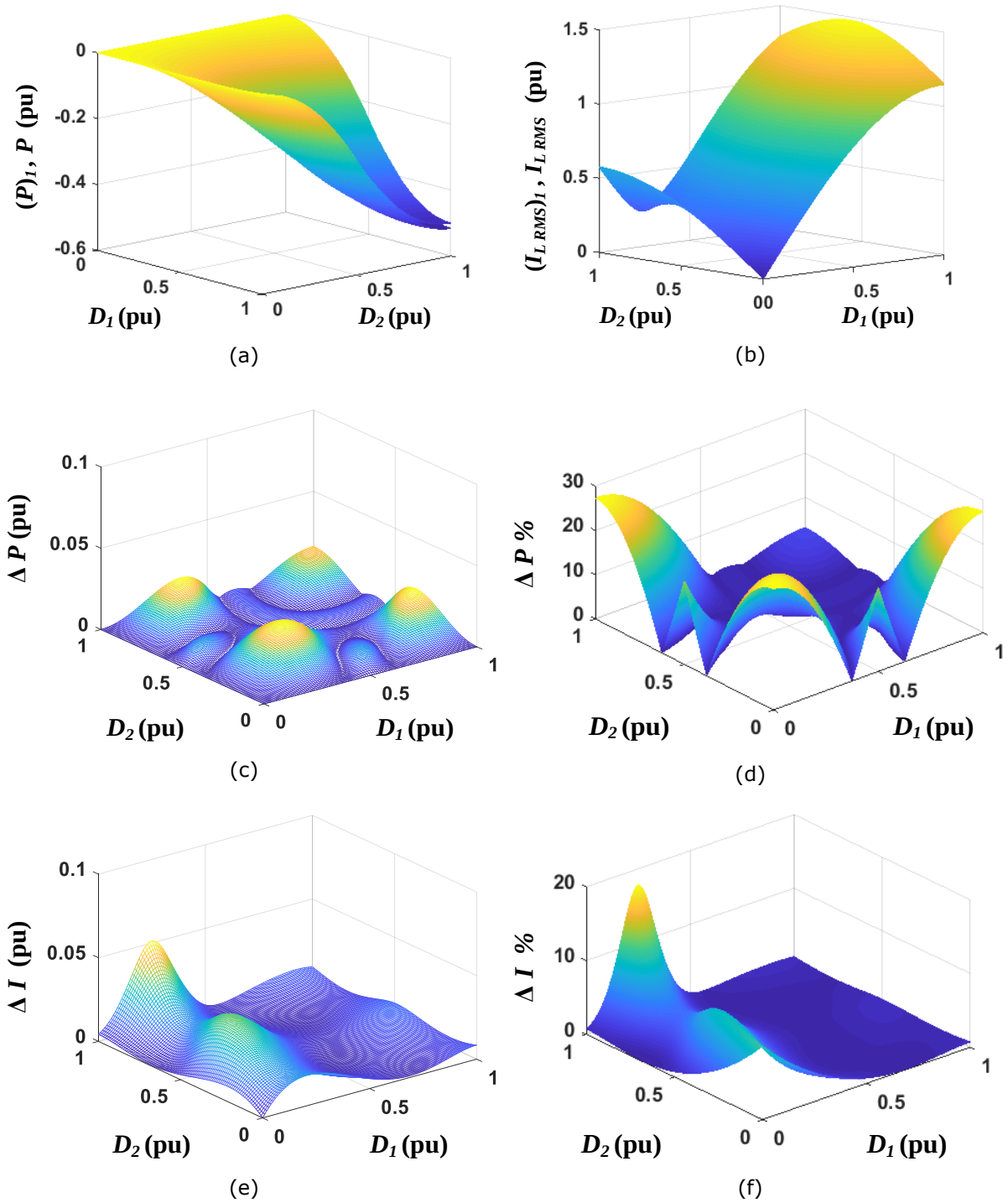

Fig. 3.10: Relative difference in active power and AC link's RMS current between exact model and approximate (FHA) model at K_{12}=0.5, D_{12}=-0.5.

3.3. Summary

In this chapter a generalised per unit model of a DAB converter, based on standardised TPS modulation and square wave analysis, was developed. The developed model is generalised for any DAB converter regardless of ratings and parameter values. It also covers all possible switching modes and includes the effect of voltage conversion ratio. The correctness of the derived model is confirmed by comparison with SIMULINK-based DAB model. The derived detailed DAB model will serve as the foundation building block in developing a generic optimised power flow DAB controller for detailed discussion later in this thesis. Then an FHA model – that does not does not involve complex switching mode classification – is derived and investigated to identify its accuracy in representing the main DAB parameters.

Chapter 4. Modelling and Analysis of MAB DC-DC Converter

This chapter contributes to the modelling and power flow analysis of the multi active bridge (MAB) DC-DC converter operating with a standardised phase shifting control scheme for MAB. A generalised circuit diagram of *n*-port MAB converter is depicted in Fig 4.1.

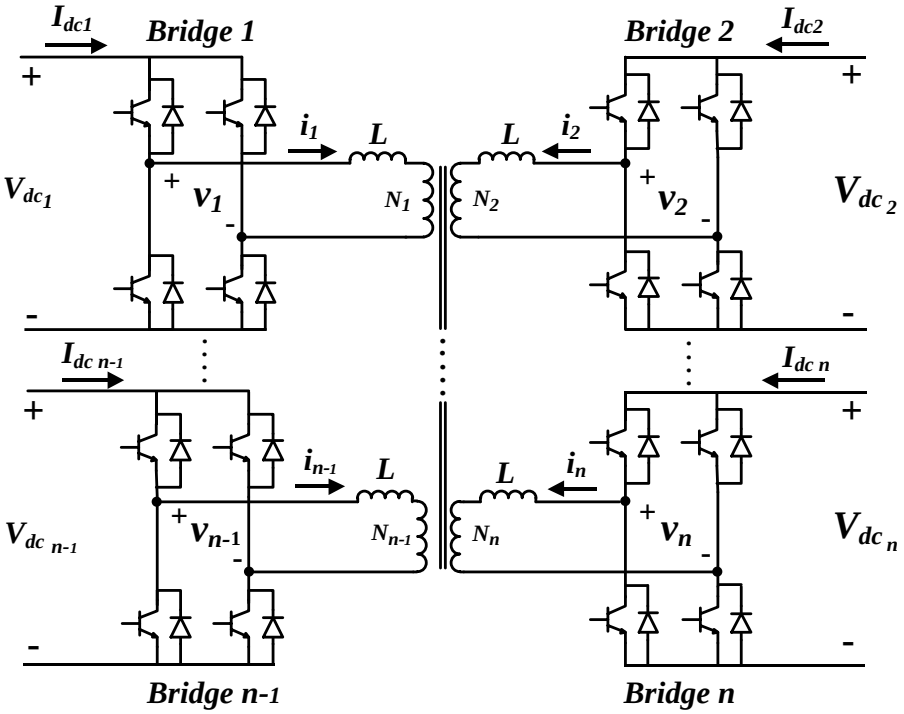

Fig. 4.1: Generalised circuit diagram of MAB converter with n ports.

The chapter also covers the study of a non-isolated MAB DC-DC converter under various purely inductor-based AC link topologies. Absence of the interface transformer in a non-isolated converter can significantly reduce the converter weight and footprint since inductors can be air-core based; which avoids magnetic saturation and mitigates the high frequency constraints imposed by high losses in magnetic cores. The objective of analysing the non-isolated version of the converter is to identify the topology that offers minimum converter footprint (i.e.: minimum value of the AC link inductors.) in addition to minimum internal RMS

current stresses and reactive power losses. The analysis is carried out for the triple active bridge (TAB) and the results/conclusions are then generalised for MAB. Finally, the chapter provides per unit power-flow analysis, which leads to developing a generic phase shift decoupler for an *n*-port MAB converter. On this basis a PI-based power flow controller is developed.

4.1. Multi Phase Shift (MPS) Control

The power flow between any two ports is essentially controlled through phase-shift-modulation of the square-wave voltages generated by their corresponding active-bridge modules. This section presents the multi phase shift modulation scheme (MPS) which acts as a common framework for applying a phase-shift modulation technique on MAB converters. MPS is an extension of triple phase shift TPS used for two-port active bridge DAB. It enables full utilisation of all possible modulation parameters (i.e.: all degrees of freedom from the control point of view.). The available degrees of freedom are duty ratios of the bridge voltages D_i and phase shifts D_{ij} defined as phase angle between the positive-going edges of v_i and v_j. These control parameters are obtained using classical phase shifting of gate signals S_{11}-S_{14} up to S_{n1}-S_{n4} such that in per unit terms $0 \leq D_i \leq 1$ and $-1 \leq D_{ij} \leq 1$. Modulation parameters are normalised with respect to half the switching cycle (T_h).

It is highly complicated to consider an exact model in this chapter as the number of operational modes will be very high for n-port MAB, so fundamental harmonic modelling is used. The closeness of the approximation has been validated in chapter three, and hence will be used thereafter in analysis of MAB converter. The representation of the MAB AC-side voltages in equivalent fundamental harmonic are given by (4.1) where K_{ri} represents the DC voltage ratio with respect to reference port's voltage (base voltage). The inclusion of this ratio

enables representation of MAB's different operating modes, such that K_{ri}=1 designates unity-gain mode between port i and reference port and K_{ri}≠1 designates buck/boost mode between port i and reference port. An illustration of the MPS modulation parameters over typical AC-side bridge voltage waveforms is shown in Fig.4.2.

$$v_i(t) = V_{i\,max}\, sin(\omega t - \delta_{ij}). \tag{4.1}$$

Such that $V_{i\,max} = \frac{4V_{base}K_{ri}}{\pi} sin\left(\frac{D_i\pi}{2}\right), K_{ri} = \frac{N_i}{N_r}\frac{V_{dci}}{V_r}, \delta_{ij} = \pi\left(D_{ij} + \frac{D_i - D_j}{2}\right)$.

Where:

- i, j=1,2,…,n.
- n is number of ports in MAB.
- r is number of reference bridge.
- N_i is turns ratio of bridge i.

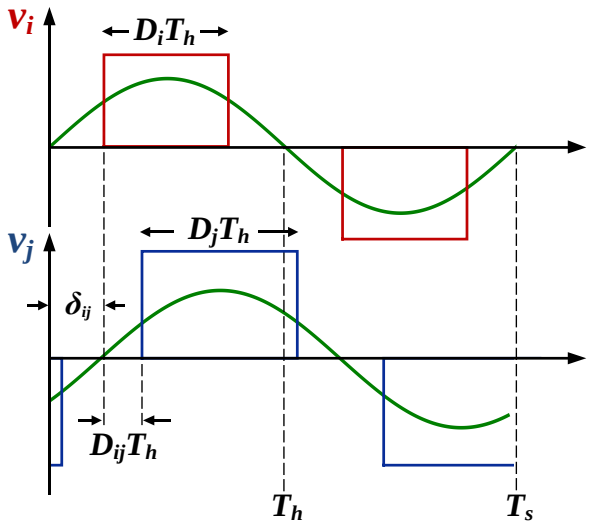

Fig. 4.2: Definition of multi phase shift control in multi active bridge.

4.2. Non-Isolated Converter AC Link Topologies

This section provides a comprehensive study of new purely inductor-based AC-link topologies in MAB converters. The absence of an interface transformer in the converter can significantly reduce converter weight and footprint in some low-power applications. Also, the transformer may not be needed for voltage matching such as in applications where DC voltage ratio is not high: for instance, in fuel-

cell-based regenerative power systems with rated power higher than 5kW as a HV battery and a non-isolated bidirectional converter may be used [121]. In addition, inductors can be air-core-based: this approach may involve larger volume but can also avoid magnetic saturation and mitigate the high switching frequency constraints imposed by large losses in magnetic cores of transformers. The analysis in this section is carried out for the TAB and the results/conclusions are generalised for MAB regardless of the number of ports.

4.2.1. Proposed AC Link Topologies

A TAB circuit diagram is shown in Fig. 4.3 where two equivalent interface inductors are utilised with each H-bridge for allowing standardised analysis. Fig.4.3 represents a generic non-isolated TAB structure with any possible AC link connection. By replacing each H-bridge by its equivalent fundamental harmonic bridge voltage, the equivalent circuit of a non-isolated TAB is obtained as shown in Fig. 4.4. From this equivalent circuit shown in Fig. 4.4 six possible topologies of the AC link can be constructed as shown in Table 4.1.

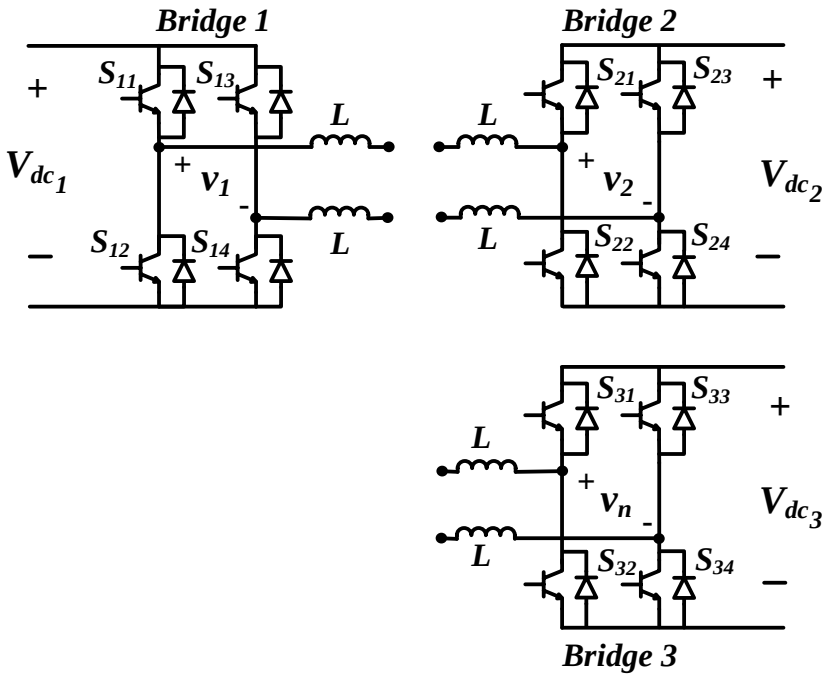

Fig. 4.3: Generic circuit diagram of non-isolated TAB.

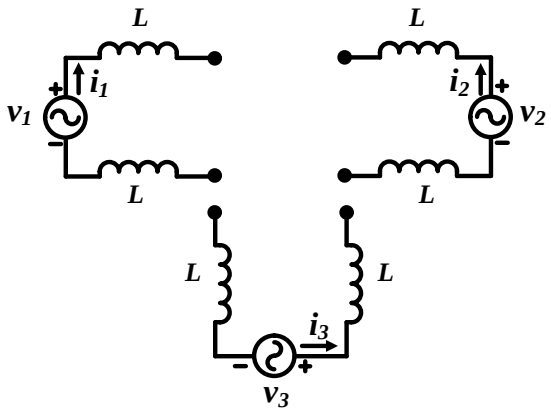

Fig. 4.4: Equivalent circuit of the non-isolated TAB.

Table 4.1: AC link Topologies for the non-isolated TAB.

AC link Topology 1	AC link Topology 2	AC link Topology 3
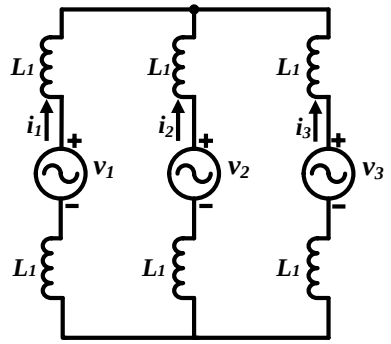	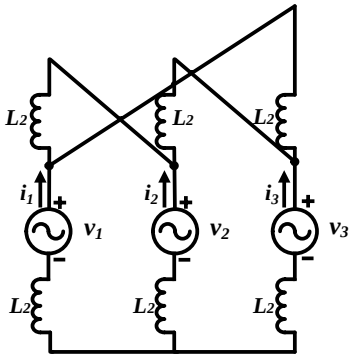	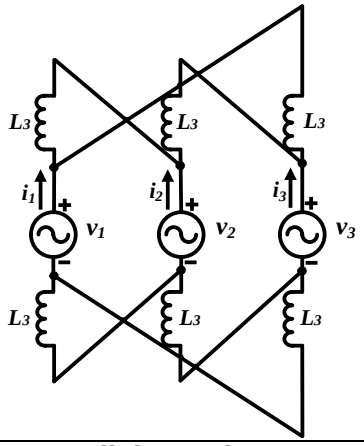
AC link Topology 4	**AC link Topology 5**	**AC link Topology 6**
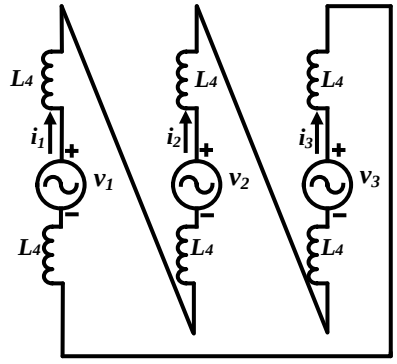	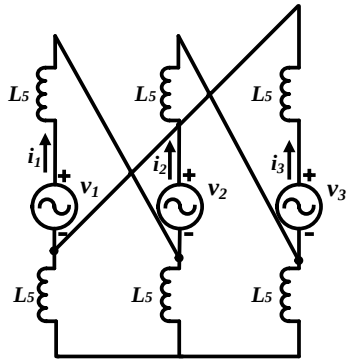	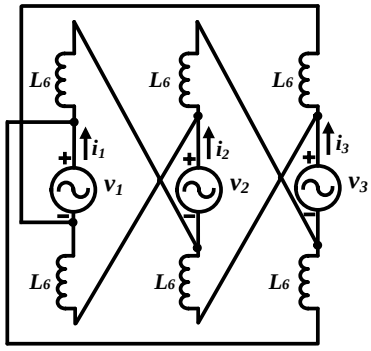

4.2.2. Steady state modelling

Studying the six TAB topologies in Table 4.1 permits identification of the optimal topology in terms of: minimum interface inductor size, minimum reactive power and current stresses. The criterion for comparison between the topologies is the

inductor value (L_i) and the total reactive power losses at same given power transfer level. For this sake a comprehensive TAB model, under all topologies, is developed in terms of active and reactive power in this section. This is achieved by assuming a fundamental frequency analysis, which is sufficient for the purpose of analysis (i.e.: identifying optimal topology.). Derived active and reactive power expressions will be used to establish the comparison between topologies in order to identify the optimal AC link topology for the non-isolated TAB converter. Per unit active and reactive power expressions at the AC terminals of each bridge are calculated using (4.3) and (4.4). Considering bridge 1 as the reference port, required phase shifts to represent power flow are D_{12} and D_{13} while δ_{11}=0, K_{11}=1.

$$P_i = V_{i\,RMS}\ I_{i\,RMS}\ cos(\delta_{1i} - \theta_i). \tag{4.3}$$

$$Q_i = V_{i\,RMS}\ I_{i\,RMS}\ sin(\delta_{1i} - \theta_i). \tag{4.4}$$

Where:
- θ_i is the angle of AC-side current's bridge i.
- $\delta_{1i} = \pi\left(D_{1i} + \frac{D_i - D_1}{2}\right), V_{i\,RMS} = \frac{4K_{1i}}{\pi\sqrt{2}} sin\left(\frac{D_i \pi}{2}\right).$

To enable the use of (4.3) and (4.4) for active/reactive power calculation, the first step is to derive the AC-side RMS current at each bridge for the investigated topologies using basic circuit analysis based on the fundamental frequency approximation of bridge voltage (4.1)-(4.2). The AC-side RMS currents are calculated in per unit normalized to I_{base} which is derived from Dual Active Bridge (DAB) analysis [69], [32]. Accordingly, the base values defined in (3.1) are adopted for the TAB as well. In this context, the interface inductor for each topology will be calculated as function of L_{base}. Equation (4.7) gives the value of L_{base} that produces maximum power transfer (P_{max}=1 pu) given the DC side voltage of bridge 1 (reference bridge) and switching frequency.

$$L_{base} = \frac{{V_{dc1}}^2}{8\, f_s\, P_{max}} \tag{4.7}$$

(a) Analysis of AC link Topology 1

This section covers the derivation of AC-side RMS current and active/reactive power for topology 1. Per unit AC-side instantaneous current at each port can be derived based on (4.8).

$$i_m(t) = \frac{v_i(t) - v_c(t)}{j2\pi f(2L_1)/Z_{base}} \tag{4.8}$$

Such that:

- m is the number of port.
- v_c is per unit common node voltage as depicted in Fig. 4.5.
- $L_1$is interface inductor of topology 1.
- $v_i(t)$ is per unit AC-side bridge voltage defined by (4.1) and (4.2).

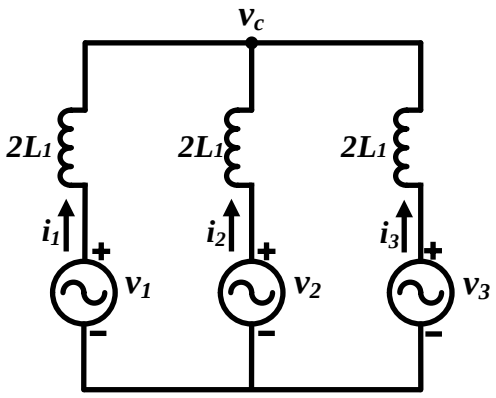

Fig. 4.5: Equivalent circuit of the non-isolated TAB under Topology 1.

On this basis, AC-side instantaneous currents are derived and represented in rectangular form as outlined by (4.9)-(4.11).

$$\bar{I}_1 = -j\frac{4L_{base}}{2\pi L_1}(V_{1\,RMS} - \bar{V}_c) \tag{4.9}$$

$$\bar{I}_2 = -j\frac{4L_{base}}{2\pi L_1}(V_{2\,RMS}\cos(\delta_2) - jV_{2\,RMS}\sin(\delta_2) - \bar{V}_c) \tag{4.10}$$

$$\bar{I}_3 = -j\frac{4L_{base}}{2\pi L_1}(V_{3\,RMS}\cos(\delta_3) - jV_{3\,RMS}\sin(\delta_3) - \bar{V}_c) \tag{4.11}$$

Since $\bar{I}_1 + \bar{I}_2 + \bar{I}_3 = 0$, it follows that

$$\bar{V}_c = \frac{1}{3}[(V_{1\,RMS} + V_{2\,RMS}\cos(\delta_2) + V_{3\,RMS}\cos(\delta_3)) - j(V_{2\,RMS}\sin(\delta_2) + V_{3\,RMS}\sin(\delta_2))]. \tag{4.12}$$

Substituting (4.12) into (4.9)-(4.11) yields:

$$\bar{I}_1 = \frac{4L_{base}}{6\pi L_1}[(V_{2\,RMS}\,\sin(\delta_2) + V_{3\,RMS}\,\sin(\delta_3)) - j(2V_{1\,RMS} - V_{2\,RMS}\,\cos(\delta_2) - V_{3\,RMS}\,\cos(\delta_3))] \tag{4.13}$$

$$\bar{I}_2 = \frac{4L_{base}}{6\pi L_1}[(-2V_{2\,RMS}\,\sin(\delta_2) + V_{3\,RMS}\,\sin(\delta_3)) + j(V_{1\,RMS} - 2V_{2\,RMS}\,\cos(\delta_2) + V_{3\,RMS}\,\cos(\delta_3))] \tag{4.14}$$

$$\bar{I}_3 = \frac{4L_{base}}{6\pi L_1}[(V_{2\,RMS}\,\sin(\delta_2) - 2V_{3\,RMS}\,\sin(\delta_3)) + j(V_{1\,RMS} + V_{2\,RMS}\,\cos(\delta_2) - 2V_{3\,RMS}\,\cos(\delta_3))] \tag{4.15}$$

Thus, the AC-side RMS currents are:

$$|I_1|_{RMS} = \frac{4L_{base}}{6\pi L_1}\sqrt{(V_{2\,RMS}\,\sin(\delta_2) + V_{3\,RMS}\,\sin(\delta_3))^2 + (2V_{1\,RMS} - V_{2\,RMS}\,\cos(\delta_2) - V_{3\,RMS}\,\cos(\delta_3))^2} \tag{4.16}$$

$$|I_2|_{RMS} = \frac{4L_{base}}{6\pi L_1}\sqrt{(-2V_{2\,RMS}\,\sin(\delta_2) + V_{3\,RMS}\,\sin(\delta_3))^2 + (V_{1\,RMS} - 2V_{2\,RMS}\,\cos(\delta_2) + V_{3\,RMS}\,\cos(\delta_3))^2} \tag{4.17}$$

$$|I_3|_{RMS} = \frac{4L_{base}}{6\pi L_1}\sqrt{(V_{2\,RMS}\,\sin(\delta_2) - 2V_{3\,RMS}\,\sin(\delta_3))^2 + (V_{1\,RMS} + V_{2\,RMS}\,\cos(\delta_2) - 2V_{3\,RMS}\,\cos(\delta_3))^2} \tag{4.18}$$

Finally, the normalised active and reactive power expressions as function of modulation parameters (D_1, D_2, D_3, D_{12}, D_{13}), AC link inductor (L_1) and base inductance (L_{base}) can be obtained by substituting in (4.5) and (4.6). Thus:

$$\begin{aligned}
P_1 &= \frac{4L_{base}}{6\pi L_1}\,V_{1\,RMS}\,(\,V_{2\,RMS}\,\sin(\delta_2) + V_{3\,RMS}\,\sin(\delta_3)\,).\\
Q_1 &= \frac{4L_{base}}{6\pi L_1}\,V_{1\,RMS}\,(\,2V_{1\,RMS} - V_{2\,RMS}\,\cos(\delta_2) - V_{3\,RMS}\,\cos(\delta_3)\,).\\
P_2 &= \frac{4L_{base}}{6\pi L_1}\,V_{2\,RMS}\,(cos(\delta_2)[-2V_{2\,RMS}\,\sin(\delta_2) + V_{3\,RMS}\,\sin(\delta_3)\,]\\
&\quad - sin(\delta_2)[\,V_{1\,RMS} - 2V_{2\,RMS}\,\cos(\delta_2) + V_{3\,RMS}\cos(\delta_3)]).\\
Q_2 &= -\frac{4L_{base}}{6\pi L_1}\,V_{2\,RMS}\,(sin(\delta_2)[-2V_{2\,RMS}\,\sin(\delta_2) + V_{3\,RMS}\,\sin(\delta_3)\,]\\
&\quad + cos(\delta_2)[\,V_{1\,RMS} - 2V_{2\,RMS}\,\cos(\delta_2) + V_{3\,RMS}\cos(\delta_3)]).\\
P_3 &= \frac{4L_{base}}{6\pi L_1}\,V_{3\,RMS}\,(cos(\delta_3)[V_{2\,RMS}\,\sin(\delta_2) - 2V_{3\,RMS}\,\sin(\delta_3)\,]\\
&\quad - sin(\delta_3)[\,V_{1\,RMS} + V_{2\,RMS}\,\cos(\delta_2) - 2\,V_{3\,RMS}\cos(\delta_3)]).\\
Q_3 &= -\frac{4L_{base}}{6\pi L_1}\,V_{3\,RMS}\,(sin(\delta_3)[V_{2\,RMS}\,\sin(\delta_2) - 2V_{3\,RMS}\,\sin(\delta_3)]\\
&\quad + cos(\delta_3)[\,V_{1\,RMS} + V_{2\,RMS}\,\cos(\delta_2) - 2\,V_{3\,RMS}\cos(\delta_3)]).
\end{aligned} \tag{4.19}$$

(b) Analysis of AC link Topologies 2-6

Similarly, a steady state model based on fundamental harmonic component can be derived for the remaining topologies. All other remaining topologies are analysed in detail in Appendix A, following a similar procedure as in the preceding derivation for Topology 1. Tables 4.2, 4.3 and 4.4 show the derived active power, reactive power and AC-side RMS currents respectively for all AC link topologies.

Table 4.2: Per Unit Active Power at Each H-Bridge Normalized to P_{base}.

Topology		Active power
1	P_1	$\frac{4L_{base}}{6\pi L_1} V_{1\,rms}\,(\,V_{2\,rms}\sin(\delta_2) + V_{3\,rms}\sin(\delta_3)\,)$
	P_2	$\frac{4L_{base}}{6\pi L_1} V_{2\,RMS}\,(cos(\delta_2)[-2V_{2\,RMS}\sin(\delta_2) + V_{3\,RMS}\sin(\delta_3)\,] - sin(\delta_2)[\,V_{1\,RMS} - 2V_{2\,RMS}\cos(\delta_2) + V_{3\,RMS}\cos(\delta_3)])$
	P_3	$\frac{4L_{base}}{6\pi L_1} V_{3\,RMS}\,(cos(\delta_3)[V_{2\,RMS}\sin(\delta_2) - 2\,V_{3\,RMS}\sin(\delta_3)\,] - sin(\delta_3)[\,V_{1\,RMS} + V_{2\,RMS}\cos(\delta_2) - 2\,V_{3\,RMS}\cos(\delta_3)])$
2	P_1	$\frac{2L_{base}}{\pi L_2} V_{1\,RMS}\,(\,0.5V_{2\,RMS}\sin(\delta_2) + 0.5V_{3\,RMS}\sin(\delta_3)\,)$
	P_2	$\frac{L_{base}}{\pi L_2} V_{2\,RMS}\,(cos(\delta_2)[-2V_{2\,RMS}\sin(\delta_2) + V_{3\,RMS}\sin(\delta_3)\,] - sin(\delta_2)[\,V_{1\,RMS} - 2V_{2\,RMS}\cos(\delta_2) + V_{3\,RMS}\cos(\delta_3)])$
	P_3	$\frac{L_{base}}{\pi L_2} V_{3\,RMS}\,(cos(\delta_3)[V_{2\,RMS}\sin(\delta_2) - 2V_{3\,RMS}\sin(\delta_3)\,] - sin(\delta_3)[\,V_{1\,RMS} + V_{2\,RMS}\cos(\delta_2) - 2\,V_{3\,RMS}\cos(\delta_3)])$
3	P_1	$\frac{2L_{base}}{\pi L_3} V_{1\,RMS}\,(\,V_{2\,RMS}\sin(\delta_2) + V_{3\,RMS}\sin(\delta_3)\,)$
	P_2	$\frac{2L_{base}}{\pi L_3} V_{2\,RMS}\,(cos(\delta_2)[\,-2V_{2\,RMS}\sin(\delta_2) + V_{3\,RMS}\sin(\delta_3)] - sin(\delta_2)[\,V_{1\,RMS} - 2V_{2\,RMS}\cos(\delta_2) + V_{3\,RMS}\cos(\delta_3)])$
	P_3	$\frac{2L_{base}}{\pi L_3} V_{3\,RMS}(cos(\delta_3)[\,V_{2\,RMS}\sin(\delta_2) - 2V_{3\,RMS}\sin(\delta_3)] - sin(\delta_3)[\,V_{1\,RMS} + V_{2\,RMS}\cos(\delta_2) - 2V_{3\,RMS}\cos(\delta_3)])$
4	P_1	$\frac{4L_{base}}{3\pi L_4} V_{1\,RMS}\,(\,V_{2\,RMS}\sin(\delta_2) + V_{3\,RMS}\sin(\delta_3))$
	P_2	$-\frac{4L_{base}}{3\pi L_4} V_{2\,RMS}\,(cos(\delta_2)\,[\,V_{2\,RMS}\sin(\delta_2) + V_{3\,RMS}\sin(\delta_3)] + sin(\delta_2)[\,V_{1\,RMS} - V_{2\,RMS}\cos(\delta_2) - V_{3\,RMS}\cos(\delta_3)])$
	P_3	$\frac{4L_{base}}{3\pi L_4} V_{3\,RMS}\,(cos(\delta_3)\,[\,V_{2\,RMS}\sin(\delta_2) + V_{3\,RMS}\sin(\delta_3)]\,) + sin(\delta_3)[\,V_{1\,RMS} - V_{2\,RMS}\cos(\delta_2) - V_{3\,RMS}\cos(\delta_3)])$
5	P_1	$\frac{L_{base}}{\pi L_5} V_{1\,RMS}\,(-V_{2\,RMS}\sin(\delta_2) - V_{3\,RMS}\sin(\delta_3))$
	P_2	$\frac{L_{base}}{\pi L_5} V_{2\,RMS}\,(cos(\delta_2)\,[-4V_{2\,RMS}\sin(\delta_2) - 2\,V_{3\,RMS}\sin(\delta_3)] + sin(\delta_2)[\,2V_{1\,RMS} + 4V_{2\,rms}\cos(\delta_2) + 2\,V_{3\,RMS}\cos(\delta_3)])$
	P_3	$\frac{L_{base}}{\pi L_5} V_{3\,RMS}\,(cos(\delta_3)\,[-2V_{2\,RMS}\sin(\delta_2) - 4\,V_{3\,RMS}\sin(\delta_3)] + sin(\delta_3)[\,2V_{1\,RMS} + 2V_{2\,RMS}\cos(\delta_2) + 4\,V_{3\,RMS}\cos(\delta_3)])$
6	P_1	$\frac{2L_{base}}{\pi L_6} V_{1\,RMS}\,(-V_{2\,RMS}\sin(\delta_2) - V_{3\,RMS}\sin(\delta_3))$
	P_2	$\frac{2L_{base}}{\pi L_6} V_{2\,RMS}\,(cos(\delta_2)\,[\,-2V_{2\,RMS}\sin(\delta_2) - V_{3\,RMS}\sin(\delta_3)] - sin(\delta_2)[-V_{1\,RMS} - 2V_{2\,RMS}\cos(\delta_2) - V_{3\,RMS}\cos(\delta_3)])$
	P_3	$\frac{2L_{base}}{\pi L_6} V_{3\,RMS}\,(cos(\delta_3)\,[\,-V_{2\,RMS}\sin(\delta_2) - 2V_{3\,RMS}\sin(\delta_3)] - sin(\delta_3)[-V_{1\,RMS} - V_{2\,RMS}\cos(\delta_2) - 2V_{3\,RMS}\cos(\delta_3)])$

Table 4.3:Per Unit Reactive Power at Each H-Bridge Normalized to P_{base}.

Topology		Reactive power
1	Q_1	$\frac{4L_{base}}{6\pi L_1} V_{1\,RMS}\,(\,2V_{1\,RMS} - V_{2\,RMS}\cos(\delta_2) - V_{3\,RMS}\cos(\delta_3)\,)$
	Q_2	$-\frac{4L_{base}}{6\pi L_1} V_{2\,RMS}\,(sin(\delta_2)[-2V_{2\,RMS}\sin(\delta_2) + V_{3\,RMS}\sin(\delta_3)\,] + cos(\delta_2)[\,V_{1\,RMS} - 2V_{2\,RMS}\cos(\delta_2) + V_{3\,RMS}\cos(\delta_3)])$
	Q_3	$-\frac{4L_{base}}{6\pi L_1} V_{3\,RMS}\,(sin(\delta_3)[V_{2\,RMS}\sin(\delta_2) - 2\,V_{3\,RMS}\sin(\delta_3)] + cos(\delta_3)[\,V_{1\,RMS} + V_{2\,RMS}\cos(\delta_2) - 2\,V_{3\,RMS}\cos(\delta_3)])$
2	Q_1	$\frac{2L_{base}}{\pi L_2} V_{1\,RMS}\,(\,V_{1\,RMS} - 0.5V_{2\,RMS}\cos(\delta_2) - 0.5V_{3\,RMS}\cos(\delta_3)\,)$
	Q_2	$-\frac{L_{base}}{\pi L_2} V_{2\,RMS}\,(sin(\delta_2)[-2V_{2\,RMS}\sin(\delta_2) + V_{3\,RMS}\sin(\delta_3)\,] + cos(\delta_2)[\,V_{1\,RMS} - 2V_{2\,RMS}\cos(\delta_2) + V_{3\,RMS}\cos(\delta_3)])$
	Q_3	$-\frac{L_{base}}{\pi L_2} V_{3\,RMS}\,(sin(\delta_3)[V_{2\,RMS}\sin(\delta_2) - 2V_{3\,RMS}\sin(\delta_3)] + cos(\delta_3)[\,V_{1\,RMS} + V_{2\,RMS}\cos(\delta_2) - 2\,V_{3\,RMS}\cos(\delta_3)])$
3	Q_1	$\frac{2L_{base}}{\pi L_3} V_{1\,RMS}\,(\,2V_{1\,RMS} - V_{2\,RMS}\cos(\delta_2) - V_{3\,RMS}\cos(\delta_3))$
	Q_2	$-\frac{2L_{base}}{\pi L_3} V_{2\,RMS}\,(sin(\delta_2)\,[-2V_{2\,RMS}\sin(\delta_2) + V_{3\,RMS}\sin(\delta_3)] + cos(\delta_2)[\,V_{1\,RMS} - 2V_{2\,rms}\cos(\delta_2) + V_{3\,RMS}\cos(\delta_3)])$
	Q_3	$-\frac{2L_{base}}{\pi L_3} V_{3\,RMS}\,(sin(\delta_3)\,[V_{2\,RMS}\sin(\delta_2) - 2V_{3\,RMS}\sin(\delta_3)] + cos(\delta_3)[\,V_{1\,RMS} + V_{2\,rms}\cos(\delta_2) - 2\,V_{3\,RMS}\cos(\delta_3)])$
4	Q_1	$\frac{4L_{base}}{3\pi L_4} V_{1\,RMS}\,(\,V_{1\,RMS} - V_{2\,RMS}\cos(\delta_2) - V_{3\,RMS}\cos(\delta_3))$
	Q_2	$\frac{4L_{base}}{3\pi L_4} V_{2\,RMS}\,(sin(\delta_2)\,[\,V_{2\,RMS}\sin(\delta_2) + V_{3\,RMS}\sin(\delta_3)] - cos(\delta_2)[\,V_{1\,RMS} - V_{2\,RMS}\cos(\delta_2) - V_{3\,RMS}\cos(\delta_3)])$
	Q_3	$\frac{4L_{base}}{3\pi L_4} V_{3\,RMS}\,(sin(\delta_3)\,[\,V_{2\,RMS}\sin(\delta_2) + V_{3\,RMS}\sin(\delta_3)]\,) - cos(\delta_3)[\,V_{1\,RMS} - V_{2\,RMS}\cos(\delta_2) - V_{3\,RMS}\cos(\delta_3)])$
5	Q_1	$\frac{L_{base}}{\pi L_5} V_{1\,RMS}\,(\,2V_{1\,RMS} + V_{2\,RMS}\cos(\delta_2) + V_{3\,RMS}\cos(\delta_3))$
	Q_2	$-\frac{L_{base}}{\pi L_5} V_{2\,RMS}\,(sin(\delta_2)\,[-4V_{2\,RMS}\sin(\delta_2) - 2\,V_{3\,RMS}\sin(\delta_3)] - cos(\delta_2)[\,2V_{1\,RMS} + 4V_{2\,rms}\cos(\delta_2) + 2\,V_{3\,RMS}\cos(\delta_3)])$
	Q_3	$-\frac{L_{base}}{\pi L_5} V_{3\,RMS}\,(sin(\delta_3)\,[-2V_{2\,RMS}\sin(\delta_2) - 4V_{3\,RMS}\sin(\delta_3)] - cos(\delta_3)[\,2V_{1\,RMS} + 2V_{2\,rms}\cos(\delta_2) + 4\,V_{3\,RMS}\cos(\delta_3)])$
6	Q_1	$\frac{2L_{base}}{\pi L_6} V_{1\,RMS}\,(\,2V_{1\,RMS} + V_{2\,RMS}\cos(\delta_2) + V_{3\,RMS}\cos(\delta_3))$
	Q_2	$-\frac{2L_{base}}{\pi L_6} V_{2\,RMS}\,(sin(\delta_2)\,[\,-2V_{2\,RMS}\sin(\delta_2) - V_{3\,RMS}\sin(\delta_3)] + cos(\delta_2)[-V_{1\,RMS} - 2V_{2\,rms}\cos(\delta_2) - V_{3\,RMS}\cos(\delta_3)])$
	Q_3	$-\frac{2L_{base}}{\pi L_6} V_{3\,RMS}\,(sin(\delta_3)\,[\,-V_{2\,RMS}\sin(\delta_2) - 2V_{3\,RMS}\sin(\delta_3)] + cos(\delta_3)[-V_{1\,RMS} - V_{2\,rms}\cos(\delta_2) - 2V_{3\,RMS}\cos(\delta_3)])$

Table 4.4:Per Unit AC-side RMS currents at Each H-Bridge Normalized to I_{base}.

Topology		Active/Reactive power expression
1	$I_{1\,RMS}$	$\frac{4L_{base}}{6\pi L_1}\sqrt{[V_{2\,RMS}\sin(\delta_2) + V_{3\,RMS}\sin(\delta_3)]^2 + ([2V_{1\,RMS} - V_{2\,RMS}\cos(\delta_2) - V_{3\,RMS}\cos(\delta_3)]^2)}$
	$I_{2\,RMS}$	$\frac{4L_{base}}{6\pi L_1}\sqrt{[-2V_{2\,RMS}\sin(\delta_2) + V_{3\,RMS}\sin(\delta_3)]^2 + ([V_{1\,RMS} - 2V_{2\,RMS}\cos(\delta_2) + V_{3\,RMS}\cos(\delta_3)]^2)}$
	$I_{3\,RMS}$	$\frac{4L_{base}}{6\pi L_1}\sqrt{[V_{2\,RMS}\sin(\delta_2) - 2V_{3\,RMS}\sin(\delta_3)]^2 + ([V_{1\,RMS} + V_{2\,RMS}\cos(\delta_2) - 2V_{3\,RMS}\cos(\delta_3)]^2)}$
2	$I_{1\,RMS}$	$\frac{L_{base}}{\pi L_2}\sqrt{[V_{2\,RMS}\sin(\delta_2) + V_{3\,RMS}\sin(\delta_3)]^2 + ([2V_{1\,RMS} - V_{2\,RMS}\cos(\delta_2) - V_{3\,RMS}\cos(\delta_3)]^2)}$
	$I_{2\,RMS}$	$\frac{L_{base}}{\pi L_2}\sqrt{[2V_{2\,RMS}\sin(\delta_2) - V_{3\,RMS}\sin(\delta_3)]^2 + ([-V_{1\,RMS} + 2V_{2\,RMS}\cos(\delta_2) - V_{3\,RMS}\cos(\delta_3)]^2)}$
	$I_{3\,RMS}$	$\frac{L_{base}}{\pi L_2}\sqrt{[V_{2\,RMS}\sin(\delta_2) - 2V_{3\,RMS}\sin(\delta_3)]^2 + ([V_{1\,RMS} + V_{2\,RMS}\cos(\delta_2) - 2V_{3\,RMS}\cos(\delta_3)]^2)}$
3	$I_{1\,RMS}$	$\frac{4L_{base}}{2\pi L_3}\sqrt{[V_{2\,RMS}\sin(\delta_2) + V_{3\,RMS}\sin(\delta_3)]^2 + ([2V_{1\,RMS} - V_{2\,RMS}\cos(\delta_2) - V_{3\,RMS}\cos(\delta_3)]^2)}$
	$I_{2\,RMS}$	$\frac{4L_{base}}{2\pi L_3}\sqrt{[-2V_{2\,RMS}\sin(\delta_2) + V_{3\,RMS}\sin(\delta_3)]^2 + ([V_{1\,RMS} - 2V_{2\,RMS}\cos(\delta_2) + V_{3\,RMS}\cos(\delta_3)]^2)}$
	$I_{3\,RMS}$	$\frac{4L_{base}}{2\pi L_3}\sqrt{[V_{2\,RMS}\sin(\delta_2) - 2V_{3\,RMS}\sin(\delta_3)]^2 + ([V_{1\,RMS} + V_{2\,RMS}\cos(\delta_2) - 2V_{3\,RMS}\cos(\delta_3)]^2)}$
4	$I_{1\,RMS}$	

	$I_{2\,RMS}$	$\frac{2L_{base}}{3\pi L_4}\sqrt{[V_{2\,RMS}\sin(\delta_2)+V_{3\,RMS}\sin(\delta_3)]^2+([V_{1\,RMS}-V_{2\,RMS}\cos(\delta_2)-V_{3\,RMS}\cos(\delta_3)]^2)}$
	$I_{3\,RMS}$	
5	$I_{1\,RMS}$	$\frac{4L_{base}}{\pi L_5}\sqrt{[0.25V_{2\,RMS}\sin(\delta_2)+0.25V_{3\,RMS}\sin(\delta_3)]^2+([0.5V_{1\,RMS}+0.25V_{2\,RMS}\cos(\delta_2)+0.25V_{3\,RMS}\cos(\delta_3)]^2)}$
	$I_{2\,RMS}$	$\frac{2L_{base}}{\pi L_5}\sqrt{[V_{2\,RMS}\sin(\delta_2)+0.5V_{3\,RMS}\sin(\delta_3)]^2+([0.5V_{1\,RMS}+V_{2\,RMS}\cos(\delta_2)+0.5V_{3\,RMS}\cos(\delta_3)]^2)}$
	$I_{3\,RMS}$	$\frac{2L_{base}}{\pi L_5}\sqrt{[0.5V_{2\,RMS}\sin(\delta_2)+V_{3\,RMS}\sin(\delta_3)]^2+([0.5V_{1\,RMS}+0.5V_{2\,RMS}\cos(\delta_2)+V_{3\,RMS}\cos(\delta_3)]^2)}$
6	$I_{1\,RMS}$	$\frac{4L_{base}}{\pi L_6}\sqrt{[0.5V_{2\,RMS}\sin(\delta_2)+0.5V_{3\,RMS}\sin(\delta_3)]^2+([V_{1\,RMS}+0.5V_{2\,RMS}\cos(\delta_2)+0.5V_{3\,RMS}\cos(\delta_3)]^2)}$
	$I_{2\,RMS}$	$\frac{4L_{base}}{\pi L_6}\sqrt{[V_{2\,RMS}\sin(\delta_2)+0.5V_{3\,RMS}\sin(\delta_3)]^2+([0.5V_{1\,RMS}+V_{2\,RMS}\cos(\delta_2)+0.5V_{3\,RMS}\cos(\delta_3)]^2)}$
	$I_{3\,RMS}$	$\frac{4L_{base}}{\pi L_6}\sqrt{[0.5V_{2\,RMS}\sin(\delta_2)+V_{3\,RMS}\sin(\delta_3)]^2+([0.5V_{1\,RMS}+0.5V_{2\,RMS}\cos(\delta_2)+V_{3\,RMS}\cos(\delta_3)]^2)}$

4.2.3. Calculation of AC inductance for each topology

The objective of the analysis in this section is to calculate the value of the interface inductor (L_i) for all investigated topologies that ensures a maximum power transfer of 1pu. The procedure is to equate the active power at bridge 1 to maximum power (P_1=1pu) and substitute with unity duty ratios D_1=D_2=D_3=1 and phase shift ratios D_{12}=D_{13}=0.5. This was necessary to mathematically simplify power equation of bridge 1 and allow calculating AC link inductance L_i as a function of base inductance (L_{base}) and DC voltage ratios (K_{12}, K_{13}) enabling a standardised comparison. The calculated AC link inductor values for investigated topologies are shown in Table 4.5.

Table 4.5: Inductor values of the TAB AC link topologies.

AC link Topology (1)	**AC link Topology (2)**	**AC link Topology (3)**
$L_1=\frac{4^3}{2*6\pi^3}(K_{12}+K_{13})L_{base}$	$L_2=\frac{4^3}{2*4\pi^3}(K_{12}+K_{13})L_{base}$	$L_3=\frac{4^3}{2*2\pi^3}(K_{12}+K_{13})L_{base}$
AC link Topology (4)	**AC link Topology (5)**	**AC link Topology (6)**
$L_4=\frac{4^3}{2*6\pi^3}(K_{12}+K_{13})L_{base}$	$L_5=\frac{4^3}{2*4\pi^3}(K_{12}+K_{13})L_{base}$	$L_6=\frac{4^3}{2*2\pi^3}(K_{12}+K_{13})L_{base}$

The definition of L_i as a function of L_{base}, K_{12}, K_{13} is generic and thus enables designing the AC link according to converter parameters. For example, the AC link design of a non-isolated TAB converter based on topology 1 with rated power of

500 Watt, f_s=2500 Hz, V_{dc1}=100 volt and V_{dc2}=40 volt, V_{dc3}=60 volt at K_{12}=0.4 and K_{13}=0.6, requires the following steps−

1- Calculate L_{base} using (4.7), then L_{base}= 1 mH.
2- Substitute L_{base} in the L_i according to the AC link topology from Table 4.3, then L_1 = 3.44e-04 H for topology 1.
3- To verify the correctness of the calculated interface inductor (L_1), employ L_1 in the active power equations of topology-1 (as outlined by Table 4.2) and use modulation parameters (D_1=D_2=D_3=1, D_{12}=D_{13}=0.5) to obtain full power. This will produce: P_1=1 pu=500 W, P_2=-0.4 pu=-200 W and P_3=-0.6 pu=-300 W, such that maximum power is delivered by port 1 while the other two ports are sinking maximum power as governed by their corresponding DC voltage ratios K_{12} and K_{13}.

Topologies 1 and 4 offer minimum value of AC link inductor (hence minimum footprint, volume and weight) considering the inductor value of the AC link for each topology shown in Table 4.5. This means that these two topologies can transfer the full range of power with the minimum AC link's inductor value, and hence minimum physical footprint.

4.2.4. Calculation of topologies' RMS current and reactive power

It is now necessary to investigate the topology that incorporates minimum current stresses (and hence minimum reactive power losses) for the same level of power transferred in the topologies under study. This can be done by evaluating the resultant RMS current of each topology (I_{RMS}) and total reactive power losses (Q_{tot}) in all topologies. For this sake unity duty ratios (D_1=D_2=D_3=1) with maximum phase shifts (D_{12}=D_{13}=0.5) are implemented, thus producing full power for all topologies. This allows standardised comparison of total reactive power (defined

as $Q_{tot}=Q_1+Q_2+Q_3$) while I_{RMS} is defined as the resultant of RMS currents of all AC link branches given by (4.20). Calculated values of RMS currents and reactive power at various DC voltage ratios are as shown Table 4.6.

$$I_{RMS} = \sqrt{\sum_{i=1}^{n} (I_{i\,RMS})^2} \tag{4.20}$$

Where $I_{i\,RMS}$ is the RMS current at AC side of each H-bridge, n=3 for triple active bridge, n=4 for quad active bridge and so on.

Table 4.6: Calculated RMS currents and reactive power at various DC voltage ratios.

Topology	K_{12}=1, K_{13}=1		K_{12}=0.4, K_{13}=0.6		K_{12}=0.7, K_{13}=0.3	
	P_1=1 pu,P_2=-0.5 pu, P_3=-0.5 pu		P_1=1 pu,P_2=-0.4 pu, P_3=-0.6pu		P_1=1 pu,P_2=-0.7 pu, P_3=-0.3 pu	
	Q_{tot}	I_{RMS}	Q_{tot}	I_{RMS}	Q_{tot}	I_{RMS}
1	2.00 pu	1.92 pu	2.56 pu	3.08 pu	2.74 pu	3.18 pu
2	2.00 pu	1.92 pu	2.56 pu	3.08 pu	2.74 pu	3.18 pu
3	2.00 pu	1.92 pu	2.56 pu	3.08 pu	2.74 pu	3.18 pu
4	2.50 pu	2.15 pu	2.00 pu	2.72 pu	2.00 pu	2.72 pu
5	4.00 pu	2.94 pu	3.52 pu	3.77 pu	3.58 pu	3.78 pu
6	4.00 pu	2.94 pu	3.52 pu	3.77 pu	3.58 pu	3.78 pu

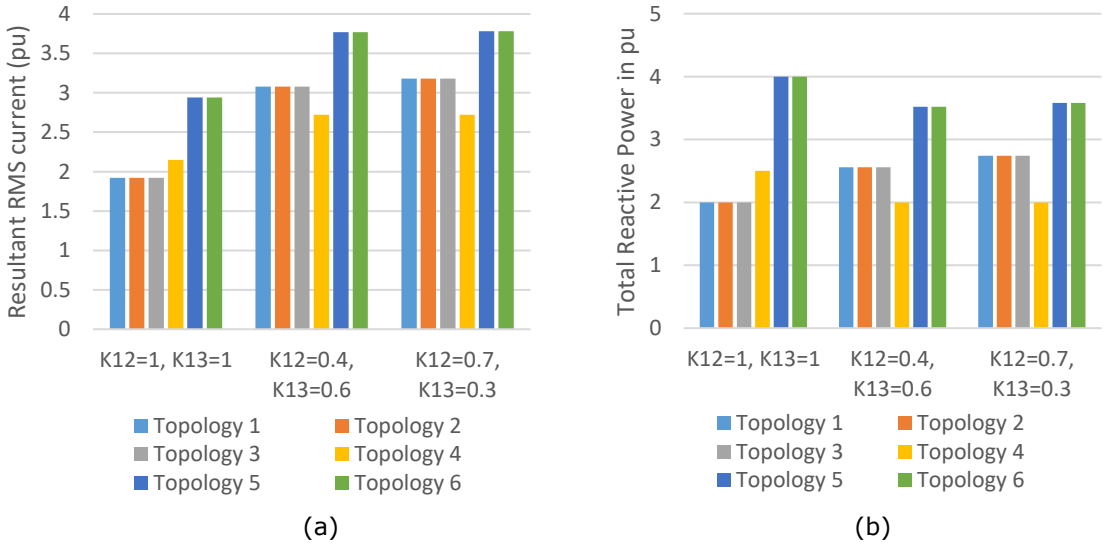

Fig. 4.6: Calculated RMS currents and reactive power for all topologies at various DC voltage ratios– (a) I_{RMS} (b) Q_{tot}.

Hence topologies 1, 2 and 3 yield minimum I_{RMS} and Q_{tot} in unity gain mode (K_2=K_3=1). However, topology 4 achieves minimum I_{RMS} and Q_{tot} and then comes topologies 1, 2 and 3 considering buck/boost modes (K_{12}=0.4, K_{13}=0.6) and (K_{12}=0.7, K_{13}=0.3) as shown in Fig 4.6. Nevertheless, topology 4 is the least reliable topology given it is basically a series configuration which means that if any of the bridges fail (i.e.: under fault condition) the entire system collapses. Therefore, topologies 1, 2, 3 are optimal topologies in the criteria of reactive power, RMS current and reliability. This is because they offer minimum RMS current and reactive power losses in unity-gain mode and achieve the best combination of reduced RMS current and reactive power along with reliability (compared to topology 4) in buck/boost modes.

4.2.5. Selection of Optimal AC Link Topology

Findings regarding the value of interface inductor outlined by Table 4.5, as well as the resultant RMS current and total reactive power losses for all investigated topologies illustrated by Fig 4.6, conclude that the star-connected AC link (**topology-1**) is the optimal topology for a purely inductive AC link for a non-isolated MAB converter. This is because it realises both minimum AC link inductance as well as minimum reactive losses.

4.3. New Decoupled Power Controller

The aim of this subsection is to develop a simple and scalable decoupled power controller for MAB converter with any number of ports. The coupled and nonlinear relationship of phase shifts with power at every H-bridge makes it vital to develop a phase shift decoupler to enable utilising conventional PI controllers for power flow regulation in MAB converter.

4.3.1. Controller Design

The non-linear relationship is shown in (4.21) which represents normalised fundamental harmonic power flow characteristics for TAB converter (3-port MAB). This is considering star-connected inductive-based AC link equivalent at unity gain mode (K_{12}=K_{13}=1), unity duty ratios (D_1=D_2=D_3=1) and port 1 as the reference port.

$$\begin{aligned} P_1 &= \frac{1}{2}[Sin\,(D_{12}) + Sin\,(D_{13})] \\ P_2 &= \frac{1}{2}[-Sin\,(D_{12}) + Sin\,(D_{13} - D_{12})] \\ P_3 &= \frac{1}{2}[-Sin\,(D_{13}) + Sin\,(D_{12} - D_{13})]. \end{aligned} \tag{4.21}$$

Power flow for MAB with *n*-ports are required in order to design a decoupler for MAB converter. Power flow in four-port (quad) active bridge (QAB) is derived as outlined by (4.22). This is considering the star-connected AC link, the approach presented in section 4.2.2 can be used to derive active power with AC link inductor value at this case calculated as ($L_1 = \frac{3*4^2}{2\pi^3} L_{base}$). By considering unity gain mode (K_{12}=K_{13}=K_{14}=1), unity duty ratio (D_1=D_2=D_3=D_4=1) and port 1 as the reference port, the normalised fundamental harmonic power flow for the QAB converter is:

$$\begin{aligned} P_1 &= \frac{1}{3}[Sin\,(D_{12}) + Sin\,(D_{13}) + Sin\,(D_{14})]. \\ P_2 &= \frac{1}{3}[-Sin\,(D_{12}) + Sin\,(D_{13} - D_{12}) + Sin\,(D_{14} - D_{12})]. \\ P_3 &= \frac{1}{3}[-Sin\,(D_{13}) + Sin\,(D_{12} - D_{13}) + Sin\,(D_{14} - D_{13})]. \\ P_4 &= \frac{1}{3}[-Sin\,(D_{14}) + Sin\,(D_{12} - D_{14}) + Sin\,(D_{13} - D_{14})]. \end{aligned} \tag{4.22}$$

By inspection of the normalised power flow analysis of both TAB and QAB converters, as outlined by (4.21) and (4.22), a trend is observed and thus generalised power flow analysis for an *n*-port MAB converter is given by (4.23) where *r* stands for reference port. The generalised form for the active power in MAB converter with N ports — outlined by (4.23) — can be also attained using superposition method, mathematical derivation of this is provided in Appendix B.

$$P_j = \frac{1}{n-1}\left[-Sin\left(D_{rj}\right) + \sum_{i=2}^{n} \text{Sin}\left(D_{ri} - D_{rj}\right)\right], j = 1,2\ldots, n \tag{4.23}$$

Where n is number of H-bridges, $n \neq 1$ and $D_{ii} = 0$.

From this, and by using Taylor's series, a general linearised form of the power flow analysis is given as follows:

$$P_j = c_j + \sum_{\substack{i=1 \\ i \neq r}}^{n} C_{ji}\, D_{ri}\ , \qquad j = 1,2,3, \ldots., n. \tag{4.24}$$

Where

$$c_i = P_i(a_1, a_2, .. a_{n-1}) + \sum_{\substack{j=1 \\ j \neq r}}^{n} \frac{\partial P_i}{\partial D_{rj}}(a_1, a_2, .. a_{n-1}) * (-a_j)$$

$$C_{ji} = \frac{\partial P_i}{\partial D_{rj}}(a_1, a_2, .. a_{n-1})$$

Such that coefficients c_i and c_{ji} are calculated at equilibrium points ($D_{ri}=a_1 \ldots\ldots D_{rn}=a_{n-1}\ r \neq i$).

Then (4.24) can be expressed as

$$\begin{bmatrix} P_1 \\ \vdots \\ P_n \end{bmatrix} = \begin{bmatrix} C_{12} & \cdots & C_{1n} \\ \vdots & \ddots & \vdots \\ C_{n2} & \cdots & C_{nn} \end{bmatrix} \begin{bmatrix} D_{ri} \\ \vdots \\ D_{rn} \end{bmatrix} + \begin{bmatrix} c_1 \\ \vdots \\ c_n \end{bmatrix} \tag{4.25}$$

However, for power flow control, we need to regulate only (n-1) bridge powers, as ($P_1+P_2+\ldots P_n=0$). This can be expressed as follows

$$\begin{bmatrix} P_1 \\ \vdots \\ P_{n-1} \end{bmatrix} = \begin{bmatrix} C_{12} & \cdots & C_{1n} \\ \vdots & \ddots & \vdots \\ C_{q2} & \cdots & C_{qn} \end{bmatrix} \begin{bmatrix} D_{ri} \\ \vdots \\ D_{rn} \end{bmatrix} + \begin{bmatrix} c_1 \\ \vdots \\ c_{n-1} \end{bmatrix}, q = n-1 \tag{4.26}$$

Then (4.28) is rewritten as follows

$$\begin{bmatrix} D_{ri} \\ \vdots \\ D_{rn} \end{bmatrix} = C^{-1} \begin{bmatrix} P_1 - c_1 \\ \vdots \\ P_{n-1} - c_{n-1} \end{bmatrix} \tag{4.27}$$

Now let $A = \begin{bmatrix} A_{12} & \cdots & A_{1n} \\ \vdots & \ddots & \vdots \\ A_{q2} & \cdots & A_{qn} \end{bmatrix} = C^{-1} = \begin{bmatrix} C_{12} & \cdots & C_{1n} \\ \vdots & \ddots & \vdots \\ C_{q2} & \cdots & C_{qn} \end{bmatrix}^{-1}$

Then (4.27) is rearranged as follows

$$\begin{bmatrix} D_{ri} \\ \vdots \\ D_{rn} \end{bmatrix} = \begin{bmatrix} A_{12} & \cdots & A_{1n} \\ \vdots & \ddots & \vdots \\ A_{q2} & \cdots & A_{qn} \end{bmatrix} \begin{bmatrix} P_1 - c_1 \\ \vdots \\ P_{n-1} - c_{n-1} \end{bmatrix} \tag{4.28}$$

The derived phase shift decoupler in (4.28) allows the use of conventional PI controllers to treat the power error (P^*-P_{act}) for every port and calculates the phase shifts needed for power regulation. The outcome is a scalable decoupled power flow controller illustrated in Fig. 4.7. This controller is applicable to MAB converter regardless of number of ports.

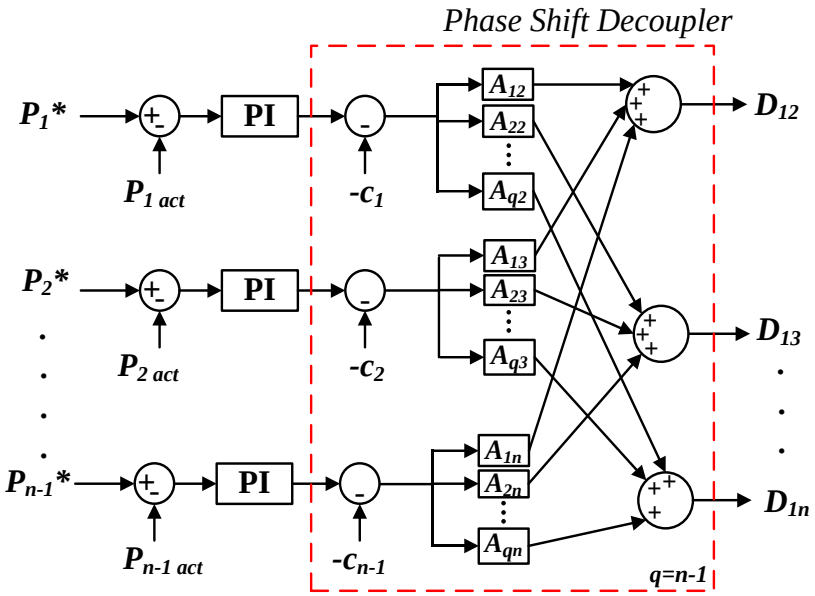

Fig. 4.7: PI-based decoupled power controller for MAB converter.

4.3.2. Simulation Results

This subsection covers the verification of the scalable PI-based power flow controller. This is achieved by applying the power flow controller on MAB converter with 3-port (TAB) and 4-port (QAB) to test the performance of the controller to

track desired power level. Simulation via Simulink/Matlab is carried out using the converter parameters shown in Table 4.7. Simulation results, shown in Figs 4.8 to 4.10, are obtained at different operating points (i.e.: power transfer levels and DC voltage ratio.) to verify the effectiveness of the controller. Figs 4.8 and 4.9 presents the implementation on TAB converter while Fig 4.10 is the implementation on QAB converter (four port active bridge). In Fig 4.9 a step change is introduced in port one only to further investigate the validity of the proposed decoupled controller.

Table 4.7: Parameters of the MAB converter.

Parameter	value
Bridge 1 DC Voltage V_{dc1}	100V
Bridge 2 DC Voltage V_{dc2}	K_{12}*100V
Bridge 2 DC Voltage V_{dc3}	K_{13}*100V
Bridge 2 DC Voltage V_{dc4}	K_{14}*100V
Switching Frequency f_s	2.5kHz
Base Power P_{base}	500W
Base Inductance L_{base}	1mH

Ppp

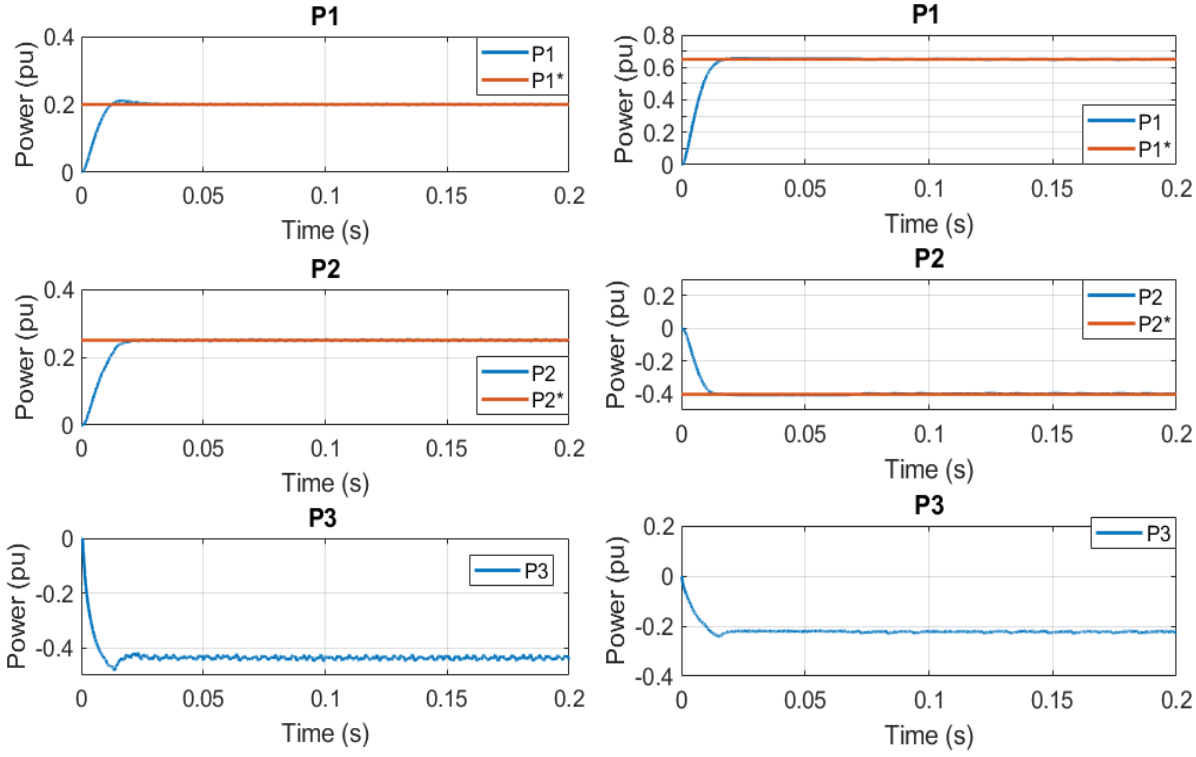

Fig. 4.8: Performance of proposed power flow controller for TAB converter at (a)K_{12}= 1, K_{13}= 1 at P_1*=0.2pu, P_2*=0.25pu(b)K_{12}= 0.7, K_{13}= 0.3 at P_1*=0.65pu, P_2*=-0.44pu.

p

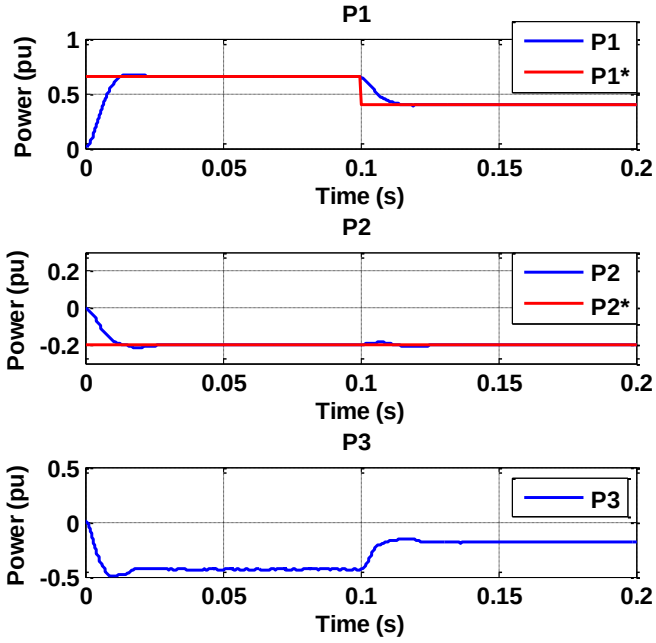

Fig. 4.9: Performance of proposed power flow controller for TAB converter at K_{12}= 0.7, K_{13}= 0.9 at P_1*=0.65pu(0-0.1sec), 0.4(0.1-0.2sec) and P_2*=-0.2pu.

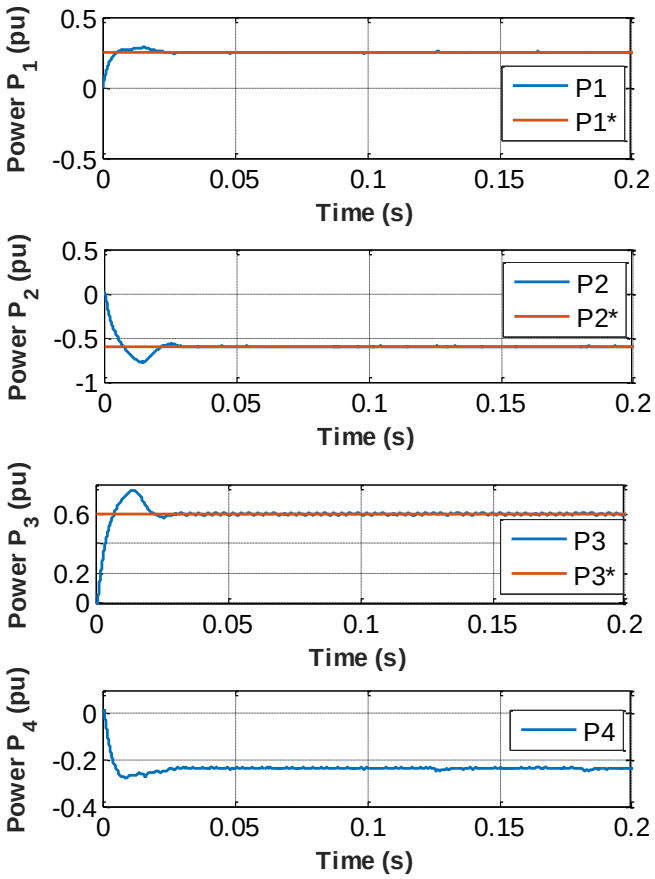

Fig. 4.10: Performance of proposed power flow controller at QAB converter for K_{12}=1, K_{13}=1 and K_{14}=1, at P_1*=0.25pu,P_2*=0.6pu and P_3*=-0.6pu.

4.4. Summary

This chapter proposes a generic circuit modelling and per unit steady state modelling, of the non-isolated triple active bridge (TAB) and multi active bridge (MAB) converters, under various purely inductor-based AC link topologies. On this basis, the topology requiring the minimum value of interface inductors (lowest footprint) as well as achieving minimum reactive power (and current stresses) is identified. Finally, generic power flow analysis is proposed besides a phase shift decoupler along with a PI-based power flow control scheme for MAB converters regardless of number of ports.

Chapter 5. Current-Stress Minimisation Based on Offline Particle Swarm Optimisation Method

This chapter presents a derivation of generalised power flow controller for the bidirectional dual active bridge (DAB) DC-DC converter under triple phase shift (TPS) control to enable closed loop power regulation while minimising current stress. The key achievement is a new simple closed loop controller, implementable in real time, to meet the desired power transfer level at minimum current stress, along with an implement standard of TPS control scheme. The methodology used to derive the controller include utilising an offline particle swarm optimisation (PSO) method (i.e.: an iterative AI-based optimisation method.) to obtain an extensive set of TPS ratios for minimising the RMS current in the entire bidirectional power range of -1 to 1 per unit. The extensive set of results achieved from PSO presents a generic data pool, which is carefully analysed to derive simple useful relations. Such relations enabled a generic closed loop controller design that can be implemented in real time avoiding the extensive computational capacity that iterative optimisation techniques require. A detailed Simulink DAB switching model is used to validate precision of the proposed closed loop controller under various operating conditions. An experimental prototype also substantiates the results achieved.

5.1 Proposed PSO Algorithm

This section presents the mathematical formulation of the minimisation problem including definition of the minimisation objective and related constraints. Optimisation in DAB has been tackled in existing literature, for example [83] used a Lagrange Multiplier method (LMM) to target the minimum current stresses

defined as peak inductor current. LMM with Karush-Kahn-Tucker (KKT) method was used in [73] to minimise the peak current in DAB. However, it is too complicated to use KKT in DAB as fourth order algebraic equations are involved. In addition, the non-convex feasible region of this optimal problem means that the LMM lacks sufficiency [74]. A Neural Network NN-based algorithm has been used in [97] to achieve minimum reactive power consumption, however the training of the neural network was done based on sub-optimal solutions calculated by tedious recursive loops. There is a need to investigate artificial-intelligence based optimisation methods such as PSO, ant colony optimisation (ACO) and genetic algorithms (GAs) for application in DAB converter. In terms of performance comparison of these methods; PSO is considered to be faster than ACO and generally requires less algorithm-parameters to handle [122], also, PSO is easier to implement compared to GAs with less parameters to adjust [123] & [124]. Therefore, PSO is selected as an optimisation tool in this chapter. In the next subsections the mathematical formulation of the proposed minimisation problem will be presented and then the PSO method is introduced for implementation on the proposed minimisation problem to obtain optimum modulation parameters. The algorithm outputs will be analysed later in this chapter to design the controller.

5.1.1. Formulation of the minimisation problem

Different parameters have been considered in existing literature as minimisation objectives, however, RMS inductor current is believed to be the most effective parameter: more so non-active power loss, peak current as minimisation objectives. This is due to the fact that the dominant portion of converter's total losses is conduction losses which is highly affected by RMS current stresses [30], [31]. In addition, copper losses and conduction losses are proportional to the square of the RMS current in the widely used MOSFET power switches [32].

Therefore, current stress minimisation in this thesis will refer to the minimisation of the RMS current of AC link's inductor. Accordingly, the minimisation objective is given by (5.1) outlining the inductor's RMS current which is calculated from (3.9). Mathematical formulation of the proposed multi-constrained minimisation problem is given as follows−

Minimise (for given K_{12})

$$Obj.Fun. = {I_{L\,RMS}}^2(K_{12}, D_1, D_2, D_{12}). \tag{5.1}$$

Subject to

Equality constraint: $P^* = \frac{1}{T_h}\int_0^{T_h} v_{br1}(t).i_L(t)dt.$

And the inequality constraints:

- $0 \leq D_1 \leq 1$, $0 \leq D_2 \leq 1$, $-1 \leq D_{12} \leq 1$ where 1≡180º.
- Operational constraints of each switching mode (see Table 3.1)

5.1.2. Optimisation technique

Due to its capability to handle multi-constraint optimisation problems, particle swarm optimisation (PSO) method [125] is chosen to obtain the optimal TPS ratios at the entire power level and different values of DC voltage ratios. This is done offline by applying PSO on the exact DAB model. This section provides the basic principles of PSO as an iterative AI-based optimisation technique. PSO basically imitates the swarm behaviour and the individuals represent points (solutions) in the *N*-dimensional search space. The *N*-dimensional search space in case of DAB is three, such that every individual (particle) is composed of three items (D_1, D_2 and D_{12}). The model equations representing PSO are outlined by (5.2) and (5.3), where $\boldsymbol{X}$ is defined as individual position (solution≡ TPS parameters) and $\boldsymbol{V}$ is defined as the velocity (deviation) needed to change the individual position $\boldsymbol{X}$ (solution) for every iteration. The velocity of each particle in the *N*-dimensional

space is obtained by (5.2). The velocity depends on three parameters: the previous velocity, personal experience of the particle and the global experience of the whole swarm. Then, every individual's position $\boldsymbol{X}$ in the N-dimensional space is updated using (5.3) depending on the previous position (solution) and the current velocity. Fig. 5.1 shows the flow diagram illustrating the principle of operation of the PSO.

$$V_i^{m+1} = w\, V_i^{m} + c_1 r_1 (\mathrm{P}best_i^{m} - X_i^{m}) + c_2 r_2 (\mathrm{G}best^{m} - X_i^{m}) \tag{5.2}$$

$$X_i^{m+1} = X_i^{m} + V_i^{m+1} \tag{5.3}$$

Where:

- m is the iteration index.
- c_1 and c_2 are two positive constants, such that $c_1=c_2=1$ as the common practice of PSO [125].
- r_1 and r_2 are two randomly generated numbers, such that $0 \le r_1 \le 1$, $0 \le r_2 \le 1$
- w is the inertia constant, such that w=*0.9-(0.005*m*).
- $\mathbf{P}\boldsymbol{best}_\mathbf{i}^{\mathbf{m}}$ is the best position particle based on its own experience.
- $\mathbf{G}\boldsymbol{best}^{\boldsymbol{m}}$ is the best position based on overall swarm's experience.

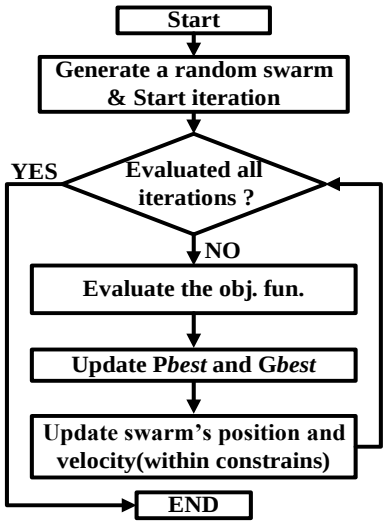

Fig. 5.1: Flow chart of PSO algorithm.

The PSO-based algorithm searches, in every iteration of the iterative loop, for the optimal modulation parameters to achieve the minimum inductor's RMS current

while simultaneously maintaining the required power level. Before executing the iterations, a vector of particle positions $\boldsymbol{X}$ is randomly generated (random values of modulation parameters). In every iteration the following steps are carried out:

- Each particle $\boldsymbol{X_i^m}$ is evaluated at iteration $\boldsymbol{m}$. The outputs of this evaluation are (power transfer evaluated at $\boldsymbol{X_i^m}$) and ($Obj.Fun.$ evaluated at$\boldsymbol{X_i^m}$).
- The ${I_{L\,RMS}}^2$ evaluation for individual $\boldsymbol{X_i^m}$ ($Obj.Fun.$ at $\boldsymbol{X_i^m}$) is compared to the evaluation of the same individual from the previous iteration; hence the particle position $\boldsymbol{X_i^m}$ achieving the minimum evaluation value is defined as personal best value $\mathbf{P}\boldsymbol{best}_\mathbf{i}^\mathbf{m}$.
- The previous comparison is done with respect to the equality constraint defined in previous section.
- Then the $\mathbf{P}\boldsymbol{best}$ achieving the minimum ${I_{L\,RMS}}^2$ value between all particles (the entire swarm) is identified as the global best value **G*best***.
- Then using (5.2) and (5.3), the velocity and position of individuals are updated respectively with respect to the inequality constraints defined in previous section.

The previous steps are carried out for all the possible switching modes according to the reference power ***P****. After all iterations are executed, the **G*best*** is identified which includes the optimal TPS ratios; hence the minimum ${I_{L\,RMS}}^2$ is obtained with associated switching mode. The MATLAB PSO program is provided in Appendix C.

5.2 Analysis of the offline PSO Algorithm Results

The off-line optimal phase shift calculations were carried out using MATLAB/m-file software, based on the proposed per unit DAB equations, associated constraints and assuming that $K_{12}\leq 1$, where $K_{12}=nV_{dc2}/V_{dc1}$: the other

condition K_{12}>1 can be analysed similarly. The buck/boost mode is included in this thesis as bi-directional power at K_{12}<1 inherently includes buck mode for operation in forward power flow and boost mode for operation in reverse power flow. The values of DC voltage ratio (K_{12}) used in this section were:

- K_{12}=0.25, 0.4 and 0.6 representing buck/boost mode.
- K_{12}=1 representing unity gain operating mode.

The PSO is applied in the entire power range for both power flow directions; such that positive power transfer indicates power flow from bridge 1 to bridge 2 and vice versa. The optimal solutions of the three modulation parameters are presented in Fig.5.2 parts (a) to (c) and Fig. 5.3 where the full per unit power range is from $-K_{12}$ to K_{12}; such that $|P_{max\text{-}pu}|=K_{12}$. This is calculated by normalising the DAB maximum power transfer from (5.4) to the base power given by (3.1).

$$P_{max} = \frac{V_{dc1} n V_{dc2}}{8 f_s L} \quad \text{, Where } nV_{dc2} = K_{12} V_{dc1} \tag{5.4}$$

The PSO output optimal TPS results (for the bidirectional power at the investigated values of K_{12}) have been carefully examined with respect to the operational constraint of switching modes (shown in Table 3.1). This allowed to define the switching modes and modulation methods (CPS, EPS or TPS) corresponding to the optimal TPS results. Based on this, a general pattern for the optimal modulation parameters in buck/boost mode is developed in Fig. 5.2 (d) where the entire power range is divided into four sections. Regarding the optimal solutions for buck/boost mode shown in Fig. 5.2 parts (a) to (c), we have:

- If desired power $|\boldsymbol{P}^*| \leq \boldsymbol{0.5K_{12}}$, optimal solutions were attained by (TPS); where minimum $i_{L\,RMS}$ is achieved by the switching modes 2’ as shown in Fig. 5.2 (d).

- If desired power $|P^*| \geq 0.5K_{12}$, then extended phase shift (EPS) [72] and conventional phase shift (CPS) achieved the optimal solution, as shown in Fig. 5.2 (d); where the minimum $I_{L\,RMS}$ is realized by switching modes 6 and 6′ for positive and negative power transfer respectively.

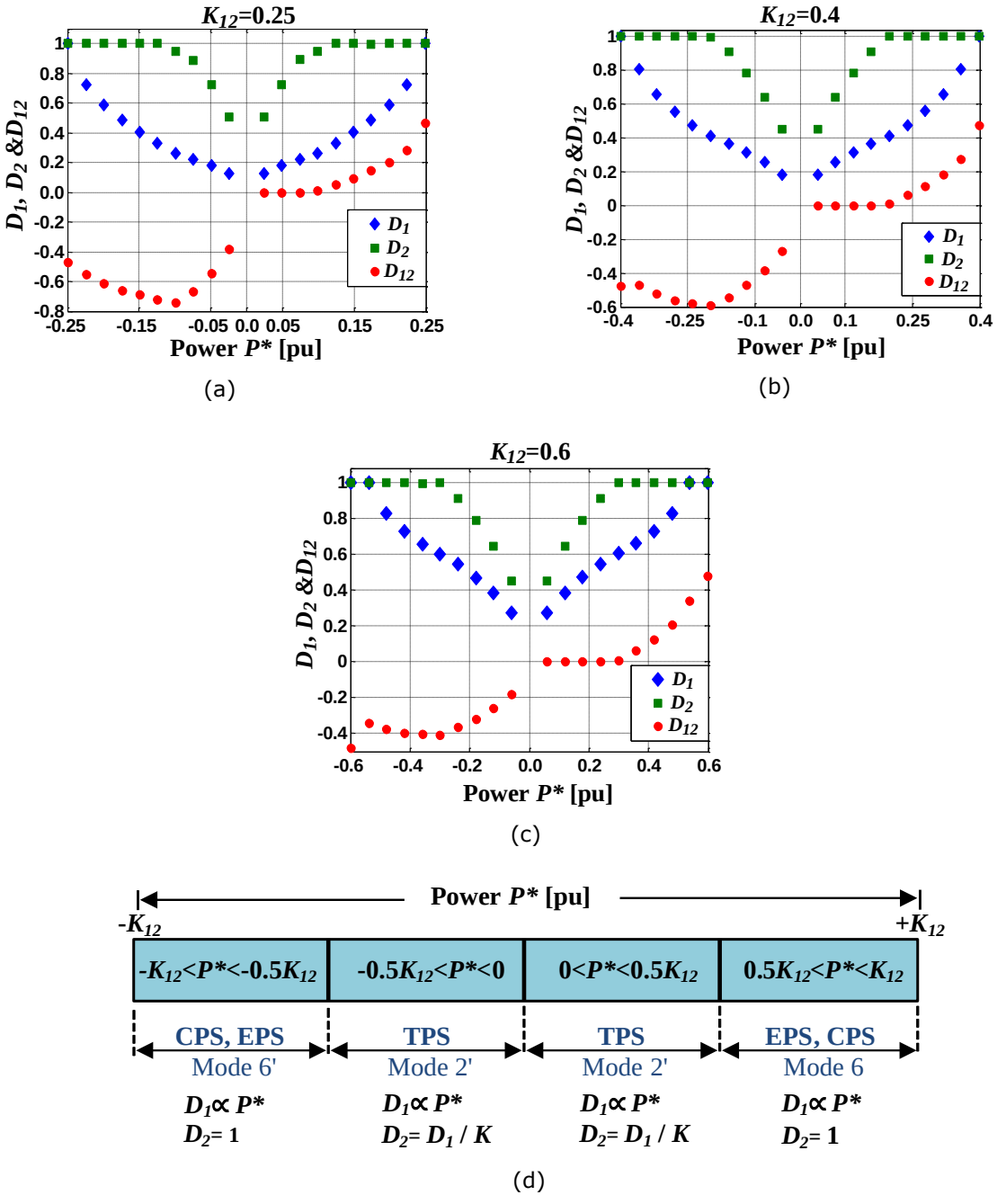

Fig. 5.2: Application of PSO to the DAB for buck/boost mode:
(a)-(c) Optimal phase shift ratios at K_{12}=0.25, 0.4 and 0.6 respectively
(d) General pattern of optimal duty ratios at buck/boost mode.

On the other hand, Fig. 5.3 shows that the conventional phase shift (CPS) [69] fulfils optimal solutions for unity gain operating mode at the entire loading range at both power flow directions. In this special case, the optimal solutions were attained by mode 6 or mode 6' with D_1=D_2=1.

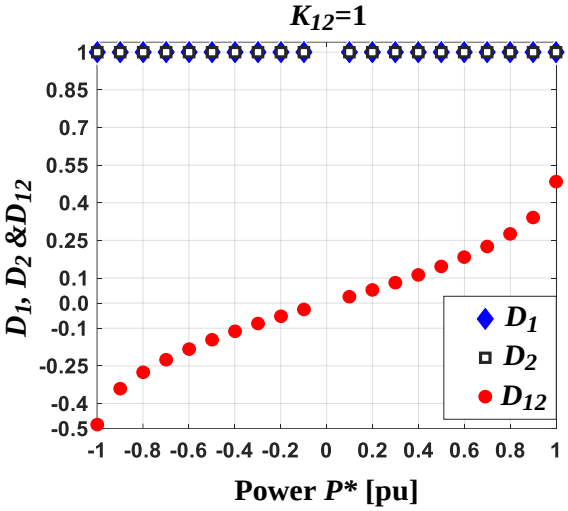

Fig. 5.3: Optimal phase shift ratios unity gain mode K_{12}=1.

5.2.1. Validation of optimal duty ratios

The relationship between duty ratios D_1 and D_2, D_2=D_1/K_{12}, to achieve minimum RMS current when P^* is between -0.5K_{12} to 0.5K_{12}, has been concluded from offline-produced optimal TPS ratios as shown in Fig.5.3 (d). This subsection provides a numerical validation of the correctness of this relationship using the optimal TPS modulation parameters shown in Fig.5.2 parts (b) and (c) as follows:

- ***K_{12}*=0.4.**

  At ***P*=-0.079,*** from Fig.5.2 (b):

  D_1=0.2563 and D_2=0.6416→ D_2=D_1/K_{12}=0.2563/0.4=0.64075.

  At ***P*= 0.119,*** from Fig.5.2 (b):

  D_1=0.3150 and D_2=0.7872 → D_2=D_1/K_{12}=0.3150/0.4=0.7875.

- ***K_{12}*=0.6.**

  At ***P*=-0.239,*** from Fig.5.2(c):

  D_1=0.5449 and D_2=0.9105 → $D_2=D_1/K_{12}$=0.5449/0.6=0.90816.

  At ***P*= 0.119,*** from Fig.5.2(c):

  D_1=0.3849 and D_2=0.6425 → $D_2=D_1/K_{12}$ =0.3849/0.6=0.6415.

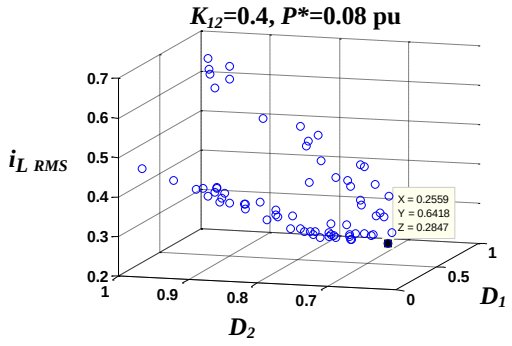

(a)
D_{1opt}=0.2559, D_{2opt}=0.6418, ($D_2 \approx D_1/K$)

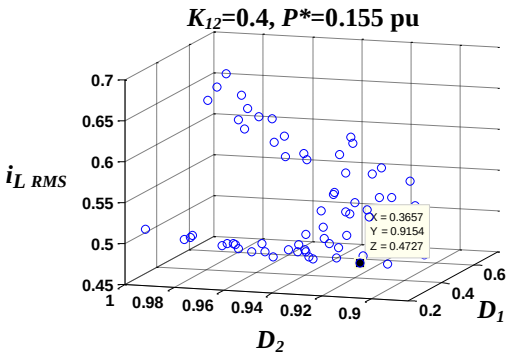

(b)
D_{1opt}=0.3657, D_{2opt}=0.9154, ($D_2 \approx D_1/K$)

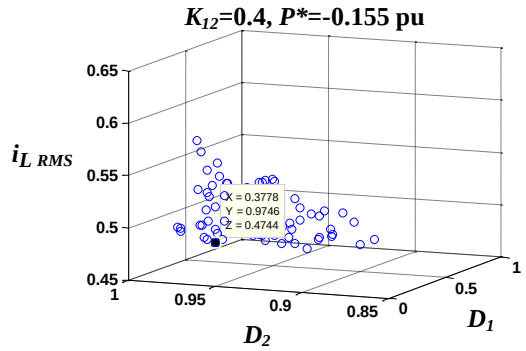

(c)
D_{1opt}=0.3778, D_{2opt}=0.9746, ($D_2 \approx D_1/K_{12}$)

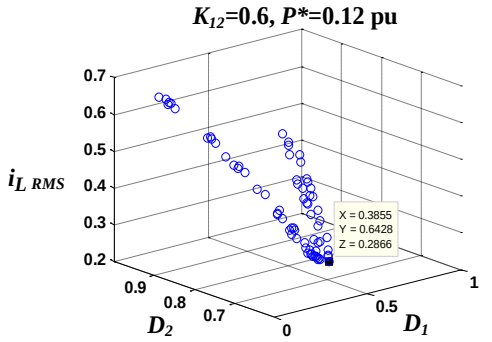

(d)
D_{1opt}=0.3855, D_{2opt}=0.6428, ($D_2 \approx D_1/K_{12}$)

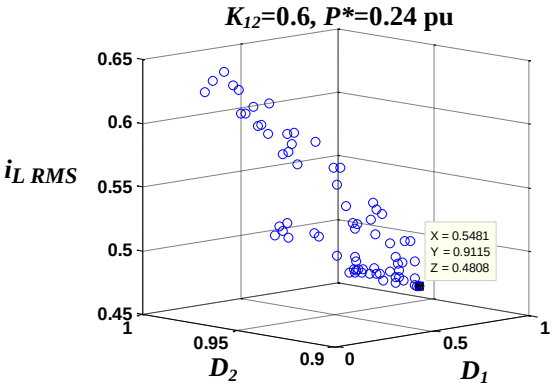

(e)
D_{1opt}=0.5481, D_{2opt}=0.9115, ($D_2 \approx D_1/K_{12}$)

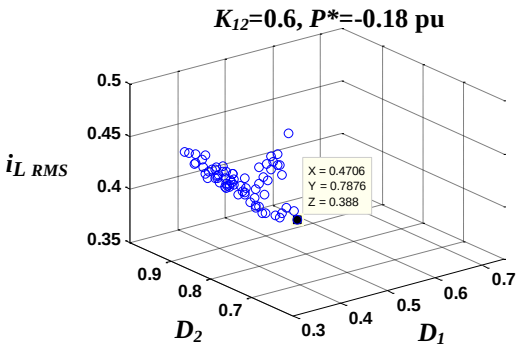

(f)
D_{1opt}=0.4706, D_{2opt}=0.7876, ($D_2 \approx D_1/K_{12}$)

Fig. 5.4: Duty ratios D_1 and D_2 at power levels from -0.5K_{12} to 0.5K_{12}: (a)-(c) K_{12}=0.4, (d)-(f) K_{12}=0.6

In fact, the RMS current will be minimal if the relationship between D_1 and D_2 for -0.5K_{12}<P^*<0.5K_{12} follows the derived relation of $D_2=D_1/K_{12}$. For further illustration, group of solutions for duty ratios D_1 and D_2 at various power levels (-0.5K_{12} to 0.5K_{12}) are presented in Fig 5.4. The optimal solution is highlighted, and Fig 5.4 verifies this matter by showing that $I_{L\,RMS}$ is minimum in the specified power range only when $D_2=D_1/K_{12}$.

5.2.2. Evaluation of modulation parameters symmetry

One of the properties of the DAB converter is the symmetry of its modulation parameters with the power flow when considering a lossless conversion. That is, changing the phase shift polarity should produce the same waveforms (i.e.: same power flow level with opposite direction.). This is, in fact, what can be observed in other optimisation results in the literature, such as [32]. This section will investigate the symmetry of phase shift D_{12} in the attained optimal results and will be divided into two parts –

(a) Unity Gain Mode (K_{12}=1)

In this case the optimal duty ratios are ($D_1=D_2=1$) as can be seen in Fig.5.3. Since the optimal operating switching mode in unity gain mode is mode 6 (in positive power) and mode 6' (in negative power) as discussed in section 5.2, then D_{12} can be expressed as function of the other variables i.e. $D_{12}=f(D_1, D_2, K_{12}, P^*)$, by rearranging power equation of mode 6 and 6' in Table.3.1 as follows –

$$D_{12}=\begin{cases}\dfrac{-(-1+D_2-D_1)-\sqrt{2D_1+2D_2-{D_1}^2-{D_2}^2-\frac{P^*}{K_{12}}-1}}{2}, for\ P^*>0 & (5.5.a)\\ \dfrac{-(1+D_2-D_1)+\sqrt{2D_1+2D_2-{D_1}^2-{D_2}^2+\frac{P^*}{K_{12}}-1}}{2}, for\ P^*<0 & (5.5.b)\end{cases}$$

Since the optimal duty ratios ($D_1=D_2=1$) in unity gain mode (K_{12}=1), then (5.5.a) and (5.5.b) reduces to

$$D_{12} = \begin{cases} \dfrac{1-\sqrt{1\ -P^*}}{2}\ , for\ P^* > 0 & (5.6.a) \\ -\dfrac{1-\sqrt{1+P^*}}{2}\ , for\ \ P^* < 0 & (5.6.b) \end{cases}$$

Mathematically, to prove symmetry around the origin of any equation, the function has to be an odd function, i.e.: f (-x) =-f (x). By applying the **x** variable to be **+*P**** in (5.6.a) and -*P** in (5.6.b), this yield

$$D_{12} = \begin{cases} \dfrac{1-\sqrt{1+(-P^*)}}{2}\ , & for\ P^* > 0 & (5.7.a) \\ -\dfrac{1-\sqrt{1+(P^*)}}{2}\ , & for\ \ P^* < 0 & (5.7.b) \end{cases}$$

By inspection of (5.7.a) and (5.7.b), it is apparent that equation (5.7.b) is identical to (5.7.a) but with negative sign, which proves the symmetry of D_{12} around the origin in the bi-directional power range for unity mode, as clearly depicted in Fig.5.3. In fact, this represents and explains the symmetry case in D_{12} already available in literature such as [32].

(b) Buck-boost Mode (K_{12}≠1)

For buck-boost DAB operating modes, where DC sides voltages are not equal V_{dc1}≠V_{dc2} (i.e.: DC voltage ratio is non-unity K_{12}=nV_{dc2}/V_{dc1}≠1.), the need to employ variable duty ratio arises to reduce the difference between bridge voltages hence achieve lower current stresses. Fig.5.3 shows that the same duty ratios D_1 and D_2 are used for any given identical power levels in the bi-directional range (i.e.: D_1 and D_2 are symmetric.). Accordingly, investigation of the relation of D_{12} with the power *P** will be provided in this section in two parts as follows−

- **For** $|P^*| \geq 0.5K$**,** then D_{12} can be examined for symmetry around the origin. For this power range, D_{12} is calculated from re-arranging mode 6 and mode 6' power equations in Table 3.1 since these are the optimal switching modes in this range. This is outlined by (5.5.a) for forward power flow, and for

reverse power flow in equation (5.5.b). To enable applying the odd function test, +P^* will be substituted in (5.5.a) and -P^* in (5.5.b). This yields:

$$D_{12} = \begin{cases} \dfrac{(1 - D_2 + D_1) - \sqrt{2D_1 + 2D_2 - {D_1}^2 - {D_2}^2 - \dfrac{(P^*)}{K_{12}} - 1}}{2}, for\ P^* \geq 0.5K_{12}. & (5.8.a) \\ -\dfrac{(1 + D_2 - D_1) - \sqrt{2D_1 + 2D_2 - {D_1}^2 - {D_2}^2 + \dfrac{(-P^*)}{K_{12}} - 1}}{2}, for\ P^* \leq -0.5K_{12}. & (5.8.b) \end{cases}$$

By inspection of (5.8.a) and (5.8.b), it is obvious that although the terms under the square root are identical, however, the preceding terms are different and (5.8.b) is not the negative complement of (5.8.a). This explains the reason behind the non-symmetry of D_{12} in this case as the odd function condition is not achieved.

- **For** $|P^*| \leq 0.5K_{12}$, the value of D_{12} is calculated from re-arranging mode 2' power equation in Table 3.1. Equation (5.9) gives the calculation of D_{12}, which shows one equation for both forward and reverse power flow since mode 2' is the same optimal switching mode for both power flow directions in this power range.

$$D_{12} = 0.5\left(D_1 - D_2 + \frac{P^*}{2K_{12}D_1}\right), \quad \text{for } -0.5K_{12} < P^* < 0.5K_{12} \qquad (5.9)$$

D_{12} can then be examined for symmetry around the origin by applying the odd function test to (5.9), this is by substituting +P^* and -P^* for positive and negative power flow respectively. This yields:

$$D_{12} = \begin{cases} 0.5\left(D_1 - D_2 + \dfrac{(P^*)}{2K_{12}D_1}\right). & (5.10.a) \\ 0.5\left(D_1 - D_2 + \dfrac{(-P^*)}{2K_{12}D_1}\right). & (5.10.b) \end{cases}$$

It is clear that (5.10.b) is not the negative complement of (5.10.a). This shows that D_{12} is not symmetric in this case, as it is not achieving the odd function

condition. This explains the non-symmetry of D_{12} around the origin in buck-boost mode ($K_{12}\neq1$) as shown in Fig.5.3.

5.3 Closed Loop Control Design

The extensive set of optimal TPS ratios, presented in previous section, presents a generic data pool. Analysing this data helped to derive simple relations, discussed in previous section, that are used to design the generalised closed loop control scheme. An overall schematic of DAB converter under the proposed control scheme is shown in Fig.5.5. The closed-loop variable (main control objective) is the sending end power (P_{se}) such that $P_{se}=P_{br1}$ for positive power flow while $P_{se}=P_{br2}$ for negative power flow, where P_{br1} and P_{br2} are the measured active power at the DC sides of bridges 1 and 2 respectively.

In buck/boost mode, D_1 can be regulated through a PI controller as the relation between power and D_1 is almost linear throughout which can be noticed in Fig. 5.2 parts (a) to (c). Whereas the relationship between the other control parameters (D_2 and D_{12}) and power is non-linear with dependency on the power level. In this context, relations concluded from Fig. 5.2 parts (a) to (c) are implemented as follows−

- **For** $|\boldsymbol{P}^*| \geq \boldsymbol{0.5K_{12}}$**,** the optimal value of D_2 is ($D_2=1$). The value of D_{12} is highly non-linear and therefore can only be calculated by re-arranging mode 6 and mode 6' power equations in Table 3.1. This is given by (5.11.a) for forward power flow and for reverse power flow this is shown in (5.11.b).
- **For** $|\boldsymbol{P}^*| < \boldsymbol{0.5K_{12}}$**,** the optimal value of D_2 is $D_2=D_1/K_{12}$. The value of D_{12} is highly non-linear and therefore can only be calculated by re-arranging mode

2’ power equation in Table 3.1. The calculation of D_{12} in this section is given by (5.11.c) for both forward and reverse power flow.

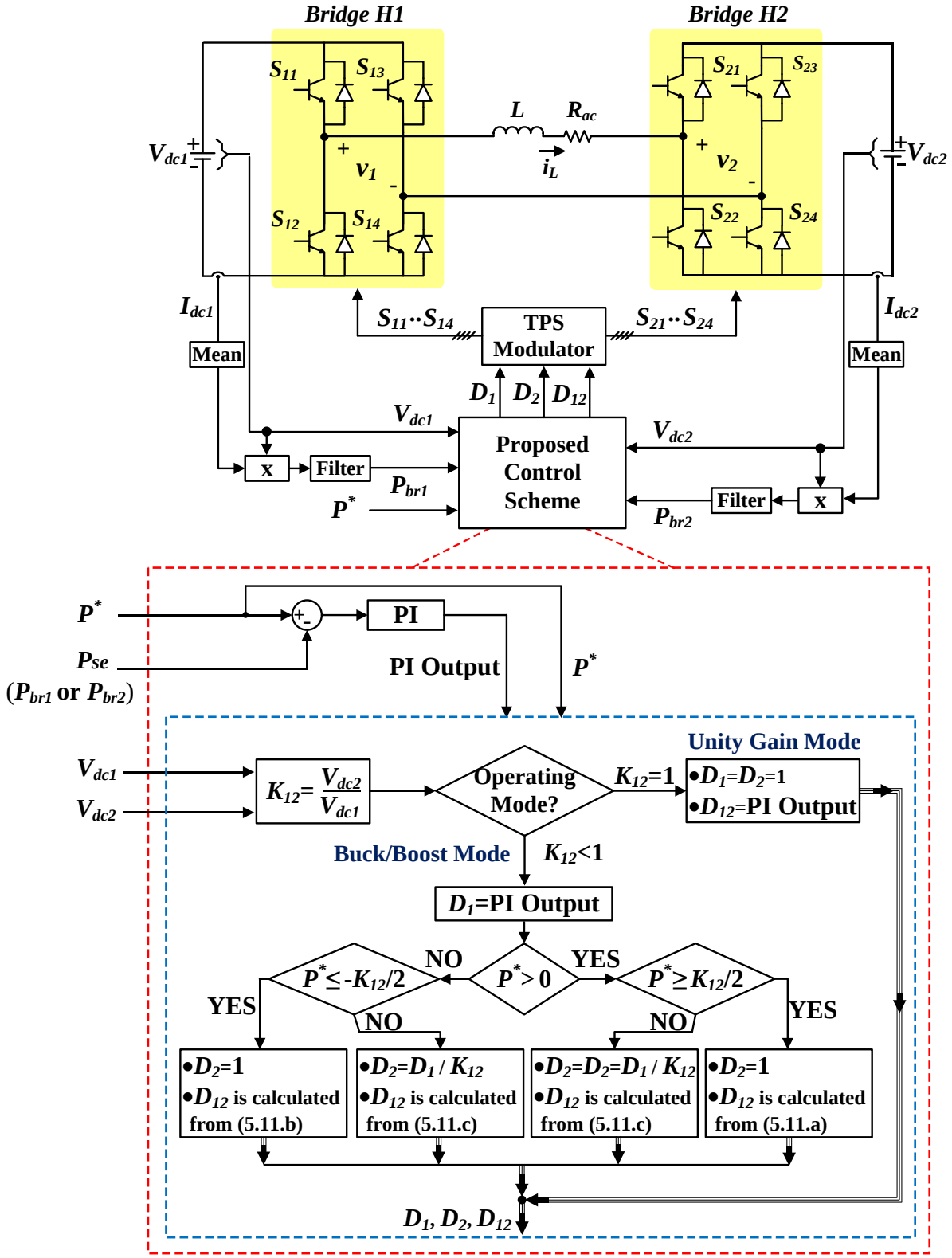

Fig. 5.5: Schematic of DAB converter under the proposed control scheme.

$$D_{12}=\begin{cases}\dfrac{-(-1+D_2-D_1)-\sqrt{2D_1+2D_2-{D_1}^2-{D_2}^2-\dfrac{P^*}{K_{12}}-1}}{2}, for\ P^*\geq 0.5K_{12} & (5.11.a)\\ \dfrac{-(1+D_2-D_1)+\sqrt{2D_1+2D_2-{D_1}^2-{D_2}^2+\dfrac{P^*}{K_{12}}-1}}{2}, for\ P^*\leq -0.5K_{12} & (5.11.b)\\ 0.5\left(D_1-D_2+\dfrac{P^*}{2K_{12}D_1}\right), \quad for\ -0.5K_{12}<P^*<0.5K_{12} & (5.11.c)\end{cases}$$

In unity gain mode, Fig. 5.3 shows that both DAB bridge AC-side voltages are full square waves (D_1=D_2=1) for the entire bidirectional power range and the only control needed to regulate power flow is on D_{12}. This can be implemented using a PI controller because the relation between the power level and value of the third phase shift D_{12} is almost linear as depicted in Fig. 5.3.

In the next sections, a Simulink/MATLAB simulation and an experimental prototype are used to validate precision of the proposed closed loop controller under various operating conditions. A transformer-less DAB is considered in simulation and experimental sections as shown in the schematic of DAB converter under the proposed control scheme in Fig 5.5. This is a permissible approach given that circuit operation will not change if a transformer is inserted as magnetising inductance is usually neglected and any equivalent leakage inductance plays the same role as interface inductor *L*. Furthermore, the transformer (especially with turns ratio 1:1) and its equivalent interface inductor have almost the same performance in steady state; especially that the scope of this chapter is power flow regulation with minimum current. In fact, in some low-power applications, absence of an interface transformer in the converter can significantly reduce converter weight and footprint. This approach may also contribute to the consistency between the RMS current minimisation, simulation, experimental verification and the DAB model presented in chapter three. The AC link of the transformer-less DAB circuit diagram, shown in Fig 5.5, includes an interface inductor *L* that works as

the energy storage element along with R_{ac} to represent the parasitic resistance of the AC link. The value for this resistance in simulation is R_{ac}=0.06pu (as obtained from the experimental test rig) normalised to $Z_{base}=8f_{sw}L$.

5.4 Simulation Results

To confirm the presented analysis, detailed simulations using SIMULINK/MATLAB platform software were performed. The simulations were carried out for the buck/boost/unity operating modes using the DAB parameters described in Table 5.1. The parasitic resistance of the AC interface inductance R_{ac} and ON-state switch resistance R_{ON} are introduced to produce realistic results from the Simulink DAB model and enable comparison with experimental prototype later in this chapter. R_{ac} enables representation of copper losses (I_2R_{ac}) in AC inductance (transformer equivalent) while R_{ON} enables representing the conduction losses in semiconductor power switches.

Table 5.1: Parameters of the experimental setup.

Parameter	value
Bridge 1 DC Voltage V_{dc1}	100V
Bridge 2 DC Voltage V_{dc2}	K_{12}*100V
Switching Frequency f_s	2.5kHz
Base Power P_{base}	500W
Interface inductor L	1mH
Parasitic Resistance R_{ac}	1.2Ω
Switch ON-state Resistance R_{ON}	0.04Ω

5.4.1. Effectiveness of the proposed control scheme

The effectiveness of the proposed control algorithm in tracking reference power level with minimum current stresses is verified in this section. This is achieved by applying bidirectional step changes of reference power level at various DC voltage ratios. The results are presented in Fig. 5.6 where the sending end power is measured and plotted against the reference power level. In addition, the associated measured inductor RMS current ($i_{L\,act}$) is shown along with the

minimum possible inductor RMS current ($i_{L\,min}$) calculated offline by the PSO. It can be noticed that the proposed power flow controller is capable of tracking the bidirectional reference power at different voltage conversion ratios. Moreover ($i_{L\,act}$) is maintained very close to ($i_{L\,min}$) which confirms minimum losses.

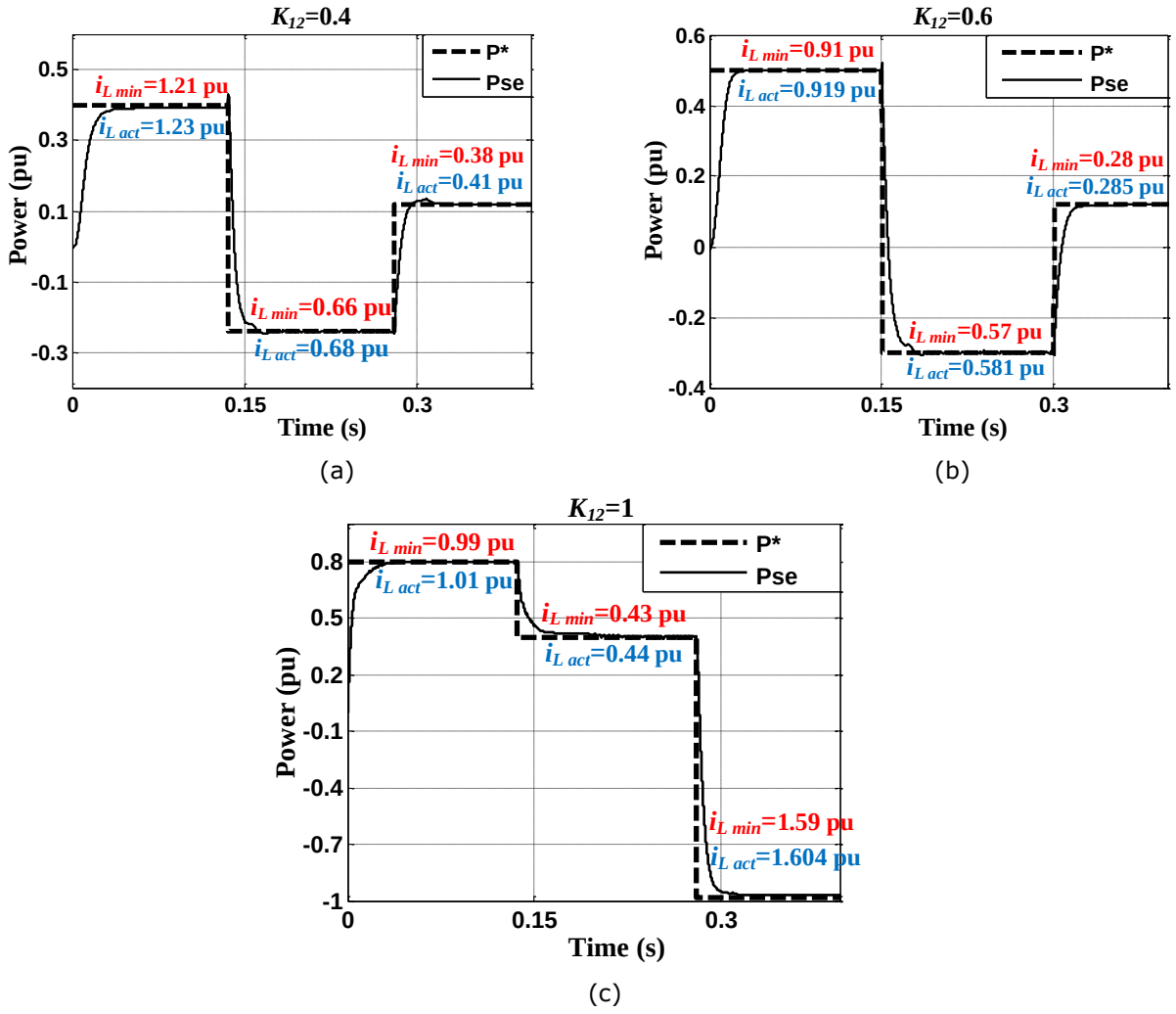

Fig. 5.6: Response of power transfer with inductor RMS current at different power levels for different DC voltage ratios: (a) K_{12}=0.4 (b) K_{12}=0.6 (c) K_{12}=1.

5.4.2. Comparison with other phase shift methods

A comprehensive comparison between the proposed phase shift technique and other phase shift techniques in literature is provided in this section. The phase shift techniques used to compare the proposed phase shift technique with are:

Conventional phase shift (CPS) [69], Dual phase shift (DPS) [77], Extended phase shift (EPS) [72], Extended dual phase shift (EDPS) [96], Triple phase shift [32] and Unified phase shift [83]. The entire per unit bi-directional power range (-K_{12} pu to K_{12} pu) is considered in all techniques. The RMS inductor current is compared for all mentioned techniques at different DC voltage ratios K_{12} as shown in Fig.5.7. The current is the main factor affecting the efficiency; hence, it is displayed first where the proposed phase shift technique is achieving the lowest current stresses.

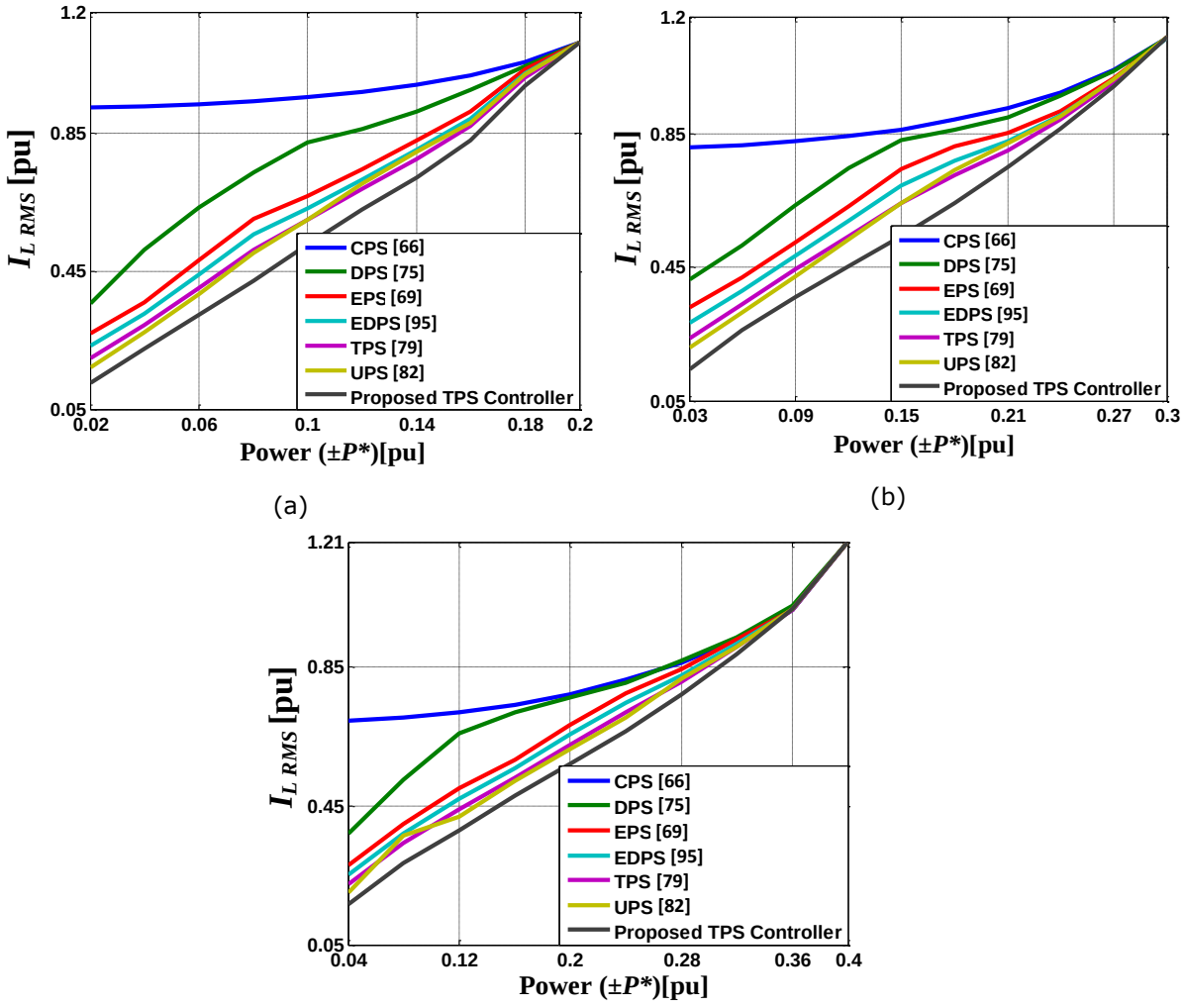

Fig. 5.7: Curves of current stress $i_{L\ RMS}$ with respect to P* and K in CPS [69], DPS [77], EPS [72], EDPS [96], TPS [32], UPS[83]and proposed TPS controller at: (a)K_{12}=0.2, (b)K_{12}=0.3, (c)K_{12}=0.4.

Moreover, the efficiency calculations outlined by (5.12), have been carried out in Simulink at the DC side terminals to include copper losses and conduction losses

of power switches such that R_{on}=0.04 ohm. The SIMULINK model is unable to model t_{on} and t_{off} of switches therefore switching losses is not included in this analysis. The DAB circuit diagram shown in Fig.5.5 illustrates the DC side readings (V_{dc1}, I_{dc1}, V_{dc2}, I_{dc2}) which are the variables used for efficiency calculation. The efficiency curves, presented in Fig.5.8, show that the proposed method achieves better performance than other existing phase shift schemes.

$$efficiency = \frac{P_{re}}{P_{se}} = \begin{cases} if\ P^* > 0\ then \begin{cases} P_{se} = V_{dc_1} I_{dc_1,avg} \\ P_{re} = V_{dc_2} I_{dc_2,avg} \end{cases} \\ if\ P^* < 0\ then \begin{cases} P_{se} = V_{dc_2} I_{dc_2,avg} \\ P_{re} = V_{dc_1} I_{dc_1,avg} \end{cases} \end{cases} \quad (5.12)$$

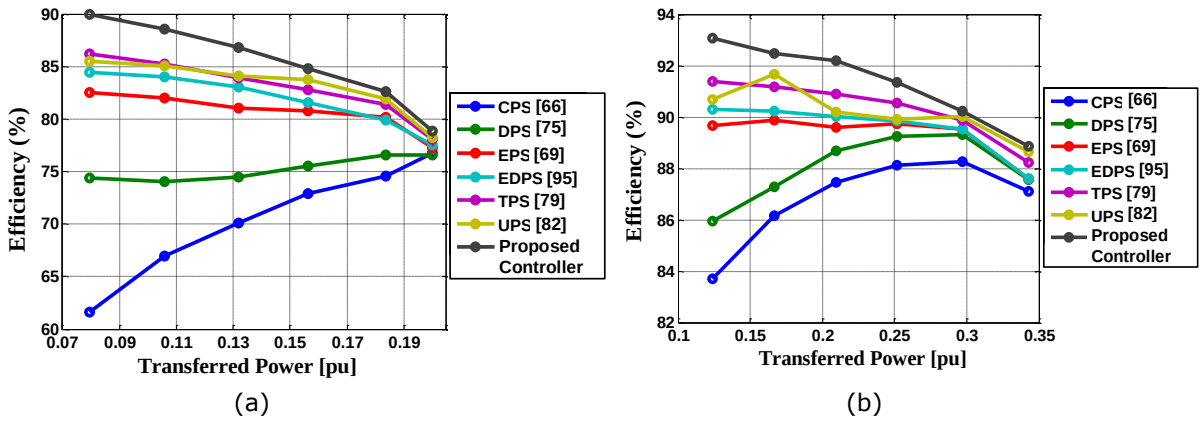

Fig. 5.8: Efficiency curves using existing phase shift techniques and the proposed TPS controller: (a) K_{12}=0.2, (b) K_{12}=0.4.

5.4.3. Robustness of the proposed control scheme

In order to test the robustness of the proposed controller and its sensitivity to circuit parameter changes, simulations have been implemented with values of inductor and its parasitic resistance (L and R_{ac} respectively) changing by ±10%. The proposed controller is applied on the DAB circuit for three cases:

- L=1mH, R_{ac}=1.2Ω, $P_{rated} = 500\,Watt$.
- L=1mH +10%, R_{ac}=1.2Ω+10%, $P_{rated} = 454.5\,Watt$
- L=1mH−10%, R_{ac}=1.2Ω−10%, $P_{rated} = 555.5\ Watt$.

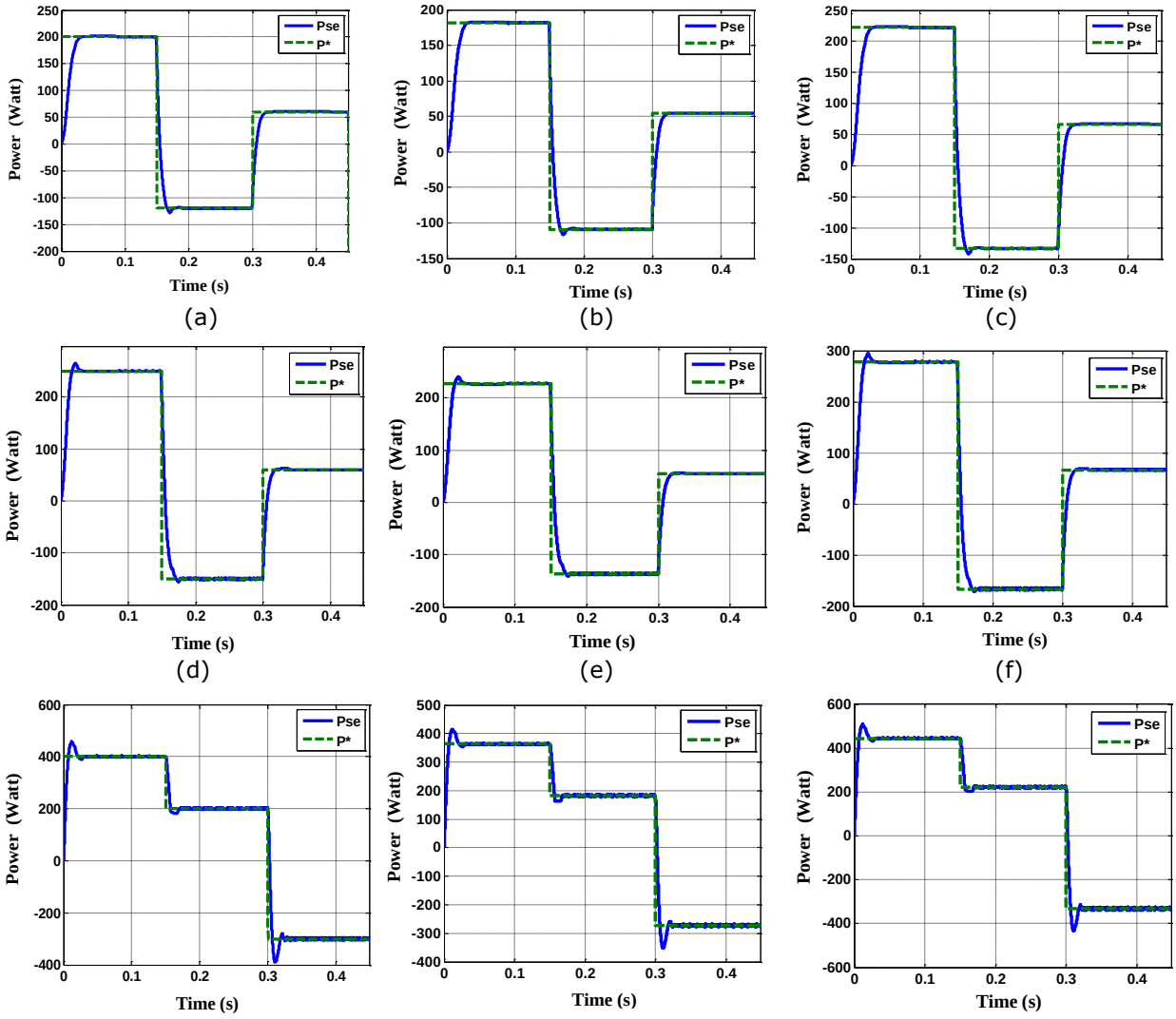

Fig. 5.9: Robustness of the proposed control algorithm to different system conditions:
(a)K_{12}=0.4,L=1mH,R_{ac}=1.2Ω, (d)K_{12}=0.6,L=1mH, R_{ac}=1.2Ω, (g)K_{12}=1.0,L=1mH, R_{ac}=1.2Ω,
(b)K_{12}=0.4,L=1mH+10%, (e)K_{12}=0.6,L=1mH+10%, (h)K_{12}=1.0,L=1mH+10%,
R_{ac}=1.2Ω+10%, R_{ac}=1.2Ω+10%, R_{ac}=1.2Ω+10%,
(c)K_{12}=0.4,L=1mH-10%, (f) K_{12}=0.6,L=1mH-10%, (i) K_{12}=1.0,L=1mH-10%,
R_{ac} =1.2Ω-10%, R_{ac} =1.2Ω-10%, R_{ac}=1.2Ω-10%.

Ll

ll The proposed controller response in terms of sending end power P_{se} plotted against desired power P^* for the three cases listed above are shown in Fig.5.9. The simulation is carried out at three different voltage conversion ratios K_{12} for each of the three cases of parameter variation described. The DAB response while parameters change show that the control algorithm is stable and robust and can be applied to any DAB converter regardless of rating and parameters. This is because the proposed analysis is all per unit and generically standardized.

5.5 Experimental Results

A low scaled experimental DAB setup is shown in Fig.5.10. This was developed according the schematic depicted in Fig. 5.6 in order to validate the proposed closed loop controller. The parameters used for designing the test rig are listed in Table 5.1. Two programmable power supplies are used to represent the behaviour of the two DC sides, and the two active H-bridges are connected through an air-core inductor as shown in Fig.5.10. Given the fact that the two implemented power supplies only deliver power (i.e. not absorb power), hence, in order to represent bidirectional power in the experimental DAB, a resistor bank is connected in shunt with the DC power supplies so in reverse power the resistor bank absorbs the power instead of the power supply itself. This means that in forward direction, the power supply will have to feed this resistor bank with power in addition to the main power transferred across the DAB, so the power supply will have to cater for this additional power. The semiconductor switches used are MOSFETs (MOSFET IRF250) while a CY8C5888LTI-LP097 PSoC 5LP microcontroller was used. The current feedback for the controller is achieved using two Hall-effect current transducers; one on each DC side of the converter. This experimental test rig is developed by an external collaborator Dr. Ibrahim Abdelsalam – from Arab Academy for science, technology and maritime transport (AASTMT) – in order to implement and test the proposed controller in this chapter.

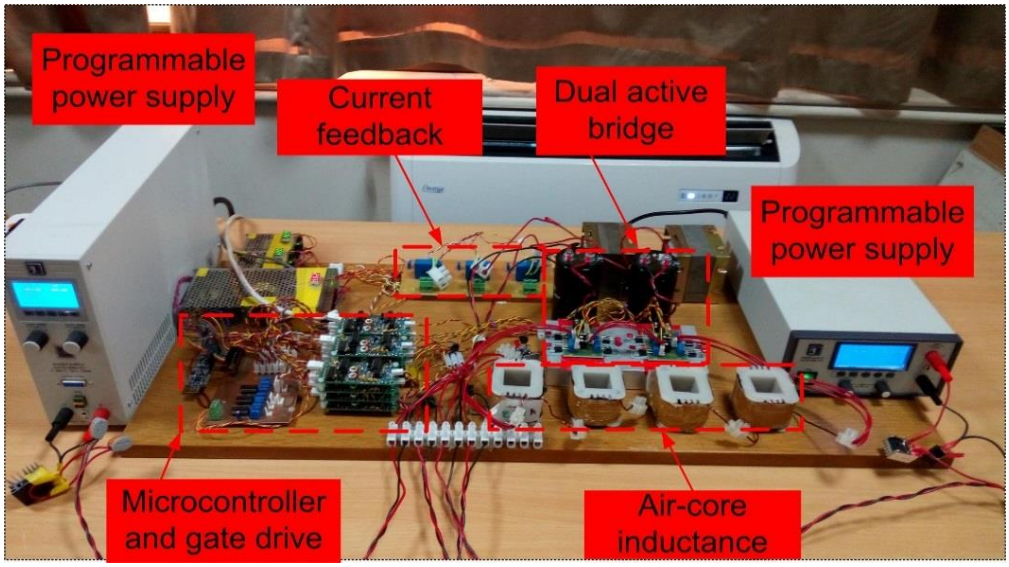

Fig. 5.10: Experimental test rig for DAB under proposed control scheme.

5.5.1. Steady state response

The proposed control scheme is verified in this section at selected steady state reference power levels for various DC voltage ratios K_{12}. Both bridge voltage (v_1, v_2) and instantaneous inductor current (i_L) are measured at the AC side presented in Fig. 5.11 where the inductor RMS current is measured and displayed on the right-hand side of the scope screenshot. Comparison between experimental setup and optimal offline results in terms of TPS ratios and the inductor RMS current is shown in Table 5.2. It is observed that the outputs of the proposed controller (D_1, D_2 and D_{12}) are closely matching the optimal TPS ratios provided in section 5.2.

Table 5.2: Comparison between experimental setup and optimal offline results.

K_{12}, P^*	TPS Modulation Parameters/Inductor current	
	From experimental setup	From PSO offline (optimal)
K_{12}=0.2, P^*=-0.08pu	D_1=0.263, D_2=1, D_{12}=-0.74	D_1=0.246, D_2=1, D_{12}=-0.78
	I_{LRMS} =2.3 A = **0.46 pu**	Min I_{LRMS} =**0.44 pu**
K_{12}=0.4, P^*= 0.15pu	D_1=0.36, D_2=0.9, D_{12}=0.0	D_1=0.35, D_2=0.89, D_{12}=0.0
	I_{LRMS} =2.07 A = **0.414 pu**	Min I_{LRMS} =**0.412 pu**
K_{12}=0.6, P^*=-0.24pu	D_1=0.57, D_2=0.95, D_{12}=-0.32	D_1=0.54, D_2=0.91, D_{12}=-0.36
	I_{LRMS} =2.39 A = **0.478 pu**	Min I_{LRMS} =**0.471 pu**
K_{12}=1, P^*=0.5pu	D_1=1, D_2=1, D_{12}=0.148	D_1=1, D_2=1, D_{12}=0.146
	I_{LRMS} =2.79 A = **0.558 pu**	Min I_{LRMS} =**0.555 pu**

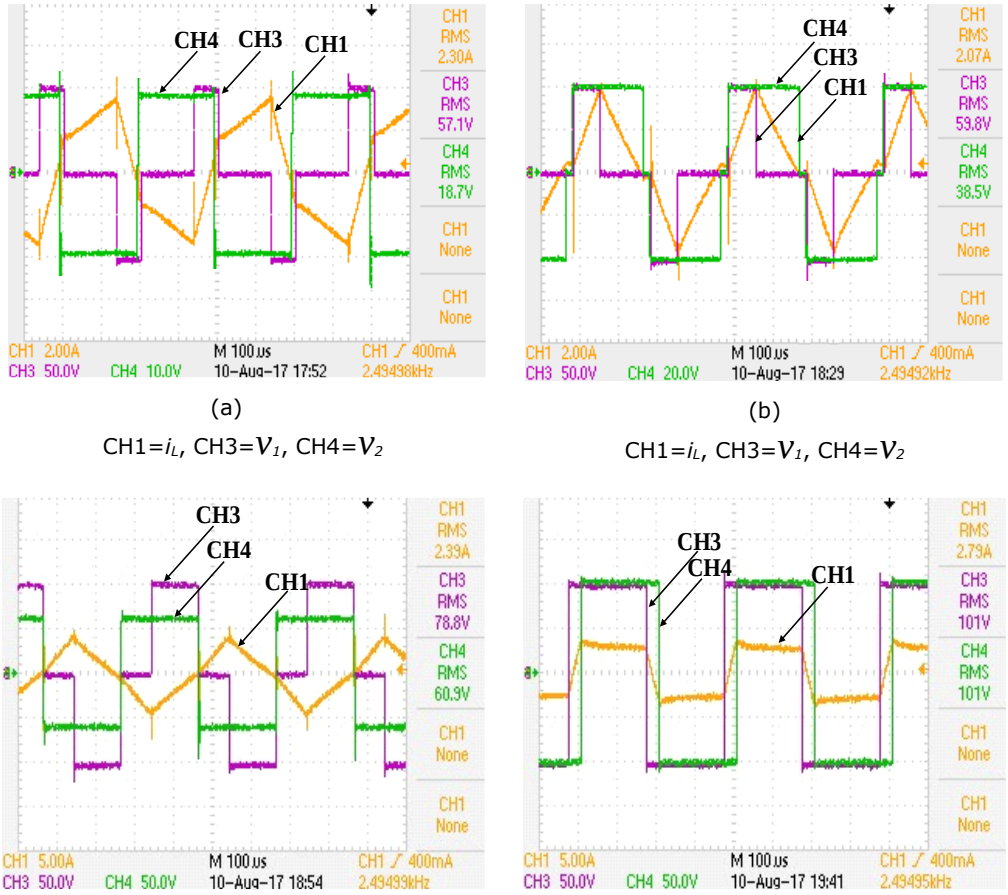

(a)

CH1=i_L, CH3=V_1, CH4=V_2

(b)

CH1=i_L, CH3=V_1, CH4=V_2

(c)

CH1=i_L, CH3=V_1, CH4=V_2

(d)

CH1=i_L, CH3=V_1, CH4=V_2

Fig. 5.11: Voltage of both bridges and inductor current (v_1,v_2,i_L) readings at the AC link from the experimetal setup: (a) K_{12}=0.2, P^*=-0.08 pu, (b) K_{12}=0.4, P^*= 0.15 pu. (c) K_{12}=0.6, P^*=-0.24 pu, (d) K_{12}=1, P^*=0.5 pu.

5.5.2. Comparison with other phase shift methods

The proposed technique and other existing phase shift methods are applied to the experimental DAB at different conditions (DC voltage ratio K_{12}) and at different power levels. The AC link readings (v_1,v_2 ,i_L and $i_{L\,RMS}$) at these different conditions are presented in Fig.5.12, where the inductor RMS current stresses using the proposed technique is lower than current stresses resulting from other existing techniques proving the significance of proposed technique.

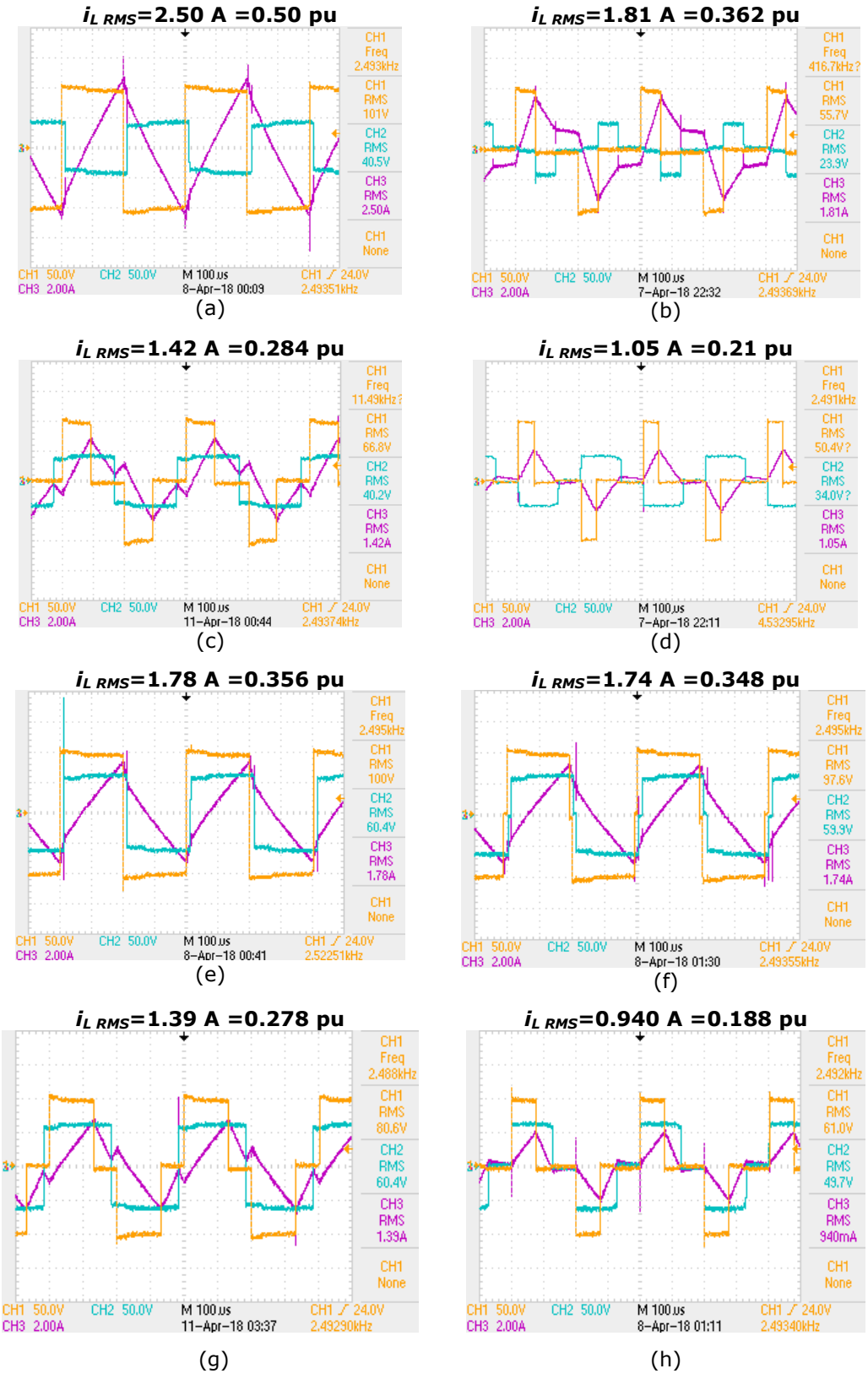

Fig. 5.12: Experimental comparison between the proposed technique and other existing phase shift methods (CH1=v_1, CH2=v_2, CH3=i_L):
(a)-(d) K_{12}=0.4, P*=0.08 pu, in CPS, DPS, EPS and Proposed technique respectively,
(e)-(h) K_{12}=0.6, P*=0.12 pu, in CPS, DPS, EPS and Proposed technique respectively.

5.5.3. Experimental and simulation comparative analysis

For further verification, efficiency calculations from the simulation and experimental prototype using the proposed technique are compared as depicted in Fig. 5.13. The efficiency calculation, outlined by (5.15), is carried out using the DAB parameters illustrated in Table 5.1. The small error between the simulation results and the experimental prototype is mainly because the physical implementation of the proposed controller incorporates real time measurements that are prone to noise and measurement errors, notwithstanding the non-ideal effects such as component parasitics and converter losses.

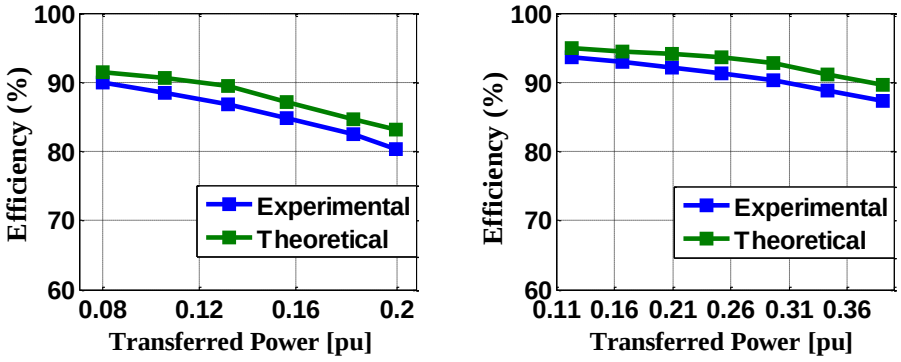

Fig. 5.13: Efficiency calculated in experimental and simulation using the proposed technique: (a) at K_{12}=0.2, (b) at K_{12}=0.4

In addition, analysis of the error between the results from the off-line PSO optimisation and the proposed controller in experiment is shown in Table 5.3: this shows the percentage relative difference in RMS inductor current between the experimental DAB and the off-line PSO optimisation. The error between the PSO optimisation and the experimental results is mainly because the PSO optimisation results are based on equations that represent an ideal lossless converter DAB model: however, the experimental implementation of the proposed controller deals with a non-ideal converter with component parasitics, converter losses and real time measurements affected by noise and measurement errors.

Table 5.3: Relative difference between experimental results and minimum offline results

K_{12}, P^*	Inductor current		Relative difference to minimum current
	From experimental setup	PSO optimal offline	
K_{12}=0.2, P^*=-0.08pu	I_{LRMS} =2.30 A= **0.460 pu**	Min I_{LRMS} =**0.440 pu**	4.3%
K_{12}=0.4, P^*= 0.15pu	I_{LRMS} =2.07 A= **0.414 pu**	Min I_{LRMS} =**0.412 pu**	0.5%
K_{12}=0.6, P^*=-0.24pu	I_{LRMS} =2.39 A= **0.478 pu**	Min I_{LRMS} =**0.471 pu**	1.5%
K_{12}=1, P^*=0.5pu	I_{LRMS} =2.79 A= **0.558 pu**	Min I_{LRMS} =**0.555 pu**	0.5%

5.6 Implementation of the Controller for Passive Load Voltage Control

This section provides further verification of the universality of the proposed control scheme. This is achieved by showing that the proposed power flow control scheme can be adapted for load voltage control not output power. The main scope of the work in this chapter has primarily been the derivation and implementation of minimised-RMS-current power flow controller for the DAB converter. This included applications utilising two fixed DC sources such as two batteries or two DC busses in a DC grid or DC microgrid and a battery as shown in Fig.5.14. In such applications, the regulation of output power (power flow) is the target of the controller. On the other hand, the second DAB circuit, shown in Fig. 5.15, assumes a DC source and a passive load where load voltage control becomes the target of the controller. However, the first DAB circuit is more generic as it treats both sides as sources/sinks of power enabling bi-directional power flow, whereas the second case is more specific (unidirectional power flow). In the second case, controlling the power would be physically controlling $\boldsymbol{V_{Load}}^2$ due to $P=V^2/R$. This means that the proposed controller in Fig. 5.5 will be exactly the same, but $\boldsymbol{V_{Load}}^2$ will simply replace $\boldsymbol{P^*}$ in the control flowchart and $\boldsymbol{V_{Load}}^2\boldsymbol{R}_{Load}$ will substitute $\boldsymbol{P^*}$ in (5.11.a) and (5.11.c) such that the control flowchart becomes as shown in Fig. 5.16.

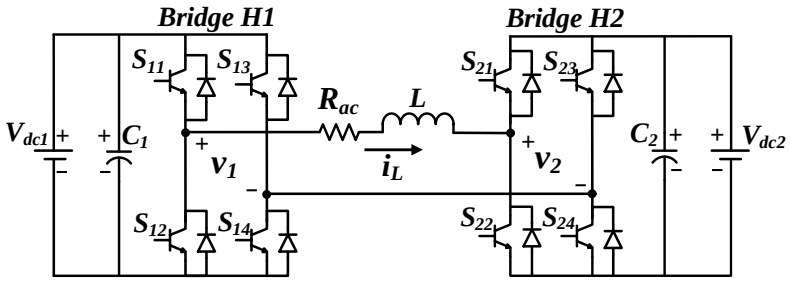

Fig. 5.14: Typical DAB circuit diagram for power distribution.

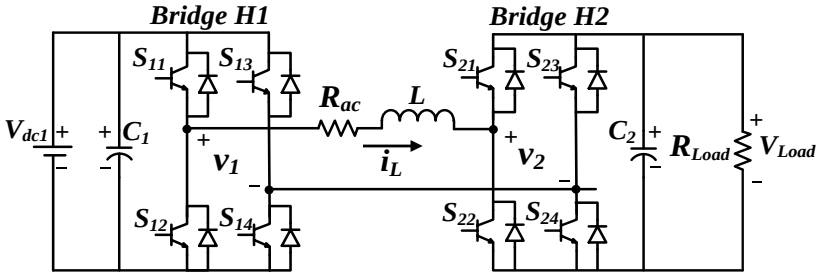

Fig. 5.15: Typical DAB circuit diagram for load voltage control.

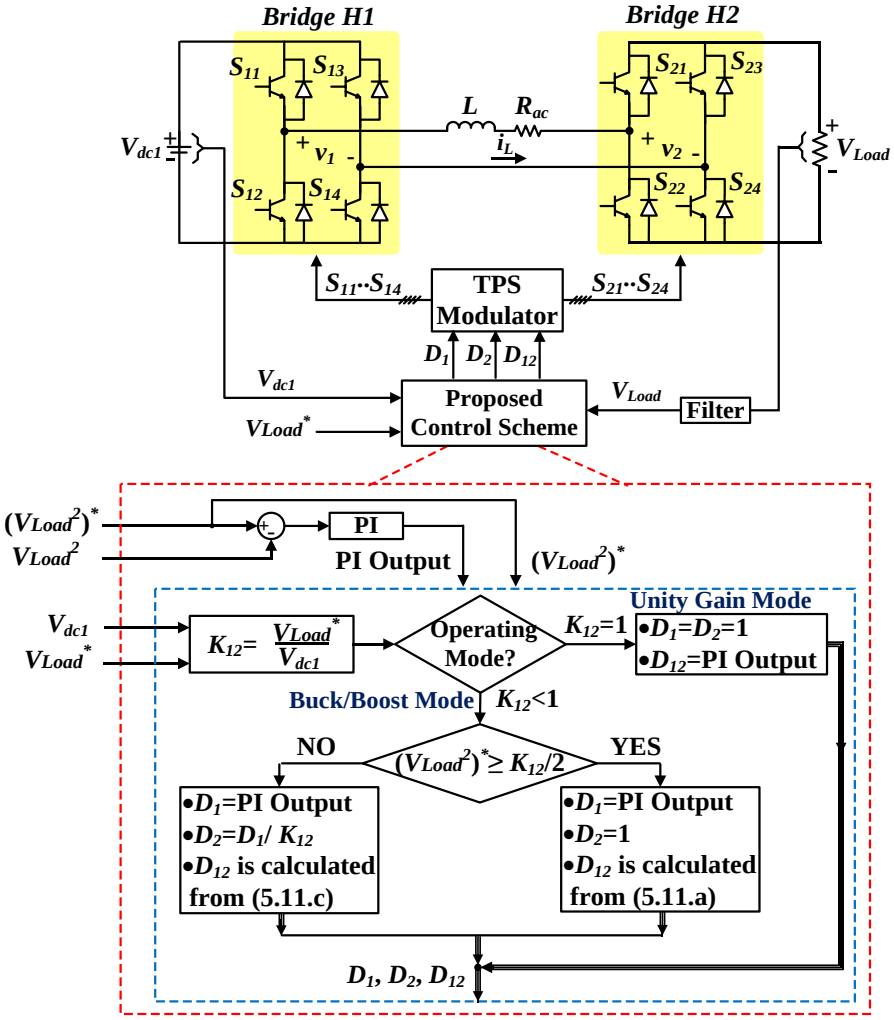

Fig. 5.16: Control flowchart of DAB for output voltage control.

Simulation using SIMULINK/MATLAB platform software is performed to confirm the capability of the proposed control scheme (in Fig. 5.16) to control load voltage. The attained simulation results — depicted in Fig. 5.17 — were carried out for the buck operating mode at two different cases using the following DAB parameters: f_s=2500 Hz, L=1 mH.

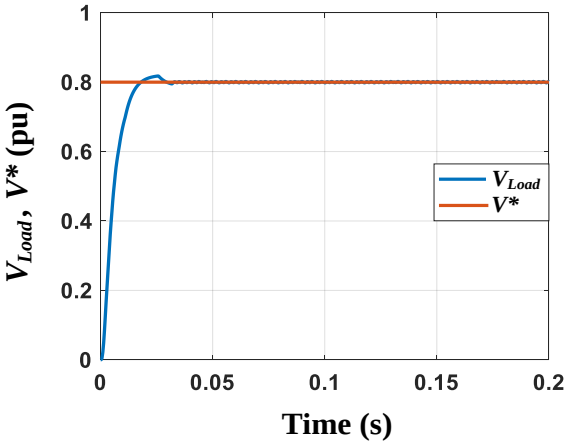

(a)

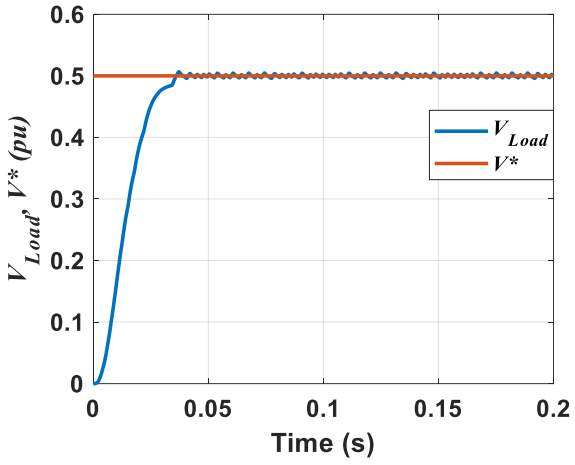

(b)

Fig.5.17: Performance of proposed controller in load voltage control at (a) R_{Load}=50 Ω, V_{dc1}=100 volt, V*=80 volt, (b) R_{Load}=15 Ω, V_{dc1}=100 volt, V*=50 volt.

5.7 Discussion

This section presents the main contributions within this chapter in addition to the limitations of the proposed controller. The novelty and contributions of this chapter are summarised in the following bullet points:

- A new utilisation of PSO in DAB studies where PSO was used to generate optimal TPS ratios based on converter per-unit derived equations.
- The results of the offline PSO are non-specific to converter rating, which makes the results generic to any DAB.
- The PSO output results are used to derive useful data trends, which led to the design of a simple closed loop PI controller that can be implemented directly without the need for user to implement PSO algorithm.
- A new minimum-RMS-current power flow controller is proposed for DAB. The proposed controller is the main contribution in this chapter due to its novelty, simplicity and universality in covering bi-directional power flow control regardless of DC voltage ratio with minimised current stress. The proposed control scheme is simple to implement and does not require any offline calculation or look-up tables.

However, using the same approach (i.e.: application of an artificial-intelligence-based technique and then analysing the optimal results.) to design a controller for multi active bridge (MAB) is very cumbersome. This is because designing a controller for minimum RMS current in MAB with high number of ports (and hence very large number of DC voltage ratios to consider) will require a huge amount of data points to be generated and further analysed. This tedious process will have to be repeated for every number of ports case by case, thus requiring a different control design depending on the number of ports. For example if genetic algorithm (GA) is used for a MAB converter with N ports with port 1 being the reference port, there will be (2N-1) control parameters (the D's: D_1 to D_N and D_{12} to D_{1N}) plus (N-1) voltage gains (i.e.: K_{12},K_{13}… K_{1n}). Consequently, the amount of permutations of (N-1) voltage gains would be massive and for each permutation, data for (2N-1) control parameters will need to be analysed, so generalization would be

computationally highly complex to achieve. Therefore, development of a new optimised power-flow control scheme that does not involve AI-based optimisation technique (PSO, GA, ...etc.) nor data point generation/analysis is discussed in the next chapter.

5.8 Summary

In this chapter, on the basis of the per unit DAB model presented in chapter 3, PSO technique was used offline at first to generate the optimal TPS ratios for the converter at the entire power level and different values of DC voltage ratios. The optimal TPS ratios obtained from this offline optimisation exercise were analysed and useful patterns (data trend) were identified. This data trend was then utilised to design a simple closed loop controller for real time power regulation in DAB converter. The control algorithm was developed with the objective of achieving the required power transfer level while minimising AC link's RMS current. Besides, the proposed control scheme can be implemented without carrying out any of the offline PSO work, as the optimised relations/functions obtained from it are final and ready for implementation. Robustness of the proposed control scheme was evaluated and presented. This was done by changing the system parameters to prove proposed controller low sensitivity to converter parameter changes. Comprehensive validation in simulation and experimental together with comparison with other existing techniques were included to verify the effectiveness of the proposed generic controller.

Chapter 6. Current-Stress Minimisation Based on Online Perturb and Observe Method

This chapter proposes a new generic current stress optimised power flow controller for multi active bridge (MAB) DC-DC converters. The main motivation of the work in this chapter is overcoming the problem with the minimised-RMS-current control scheme in chapter five, which cannot be extended to multi active bridge converters. This is due to the fact that using the same control design procedure (originally developed for the two-port active bridge DAB) for MAB is not feasible as it gets mathematically complicated. This is because using the same control design approach (i.e.: utilise PSO, produce optimal modulation parameters, analyse trend and get optimal relations.) will need a switching model which is very challenging to develop given the high number of switching states in MAB converters. Besides, in order analyse the optimal results and to discover trends, this will require huge amount of data points (i.e.: entire power range at all ports for different values of DC voltage ratios.).

The main requirement of the control scheme is to be generalised to MAB regardless of number of ports, power level and values of DC voltage ratios. The proposed controller in this chapter introduces an innovative implementation of PI-based adaptive-step perturb and observe (P&O) that enable real-time minimum current point tracking (MCPT) while maintaining the required power transfer level. The proposed control scheme introduces a new adaptation of P&O methods, such as those used for maximum power point tracking (MPPT) algorithms in PV modules. This is mainly inspired by:

- The analogy of nonlinear characteristics in both PVs and active bridge DC−DC converters, which will be covered in detail later in this chapter.

- Implementations of P&O algorithms do not require prior knowledge of the converter characteristics. This can simplify designing a universal P&O-based controller for MAB that for any power transfer levels, voltage conversion ratios, or number of ports.
- Designing a P&O-based scheme does not necessarily need an exact switching model for the converter.
- Perturb calculation using adaptive-step P&O methods are simple in terms of implementation as can be based on conventional PI controllers, generic and do not depend on converter characteristics/operating point, plus these methods can produce negligible (close to zero) oscillation in steady state.

The first part of this chapter describes in detail the rationale for the proposed minimum current point tracking (MCPT) technique by developing a new characteristic 3-D plane curve for MAB converters. This enables the next step, which is the development of adaptive-step perturb and observe method for application on MAB converter. After setting up the theoretical background, the entire closed-loop structure is presented including the MCPT method and the phase shift decoupler (covered in chapter four) to handle power flow control for *n*-port MAB. Afterwards, extensive simulation is carried out using detailed MAB switching model in MATLAB/Simulink to validate effectiveness of the proposed MCPT closed loop controller. In addition, the results are benchmarked against offline PSO optimal results for additional verification of the effectiveness of the proposed controller.

6.1 Current-Voltage Characteristics of MAB

In this section the AC current characteristics are defined for MAB with respect to the bridge voltages. The main objective is to develop a general characteristic curve of the converter that covers all operating range of the converter and represents the main specifications of the converter not the control parameters. On this basis, the independent variables in the proposed I−V MAB characteristic are the RMS bridge voltages $V_{i_{RMS}}$ and $V_{j_{RMS}}$ given by (6.1) in per unit form to provide standardised analysis (normalised to an arbitrary base voltage–reference port voltage-V_r). The AC current characteristics will be representing an AC link branch connecting any two bridges *i* and *j*.

$$V_{i_{RMS(pu)}} = \frac{4K_{ri}}{\pi\sqrt{2}} sin\left(\frac{D_i\pi}{2}\right), V_{j_{RMS(pu)}} = \frac{4K_{rj}}{\pi\sqrt{2}} sin\left(\frac{D_j\pi}{2}\right) \tag{6.1}$$

Where $0 \le V_{i_{RMS(pu)}} \le \frac{4K_{ri}}{\pi\sqrt{2}}, 0 \le V_{j_{RMS(pu)}} \le \frac{4K_{rj}}{\pi\sqrt{2}}, 0 \le D_i \le 1 \text{ and } 0 \le D_j \le 1.$

The AC link's RMS current $I_{ij_{RMS}}$ (as the dependent variable) can be derived as a function of the independent variables ($V_{i_{RMS}}$, $V_{j_{RMS}}$) for every desired level of active power transfer P_{ij}* as outlined by (6.2). To plot (6.2), a 3-D representation is used as shown in Fig. 6.1. Here $V_{i_{RMS}}$ and $V_{j_{RMS}}$ are plotted along the horizontal axes, and $I_{ij_{RMS}}$ is plotted along the vertical axis while every power level is represented in a separate plane. The entire bi-directional range is covered such that P_{ij}*=|0.1 $K_{ri}K_{rj}$| to | $K_{ri}K_{rj}$ | pu.

$$I_{ij_{RMS}}{}^2 = \frac{4^2}{\pi^2}\left(V_{i_{RMS}}{}^2 + V_{j_{RMS}}{}^2 - 2V_{i_{RMS}}V_{j_{RMS}}\cos(\delta_{ij})\right). \tag{6.2}$$

Where $\cos(\delta_{ij}) = \left(1 - \left(\frac{P_{ij}{}^*}{\frac{4}{\pi}V_{i_{RMS}}V_{j_{RMS}}}\right)^2\right)^{0.5}$.

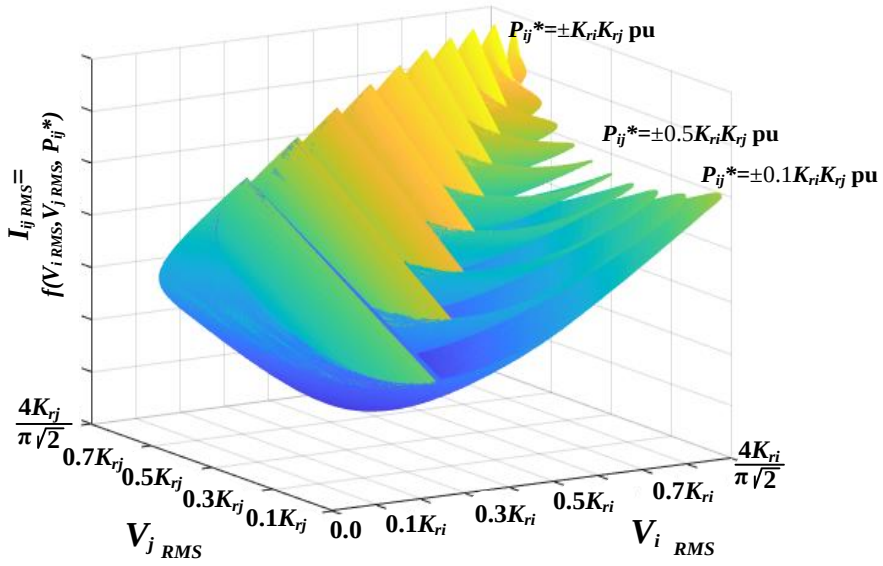

Fig. 6.1: Universal MAB I−V Characteristic Plane.

The I−V MAB characteristic plane generically applies to any AC link branch in MAB and shows that there is only one specific combination of bridge voltages (at each level of power) that gives the global minimum current. From (6.2), $V_{i_{RMS}}$ and $V_{j_{RMS}}$ are solely dependent on D_i and D_j respectively, therefore the minimum current point in AC link branch between bridges *i* and *j* can be achieved by a unique combination of D_i and D_j at a specific power. The remaining degrees of freedom are the phase shift angles, which will be regulated to realise power flow control. Consequently, the main challenge is how to obtain a unique global optimum combination of duty ratios (D_1,..D_n) which, in turn, regulate the RMS bridge voltages in order to track minimum current point in all AC link branches.

6.2 P&O-Based Minimum Current Point Tracking

The search for minimum RMS current point in the universal I-V characteristic follows what could be called as a 'hill-descent' fashion with the starting point of this hill being at maximum RMS bridge voltages. This is similar to the search for maximum power point (MPP) in PV where hill-climbing MPPT techniques such as

P&O algorithms are widely implemented to improve the utilization efficiency by tracking MPP for a given set of operating conditions [126]. P&O algorithms are simple in terms of implementation and do not require prior knowledge of the PV characteristics or the measurement of solar intensity and cell temperature. In PV systems, the P&O algorithm incorporate a control parameter that is increased or decreased by a small amount (often defined as step size), hence perturbing the operating point of the PV, along with measurement of the PV array output power before and after the perturbation [127]. The system continues to perturb in the same direction if the power increases which means that the operating point is moving toward the MPP; otherwise, the system is perturbed in the opposite direction. Similarly, this thesis proposes 'hill-descent' P&O-based MCPT that is investigated in this section on the following basis:

- Perturbing a specific control parameter, increasing or decreasing by a certain amount (step size).
- Measuring the AC link's RMS current and active power (delivered or absorbed) at each bridge before and after the perturbation.
- The algorithm should then either: continue to perturb the system in the same direction or perturb in the reverse direction until minimum current point (MCP) is reached.

6.2.1. Perturbation parameter

Development of the hill-descent P&O MCPT technique requires primarily identification of the main perturbation parameter. For the P&O is to track minimum RMS current in an AC link branch between ports i and j, then the perturbation parameter must be restricted to D_i or D_j, as the analysis in section 6.1 has revealed. Selecting D_i as the P&O perturbation parameter, a mathematical

relationship can be derived for its corresponding value of D_j that would ensure minimum current in this AC link branch. First, RMS bridge voltages of the quasi-square waves in Fig.6.1 are first derived as given by (6.3).

$$V_{i_{RMS(pu)}} = K_{ri}\sqrt{D_i},\ V_{j_{RMS(pu)}} = K_{rj}\sqrt{D_j} \tag{6.3}$$

Then, by equating the two voltages in (6.4) gives the direct relationship between the duty ratios.

$$D_j = \left(\frac{K_{ri}}{K_{rj}}\right)^2 D_i \tag{6.4}$$

Generalising for all AC link branches, this necessitates control of a single bridge RMS voltage only, while all other active bridges would have to maintain and follow the relation in (6.4). For this sake, bridge *r* is chosen as the reference, and accordingly D_r will be the main perturbation parameter. In this case, (6.4) is rewritten as:

$$D_i = \begin{cases} \dfrac{D_r}{{K_{ri}}^2} \\ 1, \quad if \ \dfrac{D_r}{{K_{ri}}^2} > 1. \end{cases} \tag{6.5}$$

Therefore, perturbing D_r while maintaining the relation in (6.5) to calculate remaining duty ratios will lead to the MCP. Investigation of D_r as a perturbation parameter is provided here to verify the effectiveness of perturbing D_r on RMS current. To achieve this, fixed-step perturbation is applied according to the following steps:

1) D_r=1 (maximum RMS voltage of reference bridge corresponding to top of hill in Fig.6.1).
2) Calculate remaining duty ratios using (6.5).
3) For given power levels (P_1*…P_n*) and DC voltage ratios (K_{ri}…K_{rn}), use power equations to calculate phase shifts (D_{ri}…D_{rn}).

4) Calculate resultant AC link RMS current.
5) Calculate new value of D_r (D_r=$D_{r\,old}$−ΔD_r), where ΔD_r is a fixed-step perturb.
6) Repeat steps (2)-(5) and stop when MCP is approached.

The above perturbation steps are applied on an approximate TAB model assuming fundamental component, derived in chapter 4, given by (6.6) and (6.7) considering bridge 1 as reference bridge such that D_{12}, D_{13} are phase shift angles of bridges 2 and 3 with respect to bridge 1. A flowchart of the adopted fixed-step perturbation is illustrated in Fig.6.2

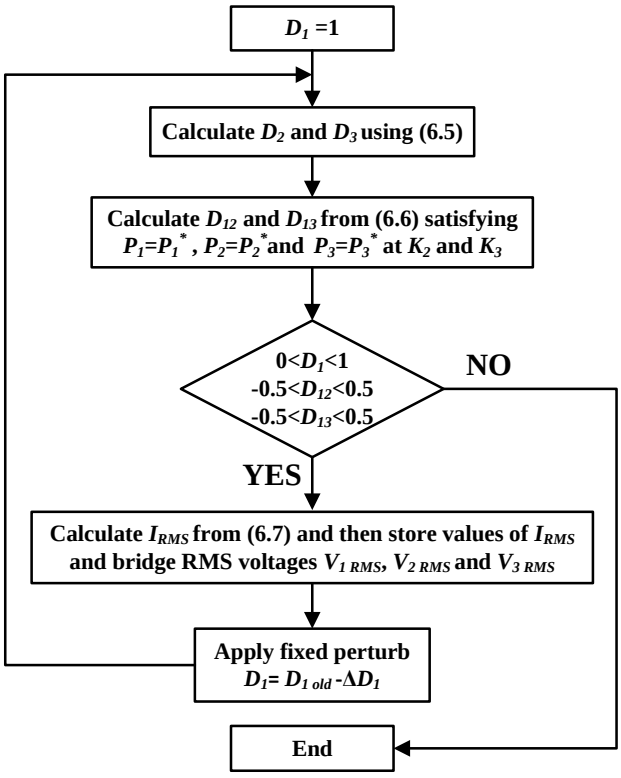

Fig. 6.2: Steps to apply fixed-step perturb on a TAB converter to investigate the effectiveness of D_1 as a perturb parameter.

$$P_1 = \left(\frac{1}{K_{12}+K_{13}}\right)\sin(0.5\pi D_1)\,[K_{12}\sin(0.5\pi D_2)]\sin(\pi[D_{12}+0.5(D_2-D_1)]) + K_{13}\sin(0.5\pi D_3)]\sin(\pi[D_{13}+0.5(D_3-D_1)])]$$

$$P_2 = \left(\frac{K_{12}}{K_{12}+K_{13}}\right)\sin(0.5\pi D_2)\,[-\sin(0.5\pi D_1)\sin(\pi[D_{12}+0.5(D_2-D_1)]) + K_{13}\sin(0.5\pi D_3)]\sin(\pi[D_{13}-D_{12}+0.5(D_3-D_2)$$

$$P_3 = \left(\frac{K_{13}}{K_{12}+K_{13}}\right)\sin(0.5\pi D_3)\,[-\sin(0.5\pi D_1)\sin(\pi[D_{13}+0.5(D_3-D_1)]) + K_{12}\sin(0.5\pi D_2)]\sin(\pi[D_{12}-D_{13}+0.5(D_2-D_3)$$

(6.6)

$$I_{RMS} = \sqrt{(I_{1\,RMS})^2 + (I_{2\,RMS})^2 + (I_{3\,RMS})^2}$$
$$= [(0.25\pi^2/(K_{12}+K_{13})^2)\,[\sin(0.5\pi D_1)^2 + (K_{12}\sin(0.5\pi D_2))^2 + (K_{13}\sin(0.5\pi D_3))^2$$
$$- K_{12}K_{13}\sin(0.5\pi D_2)\sin(0.5\pi D_3)\cos(\pi[D_{12} - D_{13} + 0.5(D_2 - D_3)])$$
$$- K_{12}\sin(0.5\pi D_1)\sin(0.5\pi D_2)\cos(\pi[D_{12} + 0.5(D_2 - D_1)])$$
$$- K_{13}\sin(0.5\pi D_1)\sin(0.5\pi D_3)\cos(\pi[D_{13} + 0.5(D_3 - D_1)])]]^{0.5} \quad (6.7)$$

Fig. 6.3 shows the simulation results (from MATLAB/m-file) where RMS current follows a 'hill-descent' profile when perturbing D_r. Results prove that utilising a single duty ratio (i.e.: duty ratio of reference bridge D_r.) as a perturbation parameter leads to minimum current point (MCP) while maintaining the desired power at the constant required rate during the perturbation process. The hill-descent profile of AC link's resultant RMS current for MAB converter is demonstrated in Fig. 6.4.

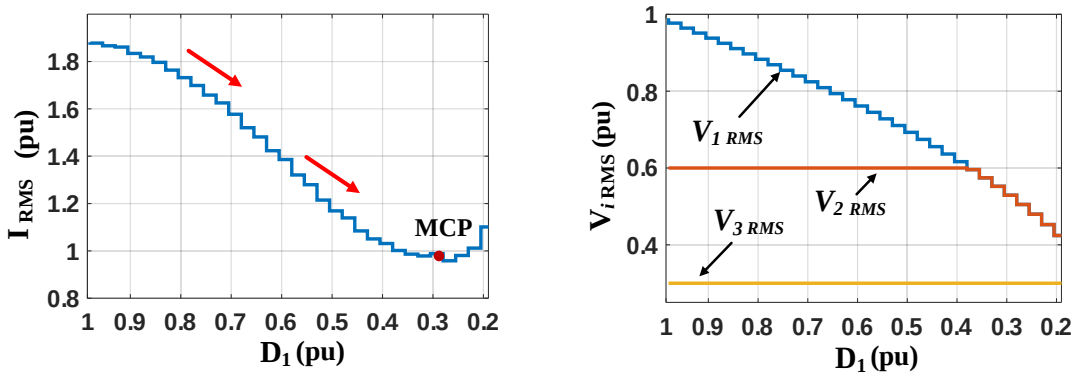

Fig. 6.3: D_1 Perturbation on TAB converter with K_{12} = 0.6, K_{13}= 0.3 at P_1*= 0.2pu, P_2*= -0.1pu, P_3*=-0.1pu.

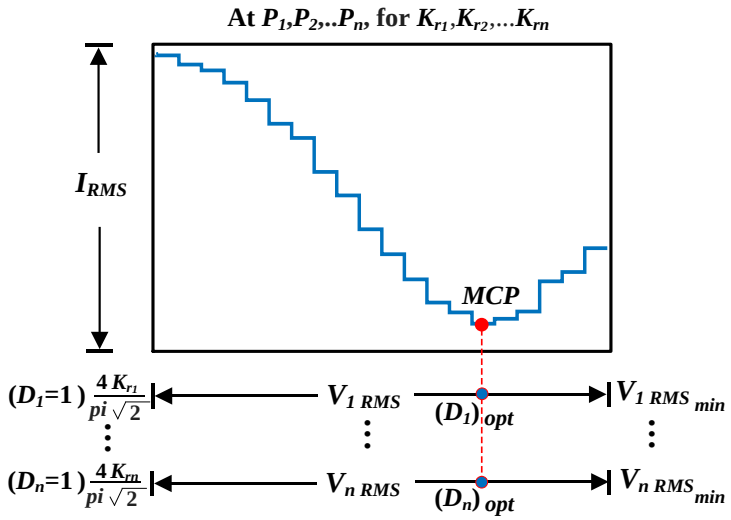

Fig. 6.4: Perturbation in MAB converter with Hill-descent RMS current profile.

6.2.2. Perturb calculation method

This section investigates perturb calculation method for tracking minimum RMS current in MAB converter. Looking at the PV literature, where P&O are widely implemented, two methods of perturb calculation are introduced; fixed-step perturb and adaptive-step perturb [128]–[132]. P&O techniques incorporating fixed-step perturb suffer from several demerits in steady-state. This is because large perturb values result in higher oscillations around the maximum power point (MPP); while smaller perturb values cause slower response, which is a trade-off problem between steady-state oscillation and faster response. Furthermore, MPPT using a fixed-step perturb is system dependent as the perturb value is not generic [128]–[131].

On this basis, this section's objective is to design an adaptive-step perturb calculator for MAB converter. The main requirement of the adaptive-step perturb is to produce large perturb steps at the start of the hill-descent technique to help reach the minimum current point MCP quickly, and as the MCP is approached, reduced perturb step sizes are utilised to avoid large oscillations around the MCP in steady state. In addition, an adaptive perturbation has to be generated according to the system variation (i.e.: is neither user dependent nor fixed.). On this basis, a dual-component adaptive-step perturb is proposed such that the adaptive perturbs are added or subtracted from the past duty ratio D_1 based on the transferred power and AC link RMS current variations. Accordingly, a PI-based adaptive-step calculator is developed as indicated by Fig. 6.5.

The first adaptive component $(\Delta D_r)_{\mathrm{I}}$ is to be calculated as a function of the change in RMS (I_{RMS}) current after and before perturbation. I_{RMS} is outlined by (4.20) and is defined as the resultant of RMS currents of all AC link branches.

$(\Delta D_r)_I$ will tune the perturbation parameter, D_r, in order to track minimum current. This is done by treating this value (i.e.: change in RMS current.) as an error signal that needs to be minimised at steady state in a closed loop system with the aid of a conventional PI controller [132]. The change in the AC link's RMS current is defined as the difference between two successive samples calculated within a fixed delay (T_d) of m sampling instants such that $T_d=m/f_{samp}$ where f_{samp} is the sampling frequency. This delay allows I_{RMS} to reach steady state after the update of modulation parameters, and is arbitrary.

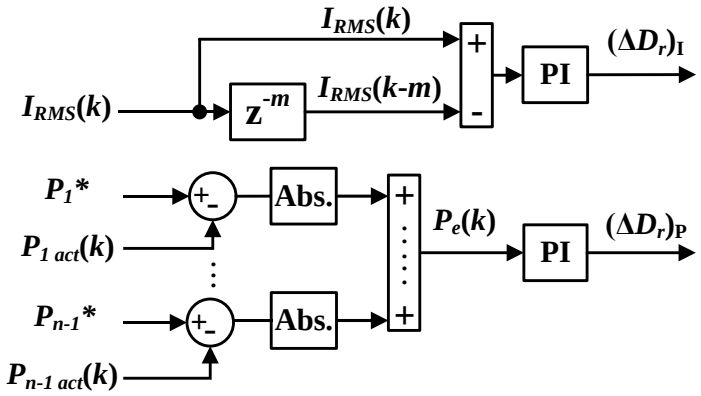

Fig. 6.5: Dual component PI-based adaptive-step perturb calculator.

Furthermore, since active power regulation is the primary objective concerning the proposed controller, then the power transfer needs monitoring during the D_1 perturbation to ensure it remains regulated. This is where the second adaptive component $(\Delta D_r)_P$ is brought into play to update D_1 with respect to the measured transferred power as depicted in Fig. 6.5. The summation of error between the measured/actual power transfer and the desired power level at each bridge, defined as $P_e=|P^*-P_{act}|$, will be handled after every perturbation by a PI controller in order to generate an adaptive perturb $(\Delta D_r)_P$ that maintains this error close to zero during D_r perturbation. This will help to decouple the impact of perturbation to D_r from the main closed loop active power regulation controller

covered in detail in section 4.3. The weights of the two perturb components are arbitrary, however, since the current minimisation totally depends on the P&O algorithm, the weight of $(\Delta D_r)_I$ should be higher than $(\Delta D_r)_P$. Especially that the main function of $(\Delta D_r)_P$ is only to finetune D_r given that a separate controller (i.e.: the previously proposed PI-based Decoupled controller in section 4.3.) will be utilised for power regulation. Accordingly the recommended limits for the perturb components are $0 \leq (\Delta D_r)_I \leq 0.2$pu and $0 \leq (\Delta D_r)_P \leq 0.1$pu. Functions of the proposed dual-component adaptive-step PI-based perturbs are therefore summarised as follows:

- $\mathbf{(\Delta D_r)_I}$ is the adaptive perturb needed to update D_r with respect to the RMS current response depending on the incremental or decremental change of I_{RMS} then $(\Delta D_r)_I$ is generated to update (correct) the value of D_r.
- $\mathbf{(\Delta D_r)_P}$ is the adaptive perturb needed to fine tune D_r to ensure error in active power is maintained close to zero during the perturbation process of D_r to decouple this from main active power regulation controller.

6.2.3. Hill-Descent P&O algorithm

The proposed P&O algorithm perturbs D_r (starting at D_r=1) while observing variation of I_{RMS} and P_e. There are eight operating conditions, outlined in Table.6.1, taking into consideration that sign of $(\Delta D_r)_I$ depends on whether the change in RMS current is positive or negative, i.e.: increase in RMS current means positive $(\Delta D_r)_I$ and decrease in RMS current means negative $(\Delta D_r)_I$. These conditions can be reduced into only four conditions given by (6.8). On this basis, the full proposed hill-descent P&O algorithm is depicted in Fig. 6.6. A delay of just one sample is introduced to $D_r(k)$ to enable instant feedback to the P&O algorithm block. In addition, a small tolerance in power error (P_{Tol}=0.005pu) is used to indicate power

error with an acceptable value, as zero tolerance can cause convergence to sub-optimum solutions.

$$D_r(k) = \begin{cases} D_r(k-m) + (\Delta D_r)_I, & [P_e(k) \le P_{Tol} \text{ AND } D_r(k) < D_r(k-m)] \\ D_r(k-m) - (\Delta D_r)_I, & [P_e(k) \le P_{Tol} \text{ AND } D_r(k) > D_r(k-m)] \\ D_r(k-m) + (\Delta D_r)_I + (\Delta D_r)_P, & [P_e(k) > P_{Tol} \text{ AND } D_r(k) < D_r(k-m)] \\ D_r(k-m) - (\Delta D_r)_I + (\Delta D_r)_P, & [P_e(k) > P_{Tol} \text{ AND } D_r(k) > D_r(k-m)] \end{cases} \quad (6.8)$$

Table 6.1: Operating conditions of P&O Algorithm.

Condition			Action	
1	$I_{RMS}(k)>I_{RMS}(k-m)$	$D_r(k)>D_r(k-m)$ & $P_e(k)\le P_{tol}$	Decrease D_r	$D_1(k)=D_r(k-m)-(\Delta D_r)_I$
2	$I_{RMS}(k)< I_{RMS}(k-m)$	$D_r(k)>D_r(k-m)$ & $P_e(k)\le P_{tol}$	Increase D_r	$D_r(k)=D_r(k-m)-(\Delta D_r)_I$
3	$I_{RMS}(k)>I_{RMS}(k-m)$	$D_r(k)>D_r(k-m)$ & $P_e(k)>P_{tol}$	-Decrease D_r -Fine tune D_r to minimise P_e	$D_r(k)=D_r(k-m)-(\Delta D_r)_I$ $+(\Delta D_r)_P$
4	$I_{RMS}(k)< I_{RMS}(k-m)$	$D_r(k)>D_r(k-m)$ & $P_e(k)>P_{tol}$	-Increase D_r -Fine tune D_r to minimise P_e	$D_r(k)=D_r(k-m)-(\Delta D_r)_I$ $+(\Delta D_r)_P$
5	$I_{RMS}(k)>I_{RMS}(k-m)$	$D_r(k)<D_r(k-m)$ & $P_e(k)\le P_{tol}$	Increase D_r	$D_r(k)=D_r(k-m)+(\Delta D_r)_I$
6	$I_{RMS}(k)< I_{RMS}(k-m)$	$D_r(k)<D_r(k-m)$ & $P_e(k)\le P_{tol}$	Decrease D_r	$D_r(k)=D_r(k-m)+(\Delta D_r)_I$
7	$I_{RMS}(k)>I_{RMS}(k-m)$	$D_r(k)<D_r(k-m)$ & $P_e(k)>P_{tol}$	-Increase D_r -Fine tune D_r to minimise P_e	$D_r(k)=D_r(k-m)+(\Delta D_r)_I$ $+(\Delta D_1)_P$
8	$I_{RMS}(k)< I_{RMS}(k-m)$	$D_r(k)<D_r(k-m)$ & $P_e(k)>P_{tol}$	-Decrease D_r -Fine tune D_r to minimise P_e	$D_r(k)=D_r(k-m)+(\Delta D_r)_I$ $+(\Delta D_1)_P$

The implementation steps of the proposed hill-descent P&O algorithm are as follows:

1) Read the signals of AC link's RMS current I_{RMS}(k) and power transfer $P_{act}(k)$ where k refers to the present sampling instant.
2) Calculate adaptive perturb values $(\Delta D_r)_I$ and $(\Delta D_r)_P$.
3) $(\Delta D_r)_I$, $(\Delta D_r)_P$ and $P_e(k)$ are sent to P&O algorithm which determines $D_r(k)$ while remaining duty ratios are calculated using (6).
4) Updated and previous values of D_r ($D_r(k\text{-}1)$ and $D_r(k\text{-}m)$.) are sent back to the P&O for next iteration.
5) Repeat steps (2)-(4).

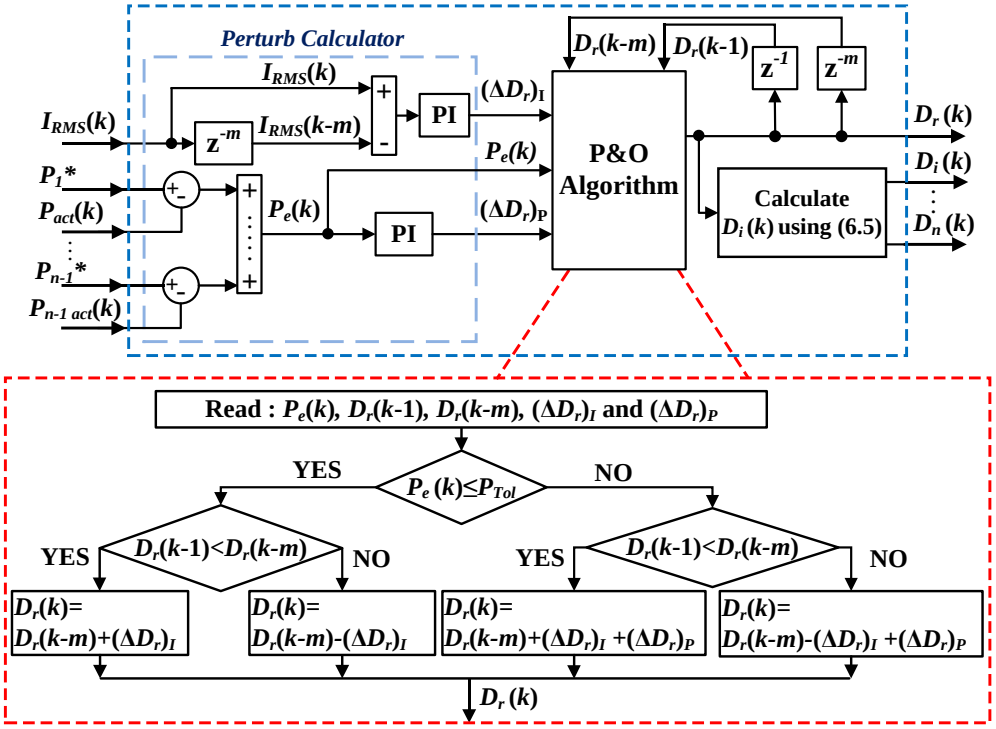

Fig. 6.6: MCPT technique composed of the Hill-Descent Perturb and Observe algorithm and the dual component PI-based adaptive-step perturb calculator.

6.3 Closed Loop Control Design

This section covers the design of the entire control structure including both decoupled power controller (presented in chapter four) and MCPT technique (section 6.2). The PI-based phase shift decoupler will handle power flow control while the MCPT technique obtains optimum duty ratios to achieve minimum AC link RMS current. Fig. 6.7 shows the proposed control scheme for the MAB converter. The control scheme is generalised for MAB converter regardless of power, voltage ratings and number of ports. In addition, it incorporates all possible operating modes, particularly: unity gain mode (K_{ri}=…=K_{rn}=1) and Buck/boost modes (K_{ri}≠1 and/or…K_{rn}≠1). In unity gain mode the MCPT technique is not applied as the minimum current in this case is obtained at unity duty ratios (D_1=…=D_n=1), which achieve equal RMS bridge voltages while keeping minimum RMS current as was proven before by PSO in section II-chapter five. At buck/boost

operating mode, the MCPT technique is utilised to obtain optimum duty ratios (D_1…D_n). Moreover, phase shifts (D_{ri}... D_{rn}) are obtained via the PI-based decoupled power controller. Associated implementation steps are:

1) Read actual measured power (P_{1act}... $P_{n\text{-}1act}$) and desired power (P_1*... P_n*).
2) PI-based decoupling controller regulates phase shifts (D_{ri}... D_{rn}) to track (P_1*... P_n*) (continuous step).
3) Read (P_{1act}... $P_{n\text{-}1act}$), (P_1*... P_n*), I_{RMS}, (V_{dc1}... $V_{dc\,n}$) and calculate DC voltage ratios (K_{ri}....K_{rn})−
   a. For Buck/boost modes (K_{ri}≠1and/or…K_{rn}≠1) then apply MCPT technique (i.e.: perturb calculation and P&O algorithm depicted in Fig. 6.6.). First iteration of P&O employs D_r=1 and second iteration employs an initial small perturb $(\Delta D_r)_1$.
   b. For unity gain mode (K_{ri}…K_{rn}=1) then D_1=…=D_n=1.
4) Duty ratios are then updated and sent to MPS switching signal generator. Then repeat steps 1-4.

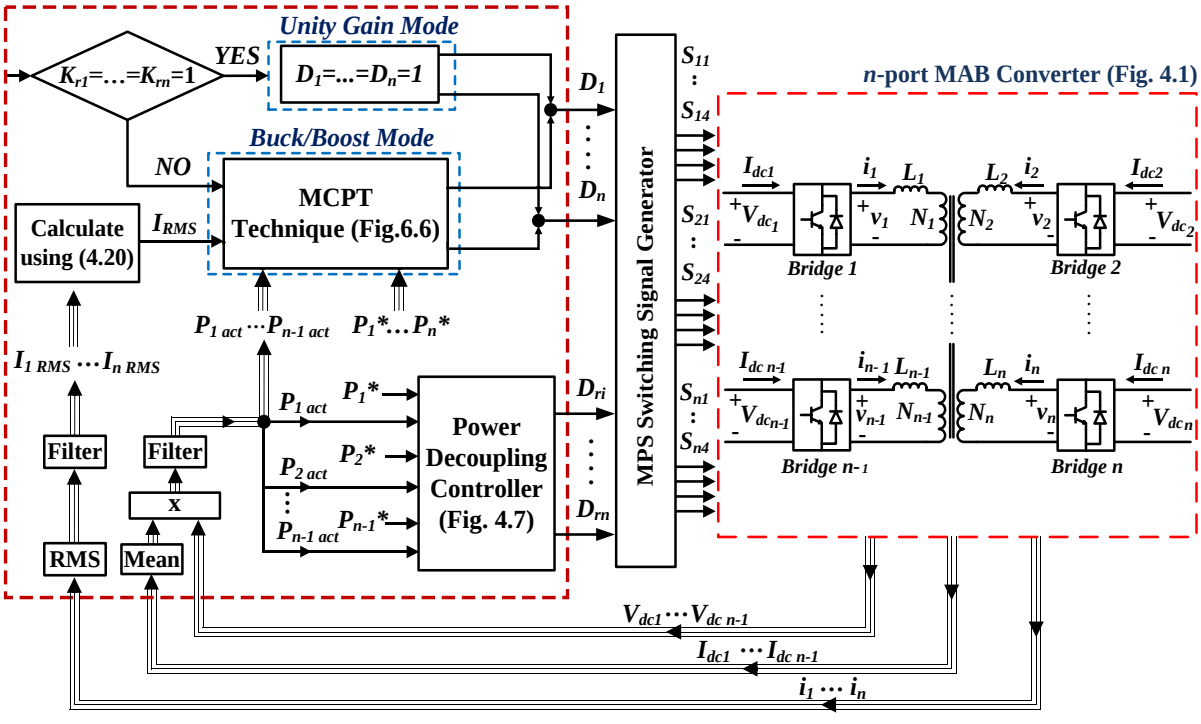

Fig. 6.7: Proposed MCPT power-flow control scheme for MAB converter.

6.4 Simulation Results

This section covers validation of the proposed control scheme in simulation via MATLAB software. Achieved RMS currents, from all investigated cases, are benchmarked with minimum RMS current obtained using the PSO-based method in chapter five to verify that minimum current is obtained. The simulations were carried out using the MAB parameters described in Table 6.2.

Table 6.2: Parameters of MAB Converter.

Parameter	value
Bridge 1 DC Voltage V_{dc1}	100V
Bridge 2 DC Voltage V_{dc2}	K_{12}*100V
Bridge 3 DC Voltage V_{dc3}	K_{13}*100V
Switching Frequency f_s	2.5kHz
Base Power P_{base}	500W
Base inductance L_{base}	1mH

Simulation results of the proposed control scheme, for power regulation with minimum RMS current, on TAB converter is presented in two case studies as shown in Fig. 6.8 and Fig. 6.9. The converter parameters are described in Table 6.2 with AC link equivalent inductors calculated by (6.9), that was derived in chapter four, ensuring maximum power at each port. The controller satisfies the required P^* at bridges 1 and 2 with negligible oscillations (ripples) as shown in Figs. 6.8 and 6.9 parts (a) and (b). The reason for the ripples is that after each perturbation (online iteration) the duty ratios (D_1, D_2 & D_3) change hence the decoupled PI-controller change phase shifts (D_{12} & D_{13}) to maintain the required power levels (P_1^* & P_2^*). The resultant of all AC side RMS currents, outlined by (6.9), is shown in Fig.6.8 (c) and Fig. 6.9 (c), along with the reference benchmark minimum RMS current. The difference at the beginning is high as unity duty ratios are employed. Then this difference starts to decrease as P&O-based control scheme moves toward optimum modulation parameters achieving negligible oscillation MCP in steady state.

$$L = (K_2 + K_3)\frac{4^3}{2 * 6\pi^3} L_{base} \tag{6.9}$$

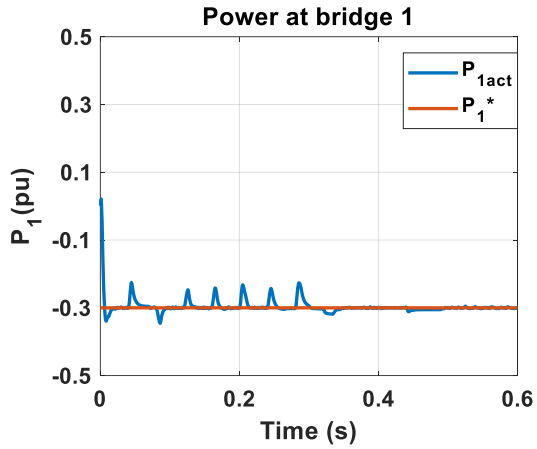

(a)

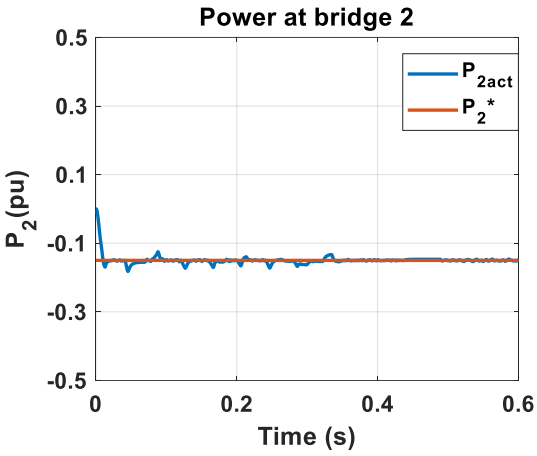

(b)

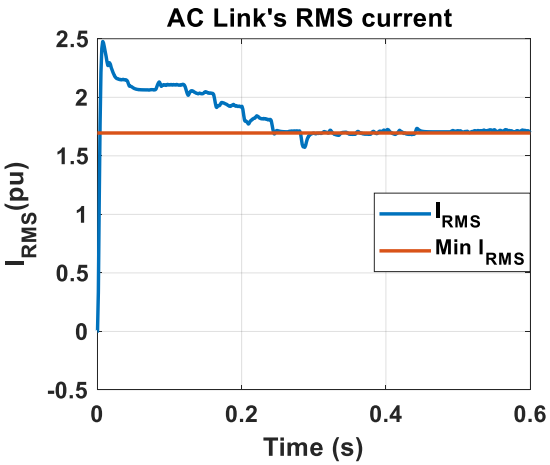

(c)

Fig. 6.8: Perfromance of TAB under proposed MCPT controller at K_{12}=0.3, K_{13}=0.6, P_1*=-0.3pu, and P_2*=-0.15pu. (a)Power at Bridge 1. (b)Power at Bridge 2. (c) RMS current of AC link branches.

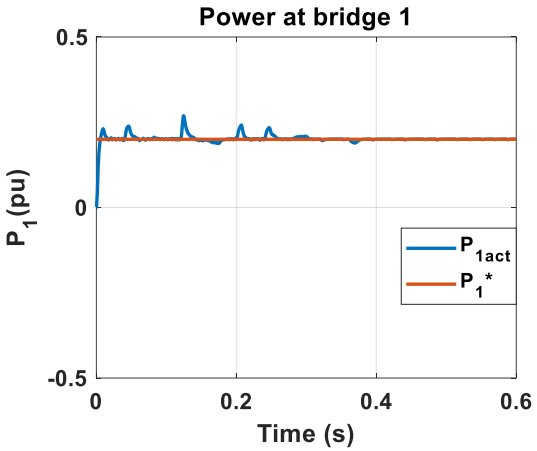

(a)

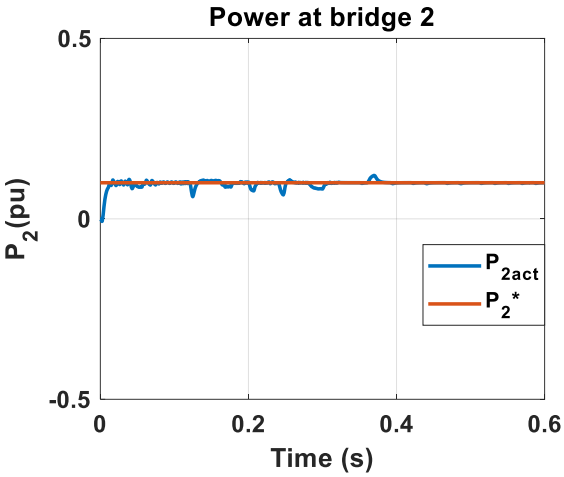

(b)

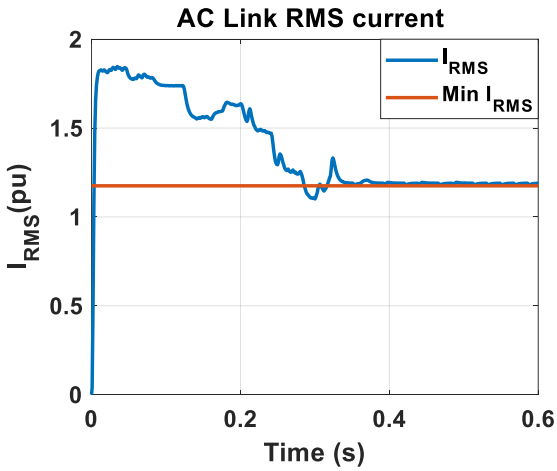

(c)

Fig. 6.9:Perfromance of TAB under proposed MCPT controller at K_{12}=0.5, K_{13}=0.4, P_1*=0.2pu, and P_2*=0.1pu. (a)Power at Bridge 1.(b)Power at Bridge 2. (c) RMS current of AC link branches.

For further demonstration of the perturbation process, values of the main perturbation parameter (D_1) and the dependent duty ratios (D_2 and D_3) – during perturbation until steady state – are shown in Fig 6.10 reflecting the performance of the controller in TAB at at K_{12}=0.3, K_{13}=0.6, P_1*=-0.3pu, and P_2*=-0.15pu (case study of Fig 6.8). Fig 6.10 shows that the algorithm starts perturbation with high adaptive perturb steps until t≈0.325s when values of duty ratio start to converge to steady state (i.e.: employing small perturb step-size reflecting the convergence to minimum RMS current as shown in Fig 6.8 part (c).). From t≈0.45s the oscillations in the duty ratios are minimal (±0.01) hence the negligible oscillations observed in the RMS current and power curves in Fig 6.8.

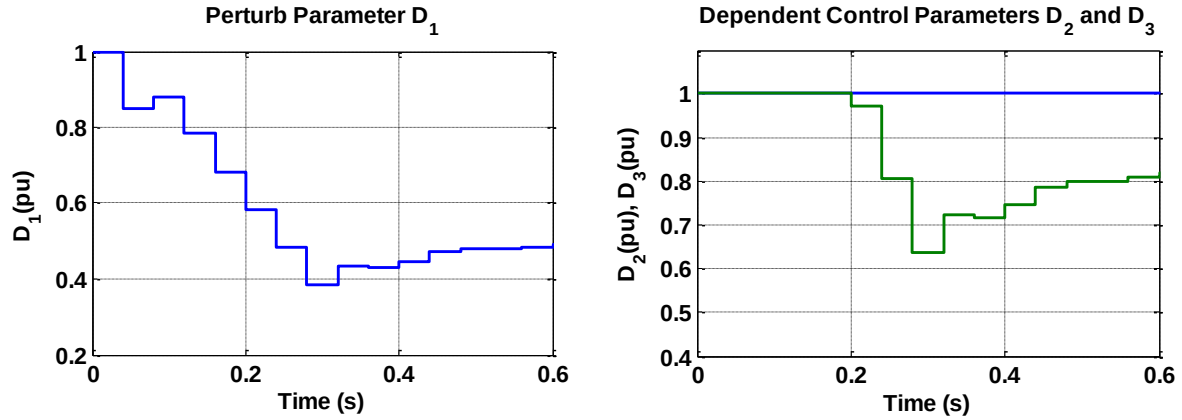

(a) (b)

Fig. 6.10: Perfromance of TAB under proposed MCPT controller at K_{12}=0.3, K_{13}=0.6, P_1*=-0.3pu, and P_2*=-0.15pu. (a)Perturbation parameter D_1. (b)Dependent control variables D_2 and D_3.

In order to demonstrate the dynamic response of the controller, a simulation including step change in reference power is shown in Fig 6.11. At the instant of the step change in reference power, the controller resets and start perturbing at D_r=1 until the minimum current point (MCP) is reached while maintaining the required power levels. It can be noticed that the first case (P_1*=0.9pu, P_2*=-0.4pu) the MCP is reached in a relatively lower transient time (compared to second case after t=0.6 sec). That is because at P_1*=0.9pu, P_2*=-

0.4pu the optimal modulation parameters are at $D_1=D_2=D_3=1$ while the perturbation always starts at $D_r=1$ which explains the corresponding lower transient time.

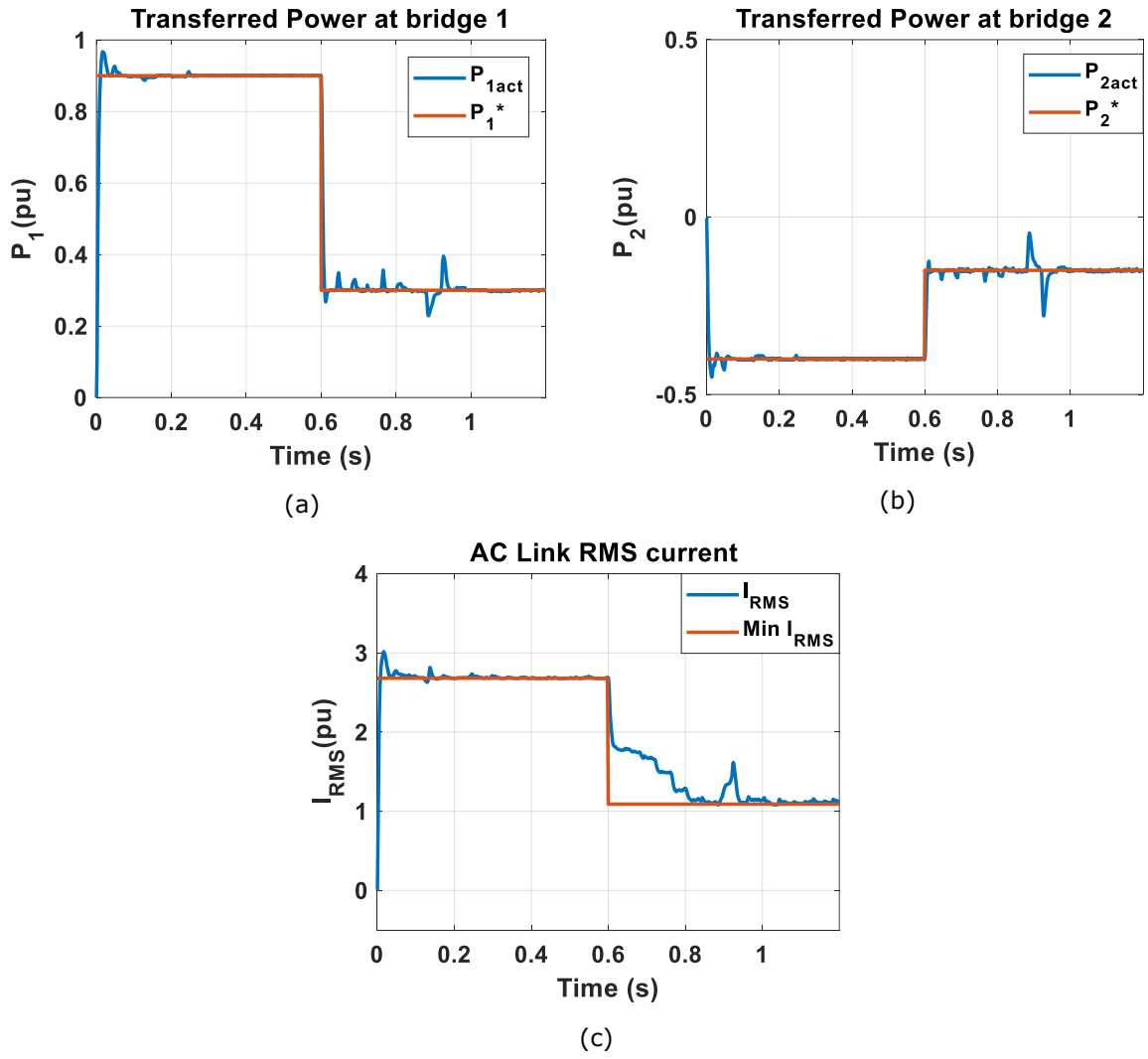

Fig. 6.11: Dynamic perfromance of TAB under proposed MCPT controller at $K_{12}=0.5$, $K_{13}=0.4$, $P_1*=0.9,0.3$ pu, and $P_2*=-0.4,-0.15$pu. (a)Power at Bridge 1. (b)Power at Bridge 2. (c) RMS current of AC link branches.

6.5 Validation of the Proposed Controller on DAB

This subsection provides the verification of the universality of the control scheme when applied to DAB converter which is considered as simplest form of the MAB (i.e.: MAB with only two ports.). For implementing the proposed controller on DAB converter, optimum duty ratios will be obtained by the MCPT technique with

perturbation parameter D_r and with the same PI-based adaptive-step calculator. Accordingly, MCPT-based closed loop scheme for DAB is presented as depicted in shown in Fig.6.12 where the only difference between this and the MAB control scheme (shown in Fig 6.7) is that a simple PI controller replaced the phase shift decoupler (used in MAB) to regulate a single phase-shift (D_{12}). This can be confirmed by considering the fundamental harmonic of DAB's transferred power outlined by (3.33), as at given duty ratios it reduces to

$$P = C_1 * \sin(\pi D_{12} + C_2) \tag{6.10}$$

Where, $C_1 = \frac{32}{\pi^3} K_{12} \sin(\frac{\pi}{2} D_1) * \sin(\frac{\pi}{2} D_2)$ and $C_2 = \pi(\frac{D_2 - D_1}{2})$

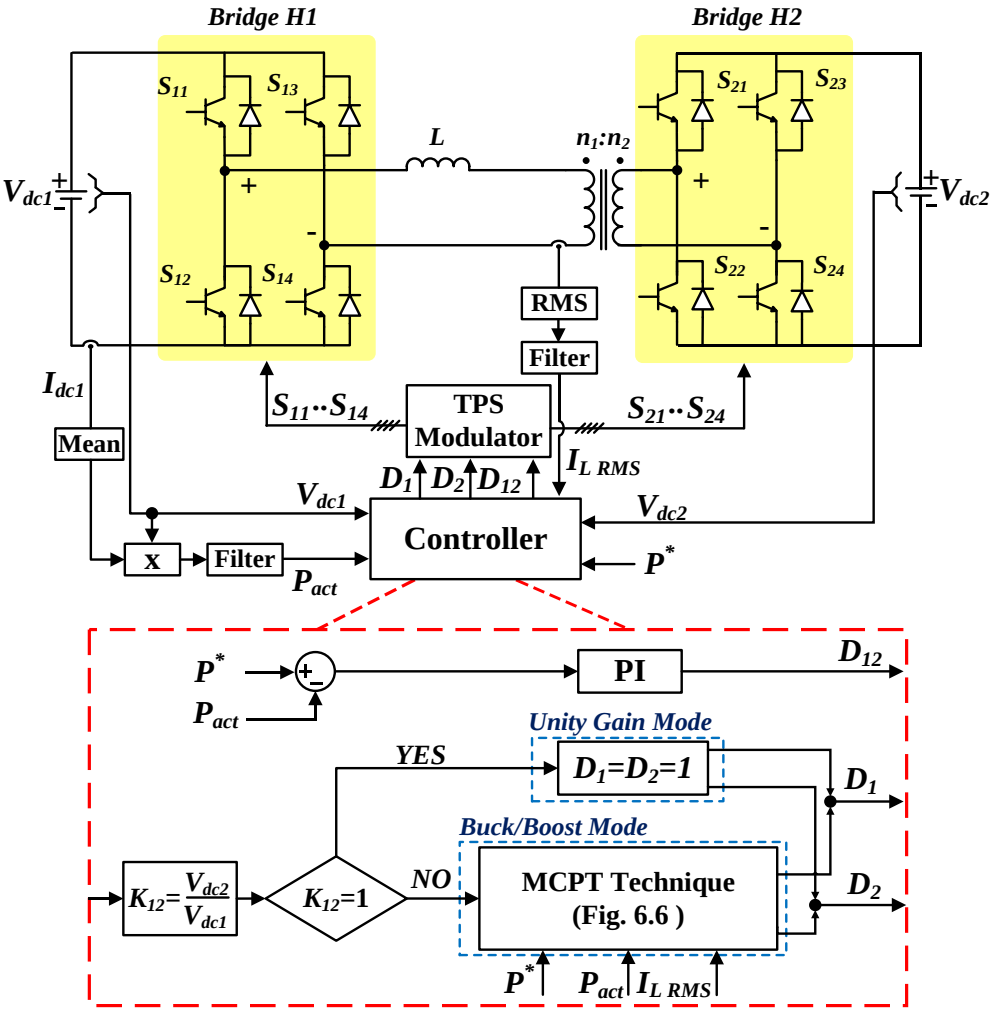

Fig. 6.12: Proposed MCPT power-flow control scheme for DAB converter.

Equation (6.10) shows that DAB's transferred power is basically a trigonometric function where $P = f(D_{12})$ at given duty ratios (D_1 and D_2). As a result, power flow is controlled via the regulation of the phase shift between the bridge voltages D_{12} with the aid of a simple PI controller.

The proposed MCPT technique is applied on a detailed switching DAB converter in MATLAB/Simulink for validation. Achieved RMS current are benchmarked with the minimum RMS current obtained using the PSO-based method in chapter five to verify that minimum current is obtained. The simulations were carried out using the DAB parameters described in Table 6.2. Simulation results for two case studies are presented in Fig. 6.13 and Fig. 6.14, thus highlighting the performance of the DAB converter under the proposed controller. Fig.6.12(a) and Fig.6.13(a) show that the controller satisfies the required P^* with negligible oscillations in both transient and steady state. These negligible oscillations (ripples) exist because after each perturbation (online iteration) the duty ratios D_1 & D_2 change hence the PI controller phase shift D_{12} to keep maintaining the reference power level P^*. Fig.6.13(b) and Fig.6.14(b) show the actual RMS current along with minimum RMS current. The relative difference at the beginning of the perturbation is high as unity duty ratios are employed. Then this difference starts to decrease as the P&O moves the operating point of the DAB converter toward the optimal TPS ratios achieving minimum RMS current with negligible oscillations in steady state. In addition, to validate the robustness of the controller to different system parameters, extra simulations were carried out with different value of AC Link equivalent inductance (L=3mH). Results are shown in Fig.6.15 showing that the controller performance is not dependent on circuit parameters.

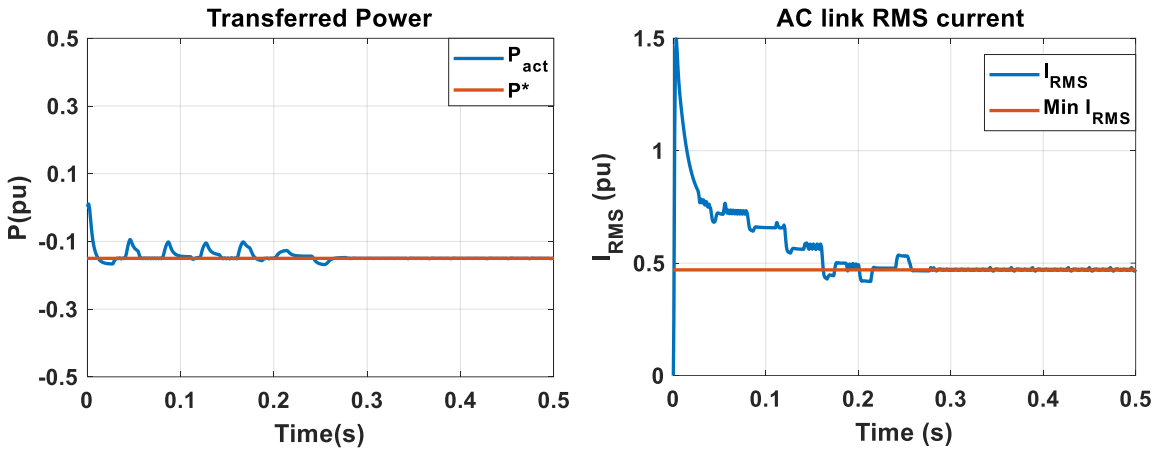

(a) (b)

Fig. 6.13: Perfromance of DAB Converter under proposed MCPT controller at K_{12}=0.4 and P*=-0.15pu : (a)Transferred Power. (b) AC Link's RMS current.

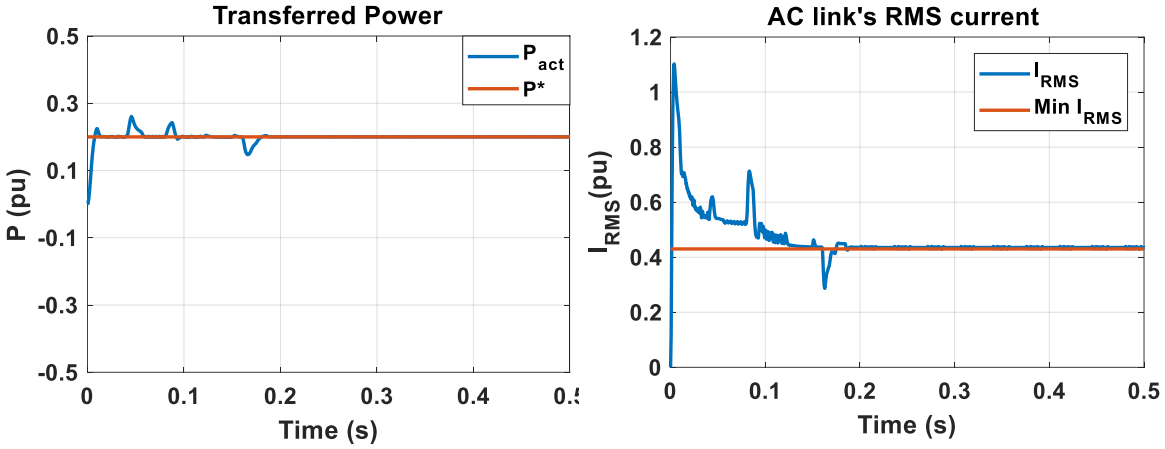

(a) (b)

Fig. 6.14: Perfromance of DAB Converter under proposed MCPT controller at K_{12}=0.6 and P*=0.2pu: (a)Transferred Power. (b) AC Link's RMS current.

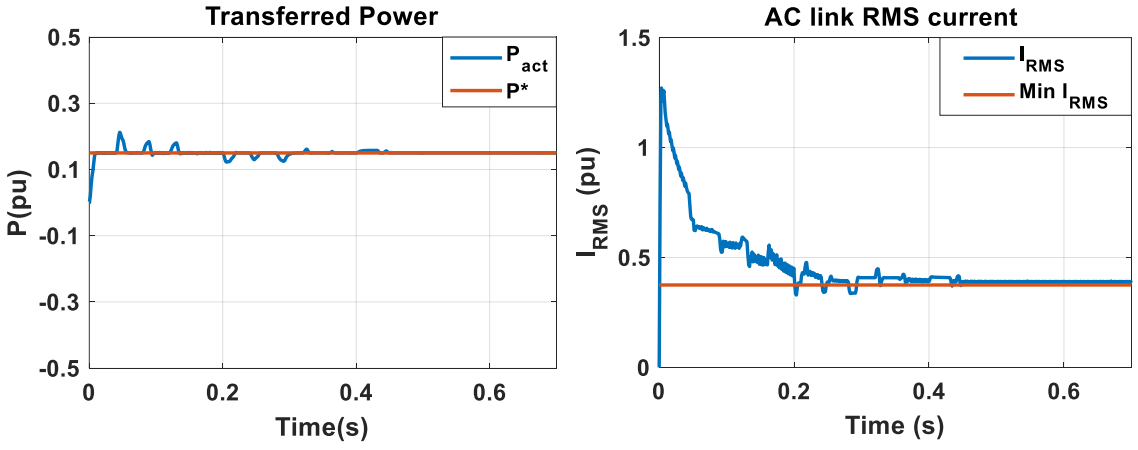

(a) (b)

Fig. 6.15: Perfromance of DAB Converter under proposed MCPT controller with different system parameters at K_{12}=0.5 and P*=0.15pu: (a)Transferred Power. (b) AC Link's RMS current.

In order to demonstrate the dynamic (transient) response of the controller, a simulation introducing step change in reference power is shown in Fig 6.16.

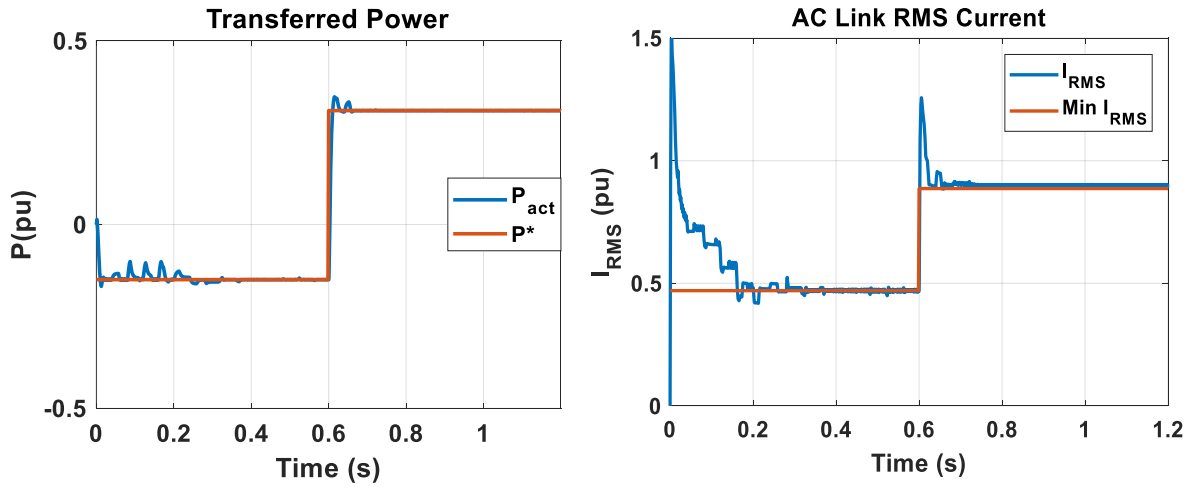

(a) (b)

Fig. 6.16: Dynamic Perfromance of DAB Converter under proposed MCPT controller with different system parameters at K_{12}=0.4 and P*=-0.15, 0.31 pu: (a)Transferred Power. (b) AC Link's RMS current.

6.6 Discussion

Considering that the main objective of the proposed MCPT controller is power flow management, the implementation of the proposed MCPT controller realises the desired transferred power while achieving negligible-oscillation-MCP in steady state. However, there are some limitations regarding the application of this controller. For example, this controller is more suitable in switching frequencies in the range of 2 to 3 kHz to allow time for implementing the needed delay and to implement the P&O algorithm outlined by (6.8). This range of operating frequency indicate that the potential application of this controller might be in MVDC/HVDC applications where the implemented switching frequencies are usually below 2 kHz [67]. This is because high switching frequency impresses extremely high *dv/dt* stress upon the transformer when operating in the kilovolts range, [133], which

complicates the design of the interfacing transformer (in terms of insulation) and reduces its reliability and lifetime [67].

Also, the transient time taken to achieve minimised RMS current is somehow slow which is mainly because the number of iterations (perturbations) needed to reach minimum RMS current. This can be partially solved by increasing the limits of perturb step size (i.e.: increasing the limits of the dual-component perturb $(\Delta D_r)_{\mathrm{I}}$ & $(\Delta D_r)_{\mathrm{P}}$.). However, this may increase peak values of the ripples (oscillates) in power and current response. Alternatively, the issue of the slow transient response of the proposed controller may require some sort of predictive algorithm to be imbedded within the controller. For example, an FHA-based calculator can be imbedded within the controller to give indicative prediction of the power and current values based on the duty ratios that are one step ahead of the present duty ratios. This has been added as a future work point later in this thesis.

6.7 Summary

This chapter has discussed the development of a control scheme for power regulation for use in multi active bridge (MAB) converters including dual active bridge (DAB). The developed MAB's I-V characteristic revealed the existence of a global minimum current point (MCP) for every level of active power transferred between the DC sides. This MCP can be tracked based on a P&O algorithm that calculates the optimum combination of duty ratios at any operating point. The proposed minimum current point tracking (MCPT) algorithm is combined with a closed loop controller to regulate power to desired level. Extensive simulations verified the effectiveness and potential of the proposed scheme. The **novelty and contributions** of this chapter are summarised in the following bullet points:

- A new I-V characteristic 3D analysis for MAB converter showing a global minimum current point (MCP) for every level of active power transferred and the dependence of MCPs on duty ratios (bridge RMS voltages).
- A new minimum-RMS-current tracking method is proposed based on P&O algorithm with adaptive-step perturb calculator.
- The proposed MCPT algorithm is combined with a closed loop controller to regulate desired active power regardless of number of ports.
- The proposed controller is generic, independent of circuit parameters and does not require complex converter modeling, look-up tables or any offline calculations prior to implementation.

Chapter 7. Conclusions and future work

7.1. Conclusions

Offering several functionalities, bidirectional MAB DC–DC converters have attracted significant research interest within HVDC, MVDC and low voltage/low power applications. Accordingly, the presented work within this thesis mainly investigated current-stress minimisation controllers for MAB converters. The research results can be summarised as follows:

- In Chapters 3, per unit steady state model of dual active bridge (DAB) converter based on the triple phase shift modulation (TPS) was developed. This included active power expressions for all possible switching modes and a new unified AC-side RMS current expression.
- In chapter 4, generalised power flow analysis has been developed and investigated for MAB converter regardless of number of ports. This allowed the derivation of a new decoupling controller for power regulation in MAB with phase shift control that enables independent regulation of active power in each bridge and simple implementation with PI controllers. Moreover, fundamental harmonic per unit modelling of triple active bridge were carried out under various purely inductive AC link topologies. The value of the AC link inductor was calculated for each topology to investigate the topology with minimum inductance, hence smallest converter footprint. The first proposed topology has proven to achieve the best performance among other topologies, in terms of minimum AC link inductance required and minimum RMS current stresses and reactive power loss.

- In Chapter 5, RMS current minimisation in DAB was defined as a multi constraint minimisation problem. Then particle swarm optimisation (PSO) method was introduced for offline application on the presented exact DAB model (in chapter 3) to generate the optimal TPS ratios for the entire bi-directional power transfer range and different values of DC voltage ratios. The output optimal TPS ratios obtained from this offline optimization exercise were analysed and the concluded patterns were utilised to design a new simple real time controller for power regulation with minimum RMS current in DAB. The devised real time controller is universal as it covers the entire bi-directional power flow range regardless of the DC voltage ratio. It is also simple to implement with a single PI controller and does not require any offline calculation or look-up tables. The simulation and experimental results validate the effectiveness of the proposed generic controller.
- Chapter 6 details the development of a new control scheme for power regulation in MAB converters. Current/voltage characteristics of MAB were developed and revealed the existence of a global minimum current for every level of active power transferred. Hence, a new online minimum current point tracking (MCPT) method was developed based on an adaptive-step P&O algorithm that was combined with the decoupler controller for active power regulation in MAB converter. The proposed controller is generic and, unlike existing efforts in this area, is independent of circuit parameters, plus it is not derived from complex converter modelling. Extensive simulations verified the effectiveness and robustness of the proposed control scheme.

7.2. Future Work

This section lists some future research areas related to multi active bridge converters in terms of modelling and control schemes. Future work topics are as follows:

- Including the nonideal effect of parasitics and short time scale factors such as switching dead time effects in the detailed mathematical derivation carried out in chapter 3. In practical aspect, the dead time is set to prevent the two switches in the same leg shorting directly. The effects of the dead time are the phenomena of voltage polarity reversal and phase drift [134], [135]. With dead-time effect, the transmission power model is not a strictly monotone increasing function, zero phase-shift ratio does not achieve the zero point and the relation curve is not symmetric around the median axis [134]. In addition, for different DC voltage ratio and dead time, the switching characterizations of the DAB converter are also different. For example, with CPS, in buck/boost modes there are six switching modes and in unity gain there are three switching modes [134]. The dead-time effect of DAB becomes even more apparent issue when operating at higher switching frequencies. On the other hand, voltage reversal increases the reactive power, decrease volt-seconds which further affect the characteristics of the steady state model in terms of transmission power, current stress and efficiency, etc [134]. Covering the above mentioned non-ideal factors when deriving the state state model will affect the calculated modulation parameters (triple phase shift values) and hence the achieved minimum current stresses. However, developing the TPS-based model will

be more challenging and that's why very few literatures is found in this area of research.

- Extensive research could be put forward to address enhancing the dynamic performance of MAB converters. Robust and fast dynamic response are required in extreme conditions facing MAB converters such as the output load distribution, no-load conditions and the input voltage fluctuation. Virtual direct power control (VDPC) scheme is proposed in [94] targeting dynamic response of DAB, however the scheme is only implemented with traditional single-phase shift (SPS) control. Authors in [94] also provided a good comparison with other methods such as load current feed-forward control, traditional voltage loop control and model-based phase-shift control. In addition, some of the existing schemes for enhancing the dynamic behaviour depend on variable frequency approach which means that transformer saturation will occur, such as [93] that proposed an excellent control scheme that achieves negligible overshoot, fast transient response in start-up and load disturbances, and few switching actions to reach steady state.
- Investigation of methods to lower transient time within the second proposed controller (MCPT controller) by introducing some sort of predictive control that can shorten the transient time by reducing number of online iterations (perturbations).
- Several DAB-based topologies have been proposed to enable utilisation of DAB in HVDC/MVDC grids such as input-series output-parallel (ISOP) topology [63], [68] and DAB-based Modular Multi level Converters (MMC) [56], [136], [137] . The investigation of the proposed new controllers within

the above-mentioned active-bridge-based configurations for MVDC/HVDC applications can be a promising future point.

References

[1] P. Notice and S. P. Release, “UK Energy Statistics , 2015 & Q4 2015,” no. March, pp. 1–16, 2016.

[2] P. Notice and S. P. Release, “UK Energy Statistics , Q1 2019,” no. June, pp. 1–14, 2019.

[3] J. M. Guerrero, J. C. Vásquez, J. Matas, M. Castilla, and L. García de Vicuna, “Control strategy for flexible microgrid based on parallel line-interactive UPS systems,” *IEEE Trans. Ind. Electron.*, vol. 56, no. 3, pp. 726–736, 2009.

[4] T. F. Wu, K. H. Sun, C. L. Kuo, and C. H. Chang, “Predictive current controlled 5-Kw single-phase bidirectional inverter with wide inductance variation for dc-microgrid applications,” *IEEE Trans. Power Electron.*, vol. 25, no. 12, pp. 3076–3084, 2010.

[5] M. G. Molina and P. E. Mercado, “Power flow stabilization and control of microgrid with wind generation by superconducting magnetic energy storage,” *IEEE Trans. Power Electron.*, vol. 26, no. 3, pp. 910–922, 2011.

[6] J. M. Guerrero, N. Berbel, J. Matas, J. L. Sosa, and L. G. de Vicuna, “Droop Control Method with Virtual Output Impedence for Parallel Operation of Uninterruptible Power Supply Systems in a Microgrid,” *APEC 07 - Twenty-Second Annu. IEEE Appl. Power Electron. Conf. Expo.*, vol. 18, pp. 1126–1132, 2007.

[7] N. Hatziargyriou, *Microgrid: Architectures and Control - Chapter 1 - The Microgrid Concept*. Hoboken, NJ, USA: Wiley, 2014.

[8] W. Medjroubi, U. P. Müller, M. Scharf, C. Matke, and D. Kleinhans, “Open Data in Power Grid Modelling: New Approaches Towards Transparent Grid Models,” *Energy Reports*, vol. 3, pp. 14–21, Nov. 2017.

[9] D. Sha, G. Xu, and X. Liao, “Control strategy for input-series-output-series high-frequency AC-link inverters,” *IEEE Trans. Power Electron.*, vol. 28, no. 11, pp. 5283–5292, 2013.

[10] T. H. P. W. M. Converter, “A Soft-Switching Scheme for an Isolated DC / DC Converter With Pulsating DC Output for a,” vol. 24, no. 10, pp. 2276–2288, 2009.

[11] L. Jia and S. K. Mazumder, “A loss-mitigating scheme for DC/pulsating-DC converter of a high-frequency-link system,” *IEEE Trans. Ind. Electron.*, vol. 59, no. 12, pp. 4537–4544, 2012.

[12] S. K. Mazumder and A. K. Rathore, “Primary-side-converter-assisted soft-switching scheme for an AC/AC converter in a cycloconverter-type high-frequency-link inverter,” *IEEE Trans. Ind. Electron.*, vol. 58, no. 9, pp. 4161–4166, 2011.

[13] J. S. Lai and D. J. Nelson, “Energy management power converters in hybrid electric and fuel cell vehicles,” *Proc. IEEE*, vol. 95, no. 4, pp. 766–777, 2007.

[14] S. Falcones, R. Ayyanar, and X. Mao, “A DC-DC Multiport-converter-based solid-state transformer integrating distributed generation and storage,” *IEEE Trans. Power Electron.*, vol. 28, no. 5, pp. 2192–2203, 2013.

[15] G. G. Karady and X. Liu, “Fault management and protection of FREEDM systems,” *IEEE PES Gen. Meet. PES 2010*, pp. 1–4, 2010.

[16] W. Chen, P. Rong, and Z. Lu, “Snubberless bidirectional DC-DC converter with new CLLC resonant tank featuring minimized switching loss,” *IEEE Trans. Ind. Electron.*, vol. 57, no. 9,

pp. 3075–3086, 2010.

[17] P. K. Jain and S. Member, “Performance of a Single-Stage UPS System for,” *Power*, vol. 13, no. 5, pp. 912–923, 1998.

[18] J. Wu, “A New UPS Scheme,” vol. 42, no. 6, 1995.

[19] B. Zhao, Q. Song, W. Liu, and Y. Sun, “Overview of dual-active-bridge isolated bidirectional DC-DC converter for high-frequency-link power-conversion system,” *IEEE Trans. Power Electron.*, vol. 29, no. 8, pp. 4091–4106, 2014.

[20] C. Zhao and T. Li, “Recovering the modular multilevel converter from a cleared or isolated fault,” *IET Gener. Transm. Distrib.*, vol. 9, no. 6, pp. 550–559, 2015.

[21] A. Arapogianni and et al. Genachte, A.-B., “Deep water,” 2013.

[22] European Wind Energy Association, “Wind in our Sails,” 2011.

[23] K. Li and X. Zhao, “Adaptive backstepping droop controller design for multi-terminal high-voltage direct current systems,” *IET Gener. Transm. Distrib.*, vol. 9, no. 10, pp. 975–983, 2015.

[24] E. Csanyi, “Analysing the costs of High Voltage Direct Current (HVDC) transmission,” 2014. [Online]. Available: https://electrical-engineering-portal.com/analysing-the-costs-of-high-voltage-direct-current-hvdc-transmission. [Accessed: 26-May-2019].

[25] M. M. C. Merlin, T. C. Green, P. D. Mitcheson, D. R. Trainer, D. R. Critchley, and R. W. Crookes, “A new hybrid multi-level voltage-source converter with DC fault blocking capability,” *9th IET Int. Conf. AC DC Power Transm. (ACDC 2010)*, pp. O56–O56, 2010.

[26] H. Zhang and D. Jovcic, “Interconnecting subsea DC collection systems into a high reliability DC grid,” *IEEE PES Innov. Smart Grid Technol. Conf. Eur.*, vol. 2015-Janua, no. January, pp. 1–5, 2015.

[27] G. P. Adam, K. H. Ahmed, S. J. Finney, K. Bell, and B. W. Williams, “New breed of network fault-tolerant voltage-source-converter HVDC transmission system,” *IEEE Trans. Power Syst.*, vol. 28, no. 1, pp. 335–345, 2013.

[28] D. Jovcic and K. Ahmed, *High voltage direct current transmission: converters, systems and DC grids*. 2015.

[29] J. Riedel, “On Frequency Domain Analysis of Dual Active Bridge DC-DC Converters,” 2017.

[30] S. Inoue and H. Akagi, “A bidirectional DC-DC converter for an energy storage system with galvanic isolation,” *IEEE Trans. Power Electron.*, vol. 22, no. 6, pp. 2299–2306, 2007.

[31] M. Kim, M. Rosekeit, S. K. Sul, and R. W. A. A. De Doncker, “A dual-phase-shift control strategy for dual-active-bridge DC-DC converter in wide voltage range,” *8th Int. Conf. Power Electron. - ECCE Asia "Green World with Power Electron. ICPE 2011-ECCE Asia*, pp. 364–371, 2011.

[32] F. Krismer and J. W. Kolar, “Closed form solution for minimum conduction loss modulation of DAB converters,” *IEEE Trans. Power Electron.*, vol. 27, no. 1, pp. 174–188, 2012.

[33] S. Shao, H. Chen, X. Wu, J. Zhang, and K. Sheng, “Circulating Current and ZVS-on of a Dual Active Bridge DC-DC Converter : A Review,” *IEEE Access*, vol. 7, pp. 50561–50572, 2019.

[34] B. Karanayil, M. G. Arregui, V. G. Agelidis, and M. Ciobotaru, “Bi-directional isolated multi-port power converter for aircraft HVDC network power transfer,” in *IECON Proceedings (Industrial Electronics Conference)*, 2012, pp. 3394–3399.

[35] R. Yapa and A. Forsyth, “Extended soft switching operation of the triple active bridge convereter,” *6th IET Int. Conf. Power Electron. Mach. Drives (PEMD 2012)*, pp. A84–A84, 2012.

[36] C. Gu, Z. Zheng, L. Xu, K. Wang, and Y. Li, “Modeling and Control of a Multiport Power Electronic Transformer (PET) for Electric Traction Applications,” *IEEE Trans. Power Electron.*, vol. 31, no. 2, pp. 915–927, 2016.

[37] M. Hajian, D. Jovcic, and B. Wu, “Evaluation of semiconductor based methods for fault isolation on high voltage DC grids,” *IEEE Trans. Smart Grid*, vol. 4, no. 2, pp. 1171–1179, 2013.

[38] “2050 Pathways.” [Online]. Available: https://www.gov.uk/guidance/2050-pathways-analysis. [Accessed: 21-Jul-2019].

[39] H. S. Chung, S. Member, W. Cheung, and K. S. Tang, “A ZCS Bidirectional Flyback DC / DC Converter,” *IEEE Trans. POWER Electron.*, vol. 19, no. 6, pp. 1426–1434, 2004.

[40] A. A. Aboulnaga and A. Emadi, “Performance Evaluation of the Isolated Bidirectional Cuk Converter with Integrated Magnetics,” in *2004 35th Annual IEEE Power Elecrronics Specialists Conference*, 2004, pp. 1557–1562.

[41] D. Murthy-bellur and M. K. Kazimierczuk, “Isolated Two-Transistor Zeta Converter With Reduced Transistor Voltage Stress,” *IEEE Trans. Circuits Syst. II Express Briefs*, vol. 58, no. 1, pp. 41–45, 2011.

[42] F. Zhang and Y. Yan, “Novel Forward – Flyback Hybrid Bidirectional,” *IEEE Trans. Ind. Electron.*, vol. 56, no. 5, pp. 1578–1584, 2009.

[43] H. Xiao and S. Xie, “A ZVS Bidirectional DC – DC Converter With Phase-Shift Plus PWM Control Scheme,” *IEEE Trans. POWER Electron.*, vol. 23, no. 2, pp. 813–823, 2008.

[44] Z. Zhang, O. C. Thomsen, and M. A. E. Andersen, “Optimal Design of a Push-Pull-Forward Half-Bridge With Variable Input Voltage,” *IEEE Trans. Ind. Electron.*, vol. 59, no. 7, pp. 2761–2771, 2012.

[45] E. V. De Souza and I. Barbi, “BIDIRECTIONAL CURRENT-FED FLYBACK-PUSH-PULL DC-DC CONVERTER,” *XI Brazilian Power Electron. Conf.*, pp. 8–13, 2011.

[46] H. Li, S. Member, F. Z. Peng, S. Member, J. S. Lawler, and S. Member, “A Natural ZVS Medium-Power Bidirectional DC – DC Converter With Minimum Number of Devices,” *IEEE Trans. Ind. Appl.*, vol. 39, no. 2, pp. 525–535, 2003.

[47] Z. Zhang, Z. Ouyang, O. C. Thomsen, and M. A. E. Andersen, “Analysis and Design of a Bidirectional Isolated DC – DC Converter for Fuel Cells and Supercapacitors Hybrid System,” *IEEE Trans. Power Electron.*, vol. 27, no. 2, pp. 848–859, 2012.

[48] J. Lee, Y. Jeong, and B. Han, “A Two-Stage Isolated / Bidirectional DC / DC Converter,” *IEEE Trans. Ind. Electron.*, vol. 59, no. 1, pp. 644–646, 2012.

[49] D. Xu, C. Zhao, and H. Fan, “A PWM Plus Phase-Shift Control Bidirectional DC – DC Converter,” *IEEE Trans. POWER Electron.*, vol. 19, no. 3, pp. 666–675, 2004.

[50] H. Chiu and L. Lin, “A Bidirectional DC – DC Converter for Fuel Cell Electric Vehicle Driving System,” *950 IEEE Trans. POWER Electron.*, vol. 21, no. 4, pp. 950–958, 2006.

[51] L. Roggia, L. Schuch, E. Baggio, and C. Rech, “Integrated Full-Bridge-Forward DC – DC Converter for a Residential Microgrid Application,” *IEEE Trans. Power Electron.*, vol. 28, no. 4, pp. 1728–1740, 2013.

[52] K. Wang, C. Y. Lin, L. Zhu, D. Qu, F. C. Lee, and J. S. Lai, “Bi-directional DC to DC Converters for Fuel Cell Systems*,” in *Proc. Power Electron. Transp*, 1998, pp. 47–51.

[53] T. Hirose and H. Matsuo, “A Consideration of Bidirectional Superposed Dual Active Bridge DC-DC Converter,” *2nd Int. Symp. Power Electron. Distrib. Gener. Syst.*, pp. 39–46, 2010.

[54] B. Zhao, S. Member, Q. Yu, Z. Leng, and X. Chen, “Switched Z-Source Isolated Bidirectional DC – DC Converter and Its Phase-Shifting Shoot-Through Bivariate Coordinated Control Strategy,” *IEEE Trans. Ind. Electron.*, vol. 59, no. 12, pp. 4657–4670, 2012.

[55] L. Zhu, “A Novel Soft-Commutating Isolated Boost Full-Bridge ZVS-PWM DC – DC Converter for Bidirectional High Power Applications,” *IEEE Trans. POWER Electron.*, vol. 21, no. 2, pp. 422–429, 2006.

[56] B. Zhao, Q. Song, J. Li, W. Liu, G. Liu, and Y. Zhao, “High-Frequency-Link DC Transformer Based on Switched Capacitor for Medium-Voltage DC Power Distribution Application,” *IEEE Trans. Power Electron.*, vol. 31, no. 7, pp. 4766–4777, 2016.

[57] J. Riedel, D. G. Holmes, B. P. McGrath, and C. Teixeira, “Active Suppression of Selected DC Bus Harmonics for Dual Active Bridge DC-DC Converters,” *IEEE Trans. Power Electron.*, vol. 32, no. 11, pp. 8857–8867, 2017.

[58] S.-T. Lin, X. Li, C. Sun, and Y. Tang, “Fast transient control for power adjustment in a dual-active-bridge converter,” *Electron. Lett.*, vol. 53, no. 16, pp. 1130–1132, 2017.

[59] M. Yaqoob, K. H. Loo, and Y. M. Lai, “Extension of soft-switching region of dual-active-bridge converter by a tunable resonant tank,” *IEEE Trans. Power Electron.*, vol. 32, no. 12, pp. 9093–9104, 2017.

[60] X. Liu *et al.*, “Novel Dual-Phase-Shift Control With Bidirectional Inner Phase Shifts for a Dual-Active-Bridge Converter Having Low Surge Current and Stable Power Control,” *IEEE Trans. Power Electron.*, vol. 32, no. 5, pp. 4095–4106, 2017.

[61] W. R. Leon Garcia, P. Tixador, B. Raison, A. Bertinato, B. Luscan, and C. Creusot, “Technical and Economic Analysis of the R-Type SFCL for HVDC Grids Protection,” *IEEE Trans. Appl. Supercond.*, vol. 27, no. 7, 2017.

[62] A. Nisar and M. S. Thomas, “Comprehensive Control for Microgrid Autonomous Operation with Demand Response,” *IEEE Trans. Smart Grid*, vol. 8, no. 5, pp. 2081–2089, 2017.

[63] B. Zhao, Q. Song, J. Li, Q. Sun, and W. Liu, “Full-Process Operation, Control, and Experiments of Modular High-Frequency-Link DC Transformer Based on Dual Active Bridge for Flexible MVDC Distribution: A Practical Tutorial,” *IEEE Trans. Power Electron.*, vol. 32, no. 9, pp. 6751–6766, 2017.

[64] S. Inoue and H. Akagi, “A Bidirectional Isolated DC – DC Converter as a Core Circuit of the Next-Generation,” *IEEE Trans. POWER Electron.*, vol. 22, no. 2, pp. 535–542, 2007.

[65] R. Dhua, D. Chatterjee, and S. K. Goswami, “Study of Improved Load Sharing Methodologies for Distributed Generation Units Connected in a Microgrid,” vol. 3, no. 3, pp. 311–320, 2017.

[66] F. Xue, R. Yu, and A. Q. Huang, “A 98.3% Efficient GaN Isolated Bidirectional DC-DC Converter for DC Microgrid Energy Storage System Applications,” *IEEE Trans. Ind. Electron.*, vol. 64, no. 11, pp. 9094–9103, 2017.

[67] G. P. Adam, I. A. Gowaid, S. J. Finney, D. Holliday, and B. W. Williams, “Review of dc–dc converters for multi-terminal HVDC transmission networks,” *IET Power Electron.*, vol. 9, no. 2, pp. 281–296, 2016.

[68] Y. A. Harrye, A. A. Aboushady, and K. H. Ahmed, “Power Sharing Controller for Modular Dual Active Bridge DC/DC Converter in Medium Voltage DC Applications,” 2017, vol. 5, pp. 3–8.

[69] R. W. De Doncker, D. M. Divan, and M. H. Kheraluwala, “A three-phase soft-switched high density DC/DC Converter,” *IEEE Trans. Ind. Appl.*, vol. 27, no. 1, pp. 63–73, 1991.

[70] J. Biela, M. Schweizer, S. Waffler, and J. W. Kolar, “SiC versus Si — Evaluation of Potentials for Performance Improvement of Inverter and DC – DC Converter Systems by SiC Power Semiconductors,” *IEEE Trans. Ind. Electron.*, vol. 58, no. 7, pp. 2872–2882, 2011.

[71] M. Lee, C. Lin, S. Wang, and T. Chin, “Soft-Magnetic Fe-Based Nano-Crystalline Thick Ribbons,” *IEEE Trans. Magn.*, vol. 44, no. 11, pp. 3836–3838, 2008.

[72] B. Zhao, Q. Yu, and W. Sun, “Extended-phase-shift control of isolated bidirectional DC-DC converter for power distribution in microgrid,” *IEEE Trans. Power Electron.*, vol. 27, no. 11, pp. 4667–4680, 2012.

[73] J. Huang, Y. Wang, Z. Li, and W. Lei, “Unified Triple-Phase-Shift Control to Minimize Current Stress and Achieve Full Soft-Switching of Isolated Bidirectional DC-DC Converter,” *IEEE Trans. Ind. Electron.*, vol. 63, no. 7, pp. 4169–4179, 2016.

[74] A. Tong, L. Hang, G. Li, X. Jiang, and S. Gao, “Modeling and Analysis of a Dual-Active-Bridge-Isolated Bidirectional DC / DC Converter to Minimize RMS Current With Whole Operating Range,” *IEEE Trans. Power Electron.*, vol. 33, no. 6, pp. 5302–5316, 2018.

[75] H. Shi, H. Wen, Y. Hu, and L. Jiang, “Reactive Power Minimization in Bidirectional DC-DC Converters Using a Unified-Phasor-Based Particle Swarm Optimization,” *IEEE Trans. Power Electron.*, vol. 33, no. 12, pp. 10990–11006, 2018.

[76] D. Jovcic and L. Zhang, “LCL DC/DC converter for DC grids,” *IEEE Trans. Power Deliv.*, vol. 28, no. 4, pp. 2071–2079, 2013.

[77] H. Bai and C. Mi, “Eliminate reactive power and increase system efficiency of isolated bidirectional dual-active-bridge dc-dc converters using novel dual-phase-shift control,” *IEEE Trans. Power Electron.*, vol. 23, no. 6, pp. 2905–2914, 2008.

[78] K. Wu, C. W. De Silva, and W. G. Dunford, “Stability analysis of isolated bidirectional dual active full-bridge DC-DC converter with triple phase-shift control,” *IEEE Trans. Power Electron.*, vol. 27, no. 4, pp. 2007–2017, 2012.

[79] S. S. Muthuraj, V. K. Kanakesh, P. Das, and S. K. Panda, “Triple Phase Shift Control of an LLL Tank Based Bidirectional Dual Active Bridge Converter,” *IEEE Trans. Power Electron.*, vol. 32, no. 10, pp. 8035–8053, 2017.

[80] Y. A. Harrye, K. H. Ahmed, G. P. Adam, and A. A. Aboushady, “Comprehensive steady state analysis of bidirectional dual active bridge DC/DC converter using triple phase shift control,” *IEEE Int. Symp. Ind. Electron.*, pp. 437–442, 2014.

[81] L. Yuan, Z. Zhao, J. Sun, J. Nie, and Q. Gu, “Current Stress Minimization of Dual Active Bridge DC-DC Converter within the Whole Operating Range,” *IEEE J. Emerg. Sel. Top. Power Electron.*, vol. 7, no. 1, pp. 1–1, 2018.

[82] H. Wen and W. Xiao, “Bidirectional Dual-Active-Bridge DC-DC Converter with Triple-Phase-Shift Control,” *2013 Twenty-Eighth Annu. IEEE Appl. Power Electron. Conf. Expo.*, pp. 1972–1978, 2013.

[83] N. Hou, W. Song, and M. Wu, “Minimum-Current-Stress Scheme of Dual Active Bridge DC-DC Converter with Unified Phase-Shift Control,” *IEEE Trans. Power Electron.*, vol. 31, no. 12, pp.

8552–8561, 2016.

[84] H. Wen, “Determination of the Optimal Sub-mode for Bidirectional Dual-Active-Bridge DC-DC Converter with Multi-Phase-Shift Control,” *2013 IEEE ECCE Asia Downunder*, pp. 596–600.

[85] A. K. Jain, S. Member, R. Ayyanar, and S. Member, “PWM Control of Dual Active Bridge : Comprehensive Analysis and Experimental Verification,” *IEEE Trans. Power Electron.*, vol. 26, no. 4, pp. 1215–1227, 2011.

[86] H. Gu, D. Jiang, R. Yin, S. Huang, Y. Liang, and Y. Wang, “Power characteristics analysis of bidirectional full-bridge DC-DC converter with triple-phase-shift control,” *Proc. 2015 10th IEEE Conf. Ind. Electron. Appl. ICIEA 2015*, pp. 363–368, 2015.

[87] B. Zhao, Q. Song, W. Liu, and W. Sun, “Current-stress-optimized switching strategy of isolated bidirectional DC-DC converter with dual-phase-shift control,” *IEEE Trans. Ind. Electron.*, vol. 60, no. 10, pp. 4458–4467, 2013.

[88] B. Zhao, Q. Song, and W. Liu, “Efficiency characterization and optimization of isolated bidirectional DC-DC converter based on dual-phase-shift control for DC distribution application,” *IEEE Trans. Power Electron.*, vol. 28, no. 4, pp. 1711–1727, 2013.

[89] W. Choi, K. M. Rho, and B. H. Cho, “Fundamental Duty Modulation of Dual-Active-Bridge Converter for Wide-Range Operation,” *IEEE Trans. Power Electron.*, vol. 31, no. 6, pp. 4048–4064, 2016.

[90] B. Zhao, Q. Song, W. Liu, G. Liu, and Y. Zhao, “Universal High-Frequency-Link Characterization and Practical Fundamental-Optimal Strategy for Dual-Active-Bridge DC-DC Converter under PWM Plus Phase-Shift Control,” *IEEE Trans. Power Electron.*, vol. 30, no. 12, pp. 6488–6494, 2015.

[91] J. Ge, Z. Zhao, L. Yuan, and T. Lu, “Energy Feed-Forward and Direct Feed-Forward Control for Solid-State Transformer,” *IEEE Trans. Power Electron.*, vol. 30, no. 8, pp. 4042–4047, 2015.

[92] Z. Shan, J. Jatskevich, H. H. C. Iu, and T. Fernando, “Simplified load-feedforward control design for dual-active-bridge converters with current-mode modulation,” *IEEE J. Emerg. Sel. Top. Power Electron.*, vol. 6, no. 4, pp. 2073–2085, 2018.

[93] G. G. Oggier, M. Ordonez, J. M. Galvez, and F. Luchino, “Fast transient boundary control and steady-state operation of the dual active bridge converter using the natural switching surface,” *IEEE Trans. Power Electron.*, vol. 29, no. 2, pp. 946–957, 2014.

[94] W. Song, N. Hou, and M. Wu, “Virtual Direct Power Control Scheme of Dual Active Bridge DC-DC Converters for Fast Dynamic Response,” *IEEE Trans. Power Electron.*, vol. 33, no. 2, pp. 1750–1759, 2018.

[95] G. G. G. O. G. A. Oggier, “Switching Control Strategy to Minimize Dual Active Bridge Converter Losses,” *IEEE Trans. Power Electron.*, vol. 24, no. 7, pp. 1826–1838, 2009.

[96] H. Wen, W. Xiao, and B. Su, “Nonactive power loss minimization in a bidirectional isolated DC-DC converter for distributed power systems,” *IEEE Trans. Ind. Electron.*, vol. 61, no. 12, pp. 6822–6831, 2014.

[97] Y. A. Harrye, K. H. Ahmed, and A. A. Aboushady, “Reactive power minimization of dual active bridge DC/DC converter with triple phase shift control using neural network,” *3rd Int. Conf. Renew. Energy Res. Appl. ICRERA 2014*, pp. 566–571, 2014.

[98] H. Shi *et al.*, “Minimum-Reactive-Power Scheme of Dual-Active-Bridge DC – DC Converter With Three-Level Modulated Phase-Shift Control,” *IEEE Trans. Ind. Appl.*, vol. 53, no. 6, pp.

5573–5586, 2017.

[99] G. Xu, D. Sha, J. Zhang, and X. Liao, “Unified Boundary Trapezoidal Modulation Control Utilizing Fixed Duty Cycle Compensation and Magnetizing Current Design for Dual Active Bridge DC-DC Converter,” *IEEE Trans. Power Electron.*, vol. 32, no. 3, pp. 2243–2252, 2017.

[100] G. Ortiz, H. Uemura, D. Bortis, J. W. Kolar, and O. Apeldoorn, “Modeling of soft-switching losses of IGBTs in high-power high-efficiency dual-active-bridge DC/DC converters,” *IEEE Trans. Electron Devices*, vol. 60, no. 2, pp. 587–597, 2013.

[101] F. Krismer and J. W. Kolar, “Efficiency-optimized high-current dual active bridge converter for automotive applications,” *IEEE Trans. Ind. Electron.*, vol. 59, no. 7, pp. 2745–2760, 2012.

[102] J. Everts, F. Krismer, J. Van Den Keybus, J. Driesen, and J. W. Kolar, “Optimal zvs modulation of single-phase single-stage bidirectional dab ac-dc converters,” *IEEE Trans. Power Electron.*, vol. 29, no. 8, pp. 3954–3970, 2014.

[103] C. Zhao, S. D. Round, and J. W. Kolar, “An isolated three-port bidirectional dc-dc converter with decoupled power flow management,” *IEEE Trans. Power Electron.*, vol. 23, no. 5, pp. 2443–2453, 2008.

[104] V. N. S. R. Jakka and A. Shukla, “A triple port active bridge converter based multi-fed power electronic transformer,” *ECCE 2016 - IEEE Energy Convers. Congr. Expo. Proc.*, vol. 1, pp. 1–8, 2016.

[105] G. Wang *et al.*, “Design and hardware implementation of Gen-1 silicon based solid state transformer,” *Conf. Proc. - IEEE Appl. Power Electron. Conf. Expo. - APEC*, pp. 1344–1349, 2011.

[106] M. Phattanasak, R. Gavagsaz-Ghoachani, J. P. Martin, S. Pierfederici, and B. Davat, “Flatness based control of an isolated three-port bidirectional DC-DC converter for a fuel cell hybrid source,” *IEEE Energy Convers. Congr. Expo. Energy Convers. Innov. a Clean Energy Futur. ECCE 2011, Proc.*, vol. 10, no. 1, pp. 977–984, 2011.

[107] Z. Wang and H. Li, “An integrated three-port bidirectional DC-DC converter for PV application on a DC distribution system,” *IEEE Trans. Power Electron.*, vol. 28, no. 10, pp. 4612–4624, 2013.

[108] H. Tao, A. Kotsopoulos, J. L. Duarte, and M. A. M. Hendrix, “Triple-Half-Bridge Bidirectional Converter Controlled by Phase Shift and PWM,” *Triple-Half-Bridge Bidirectional Convert. Control. by Phase Shift PWM*, pp. 1256–1262, 2006.

[109] H. Tao, A. Kotsopoulos, J. L. Duarte, and M. A. M. Hendrix, “Family of multiport bidirectional DC–DC converters,” *IEE Proc-Electro. Power Appl.*, vol. 153, pp. 978–982, 2006.

[110] B. J. D. Vermulst, J. L. Duarte, E. A. Lomonova, and K. G. E. Wijnands, “Scalable multi-port active-bridge converters: modelling and optimised control,” *IET Power Electron.*, vol. 10, no. 1, pp. 80–91, 2017.

[111] S. Nakagawa, J. Arai, R. Kasashima, K. Nishimoto, Y. Kado, and K. Wada, “Dynamic performance of triple-active bridge converter rated at 400 V, 10 kW, and 20 kHz,” *2017 IEEE 3rd Int. Futur. Energy Electron. Conf. ECCE Asia, IFEEC - ECCE Asia 2017*, pp. 1090–1094, 2017.

[112] K. Nishimoto, Y. Kado, R. Kasashima, S. Nakagawa, and K. Wada, “Decoupling power flow control system in triple active bridge converter rated at 400 V, 10 kW, and 20 kHz,” *2017 IEEE 8th Int. Symp. Power Electron. Distrib. Gener. Syst. PEDG 2017*, pp. 1–6, 2017.

[113] H. Tao, A. Kotsopoulos, J. L. Duarte, and M. A. M. Hendrix, “A soft-switched three-port

bidirectional converter for fuel cell and supercapacitor applications," *PESC Rec. - IEEE Annu. Power Electron. Spec. Conf.*, vol. 2005, no. 1, pp. 2487–2493, 2005.

[114] H. Tao, A. Kotsopoulos, J. L. Duarte, and M. A. M. Hendrix, "Transformer-Coupled Multiport ZVS Bidirectional DC--DC Converter With Wide Input Range," *IEEE Trans. Power Electron.*, vol. 23, no. 2, pp. 771–781, 2008.

[115] Z. Gao and F. Jiang, "Isolated multi-port DC-DC converter based on a high frequency transformer," *2015 18th Int. Conf. Electr. Mach. Syst. ICEMS 2015*, pp. 564–568, 2016.

[116] M. Qiang, X. Zhen-lin, and W. Wei-Yang, "A novel multi-port DC-DC converter for hybrid renewable energy distributed generation systems connected to power grid," *Proc. IEEE Int. Conf. Ind. Technol.*, pp. 1–5, 2008.

[117] O. M. Hebala, A. A. Aboushady, K. H. Ahmed, and I. Abdelsalam, "Generic Closed-Loop Controller for Power Regulation in Dual Active Bridge DC-DC Converter With Current Stress Minimization," *IEEE Trans. Ind. Electron.*, vol. 66, no. 6, pp. 4468–4478, 2019.

[118] B. J. D. Vermulst, J. L. Duarte, C. G. E. Wijnands, and E. A. Lomonova, "Single-stage three-phase AC to DC conversion with isolation and Bi-directional power flow," *IECON Proc. (Industrial Electron. Conf.*, pp. 4378–4383, 2014.

[119] V. N. S. R. Jakka, A. Shukla, and G. D. Demetriades, "Dual-Transformer-Based Asymmetrical Triple-Port Active Bridge (DT-ATAB) Isolated DC-DC Converter," *IEEE Trans. Ind. Electron.*, vol. 64, no. 6, pp. 4549–4560, 2017.

[120] Y. A. Harrye, "Modular Dual Active Bridge DC-DC Converter for HVDC Applications," 2017.

[121] F. Krismer, "Modeling and optimization of bidirectional dual active bridge DC-DC converter topologies," ETH Zurich, 2010.

[122] M. Kotti *et al.*, "Comparison between PSO and ACO techniques for analog circuit performance optimization," *Proc. Int. Conf. Microelectron. ICM*, no. i, pp. 1–6, 2011.

[123] Y. Chaturvedi, S. Kumar, P. Bansal, and S. Yadav, "Comparison among APSO, PSO GA for performance investigation of SEIG with balanced loading," *Proc. 9th Int. Conf. Cloud Comput. Data Sci. Eng. Conflu. 2019*, pp. 459–463, 2019.

[124] S. Debnath and R. N. Ray, "Harmonic elimination in multilevel inverter using GA and PSO: A comparison," *2012 IEEE Students' Conf. Electr. Electron. Comput. Sci. Innov. Humanit. SCEECS 2012*, no. 2, pp. 1–5, 2012.

[125] J. Kennedy and R. Eberhart, "Particle swarm optimization," *IEEE Int. Conf. Neural Networks*, pp. 1942–1948, 1995.

[126] N. Femia, G. Petrone, G. Spagnuolo, and M. Vitelli, "Optimization of perturb and observe maximum power point tracking method," *IEEE Trans. Power Electron.*, vol. 20, no. 4, pp. 963–973, 2005.

[127] M. A. Elgendy, B. Zahawi, and D. J. Atkinson, "Assessment of perturb and observe MPPT algorithm implementation techniques for PV pumping applications," *IEEE Trans. Sustain. Energy*, vol. 3, no. 1, pp. 21–33, 2012.

[128] N. Femia, G. Lisi, G. Petrone, G. Spagnuolo, and M. Vitelli, "Distributed Maximum Power Point Tracking of Photovoltaic Arrays : Novel Approach and System Analysis," vol. 55, no. 7, pp. 2610–2621, 2008.

[129] M. Fortunato, A. Giustiniani, G. Petrone, G. Spagnuolo, and M. Vitelli, "Maximum Power Point

Tracking in a Photovoltaic Inverter," *IEEE Trans. Ind. Electron.*, vol. 55, no. 7, pp. 2684–2693, 2008.

[130] H. P. V Agarwal, "Investigations into the performance of photovoltaics-based active filter configurations and their control schemes under uniform and non-uniform radiation conditions," vol. 4, no. September 2008, pp. 12–22, 2010.

[131] S. Park, G. Cha, Y. Jung, C. Won, and S. Member, "Design and Application for PV Generation System Using a Soft-Switching Boost Converter With SARC," *IEEE Trans. Ind. Electron.*, vol. 57, no. 2, pp. 515–522, 2010.

[132] A. K. Abdelsalam, A. M. Massoud, S. Ahmed, and P. N. Enjeti, "High-performance adaptive Perturb and observe MPPT technique for photovoltaic-based microgrids," *IEEE Trans. Power Electron.*, vol. 26, no. 4, pp. 1010–1021, 2011.

[133] D. Jovcic, "Bidirectional , High-Power DC Transformer," *IEEE Trans. POWER Deliv.*, vol. 24, no. 4, pp. 2276–2283, 2009.

[134] B. Zhao, Q. Song, W. Liu, and Y. Sun, "Dead-Time Effect of the High-Frequency Isolated Bidirectional Full-Bridge DC – DC Converter : Comprehensive Theoretical Analysis and," *IEEE Trans. Power Electron.*, vol. 29, no. 4, pp. 1667–1680, 2014.

[135] Y. Xie, S. Member, J. Sun, and J. S. Freudenberg, "Power Flow Characterization of a Bidirectional Galvanically Isolated High-Power DC / DC Converter Over a Wide Operating Range," vol. 25, no. 1, pp. 54–66, 2010.

[136] B. Zhao, Q. Song, J. Li, and W. Liu, "A Modular Multilevel DC-Link Front-to-Front DC Solid-State Transformer Based on High-Frequency Dual Active Phase Shift for HVDC Grid Integration," *IEEE Trans. Ind. Electron.*, vol. 64, no. 11, pp. 8919–8927, 2017.

[137] Y. Wang, Q. Song, Q. Sun, B. Zhao, J. Li, and A. B. Modulation, "Multilevel MVDC Link Strategy of High-Frequency-Link DC Transformer Based on Switched Capacitor for MVDC Power Distribution," *IEEE Trans. Ind. Electron.*, vol. 64, no. 4, pp. 2829–2835, 2017.

Appendix A Analysis of Non-isolated AC Link Topologies

This appendix provides the mathematical analysis for non-isolated AC link topologies (topologies 2 to 6) in MAB outlined in Table 3.4. This includes derivation of active power and RMS current at the AC side of every port for the investigated topologies.

A.1. Analysis of MAB AC link Topology 2

In order to simplify the analysis for this topology, the upper delta connection is transformed to equivalent star connection. In this case, topology 2 becomes as shown in Fig.A.1.

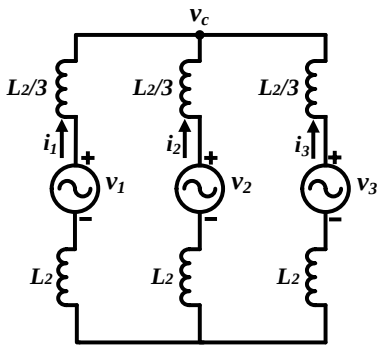

Fig. A.1: Topology 2 with upper delta transformed to star equivalent.

Accordingly, per unit AC-side instantaneous current at each port can be derived based on:

$$i_i(t) = \frac{v_i(t) - v_c(t)}{j2\pi f(L_2 + \frac{L_2}{3})/Z_{base}} \tag{A.1}$$

Such that:

- v_c is per unit common node voltage as depicted in Fig. A.1.
- $L_2$is interface inductor of topology 2.
- $v_i(t)$ is per unit AC-side bridge voltage defined by (4.1) and (4.2).

On this basis, AC-side instantaneous currents are derived and represented in rectangular form as outlined by (A.2)-(A.4)

$$\bar{I}_1 = -j\frac{3L_{base}}{\pi L_2}(V_{1\,RMS} - \bar{V}_c) \tag{A.2}$$

$$\bar{I}_2 = -j\frac{3L_{base}}{\pi L_2}(V_{2\,RMS}\cos(\delta_2) - jV_{2\,RMS}\sin(\delta_2) - \bar{V}_c) \tag{A.3}$$

$$\bar{I}_3 = -j\frac{3L_{base}}{\pi L_2}(V_{3\,RMS}\cos(\delta_3) - jV_{3\,RMS}\sin(\delta_3) - \bar{V}_c) \tag{A.4}$$

Since $\bar{I}_1 + \bar{I}_2 + \bar{I}_3 = 0$, then

$$\bar{V}_c = \frac{1}{3}[(V_{1\,RMS} + V_{2\,RMS}\cos(\delta_2) + V_{3\,RMS}\cos(\delta_3)) - j(V_{2\,RMS}\sin(\delta_2) + V_{3\,RMS}\sin(\delta_3))] \tag{A.5}$$

Substituting (A.5) into (A.2)-(A.4) yields:

$$\bar{I}_1 = \frac{L_{base}}{\pi L_2}[(V_{2\,RMS}\sin(\delta_2) + V_{3\,RMS}\sin(\delta_3)) - j(2V_{1\,RMS} - V_{2\,RMS}\cos(\delta_2) - V_{3\,RMS}\cos(\delta_3))] \tag{A.6}$$

$$\bar{I}_2 = \frac{L_{base}}{\pi L_2}[(-2V_{2\,RMS}\sin(\delta_2) + V_{3\,RMS}\sin(\delta_3)) + j(V_{1\,RMS} - 2V_{2\,RMS}\cos(\delta_2) + V_{3\,RMS}\cos(\delta_3))] \tag{A.7}$$

$$\bar{I}_3 = \frac{L_{base}}{\pi L_2}[(V_{2\,RMS}\sin(\delta_2) - 2V_{3\,RMS}\sin(\delta_3)) + j(V_{1\,RMS} + V_{2\,RMS}\cos(\delta_2) - 2V_{3\,RMS}\cos(\delta_3))] \tag{A.8}$$

Thus, the AC-side RMS currents are:

$$|I_1|_{RMS} = \frac{L_{base}}{\pi L_2}\sqrt{(V_{2\,RMS}\sin(\delta_2) + V_{3\,RMS}\sin(\delta_3))^2 + (2V_{1\,RMS} - V_{2\,RMS}\cos(\delta_2) - V_{3\,RMS}\cos(\delta_3))^2} \tag{A.9}$$

$$|I_2|_{RMS} = \frac{L_{base}}{\pi L_2}\sqrt{(-2V_{2\,RMS}\sin(\delta_2) + V_{3\,RMS}\sin(\delta_3))^2 + (V_{1\,RMS} - 2V_{2\,RMS}\cos(\delta_2) + V_{3\,RMS}\cos(\delta_3))^2} \tag{A.10}$$

$$|I_3|_{RMS} = \frac{L_{base}}{\pi L_2}\sqrt{(V_{2\,RMS}\sin(\delta_2) - 2V_{3\,RMS}\sin(\delta_3))^2 + (V_{1\,RMS} + V_{2\,RMS}\cos(\delta_2) - 2V_{3\,RMS}\cos(\delta_3))^2} \tag{A.11}$$

Afterwards, the normalised active and reactive power expressions as function of modulation parameters (D_1, D_2, D_3, D_{12}, D_{13}), AC link inductor (L_2) and base inductance (L_{base}) can be obtained by substituting in (4.5) and (4.6). Thus:

$$
\begin{aligned}
P_1 &= \frac{L_{base}}{\pi L_2}\, V_{1\,RMS}\,(\,V_{2\,RMS}\,\sin(\delta_2) + \,V_{3\,RMS}\,\sin(\delta_3)\,)\\
Q_1 &= \frac{L_{base}}{\pi L_2}\, V_{1\,RMS}\,(\,2V_{1\,RMS} - V_{2\,RMS}\,\cos(\delta_2) - V_{3\,RMS}\,\cos(\delta_3)\,)\\
P_2 &= \frac{L_{base}}{\pi L_2}\, V_{2\,RMS}\,(cos(\delta_2)[-2V_{2\,RMS}\,\sin(\delta_2) + \,V_{3\,RMS}\,\sin(\delta_3)\,]\\
&\quad - sin(\delta_2)[\,V_{1\,RMS}\, - 2V_{2\,RMS}\,\cos(\delta_2) + V_{3\,RMS}\cos(\delta_3)])\\
Q_2 &= -\frac{L_{base}}{\pi L_2}\, V_{2\,RMS}\,(sin(\delta_2)[-2V_{2\,RMS}\,\sin(\delta_2) + V_{3\,RMS}\,\sin(\delta_3)\,]\\
&\quad + cos(\delta_2)[\,V_{1\,RMS}\, - 2V_{2\,RMS}\,\cos(\delta_2) + V_{3\,RMS}\cos(\delta_3)])\\
P_3 &= \frac{L_{base}}{\pi L_2}\, V_{3\,RMS}\,(cos(\delta_3)[V_{2\,RMS}\,\sin(\delta_2) - 2V_{3\,RMS}\,\sin(\delta_3)\,]\\
&\quad - sin(\delta_3)[\,V_{1\,RMS}\, + V_{2\,RMS}\,\cos(\delta_2) - 2\,V_{3\,RMS}\cos(\delta_3)])\\
Q_3 &= -\frac{L_{base}}{\pi L_2}\, V_{3\,RMS}\,(sin(\delta_3)[V_{2\,RMS}\,\sin(\delta_2) - 2V_{3\,RMS}\,\sin(\delta_3)]\\
&\quad + cos(\delta_3)[\,V_{1\,RMS}\, + V_{2\,RMS}\,\cos(\delta_2) - 2\,V_{3\,RMS}\cos(\delta_3)])
\end{aligned}
\qquad \text{(A.12)}
$$

A.2. Analysis of MAB AC link Topology 3

The concept of superposition is used to analyse the AC-side currents of topology3. In this case, AC-side currents within this topology is analysed as illustrated by Fig A.2 – Fig A.4.

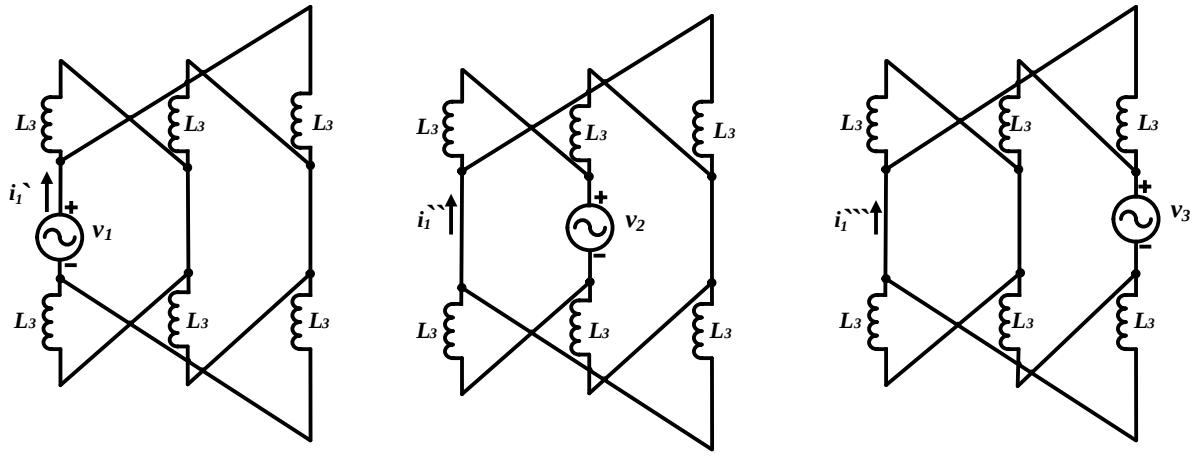

Fig. A.2:Topology 3 when applying superposition to analyse $i_1(t)$.

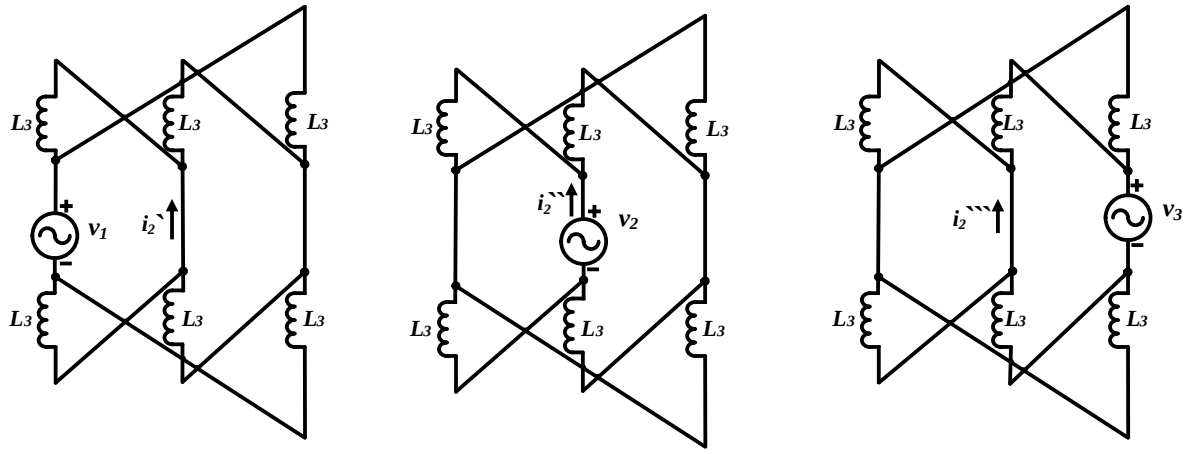

Fig. A.3: Topology 3 when applying superposition to analyse $i_2(t)$.

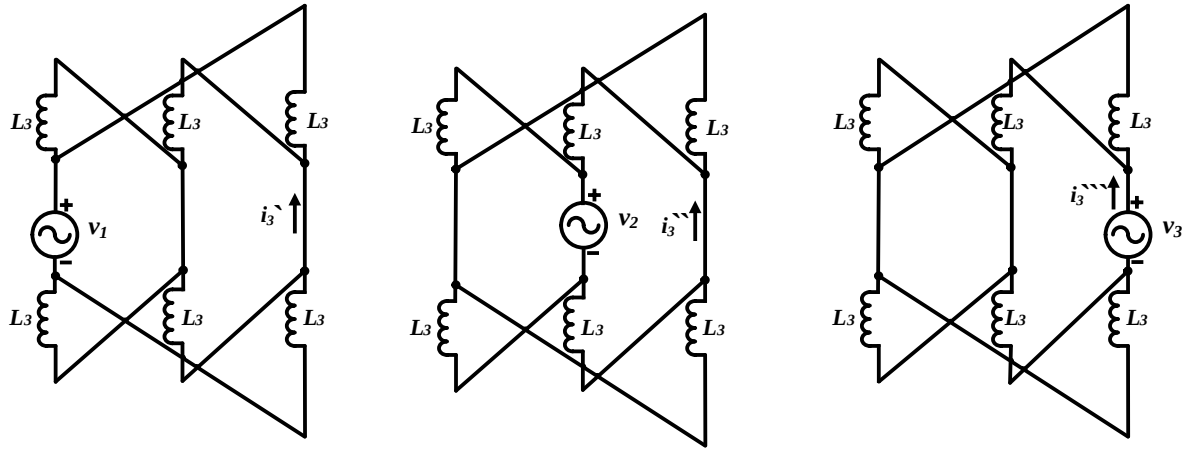

Fig. A.4: Topology 3 when applying superposition to analyse $i_3(t)$.

From Fig A.2:

$$\bar{I}_1' = \frac{\bar{V}_1}{jwL_3} \quad ,\bar{I}_1'' = -\frac{\bar{V}_2}{j2wL_3} \quad \text{and} \quad \bar{I}_1''' = -\frac{\bar{V}_3}{j2wL_3}$$

Since $\bar{I}_1' = \bar{I}_1' + \bar{I}_1'' + \bar{I}_1'''$, then per unit AC-side current of port one is as follows:

$$\bar{I}_1 = \frac{2L_{base}}{\pi L_3}[(V_{2\,RMS}\,\sin(\delta_2) + V_{3\,RMS}\,\sin(\delta_3)) - j(2V_{1\,RMS} - V_{2\,RMS}\,\cos(\delta_2) - V_{3\,RMS}\,\cos(\delta_3))]$$

(A.13)

From Fig A.3:

$$\bar{I}_2' = -\frac{\bar{V}_1}{j2wL_3} \qquad \bar{I}_2'' = \frac{\bar{V}_2}{jwL_3} \qquad \bar{I}_2''' = -\frac{\bar{V}_3}{j2wL_3}$$

Since $\bar{I}_2' = \bar{I}_2' + \bar{I}_2'' + \bar{I}_2'''$, then per unit AC-side current of port two is as follows:

$$\bar{I}_2 = \frac{2L_{base}}{\pi L_3}[(-2V_{2\,RMS}\,\sin(\delta_2) + V_{3\,RMS}\,\sin(\delta_3)) - j(V_{1\,RMS} - 2V_{2\,RMS}\,\cos(\delta_2) + V_{3\,RMS}\,\cos(\delta_3))]$$

(A.14)

From Fig A.4:

$$\bar{I_3}' = -\frac{\bar{V_1}}{j2wL_3} \quad ,\bar{I_3}'' = -\frac{\bar{V_2}}{j2wL_3} \quad \text{and} \quad \bar{I_3}''' = \frac{\bar{V_3}}{jwL_3}$$

Since $\bar{I_3}' = \bar{I_3}' + \bar{I_3}'' + \bar{I_3}'''$, then per unit AC-side current of port three is as follows:

$$\bar{I_3} = \frac{2L_{base}}{\pi L_3}[(V_{2\,RMS}\,\sin(\delta_2) - 2V_{3\,RMS}\,\sin(\delta_3)) - j(V_{1\,RMS} + V_{2\,RMS}\,\cos(\delta_2) - 2V_{3\,RMS}\,\cos(\delta_3))] \tag{A.15}$$

Thus, the AC-side RMS currents are:

$$|I_1|_{RMS} = \frac{2L_{base}}{\pi L_3}\sqrt{[V_{2\,RMS}\,\sin(\delta_2) + V_{3\,RMS}\,\sin(\delta_3)]^2 + ([2V_{1\,RMS} - V_{2\,RMS}\,\cos(\delta_2) - V_{3\,RMS}\,\cos(\delta_3)]^2)} \tag{A.16}$$

$$|I_2|_{RMS} = \frac{2L_{base}}{\pi L_3}\sqrt{[-2V_{2\,RMS}\,\sin(\delta_2) + V_{3\,RMS}\,\sin(\delta_3)]^2 + ([V_{1\,RMS} - 2V_{2\,RMS}\,\cos(\delta_2) + V_{3\,RMS}\,\cos(\delta_3)]^2)} \tag{A.17}$$

$$|I_3|_{RMS} = \frac{2L_{base}}{\pi L_3}\sqrt{[V_{2\,RMS}\,\sin(\delta_2) - 2V_{3\,RMS}\,\sin(\delta_3)]^2 + ([V_{1\,RMS} + V_{2\,RMS}\,\cos(\delta_2) - 2V_{3\,RMS}\,\cos(\delta_3)]^2)} \tag{A.18}$$

Afterwards, the normalised active and reactive power expressions can be obtained by substituting in (4.5) and (4.6). Thus:

$$\begin{aligned}
P_1 &= \frac{2L_{base}}{\pi L_3}\,V_{1\,RMS}\,(V_{2\,RMS}\,\sin(\delta_2) + V_{3\,RMS}\,\sin(\delta_3)) \\
P_2 &= \frac{2L_{base}}{\pi L_3}\,V_{2\,RMS}\,(cos(\delta_2)\,[-2V_{2\,RMS}\,\sin(\delta_2) + V_{3\,RMS}\,\sin(\delta_3)] \\
&\quad - sin(\delta_2)[\,V_{1\,RMS} - 2V_{2\,rms}\,\cos(\delta_2) + V_{3\,RMS}\cos(\delta_3)]) \\
P_3 &= \frac{2L_{base}}{\pi L_3}\,V_{3\,RMS}\,(cos(\delta_3)\,[V_{2\,RMS}\,\sin(\delta_2) - 2V_{3\,RMS}\,\sin(\delta_3)] \\
&\quad - sin(\delta_3)[\,V_{1\,RMS} + V_{2\,RMS}\,\cos(\delta_2) - 2\,V_{3\,RMS}\cos(\delta_3)]) \\
Q_1 &= \frac{2L_{base}}{\pi L_3}\,V_{1\,RMS}\,(\,2V_{1\,RMS} - V_{2\,RMS}\,\cos(\delta_2) - V_{3\,RMS}\cos(\delta_3)) \\
Q_2 &= -\frac{2L_{base}}{\pi L_3}\,V_{2\,RMS}\,(sin(\delta_2)\,[-2V_{2\,RMS}\,\sin(\delta_2) + V_{3\,RMS}\,\sin(\delta_3)] \\
&\quad + cos(\delta_2)[\,V_{1\,RMS} - 2V_{2\,rms}\,\cos(\delta_2) + V_{3\,RMS}\cos(\delta_3)]) \\
Q_3 &= -\frac{2L_{base}}{\pi L_3}\,V_{3\,RMS}\,(sin(\delta_3)\,[V_{2\,RMS}\,\sin(\delta_2) - 2V_{3\,RMS}\,\sin(\delta_3)] \\
&\quad + cos(\delta_3)[\,V_{1\,RMS} + V_{2\,rms}\,\cos(\delta_2) - 2\,V_{3\,RMS}\cos(\delta_3)])
\end{aligned} \tag{A.19}$$

A.3. Analysis of MAB AC link Topology 4

Since topology 4 is basically a series connection, then

$$\overline{I_1} = \overline{I_2} = \overline{I_3} = \overline{I} = \frac{\overline{V_1} - \overline{V_2} - \overline{V_3}}{j(3wL_4)}$$

Thus, per unit AC-side current is as follows:

$$\bar{I} = \frac{2L_{base}}{3\pi L_4}([V_{2\,RMS}\ \sin(\delta_2) + V_{3\,RMS}\ \sin(\delta_3)] - j[V_{1\,RMS} - V_{2\,RMS}\ \cos(\delta_2) - V_{3\,RMS}\ \cos(\delta_3)]) \qquad \text{(A.20)}$$

A.4. Analysis of MAB AC link Topology 5

The concept of superposition is used to analyse the AC-side currents of topology6. In this case, AC-side currents within this topology is analysed as illustrated by Fig A.5 – Fig A.7.

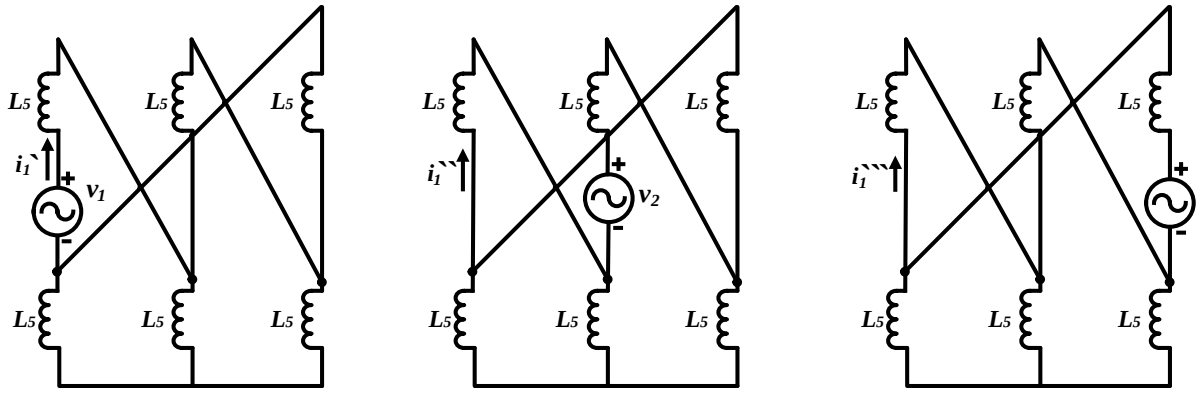

Fig. A.5: Topology 5 when applying superposition to analyse $i_1(t)$.

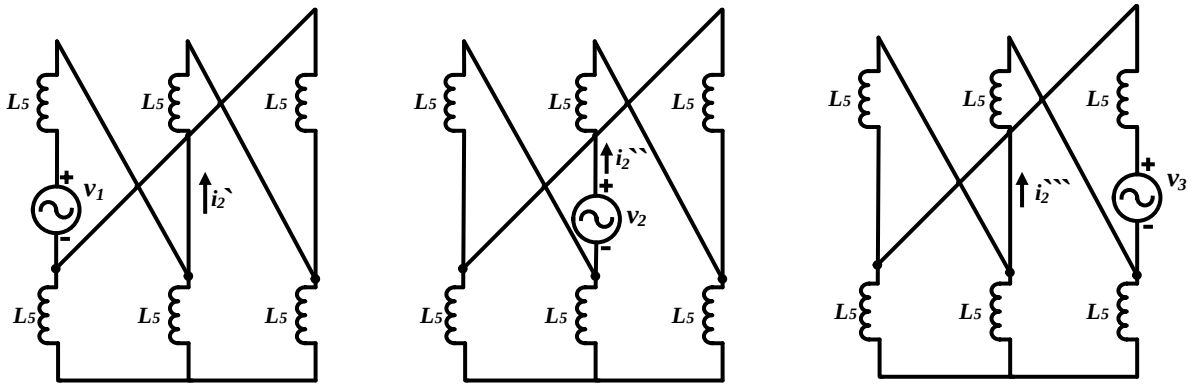

Fig. A.6: Topology 5 when applying superposition to analyse $i_2(t)$.

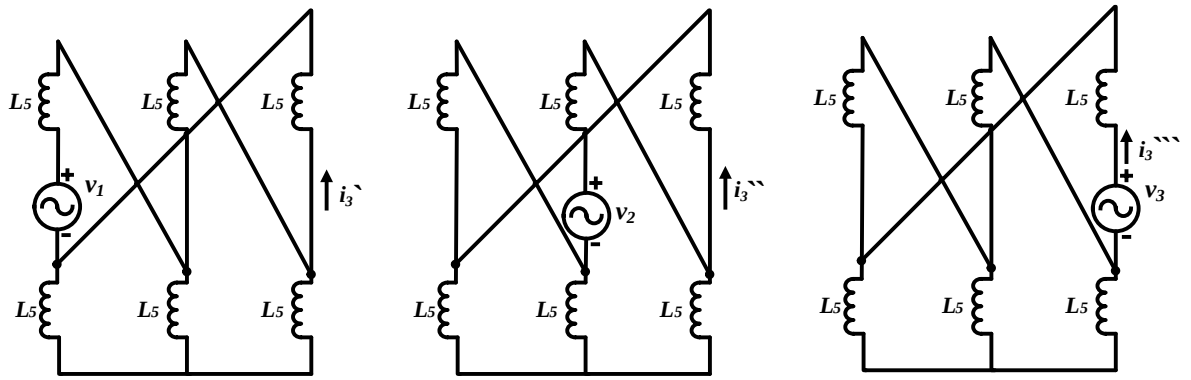

Fig. A.7: Topology 5 when applying superposition to analyse $i_3(t)$.

From Fig A.5:

$$\bar{I}_1' = \frac{\bar{V}_1}{j2wL_5} \quad , \bar{I}_1'' = \frac{\bar{V}_2}{j4wL_5} \quad \text{and} \quad \bar{I}_1''' = \frac{\bar{V}_3}{j4wL_5}$$

Since $\bar{I}_1' = \bar{I}_1' + \bar{I}_1'' + \bar{I}_1'''$, then per unit AC-side current of port one is as follows:

$$\bar{I}_1 = \frac{L_{base}}{\pi L_5}[-(V_{2\,RMS}\,\sin(\delta_2) + V_{3\,RMS}\,\sin(\delta_3)) - j(2V_{1\,RMS} + V_{2\,RMS}\,\cos(\delta_2) + V_{3\,RMS}\,\cos(\delta_3))]$$

(A.21)

From Fig A.6:

$$\bar{I}_2' = \frac{\bar{V}_1}{j4wL_5} \quad , \bar{I}_2'' = \frac{\bar{V}_2}{j2wL_5} \quad \text{and} \quad \bar{I}_2''' = \frac{\bar{V}_3}{j4wL_5}$$

Since $\bar{I}_2' = \bar{I}_2' + \bar{I}_2'' + \bar{I}_2'''$, then per unit AC-side current of port two is as follows:

$$\bar{I}_2 = \frac{L_{base}}{\pi L_5}[-(2V_{2\,RMS}\,\sin(\delta_2) + V_{3\,RMS}\,\sin(\delta_3)) - j(V_{1\,RMS} + 2V_{2\,RMS}\,\cos(\delta_2) + V_{3\,RMS}\,\cos(\delta_3))]$$

(A.22)

From Fig A.7:

$$\bar{I}_3' = \frac{\bar{V}_1}{j4wL_5} \quad , \bar{I}_3'' = \frac{\bar{V}_2}{j4wL_5} \quad \text{and} \quad \bar{I}_3''' = \frac{\bar{V}_3}{j2wL_5}$$

Since $\bar{I}_3' = \bar{I}_3' + \bar{I}_3'' + \bar{I}_3'''$, then per unit AC-side current of port three is as follows:

$$\bar{I}_3 = \frac{L_{base}}{\pi L_5}[-(V_{2\,RMS}\,\sin(\delta_2) + 2V_{3\,RMS}\,\sin(\delta_3)) - j(V_{1\,RMS} + V_{2\,RMS}\,\cos(\delta_2) + 2V_{3\,RMS}\,\cos(\delta_3))]$$

(A.23)

Thus, the AC-side RMS currents are:

$$|I_1|_{RMS} = \frac{L_{base}}{\pi L_5}\sqrt{[V_{2\,RMS}\,\sin(\delta_2) + V_{3\,RMS}\,\sin(\delta_3)]^2 + [2V_{1\,RMS} + V_{2\,RMS}\,\cos(\delta_2) + V_{3\,RMS}\,\cos(\delta_3)]^2} \tag{A.24}$$

$$|I_2|_{RMS} = \frac{L_{base}}{\pi L_5}\sqrt{[2V_{2\,RMS}\,\sin(\delta_2) + V_{3\,RMS}\,\sin(\delta_3)]^2 + [V_{1\,RMS} + 2V_{2\,RMS}\,\cos(\delta_2) + V_{3\,RMS}\,\cos(\delta_3)]^2} \tag{A.25}$$

$$|I_3|_{RMS} = \frac{L_{base}}{\pi L_5}\sqrt{[V_{2\,RMS}\,\sin(\delta_2) + 2V_{3\,RMS}\,\sin(\delta_3)]^2 + [V_{1\,RMS} + V_{2\,RMS}\,\cos(\delta_2) + 2V_{3\,RMS}\,\cos(\delta_3)]^2} \tag{A.26}$$

Afterwards, the normalised active and reactive power expressions can be obtained by substituting in (4.5) and (4.6). Thus:

$$\begin{aligned}
P_1 &= \frac{L_{base}}{\pi L_5}\,V_{1\,RMS}\,(-V_{2\,RMS}\,\sin(\delta_2) - V_{3\,RMS}\,\sin(\delta_3)) \\
P_2 &= \frac{L_{base}}{\pi L_5}\,V_{2\,RMS}\,(cos(\delta_2)\,[-4V_{2\,RMS}\,\sin(\delta_2) - 2\,V_{3\,RMS}\,\sin(\delta_3)] \\
&\quad + sin(\delta_2)[\,2V_{1\,RMS} + 4V_{2\,rms}\,\cos(\delta_2) + 2\,V_{3\,RMS}\cos(\delta_3)]) \\
P_3 &= \frac{L_{base}}{\pi L_5}\,V_{3\,RMS}\,(cos(\delta_3)\,[-2V_{2\,RMS}\,\sin(\delta_2) - 4\,V_{3\,RMS}\,\sin(\delta_3)] \\
&\quad + sin(\delta_3)[\,2V_{1\,RMS} + 2V_{2\,RMS}\,\cos(\delta_2) + 4\,V_{3\,RMS}\cos(\delta_3)]) \\
Q_1 &= \frac{L_{base}}{\pi L_5}\,V_{1\,RMS}\,(\,2V_{1\,RMS} + V_{2\,RMS}\,\cos(\delta_2) + V_{3\,RMS}\cos(\delta_3)) \\
Q_2 &= -\frac{L_{base}}{\pi L_5}\,V_{2\,RMS}\,(sin(\delta_2)\,[-4V_{2\,RMS}\,\sin(\delta_2) - 2\,V_{3\,RMS}\,\sin(\delta_3)] \\
&\quad - cos(\delta_2)[\,2V_{1\,RMS} + 4V_{2\,rms}\,\cos(\delta_2) + 2\,V_{3\,RMS}\cos(\delta_3)]) \\
Q_3 &= -\frac{L_{base}}{\pi L_5}\,V_{3\,RMS}\,(sin(\delta_3)\,[-2V_{2\,RMS}\,\sin(\delta_2) - 4V_{3\,RMS}\,\sin(\delta_3)] \\
&\quad - cos(\delta_3)[\,2V_{1\,RMS} + 2V_{2\,rms}\,\cos(\delta_2) + 4\,V_{3\,RMS}\cos(\delta_3)])
\end{aligned} \tag{A.27}$$

A.5. Analysis of MAB AC link Topology 6

The concept of superposition is used to analyse the AC-side currents of topology6. In this case, AC-side currents within this topology is analysed as illustrated by Fig A.8 – Fig A.10.

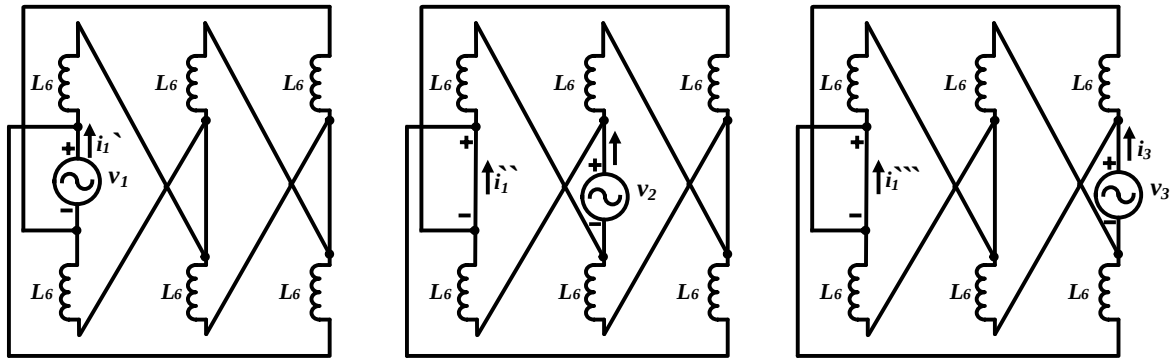

Fig. A.8: Topology 6 when applying superposition to analyse $i_1(t)$.

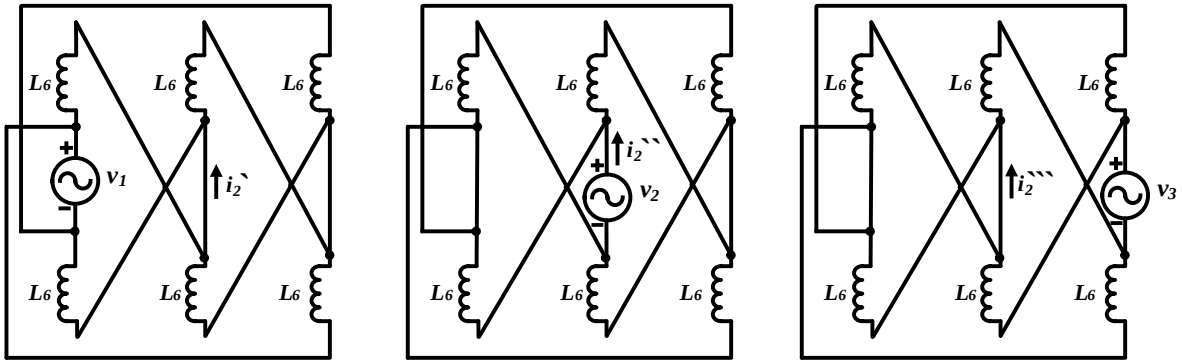

Fig. A.9: Topology 6 when applying superposition to analyse $i_2(t)$.

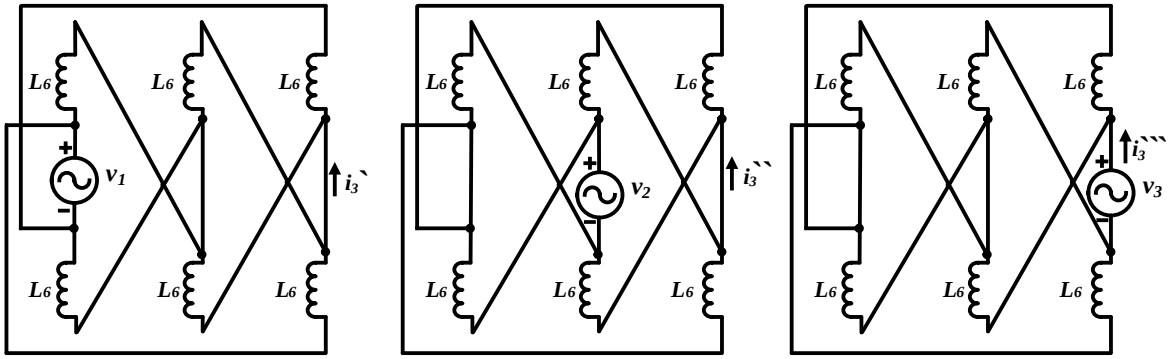

Fig. A.10: Topology 6 when applying superposition to analyse $i_3(t)$.

From Fig A.8:

$$\bar{I}_1' = \frac{\bar{V}_1}{jwL_6} \quad ,\bar{I}_1'' = \frac{\bar{V}_2}{jw(2L_6)} \quad \text{and} \quad \bar{I}_1''' = \frac{\bar{V}_3}{jw(2L_6)}$$

Since $\bar{I}_1' = \bar{I}_1' + \bar{I}_1'' + \bar{I}_1'''$, then per unit AC-side current of port one is as follows:

$$\bar{I}_1 = \frac{2L_{base}}{\pi L_6}[-(V_{2\,RMS}\,\sin(\delta_2) + V_{3\,RMS}\,\sin(\delta_3)) - j(2V_{1\,RMS} + V_{2\,RMS}\,\cos(\delta_2) + V_{3\,RMS}\,\cos(\delta_3))]$$

(A.28)

From Fig A.9:

$$\bar{I}_2' = \frac{\bar{V}_2}{jw(2L_6)} \quad , \bar{I}_2'' = \frac{\bar{V}_2}{jwL_6} \quad \text{and} \quad \bar{I}_2''' = \frac{\bar{V}_3}{jw(2L_6)}$$

Since $\bar{I}_2' = \bar{I}_2' + \bar{I}_2'' + \bar{I}_2'''$, then per unit AC-side current of port two is as follows:

$$\bar{I}_2 = \frac{2L_{base}}{\pi L_6}[-(2V_{2\,RMS}\,\sin(\delta_2) + V_{3\,RMS}\,\sin(\delta_3)) - j(V_{1\,RMS} + 2V_{2\,RMS}\,\cos(\delta_2) + V_{3\,RMS}\,\cos(\delta_3))] \tag{A.29}$$

From Fig A.10:

$$\bar{I}_3' = \frac{\bar{V}_2}{jw(2L_6)} \quad , \bar{I}_3'' = \frac{\bar{V}_2}{jw(2L_6)} \quad \text{and} \quad \bar{I}_3''' = \frac{\bar{V}_2}{jwL_6}$$

Since $\bar{I}_3' = \bar{I}_3' + \bar{I}_3'' + \bar{I}_3'''$, then per unit AC-side current of port three is as follows:

$$\bar{I}_3 = \frac{2L_{base}}{\pi L_6}[-(V_{2\,RMS}\,\sin(\delta_2) + 2V_{3\,RMS}\,\sin(\delta_3)) - j(V_{1\,RMS} + V_{2\,RMS}\,\cos(\delta_2) + 2V_{3\,RMS}\,\cos(\delta_3))] \tag{A.30}$$

Thus, the AC-side RMS currents are:

$$|I_1|_{RMS} = \frac{2L_{base}}{\pi L_6}\sqrt{[V_{2\,RMS}\,\sin(\delta_2) + V_{3\,RMS}\,\sin(\delta_3)]^2 + [2V_{1\,RMS} + V_{2\,RMS}\,\cos(\delta_2) + V_{3\,RMS}\,\cos(\delta_3)]^2} \tag{A.31}$$

$$|I_2|_{RMS} = \frac{2L_{base}}{\pi L_6}\sqrt{[2V_{2\,RMS}\,\sin(\delta_2) + V_{3\,RMS}\,\sin(\delta_3)]^2 + [V_{1\,RMS} + 2V_{2\,RMS}\,\cos(\delta_2) + V_{3\,RMS}\,\cos(\delta_3)]^2} \tag{A.32}$$

$$|I_3|_{RMS} = \frac{2L_{base}}{\pi L_6}\sqrt{[V_{2\,RMS}\,\sin(\delta_2) + 2V_{3\,RMS}\,\sin(\delta_3)]^2 + [V_{1\,RMS} + V_{2\,RMS}\,\cos(\delta_2) + 2V_{3\,RMS}\,\cos(\delta_3)]^2} \tag{A.33}$$

Afterwards, the normalised active and reactive power expressions can be obtained by substituting in (4.5) and (4.6). Thus:

$$P_1 = \frac{2L_{base}}{\pi L_6}\,V_{1\,RMS}\,(-V_{2\,RMS}\,\sin(\delta_2) - V_{3\,RMS}\,\sin(\delta_3))$$

$$
\begin{aligned}
P_2 &= \frac{2L_{base}}{\pi L_6}\, V_{2\,RMS}\,(cos(\delta_2)\,[-2V_{2\,RMS}\,\sin(\delta_2) - V_{3\,RMS}\,\sin(\delta_3)] \\
&\quad - sin(\delta_2)[-V_{1\,RMS} - 2V_{2\,RMS}\,\cos(\delta_2) - V_{3\,RMS}\,\cos(\delta_3)]) \\
P_3 &= \frac{2L_{base}}{\pi L_6}\, V_{3\,RMS}\,(cos(\delta_3)\,[-V_{2\,RMS}\,\sin(\delta_2) - 2V_{3\,RMS}\,\sin(\delta_3)] \\
&\quad - sin(\delta_3)[-V_{1\,RMS} - V_{2\,RMS}\,\cos(\delta_2) - 2V_{3\,RMS}\,\cos(\delta_3)]) \\
Q_1 &= \frac{2L_{base}}{\pi L_6}\, V_{1\,rms}\,(\,2V_{1\,RMS} + V_{2\,RMS}\,\cos(\delta_2) + V_{3\,RMS}\,\cos(\delta_3)) \\
Q_2 &= -\frac{2L_{base}}{\pi L_6}\, V_{2\,RMS}\,(sin(\delta_2)\,[-2V_{2\,RMS}\,\sin(\delta_2) - V_{3\,RMS}\,\sin(\delta_3)] \\
&\quad + cos(\delta_2)[-V_{1\,RMS} - 2V_{2\,rms}\,\cos(\delta_2) - V_{3\,RMS}\,\cos(\delta_3)]) \\
Q_3 &= -\frac{2L_{base}}{\pi L_6}\, V_{3\,RMS}\,(sin(\delta_3)\,[-V_{2\,RMS}\,\sin(\delta_2) - 2V_{3\,RMS}\,\sin(\delta_3)] \\
&\quad + cos(\delta_3)[-V_{1\,RMS} - V_{2\,rms}\,\cos(\delta_2) - 2V_{3\,RMS}\,\cos(\delta_3)])
\end{aligned}
\tag{A.34}
$$

Appendix B Generalised Form for The Active Power in MAB Converter

This appendix provides the mathematical derivation using superposition method to attain a generalised form for the active power in MAB converter with N ports. A star-connected AC link in a MAB converter with N-ports is shown in Fig B.1 where port 1 is the reference port and K_{12}= … = K_{1N}=1 such that ac-side voltage of any bridge *i* volt is outlined by (B.1). Also, all AC link inductors are equal, and all of them are normalised to base impedance $Z_{base}=8fL_{base}$ so impedances of all inductors are equals as outlined by (B.2).

$$v_i = V_i \angle -D_{1i}\, pu \quad where\ V_i = \frac{4}{\pi\sqrt{2}} \tag{B.1}$$

$$Z = j\frac{2\pi L_1}{4L_b} \tag{B.2}$$

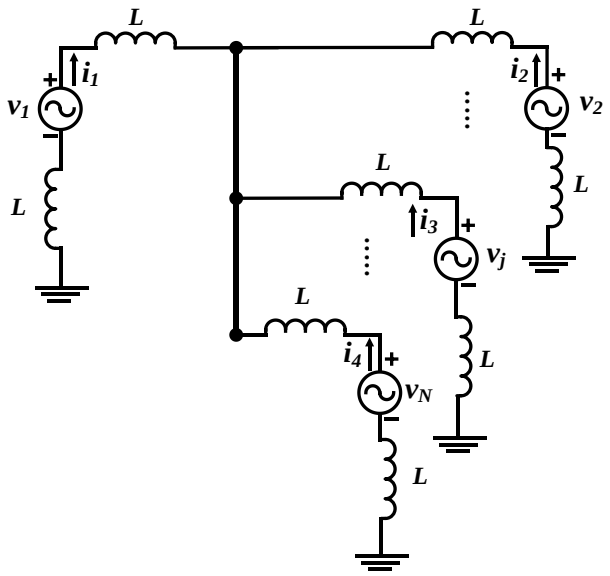

Fig. B.1: N-port MAB converter with star-connected Inductive Equivalent AC link.

This circuit can be solved N times to get all components of current. Every time all sources are treated as short circuit and only one source is considered; if source *j*

is considered, then the circuit becomes as depicted in Fig B.2. In this case, the total inductance is equivalent to (N-1) paralleled inductors which are in series with port j inductor, such that:

$$Z_{total} = j\frac{2\pi/4}{N-1} + j\frac{2\pi}{4} = j\ \frac{2\pi}{4}\frac{N}{N-1}\ pu.$$

$$i_{jj} = \frac{v_j}{Z_{total}} = \left(\frac{4V_j}{2\pi}\right)\frac{\cos\left(D_{1j}\right) - j\sin\left(D_{1j}\right)}{j\ \frac{N}{N-1}} = \left(\frac{4V_j}{2\pi}\right)\frac{N-1}{N}\left[-\sin\left(D_{1j}\right) - j\cos\left(D_{1j}\right)\right] \qquad \text{(B.3)}$$

Then

$$i_{jk} = \frac{-i_{jj}}{N-1} = \left(\frac{4V_j}{2\pi}\right)\frac{1}{N}\left[\sin\left(D_{1j}\right) + j\cos\left(D_{1j}\right)\right] \quad \text{where } k = 1,2,\dots N\ \&\ k \neq j \qquad \text{(B.4)}$$

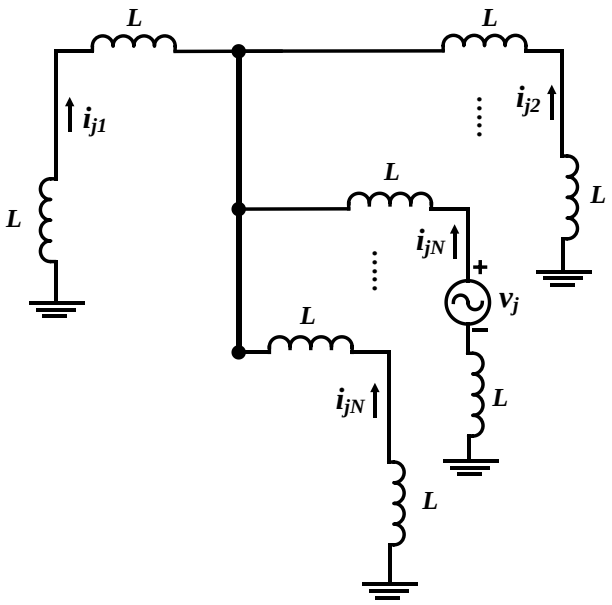

Fig. B.2: N-port MAB converter with star-connected Inductive Equivalent AC link with superposition.

Now, the same needs to be done for all ports, and by superposition, current of each port is the summation of that component in all circuits, such that

$$i_1 = i_{11} + i_{12} + i_{13} + \cdots + i_{1j} + \cdots + i_{1N}$$

$$i_2 = i_{21} + i_{22} + i_{23} + \cdots + i_{2j} + \cdots + i_{2N}$$

$$i_j = i_{j1} + i_{j2} + i_{j3} + \cdots + i_{jj} + \cdots i_{jN}$$

$$i_N = i_{N1} + i_{N2} + i_{N3} + \cdots + i_{Nj} + \cdots i_{NN}$$

Therefore, combining (B.3) and (B.4), a general form can be written for current at each port as follows:

$$i_j = \left(\frac{4V_j}{2\pi}\right)\sum_{k=1}^{N} i_{jk} \quad where\ \ i_{jk} = \begin{cases} \frac{N-1}{N}\left[-\sin\left(D_{1j}\right) - j\cos\left(D_{1j}\right)\right] & j = k \\ \frac{1}{N}\left[\sin\left(D_{1j}\right) + j\cos\left(D_{1j}\right)\right] & j \neq k \end{cases} \tag{B.5}$$

Since active power at each port equals to

$$P = Real\left(v_j i_j{}^*\right) \text{ where } v_j = 1\angle D_{rj} \text{ and } i_j \text{ is defined in (B. 5)} \tag{B.6}$$

Now $i_j{}^*$needs to be calculated which can be done after simplifying i_j. Since i_j has (N-1) similar elements (i.e.: when $j \neq k$.) and only one different element (i.e.: when $j = k$.), then i_j in (B.5) can be rearranged as follows:

$$i_j = \left(\frac{4V_j}{2\pi}\right)\frac{N-1}{N}\left[-\sin\left(D_{1j}\right) - j\cos\left(D_{1j}\right)\right] + \left(\frac{4V_j}{2\pi}\right)\sum_{\substack{k=1 \\ k\neq j}}^{N}\frac{1}{N}\left[\sin(D_{1k}) + j\cos(D_{1k})\right] \tag{B.7}$$

Gathering real and imaginary terms of (B.7):

$$i_j = \frac{4V_j}{2\pi}\left[-\frac{N-1}{N}\sin\left(D_{1j}\right) + \sum_{\substack{k=1 \\ k\neq j}}^{N}\frac{1}{N}\sin(D_{1k})\right] + j\frac{4V_j}{2\pi}\left[-\frac{(N-1)}{N}\cos\left(D_{rj}\right) + \sum_{\substack{k=1 \\ k\neq j}}^{N}\frac{1}{N}\cos(D_{1k})\right]$$

Then

$$i_j{}^* = \frac{4V_j}{2\pi}\left[-\frac{N-1}{N}\sin(D_{1j}) + \sum_{\substack{k=1\\k\neq j}}^{N}\frac{1}{N}\sin(D_{1k})\right] + j\frac{4V_j}{2\pi}\left[\frac{(N-1)}{N}\cos(D_{rj}) - \sum_{\substack{k=1\\k\neq j}}^{N}\frac{1}{N}\cos(D_{1k})\right]$$

Now P can be calculated according to (B.6)

$$P_j = \frac{4L_b}{2\pi L_1}{V_j}^2\cos(D_{1j})\left[-\frac{N-1}{N}\sin(D_{rj}) + \sum_{\substack{k=1\\k\neq j}}^{N}\frac{1}{N}\sin(D_{1k})\right] + \frac{4L_b}{2\pi L_1}{V_j}^2\sin(D_{rj})\left[\frac{(N-1)}{N}\cos(D_{rj}) - \sum_{\substack{k=1\\k\neq j}}^{N}\frac{1}{N}\cos(D_{1k})\right]$$

Then

$$P_j = \frac{4^3 L_b}{2 * 2\pi^3 L_1}\left[\cos(D_{1j})\sum_{\substack{k=1\\k\neq j}}^{N}\frac{1}{N}\sin(D_{1k}) - \sin(D_{1j})\sum_{\substack{k=1\\k\neq j}}^{N}\frac{1}{N}\cos(D_{1k})\right] \qquad \text{(B.8)}$$

Verification of (B.8) can be done as follows; for a 3-port converter *N=3* and for power at port 2 (*j=2*) then,

$$P_2 = \frac{4^3 L_b}{2 * 2\pi^3 L_1}\left[\cos(D_{12})\left(\frac{1}{3}\sin(D_{11}) + \frac{1}{3}\sin(D_{13})\right) - \sin(D_{12})\left(\frac{1}{3}\cos(D_{11}) + \frac{1}{3}\cos(D_{13})\right)\right] \qquad \text{(B.9)}$$

But D_{11}=0 and using value of L_1 as a function of L_b from Table 4.5 where

$$L_1 = \frac{4^3}{6\pi^3}L_{base}\,, \qquad (K_{12} = K_{13} = 1)$$

Then (B.9) reduces to

$$P_2 = \frac{1}{2}[-Sin\,(D_{12}) + Sin\,(D_{13} - D_{12})]$$

Which matches (4.21) proving the correctness of the general form of active power in MAB converter.

Appendix C MATLAB code of The Minimisation Algorithm

In this appendix, Matlab/m-file code of the proposed RMS-current minimisation algorithm presented in chapter five is given. Minimisation for only the forward power flow is shown while the code for the negative (reverse) power flow is omitted due to space constraint and since it is similar code to that of the forward power flow with minor changes.

C.1. MATLAB Code of PSO Minimisation Algorithm

```
%************************************************************************
% Program Code to Minimise IRMS at entire power range for given DC voltage
%ratio K12. Input to the program: K12, Pref, iterations and particles
%************************************************************************


clear
warning off

K12=0.6 ;

iter_amount=100;
particles=170;

tolerance= 0.001;

w1=0.5 ;
w2=0.5 ;
xp_up=1000;
xp_low=zeros(1,3);


%%%%%%%%%%%%%%%%%%%%%%%%%%%%%%%%%%%%%%%%%%%%%%%%%%%%%%%%%%%%%%%%%%%%%%%%%%%%

for xx=0.1:0.1:1

    P_ref=(xx)*K12;

    %%%%%%%%%%%%%%%%%%%%%%%%%%%%%%%%%%%%%%%%%%%%%%%%%%%%%%%%%%%%%%%%%%%%%%%%%%%%
    Results_mode1 (1,5)=0;
    Results_mode11(1,5)=0;    %%%% mode11= mode 1'
    Results_mode2 (1,5)=0;
    Results_mode22(1,5)=0;    %%%% mode22= mode 2'
    Results_mode3 (1,5)=0;
    Results_mode4 (1,5)=0;
    Results_mode5 (1,5)=0;
    Results_mode6 (1,5)=0;

    Results_mode1 (1,6)=0;
    Results_mode11(1,6)=0;
    Results_mode2 (1,6)=0;
    Results_mode22(1,6)=0;
    Results_mode3 (1,6)=0;
    Results_mode4 (1,6)=0;
    Results_mode5 (1,6)=0;
```

```
Results_mode6 (1,6)=0;

activate_mode_1 =0;
activate_mode_11=0;
activate_mode_2 =0;
activate_mode_22=0;
activate_mode_3 =0;
activate_mode_4 =0;
activate_mode_5 =0;
activate_mode_6 =0;

%%%%%%%^^ Selecting Appropriate modes according to P_ref %%%%%%%

if P_ref>= (0.49*K12) && P_ref>= (0.667*K12)

    activate_mode_6=1;
end
if P_ref>= (0.49*K12) && P_ref<= (0.67*K12)

    activate_mode_4=1;
    activate_mode_5=1;
    activate_mode_6=1;

end
if P_ref>= (0.49*K12) && P_ref<= (0.667*K12)

    activate_mode_5=1;
    activate_mode_6=1;

end
if P_ref>=0  && P_ref<= (0.5*K12)

    activate_mode_1=1;
    activate_mode_11=1;
    activate_mode_2=1;
    activate_mode_22=1;
    activate_mode_3=1;
    activate_mode_4=1;
    activate_mode_5=1;
    activate_mode_6=1;
end
%%%%%%%%%%%%%%%%%%%%%%%%%%%%%


%%%%%% Applying PSO on the SELECTED MODES  %%%%%%%%%%%%%%

%%%%%%%_________ Start of MODE 1 ____________%%%%%%%%%%%%%%%%%%%%%%%%%

if activate_mode_1==1

    %generation of initial generation
    x_particles=zeros(particles,3);
    xgbest=zeros(1,3);
    xpbest=zeros(particles,3);
    vx=rand(particles,3);  % velocity of particle x
    fit=zeros(1,particles);
    fit_old=99999999999*(ones(1,particles));
    fit_max_old=0 ;     % max value of fitness
    fit_min=99999999999999 ;     % initial max value of fitness
    fitnesses1=zeros(1,iter_amount); % fitness value at every iteration
    P_group=zeros(1,particles);

    i=1;

    while i < (particles+1)

        for jj=1:1:3
```

```
                x_particles(i,jj)=1000*( rand(1,1));

            end

            if x_particles(i,3)< (x_particles(i,1)- x_particles(i,2) ) &&
            x_particles(i,2)<  x_particles(i,1)
                i=i+1;
            end
        end


        for iter=1:1:iter_amount

            for   ii=1:1:particles
%%number of loops = number of particles and every loop evaluate fitness and store
in the xpbest matrix

                D1= (x_particles(ii,1))/1000 ;
                D2= (x_particles(ii,2))/1000 ;
                D12=(x_particles(ii,3))/1000 ;
                %%%%%%%%%%%%%%%%%%%%%%%%%%%%

                %%% Call exact model function and return P and I RMS

                exact_ans=Mode1(D1,D2,D12,K12) ;

                P_group(1,ii)=exact_ans (1,1);

                fit(1,ii)=  exact_ans (1,2);

                %%forming the xpbest
                if fit(1,ii)<fit_old(1,ii)

                    fit_old(1,ii)=fit(1,ii);

                    for  gj=1:1:3
                        xpbest(ii,gj)=x_particles(ii,gj) ;
%formation of matrix repersenting xpbest for every partcile
                    end
                end
            end

%%%%%%%%%at the end of each iteration, for all particles: chossing gbest

            for i=1:1:particles
                if fit(1,i)<fit_min   && P_group(1,i)>(P_ref-tolerance)  &&
                P_group(1,i)<(P_ref+tolerance)

                    fit_min=fit(1,i);

                    xgbest_n=i;        % number of particle that achieved maximux
fitness and max nearst power to the required power level, which will be xgbest

                    for j=1:1:3

                        xgbest(1,j)=x_particles(i,j);

                    end
                end
            end
            fitnesses1(1,iter)=fit_min;
            %%%%%%%%%%%%%%%%%%%%%%%%%%%%%%%%%%
            ji=1;
            for ii=1:1:particles

                w=0.9-(0.005*iter);

 %%%%***SETTING CONTRAINTS of MODE 1 after each update of particle***%%%%
```

```
%%%%%%%%%%%%  ----- the constraint with D1 ------- %%%%%%%%%%%%%
            ji=1;

            vx(ii,ji)= w*vx(ii,ji)+ 2*rand(1,1)*(xpbest(ii,ji)- x_particles(ii,ji))
            + 2*rand(1,1)*(xgbest(1,ji)- x_particles(ii,ji)) ;
            x_particles(ii,ji)=x_particles(ii,ji)+vx(ii,ji);


            if x_particles(ii,ji)> xp_up
                vx(ii,ji)=x_particles(ii,ji)- xp_up ;
                x_particles(ii,ji)=xp_up ;
            end
            if x_particles(ii,ji)< xp_low(1,ji)
                vx(ii,ji)=xp_low(1,ji)- x_particles(ii,ji);
                x_particles(ii,ji)=xp_low(1,ji);
            end
            %%%%%%

            %%%%%%  ----- the constraint with D2 ------- %%%%%%%%%%%
            ji=2;

            vx(ii,ji)= w*vx(ii,ji)+ 2*rand(1,1)*(xpbest(ii,ji)- x_particles(ii,ji))
            + 2*rand(1,1)*(xgbest(1,ji)- x_particles(ii,ji)) ;
            x_particles(ii,ji)=x_particles(ii,ji)+vx(ii,ji);

            if x_particles(ii,ji)< xp_low(1,ji)
                vx(ii,ji)=xp_low(1,ji)- x_particles(ii,ji);
                x_particles(ii,ji)=xp_low(1,ji);
            end

            %%%added
            if x_particles(ii,ji)> x_particles(ii,1)
                vx(ii,ji)=x_particles(ii,ji)-x_particles(ii,1);
                x_particles(ii,ji)=x_particles(ii,1);
            end

            %%%%%%%  ----- the constraint with D12  ------- %%%%%
            ji=3 ;

            vx(ii,ji)= w*vx(ii,ji)+ 2*rand(1,1)*(xpbest(ii,ji)-
            x_particles(ii,ji)) + 2*rand(1,1)*(xgbest(1,ji)- x_particles(ii,ji)) ;
            x_particles(ii,ji)=x_particles(ii,ji)+vx(ii,ji);

            if x_particles(ii,ji)< xp_low(1,ji)
                vx(ii,ji)=xp_low(1,ji)- x_particles(ii,ji);
                x_particles(ii,ji)=xp_low(1,ji);
            end
            if x_particles(ii,ji)>  ( x_particles(ii,1)-x_particles(ii,2)  )
                vx(ii,ji)= x_particles(ii,ji) - ( x_particles(ii,1)-
               x_particles(ii,2)) ;
                x_particles(ii,ji)= ( x_particles(ii,1)-x_particles(ii,2)  )  ;
            end
        end
    end

    %%getting results of Xgbest

    D1 =xgbest(1,1)/1000;
    D2 =xgbest(1,2)/1000;
    D12=xgbest(1,3)/1000;

    %%% Call mode 1 function and return P and I RMS

    exact_ans=Mode1(D1,D2,D12,K12) ;

    P=exact_ans (1,1);
    iL_rms=exact_ans (1,2);
```

```
        %%%%%%%% Storing optimal solutions %%%%%%
        Results_mode1(1,1)=D1;
        Results_mode1(1,2)=D2;
        Results_mode1(1,3)=D12;
        Results_mode1(1,4)=P;
        Results_mode1(1,5)=iL_rms;


    end
    %%%%%%%%_________ Start of MODE 11 (mode 1') ____________%%%%%%%%%%%%

    if activate_mode_11==1

        %generation of initial generation
        x_particles=zeros(particles,3);
        xgbest=zeros(1,3);
        xpbest=zeros(particles,3);
        vx=rand(particles,3);
        fit=zeros(1,particles);
        fit_old=99999999999*(ones(1,particles));
        fit_max_old=0 ;
        fit_min=99999999999999 ;
        fitnesses1=zeros(1,iter_amount);
        P_group=zeros(1,particles);

        i=1;

        while i < (particles+1)

            x_particles(i,1)=1000*( rand(1,1));
            x_particles(i,2)=1000*( rand(1,1));
            x_particles(i,3)=1000*( rand(1,1))-1000*( rand(1,1));


            if (x_particles(i,3)+1000)< (x_particles(i,1)- x_particles(i,2) ) &&
            x_particles(i,2)<  x_particles(i,1)
                D1= (x_particles(i,1))/1000 ;
                D2= (x_particles(i,2))/1000 ;
                D12= (x_particles(i,3))/1000 ;

                P=-2*K12*( D2^2 - D1*D2 + 2*D2*(D12+1) );

                if P>0

                    i=i+1;
                end
            end
        end


        for iter=1:1:iter_amount

            for   ii=1:1:particles       %%loops = number of particles and each
loop evaluate fitness and store in the xpbest matrix

                D1= (x_particles(ii,1))/1000 ;
                D2= (x_particles(ii,2))/1000 ;
                D12=(x_particles(ii,3))/1000 ;

                %%% Call exact mode 1' function and return P and I RMS

                exact_ans=Mode11(D1,D2,D12,K12) ;

                P_group(1,ii)=exact_ans (1,1);

                fit(1,ii)=  exact_ans (1,2);
```

```
                %%forming the xpbest
                if fit(1,ii)<fit_old(1,ii)

                    fit_old(1,ii)=fit(1,ii);

                    for  gj=1:1:3
                        xpbest(ii,gj)=x_particles(ii,gj) ;
%formation of matrix representing xpbest for every particle
                    end
                end
            end

%%%%%%%%%at the end of each iteration, for all particles: choosing gbest

            for i=1:1:particles
                if fit(1,i)<fit_min   && P_group(1,i)>(P_ref-tolerance)  &&
                P_group(1,i)<(P_ref+tolerance)

                    fit_min=fit(1,i);

                    xgbest_n=i;
% number of particle that achieved maximum fitness and max nearest power to the
required power level, which will be xgbest

                    for j=1:1:3

                        xgbest(1,j)=x_particles(i,j);

                    end
                end
            end
            fitnesses11(1,iter)=fit_min;
            %%%%%%%%%%%%%%%%%%%%%%%%%%%%%%%%%%%%
            ji=1;
            for ii=1:1:particles

                w=0.9-(0.005*iter);

        %***SETTING CONSTRAINTS of MODE 1' after each update of particle*%%
        %%%%%%%%%%%%  constraint of D1 -------  %%%%%%%%%%%%%
                ji=1;

                vx(ii,ji)= w*vx(ii,ji)+ 2*rand(1,1)*(xpbest(ii,ji)- x_particles(ii,ji))
                + 2*rand(1,1)*(xgbest(1,ji)- x_particles(ii,ji)) ;
                x_particles(ii,ji)=x_particles(ii,ji)+vx(ii,ji);


                if x_particles(ii,ji)> 1000
                    vx(ii,ji)=x_particles(ii,ji)- 1000;
                    x_particles(ii,ji)=1000;
                end
                if x_particles(ii,ji)< xp_low(1,ji)
                    vx(ii,ji)=xp_low(1,ji)- x_particles(ii,ji);
                    x_particles(ii,ji)=xp_low(1,ji);
                end
                %%%%%%

                %%%%%%%%%%%% constraint of D2 -------  %%%%%%%%%

                ji=2;

                vx(ii,ji)= w*vx(ii,ji)+ 2*rand(1,1)*(xpbest(ii,ji)- x_particles(ii,ji))
                + 2*rand(1,1)*(xgbest(1,ji)- x_particles(ii,ji)) ;
                x_particles(ii,ji)=x_particles(ii,ji)+vx(ii,ji);

                if x_particles(ii,ji)< xp_low(1,ji)
                    vx(ii,ji)=xp_low(1,ji)- x_particles(ii,ji);
                    x_particles(ii,ji)=xp_low(1,ji);
```

```
            end

            %%% upper constraint
            if x_particles(ii,ji)> x_particles(ii,1)
                vx(ii,ji)=x_particles(ii,ji)-x_particles(ii,1);
                x_particles(ii,ji)=x_particles(ii,1);
            end

            %%%%%%%%%%%%  constraint of D12 ------- %%%%%%%%%%%%
            ji=3 ;

            vx(ii,ji)= w*vx(ii,ji)+ 2*rand(1,1)*(xpbest(ii,ji)- x_particles(ii,ji))
            + 2*rand(1,1)*(xgbest(1,ji)- x_particles(ii,ji)) ;
            x_particles(ii,ji)=x_particles(ii,ji)+vx(ii,ji);

            %%% lower constraint
            if x_particles(ii,ji)< -1000
                vx(ii,ji)=-1000- x_particles(ii,ji);
                x_particles(ii,ji)=-1000;
            end
            %%% upper constraint
            if x_particles(ii,ji)> ( x_particles(ii,1)-x_particles(ii,2)- 1000)
                vx(ii,ji)=x_particles(ii,ji)-( x_particles(ii,1)-x_particles(ii,2)-1000);
                x_particles(ii,ji)=(x_particles(ii,1)-x_particles(ii,2)-1000) ;
            end
        end
    end
    %%getting results of Xgbest

    D1=xgbest(1,1)/1000;
    D2=xgbest(1,2)/1000;
    D12=xgbest(1,3)/1000;

    %%% Call exact mode 1' function and return P and I RMS

    exact_ans=Mode11(D1,D2,D12,K12) ;

    P=exact_ans (1,1);
    iL_rms=exact_ans (1,2);

    %%%%%%%% Storing optimal solution%%%%%%
    Results_mode11(1,1)=D1;
    Results_mode11(1,2)=D2;
    Results_mode11(1,3)=D12;
    Results_mode11(1,4)=P;
    Results_mode11(1,5)=iL_rms;

end

%%%%%%%%%%_________ Start of MODE 2 __________%%%%%%%%%%

if activate_mode_2==1
    %generation of initial paticles

    x_particles=zeros(particles,3);
    xgbest=zeros(1,3);
    xpbest=zeros(particles,3);
    vx=rand(particles,3);
    fit=zeros(1,particles);
    fit_old=99999999999*(ones(1,particles));
    fit_max_old=0 ;
    fit_min=99999999999999 ;
    fitnesses2=zeros(1,iter_amount);
    P_group=zeros(1,particles);

    i=1;

    while i < (particles+1)
```

```
            for jj=1:1:3


                x_particles(i,jj)=1000*( round((rand(1,1)),4));

            end

            if  x_particles(i,2)> x_particles(i,1) && x_particles(i,3)> ( 1000+
x_particles(i,1)- x_particles(i,2) )
                i=i+1;
            end
        end


        for iter=1:1:iter_amount

            for   ii=1:1:particles
%%loops=number of particles and each loop evaluate fitness and store in the xpbest
matrix

                D1=  (x_particles(ii,1))/1000 ;
                D2=  (x_particles(ii,2))/1000 ;
                D12= (x_particles(ii,3))/1000 ;

                %%% Call mode 2 function and return P and I RMS

                exact_ans=Mode2(D1,D2,D12,K12) ;

                P_group(1,ii)=exact_ans (1,1);

                fit(1,ii)=    exact_ans (1,2);


                %%forming the xpbest
                if fit(1,ii)<fit_old(1,ii)

                    fit_old(1,ii)=fit(1,ii);

                    for  gj=1:1:3
                        xpbest(ii,gj)=x_particles(ii,gj) ;
%formation of matrix representing xpbest for every particle
                    end
                end
            end

%%%%%%%%%at the end of each iteration, for all particles: choosing gbest

            for i=1:1:particles
                if fit(1,i)<fit_min && P_group(1,i)>((P_ref-tolerance)) &&
                P_group(1,i)<((P_ref))

                    fit_min=fit(1,i);

                    xgbest_n=i;
% number of particle that achieved maximum fitness and max nearest power to the
required power level,which will be xgbest

                    for j=1:1:3

                        xgbest(1,j)=x_particles(i,j);

                    end
                end
            end
            fitnesses2(1,iter)=fit_min;
            %%%%%%%%%%%%%%%%%%%%%%%%%%%%%%%%%%%%
```

```
            for ii=1:1:particles

                w=0.9-(0.005*iter);

                ji=1 ;

                vx(ii,ji)= w*vx(ii,ji)+ 2*rand(1,1)*(xpbest(ii,ji)- x_particles(ii,ji)) +
                2*rand(1,1)*(xgbest(1,ji)- x_particles(ii,ji)) ;
                x_particles(ii,ji)=x_particles(ii,ji)+vx(ii,ji);

%********  upper CONSTRAINT  *****%%%%%%%%%%%%%%
                if x_particles(ii,ji)> xp_up
                    vx(ii,ji)=x_particles(ii,ji)- xp_up;
                    x_particles(ii,ji)=xp_up;
                end
%%%%%%%%** lower CONSTRAINT  %%%%%%%%%%

                if x_particles(ii,ji)<xp_low(1,ji)
                    vx(ii,ji)=xp_low(1,ji)- x_particles(ii,ji);
                    x_particles(ii,ji)=xp_low(1,ji);
                end
                ji=2 ;

                vx(ii,ji)= w*vx(ii,ji)+ 2*rand(1,1)*(xpbest(ii,ji)- x_particles(ii,ji)) +
                2*rand(1,1)*(xgbest(1,ji)- x_particles(ii,ji)) ;
                x_particles(ii,ji)=x_particles(ii,ji)+vx(ii,ji);

%%%%%%%%%%%%%%%%%%** upper CONSTRAINT*****%%%%%%%%%%%%%%%%%%%%%%%%%
                if x_particles(ii,ji)> xp_up
                    vx(ii,ji)=x_particles(ii,ji)- xp_up;
                    x_particles(ii,ji)=xp_up;
                end

%%%%%%%%%%%%%%%%%%** lower CONSTRAINT *****%%%%%%%%%%%%%%%%%%%%%%%%%
                if x_particles(ii,ji)< x_particles(ii,1)
                    vx(ii,ji)=x_particles(ii,1)-x_particles(ii,ji);
                    x_particles(ii,ji)=x_particles(ii,1);
                end
                %%%
                ji=3 ;

                vx(ii,ji)= w*vx(ii,ji)+ 2*rand(1,1)*(xpbest(ii,ji)- x_particles(ii,ji)) +
                2*rand(1,1)*(xgbest(1,ji)- x_particles(ii,ji)) ;
                x_particles(ii,ji)=x_particles(ii,ji)+vx(ii,ji);

%%%%%%%%%%%%%%%%%%** upper CONSTRAINT*****%%%%%%%%%%%%%%%%%%%%%%%%%
                if x_particles(ii,ji)> xp_up
                    vx(ii,ji)=x_particles(ii,ji)- xp_up;
                    x_particles(ii,ji)=xp_up;
                end

%%%%%%%%%%%%%%%%%%** lower CONSTRAINT *****%%%%%%%%%%%%%%%%%%%%%%%%%
                if x_particles(ii,ji)<( 1000+ x_particles(ii,1)- x_particles(ii,2) )
                    vx(ii,ji)= ( 1000+ x_particles(ii,1)- x_particles(ii,2) ) -
                    x_particles(ii,ji) ;
                    x_particles(ii,ji)= ( 1000+ x_particles(ii,1)- x_particles(ii,2) ) ;
                end
            end
        end

        %%getting results of Xgbest

        D1 =xgbest(1,1)/1000;
        D2 =xgbest(1,2)/1000;
        D12=xgbest(1,3)/1000;

        %%% Call mode 2 function and return P and I RMS
```

```
        exact_ans=Mode2(D1,D2,D12,K12) ;

        P  =   exact_ans (1,1);
        iL_rms=exact_ans (1,2);

        %%%%%%%% Storing optimal solution%%%%%%
        Results_mode2(1,1)=D1;
        Results_mode2(1,2)=D2;
        Results_mode2(1,3)=D12;
        Results_mode2(1,4)=P;
        Results_mode2(1,6)=iL_rms;

    end

%%%%%%%________ Start of MODE 22 (Mode2')____%%%% %%%%%%%%%%%%%%

    if activate_mode_22==1
        %generation of initial paticles

        x_particles=zeros(particles,3);
        xgbest=zeros(1,3);
        xpbest=zeros(particles,3);
        vx=rand(particles,3);
        fit=zeros(1,particles);
        fit_old=99999999999*(ones(1,particles));
        fit_max_old=0 ;
        fit_min=99999999999999 ;
        fitnesses2=zeros(1,iter_amount);
        P_group=zeros(1,particles);

        i=1;

        while i < (particles+1)

            x_particles(i,1)=1000*( rand(1,1));
            x_particles(i,2)=1000*( rand(1,1));
            x_particles(i,3)=1000*( rand(1,1))-1000*( rand(1,1));


           if (x_particles(i,3))<= 0 && x_particles(i,2)>= x_particles(i,1) &&
           (x_particles(i,3)+1000)>= ( 1000+ x_particles(i,1)- x_particles(i,2) )
                D1= (x_particles(i,1))/1000 ;
                D2= (x_particles(i,2))/1000 ;
                D12= (x_particles(i,3))/1000 ;

                P= -2*K12*(  (D1^2)-(D1*D2)+(2*D1)-(2*D1*(D12+1) )) ;

                if P>0

                    i=i+1;
                end
            end
        end


        for iter=1:1:iter_amount

            for   ii=1:1:particles
%%loops= number of particles and each loop evaluate fitness and store in the xpbest
matrix

                D1= (x_particles(ii,1))/1000 ;
                D2= (x_particles(ii,2))/1000 ;
                D12=(x_particles(ii,3))/1000 ;

                %%% Call mode 2' function and return P and I RMS

                exact_ans=Mode22(D1,D2,D12,K12) ;
```

```
                P_group(1,ii)=exact_ans (1,1);

                fit(1,ii)=  exact_ans (1,2);

                %%forming the xpbest
                %%for best particle in the fi
                if fit(1,ii)<fit_old(1,ii)

                    fit_old(1,ii)=fit(1,ii);

                    for  gj=1:1:3
                        xpbest(ii,gj)=x_particles(ii,gj) ;
%formation of matrix repersenting xpbest for every partcile
                    end
                end
            end

%%%%%%%%%at the end of each iteration, for all particles: choosing gbest

            for i=1:1:particles
                if fit(1,i)<fit_min && P_group(1,i)>((P_ref-tolerance)) &&
                P_group(1,i)<((P_ref+tolerance))

                    fit_min=fit(1,i);

                    xgbest_n=i;
% number of particle that achieved maximum fitness and max nearest power to the
required power level, which will be xgbest

                    for j=1:1:3

                        xgbest(1,j)=x_particles(i,j);

                    end
                end
            end
            fitnesses22(1,iter)=fit_min;
            %%%%%%%%%%%%%%%%%%%%%%%%%%%%%%%%%%%%

            for ii=1:1:particles
                for ji=1:1:3
                    w=0.9-(0.005*iter);
                    vx(ii,ji)= w*vx(ii,ji)+ 2*rand(1,1)*(xpbest(ii,ji)-
                    x_particles(ii,ji)) + 2*rand(1,1)*(xgbest(1,ji)-
                    x_particles(ii,ji)) ;
                    x_particles(ii,ji)=x_particles(ii,ji)+vx(ii,ji);

%%%%%%%%%%%%%%%%%%%%%%General CONSTRAINT*****%%%%%%%%%%%%%%%%%%%%%%%%
                    if x_particles(ii,ji)> xp_up
                        vx(ii,ji)=x_particles(ii,ji)- xp_up;
                        x_particles(ii,ji)=xp_up;
                    end
                    if ji==1 || ji== 2

                        if x_particles(ii,ji)<xp_low(1,ji)
                            vx(ii,ji)=xp_low(1,ji)- x_particles(ii,ji);
                            x_particles(ii,ji)=xp_low(1,ji);
                        end
                    end

%%%%%%**SETTING CONSTRAINTS of MODE 2 after each update of particle***%%%%%

                    %%% constraint of D2
                    if ji==2
                        if x_particles(ii,ji)< x_particles(ii,1)
                            vx(ii,ji)=x_particles(ii,1)-x_particles(ii,ji);
                            x_particles(ii,ji)=x_particles(ii,1);
```

```
                    end
                end
                %%%
                %%% Lower constraint of D12

                if ji==3

                    if x_particles(ii,ji)< ( x_particles(ii,1)- x_particles(ii,2) )
                       vx(ii,ji)= (  x_particles(ii,1)- x_particles(ii,2) ) -
                        x_particles(ii,ji) ;
                       x_particles(ii,ji)= ( x_particles(ii,1)-x_particles(ii,2) ) ;
                    end
                end
            end
        end
    end


    %%getting results of Xgbest

    D1=xgbest(1,1)/1000;
    D2=xgbest(1,2)/1000;
    D12=xgbest(1,3)/1000;

    %%% Call mode 2' function and return P and I RMS

    exact_ans=Mode22(D1,D2,D12,K12) ;

    P=exact_ans (1,1);
    iL_rms=exact_ans (1,2);

    %%%%%%%% Storing optimal solution%%%%%%
    Results_mode22(1,1)=D1;
    Results_mode22(1,2)=D2;
    Results_mode22(1,3)=D12;
    Results_mode22(1,4)=P;
    Results_mode22(1,5)=iL_rms;

end
%%%%%%%%_________ Start of MODE 3 ____________%%%%%%%%%%%%%%%%%%

if activate_mode_3==1

    x_particles=zeros(particles,3);
    xgbest=zeros(1,3);
    xpbest=zeros(particles,3);
    vx=rand(particles,3);
    fit=zeros(1,particles);
    fit_old=99999999999*(ones(1,particles));
    fit_max_old=0 ;
    fit_min=99999999999999 ;
    fitnesses3=zeros(1,iter_amount);
    P_group=zeros(1,particles);

%generation of initial generation
    i=1;

    while i < (particles+1)

        for jj=1:1:3

            x_particles(i,jj)=1000*( rand(1,1));

        end

        if x_particles(i,2)< (1000- x_particles(i,1) ) && x_particles(i,3)>
        x_particles(i,1) && x_particles(i,3)<  (1000-x_particles(i,2))
            i=i+1;
```

```
            end
        end

        for iter=1:1:iter_amount

            for   ii=1:1:particles
%%loops = number of particles and each loop evaluate fitness and store in the
xpbest matrix

                D1= (x_particles(ii,1))/1000 ;
                D2= (x_particles(ii,2))/1000 ;
                D12= (x_particles(ii,3))/1000 ;

                %%% Call mode 3 function and return P and I RMS

                exact_ans=Mode3(D1,D2,D12,K12) ;

                P_group(1,ii)=exact_ans (1,1);

                fit(1,ii)=  exact_ans (1,2);

                %%forming the xpbest
                if fit(1,ii)<fit_old(1,ii)

                    fit_old(1,ii)=fit(1,ii);

                    for  gj=1:1:3
                        xpbest(ii,gj)=x_particles(ii,gj) ;
%formation of matrix representing xpbest for every particle
                    end
                end
            end

%%%%%%%%%at the end of each iteration, for all particles: choosing gbest

            for i=1:1:particles
                if fit(1,i)<fit_min && P_group(1,i)>((P_ref-0.001)) &&
P_group(1,i)<((P_ref))

                    fit_min=fit(1,i);

                    xgbest_n=i;
% number of particle that achieved maximum fitness and max nearest power to the
required power level, which will be xgbest

                    for j=1:1:3

                        xgbest(1,j)=x_particles(i,j);

                    end
                end
            end
            fitnesses3(1,iter)=fit_min;
            %%%%%%%%%%%%%%%%%%%%%%%%%%%%%%%%%%%%

            for ii=1:1:particles
                for ji=1:1:3
                    w=0.9-(0.005*iter);
                    vx(ii,ji)= w*vx(ii,ji)+ 2*rand(1,1)*(xpbest(ii,ji)- x_particles(ii,ji)) +
                    2*rand(1,1)*(xgbest(1,ji)- x_particles(ii,ji)) ;
                    x_particles(ii,ji)=x_particles(ii,ji)+vx(ii,ji);
 %%%%%%%%%%%%%%%%%%%%*********General CONSTRAINT*****%%%%%%%%%%%%%%%%%%%%%%%

                    if x_particles(ii,ji)> xp_up
                        vx(ii,ji)=x_particles(ii,ji)- xp_up;
                        x_particles(ii,ji)=xp_up;
                    end
                    if x_particles(ii,ji)<xp_low(1,ji)
```

```
                    vx(ii,ji)=xp_low(1,ji)- x_particles(ii,ji);
                    x_particles(ii,ji)=xp_low(1,ji);
                end

%%%%%***SETTING CONSTRAINTS of MODE 3 after each update of particle****%%%

                %%% constraint of D2
                if ji==2
                    if x_particles(ii,ji)> (1000-x_particles(ii,1))
                        vx(ii,ji)=x_particles(ii,ji)-(1000-x_particles(ii,1) );
                        x_particles(ii,ji)= (1000-x_particles(ii,1)) ;
                    end
                end

                %%% constraint of D12
                if ji==3

                    if x_particles(ii,ji)<  x_particles(ii,1)
                        vx(ii,ji)= x_particles(ii,1) - x_particles(ii,ji) ;
                        x_particles(ii,ji)= x_particles(ii,1)  ;
                    end

                    if x_particles(ii,ji)>  ( 1000-x_particles(ii,2) )
                       vx(ii,ji)= x_particles(ii,ji) - ( 1000-x_particles(ii,2) ) ;
                        x_particles(ii,ji)= (1000-x_particles(ii,2))  ;
                    end
                end
            end
        end
    end


    %%getting results of Xgbest

    D1=xgbest(1,1)/1000;
    D2=xgbest(1,2)/1000;
    D12=xgbest(1,3)/1000;

    %%% Call mode 3 function and return P and I RMS

    exact_ans=Mode3(D1,D2,D12,K12) ;

    P=     exact_ans (1,1);
    iL_rms=exact_ans (1,2);

    %%%%%%%% Storing optimal solution%%%%%%
    Results_mode3(1,1)=D1;
    Results_mode3(1,2)=D2;
    Results_mode3(1,3)=D12;
    Results_mode3(1,4)=P;
    Results_mode3(1,5)=iL_rms;

end
%%%%%%________ Start of MODE 4 ___________%%%%%%%%%%%%%%%%%%%%%%%%%%%

if activate_mode_4==1

    x_particles=zeros(particles,3);
    xgbest=zeros(1,3);
    xpbest=zeros(particles,3);
    vx=rand(particles,3);
    fit=zeros(1,particles);
    fit_old=99999999999*(ones(1,particles));
    fit_max_old=0 ;
    fit_min=99999999999999 ;
    fitnesses4=zeros(1,iter_amount);
    P_group=zeros(1,particles);
```

```
%generation of initial generation

        i=1;

        while i < (particles+1)


            for jj=1:1:3

                x_particles(i,jj)=1000*( rand(1,1));

            end

            if  x_particles(i,3)> x_particles(i,1) && x_particles(i,2)>(1000-
            x_particles(i,3))&& x_particles(i,2)<(1000-x_particles(i,3)+x_particles(i,1))
                i=i+1;
            end
        end


        for iter=1:1:iter_amount

            for   ii=1:1:particles
%%loops =number of particles and each loop evaluate fitness and store in the xpbest
matrix

                D1= (x_particles(ii,1))/1000 ;
                D2= (x_particles(ii,2))/1000 ;
                D12= (x_particles(ii,3))/1000 ;

             %%% Call exact mode 4 function and return P and I RMS

                exact_ans=Mode4(D1,D2,D12,K12) ;

                P_group(1,ii)=exact_ans (1,1);

                fit(1,ii)=  exact_ans (1,2);


                %%forming the xpbest
                if fit(1,ii)<fit_old(1,ii)

                    fit_old(1,ii)=fit(1,ii);

                    for  gj=1:1:3
                        xpbest(ii,gj)=x_particles(ii,gj) ;
%formation of matrix representing xpbest for every particle
                    end
                end
            end

%%%%%%%%%at the end of each iteration, for all particles: choosing gbest

            for i=1:1:particles
                if fit(1,i)<fit_min && P_group(1,i)>(P_ref-0.0005)  &&
                P_group(1,i)<(P_ref)

                    fit_min=fit(1,i);

                    xgbest_n=i;
% number of particle that achieved maximum fitness and max nearest power to the
required power level, which will be xgbest

                    for j=1:1:3

                        xgbest(1,j)=x_particles(i,j);

                    end
```

```
            end
        end
        fitnesses4(1,iter)=fit_min;
        %%%%%%%%%%%%%%%%%%%%%%%%%%%%%%%%%%%%
        ji=1;
        for ii=1:1:particles

            w=0.9-(0.005*iter);

%%%%***SETTING CONSTRAINTS of MODE 4 after each update of particle***%%%

            %%% constraint of D1

            ji=1 ;

            vx(ii,ji)= w*vx(ii,ji)+ 2*rand(1,1)*(xpbest(ii,ji)- x_particles(ii,ji)) +
            2*rand(1,1)*(xgbest(1,ji)- x_particles(ii,ji)) ;
            x_particles(ii,ji)=x_particles(ii,ji)+vx(ii,ji);

            if x_particles(ii,ji)> xp_up
                vx(ii,ji)=x_particles(ii,ji)- xp_up;
                x_particles(ii,ji)=xp_up;
            end

            if x_particles(ii,ji)<xp_low(1,ji)
                vx(ii,ji)=xp_low(1,ji)- x_particles(ii,ji);
                x_particles(ii,ji)=xp_low(1,ji);
            end

            %%% constraint of D12

            ji=3;

            vx(ii,ji)= w*vx(ii,ji)+ 2*rand(1,1)*(xpbest(ii,ji)-x_particles(ii,ji)) +
            2*rand(1,1)*(xgbest(1,ji)- x_particles(ii,ji)) ;
            x_particles(ii,ji)=x_particles(ii,ji)+vx(ii,ji);

            if x_particles(ii,ji)<   x_particles(ii,1)
                vx(ii,ji)= x_particles(ii,1)  - x_particles(ii,ji)  ;
                x_particles(ii,ji)= x_particles(ii,1)   ;
            end

            if x_particles(ii,ji)> xp_up
                vx(ii,ji)=x_particles(ii,ji)- xp_up;
                x_particles(ii,ji)=xp_up;
            end


            %%% constraint of D2
            ji=2;

            vx(ii,ji)= w*vx(ii,ji)+ 2*rand(1,1)*(xpbest(ii,ji)- x_particles(ii,ji))
            + 2*rand(1,1)*(xgbest(1,ji)- x_particles(ii,ji)) ;
            x_particles(ii,ji)=x_particles(ii,ji)+vx(ii,ji);

            if x_particles(ii,ji)<  ( 1000- x_particles(ii,3)  )
                vx(ii,ji)= ( 1000- x_particles(ii,3)  )- x_particles(ii,ji)  ;
                x_particles(ii,ji)= ( 1000- x_particles(ii,3)  )  ;
            end

            if x_particles(ii,ji)>(1000- x_particles(ii,3)+x_particles(ii,1)  )
                vx(ii,ji)= x_particles(ii,ji) - ( 1000-
                x_particles(ii,3)+x_particles(ii,1)  )   ;
                x_particles(ii,ji)=(1000-x_particles(ii,3)+x_particles(ii,1)) ;
            end
        end
    end
```

```
        %%getting results of Xgbest

        D1=xgbest(1,1)/1000;
        D2=xgbest(1,2)/1000;
        D12=xgbest(1,3)/1000;
        %%% Call mode 4 function and return P and I RMS

        exact_ans=Mode4(D1,D2,D12,K12) ;

        P=exact_ans (1,1);
        iL_rms=exact_ans (1,2);

        %%%%%%%% Storing optimal solution%%%%%%
        Results_mode4(1,1)=D1;
        Results_mode4(1,2)=D2;
        Results_mode4(1,3)=D12;
        Results_mode4(1,4)=P;
        Results_mode4(1,5)=iL_rms;

    end

%%%%%%%%%%%_________ Start of MODE 5 ___________%%%%%%%%%%%%%%%%%%%

    if activate_mode_5==1

        x_particles=zeros(particles,3);
        xgbest=zeros(1,3);
        xpbest=zeros(particles,3);
        vx=rand(particles,3);
        fit=zeros(1,particles);
        fit_old=99999999999*(ones(1,particles));
        fit_max_old=0 ;
        fit_min=99999999999999 ;
        fitnesses5=zeros(1,iter_amount);
        P_group=zeros(1,particles);

        i=1;

        while i < (particles+1)


            for jj=1:1:3

                x_particles(i,jj)=1000*( rand(1,1));

            end

            if x_particles(i,2)< (1000- x_particles(i,3) ) && x_particles(i,1)>
x_particles(i,3) && x_particles(i,2)>  (x_particles(i,1)-x_particles(i,3))

                i=i+1;
            end
        end


        for iter=1:1:iter_amount

            for   ii=1:1:particles
%%loops = number of particles and each loop evaluate fitness and store in the
xpbest matrix

                D1= (x_particles(ii,1))/1000 ;
                D2= (x_particles(ii,2))/1000 ;
                D12= (x_particles(ii,3))/1000 ;

                %%% Call mode 5 function and return P and I RMS
```

```
                exact_ans=Mode5(D1,D2,D12,K12) ;

                P_group(1,ii)=exact_ans (1,1);

                fit(1,ii)=  exact_ans (1,2);


                %%forming the xpbest
                if fit(1,ii)<fit_old(1,ii)

                    fit_old(1,ii)=fit(1,ii);

                    for  gj=1:1:3
                        xpbest(ii,gj)=x_particles(ii,gj) ;
%formation of matrix representing xpbest for every particle
                    end
                end
            end


%%%%%%%%%at the end of every iteration, for all particles: choosing gbest

            for i=1:1:particles
                if fit(1,i)<fit_min && P_group(1,i)>(P_ref-tolerance)  &&
P_group(1,i)<(P_ref+tolerance)

                    fit_min=fit(1,i);

                    xgbest_n=i;
% number of particle that achieved maximum fitness and max nearest power to the
required power level, which will be xgbest

                    for j=1:1:3

                        xgbest(1,j)=x_particles(i,j);

                    end
                end
            end
            fitnesses5(1,iter)=fit_min;
            %%%%%%%%%%%%%%%%%%%%%%%%%%%%%%%%%%%
            ji=1;
            for ii=1:1:particles

                w=0.9-(0.005*iter);
                vx(ii,ji)= w*vx(ii,ji)+ 2*rand(1,1)*(xpbest(ii,ji)- x_particles(ii,ji))
                + 2*rand(1,1)*(xgbest(1,ji)- x_particles(ii,ji)) ;
                x_particles(ii,ji)=x_particles(ii,ji)+vx(ii,ji);

%%%***SETTING CONSTRAINTS of MODE 5 after each update of particle**%%%%%

                ji=1;

                vx(ii,ji)= w*vx(ii,ji)+ 2*rand(1,1)*(xpbest(ii,ji)- x_particles(ii,ji))
                + 2*rand(1,1)*(xgbest(1,ji)- x_particles(ii,ji)) ;
                x_particles(ii,ji)=x_particles(ii,ji)+vx(ii,ji);

                if x_particles(ii,ji)> xp_up
                    vx(ii,ji)=x_particles(ii,ji)- xp_up;
                    x_particles(ii,ji)=xp_up;
                end
                if x_particles(ii,ji)<xp_low(1,ji)
                    vx(ii,ji)=xp_low(1,ji)- x_particles(ii,ji);
                    x_particles(ii,ji)=xp_low(1,ji);
                end


                %%% constraint of D12
```

```
                ji=3;
                vx(ii,ji)= w*vx(ii,ji)+ 2*rand(1,1)*(xpbest(ii,ji)-
                x_particles(ii,ji)) + 2*rand(1,1)*(xgbest(1,ji)- x_particles(ii,ji)) ;
                x_particles(ii,ji)=x_particles(ii,ji)+vx(ii,ji);

                if x_particles(ii,ji)<xp_low(1,ji)
                    vx(ii,ji)=xp_low(1,ji)- x_particles(ii,ji);
                    x_particles(ii,ji)=xp_low(1,ji);
                end
                if x_particles(ii,ji)> x_particles(ii,1)
                    vx(ii,ji)=x_particles(ii,ji)- x_particles(ii,1);
                    x_particles(ii,ji)=x_particles(ii,1);
                end


                %%% constraint of D2
                ji=2;
                vx(ii,ji)= w*vx(ii,ji)+ 2*rand(1,1)*(xpbest(ii,ji)-
                x_particles(ii,ji)) + 2*rand(1,1)*(xgbest(1,ji)- x_particles(ii,ji)) ;
                x_particles(ii,ji)=x_particles(ii,ji)+vx(ii,ji);

                if x_particles(ii,ji)> ( 1000-x_particles(ii,3) )
                    vx(ii,ji)= x_particles(ii,ji)- ( 1000-x_particles(ii,3) ) ;
                    x_particles(ii,ji)= ( 1000-x_particles(ii,3) ) ;
                end
                if x_particles(ii,ji)<  ( x_particles(ii,1)-x_particles(ii,3)  )
                    vx(ii,ji)= (x_particles(ii,1)-x_particles(ii,3))-
                    x_particles(ii,ji);
                    x_particles(ii,ji)= ( x_particles(ii,1)-x_particles(ii,3)  )  ;
                end

            end
        end

        %%getting results of Xgbest

        D1=xgbest(1,1)/1000;
        D2=xgbest(1,2)/1000;
        D12=xgbest(1,3)/1000;

        %%% Call mode 5 function and return P and I RMS

        exact_ans=Mode5(D1,D2,D12,K12) ;

        P=exact_ans (1,1);
        iL_rms=exact_ans (1,2);

        %%%%%%%% Storing optimal solution%%%%%%
        Results_mode5(1,1)=D1;
        Results_mode5(1,2)=D2;
        Results_mode5(1,3)=D12;
        Results_mode5(1,4)=P;
        Results_mode5(1,5)=iL_rms;

    end
%%%%%%%%%_________ Start of MODE 6 __________%%%%%%%%%%%%%%%%%%%%%%%%%%%%

    if activate_mode_6==1

        x_particles=zeros(particles,3);
        xgbest=zeros(1,3);
        xpbest=zeros(particles,3);
        vx=rand(particles,3);
        fit=zeros(1,particles);
        fit_old=99999999999*(ones(1,particles));
        fit_max_old=0 ;
        fit_min=99999999999999 ;
        fitnesses6=zeros(1,iter_amount);
```

```
        P_group=zeros(1,particles);

        %%generate initial generation

        i=1;

        while i < (particles+1)

            for jj=1:1:3

                x_particles(i,jj)=1000*( rand(1,1));

            end

            if x_particles(i,1)> (1000- x_particles(i,2) ) && x_particles(i,3)<
x_particles(i,1) && x_particles(i,3)>  (1000-x_particles(i,2))
                i=i+1;
            end
        end


        for iter=1:1:iter_amount

            for   ii=1:1:particles
%%loops = number of particles and each loop evaluate fitness and store in the
xpbest matrix

                D1= (x_particles(ii,1))/1000 ;
                D2= (x_particles(ii,2))/1000 ;
                D12=(x_particles(ii,3))/1000 ;

%%% Call mode 6 function and return P and I RMS

                exact_ans=Mode6(D1,D2,D12,K12) ;

                P_group(1,ii)=exact_ans (1,1);

                fit(1,ii)=  exact_ans (1,2);

                %%forming the xpbest
                %%for best particle in the fi
                if fit(1,ii)<fit_old(1,ii)

                    fit_old(1,ii)=fit(1,ii);

                    for  gj=1:1:3
                        xpbest(ii,gj)=x_particles(ii,gj) ;
%formation of matrix repersenting xpbest for every partcile
                    end
                end
            end
%%%%%%%%%at the end of each iteration, for all particles: chossing gbest

            for i=1:1:particles
                if fit(1,i)<fit_min   && P_group(1,i)>(P_ref-tolerance)  &&
                P_group(1,i)<(P_ref+tolerance)

                    fit_min=fit(1,i);

                    xgbest_n=i;
% number of particle that achieved maximux fitness and max nearst power to the
required power level, which will be xgbest

                    for j=1:1:3

                        xgbest(1,j)=x_particles(i,j);

                    end
```

```
            end
        end
        fitnesses6(1,iter)=fit_min;
        %%%%%%%%%%%%%%%%%%%%%%%%%%%%%%%%%%%%
        ji=1;
        for ii=1:1:particles

            w=0.9-(0.005*iter);

%%%%%%%%SETTING CONTRAINTS of MODE 6 after update of every particle %%%%%%%%%%%%%%

            %%%%%%%%%%%%  ----- the constraint of D2  ------- %%%%%%%%%%%%%%

            ji=2;

            vx(ii,ji)= w*vx(ii,ji)+ 2*rand(1,1)*(xpbest(ii,ji)-
x_particles(ii,ji)) + 2*rand(1,1)*(xgbest(1,ji)- x_particles(ii,ji)) ;
            x_particles(ii,ji)=x_particles(ii,ji)+vx(ii,ji);


            if x_particles(ii,ji)> 1000
                vx(ii,ji)=x_particles(ii,ji)- 1000;
                x_particles(ii,ji)=1000;
            end
            if x_particles(ii,ji)< xp_low(1,ji)
                vx(ii,ji)=xp_low(1,ji)- x_particles(ii,ji);
                x_particles(ii,ji)=xp_low(1,ji);
            end

            %%%%%%%%%%%%  ----- the constraint of D1  ------- %%%%%%%%%%%%%%

            ji=1;

            vx(ii,ji)= w*vx(ii,ji)+ 2*rand(1,1)*(xpbest(ii,ji)-
x_particles(ii,ji)) + 2*rand(1,1)*(xgbest(1,ji)- x_particles(ii,ji)) ;
            x_particles(ii,ji)=x_particles(ii,ji)+vx(ii,ji);
            %%% lower constaint
            if x_particles(ii,ji)<  ( 1000-x_particles(ii,2)  )
                vx(ii,ji)= ( 1000- x_particles(ii,2) ) - x_particles(ii,ji)  ;
                x_particles(ii,ji)= ( 1000-x_particles(ii,2)  )  ;
            end

            %%% upper constaint
            if x_particles(ii,ji)> xp_up
                vx(ii,ji)=x_particles(ii,ji)- xp_up;
                x_particles(ii,ji)=xp_up;
            end

            %%%%%%%%%%%%  ----- the constraint of D12  ------- %%%%%%%%%%%%%%

            ji=3 ;

            vx(ii,ji)= w*vx(ii,ji)+ 2*rand(1,1)*(xpbest(ii,ji)-
            x_particles(ii,ji)) + 2*rand(1,1)*(xgbest(1,ji)- x_particles(ii,ji)) ;
            x_particles(ii,ji)=x_particles(ii,ji)+vx(ii,ji);

            if x_particles(ii,ji)> ( x_particles(ii,1)  )
                vx(ii,ji)= x_particles(ii,ji) - ( x_particles(ii,1) )    ;
                x_particles(ii,ji)= ( x_particles(ii,1)  )  ;
            end
            %%%added
            if x_particles(ii,ji)<  ( 1000-x_particles(ii,2)  )
                vx(ii,ji)= ( 1000- x_particles(ii,2) ) - x_particles(ii,ji)  ;
                x_particles(ii,ji)= ( 1000-x_particles(ii,2)  )  ;
            end
        end
    end
```

```
        %%getting results of Xgbest
        D1=xgbest(1,1)/1000;
        D2=xgbest(1,2)/1000;
        D12=xgbest(1,3)/1000;

        %%% Call mode 6 function and return P and I RMS

        exact_ans=Mode6(D1,D2,D12,K12) ;

        P=exact_ans (1,1);
        iL_rms=exact_ans (1,2);

        %%%%%%%% Storing optimal solution%%%%%%
        Results_mode6(1,1)=D1;
        Results_mode6(1,2)=D2;
        Results_mode6(1,3)=D12;
        Results_mode6(1,4)=P;
        Results_mode6(1,5)=iL_rms;

    end
    %%%%%%%_________ END of MODE 6 __________%%%%%% %%%%%%%%%%%%%%%%%%%%%%%%%

    %%%%%% Figuring out the optimal switchin mode at a specific power level    %%%%

    I_modes(1,1)= Results_mode1(1,5);
    I_modes(1,2)= Results_mode2(1,5);
    I_modes(1,3)= Results_mode3(1,5);
    I_modes(1,4)= Results_mode4(1,5);
    I_modes(1,5)= Results_mode5(1,5);
    I_modes(1,6)= Results_mode6(1,5);
    I_modes(1,7)= Results_mode11(1,5);
    I_modes(1,8)= Results_mode22(1,5);

    I_min=999;

    for i=1:1:8

        if  I_modes(1,i)<I_min    && I_modes(1,i)>0

            I_min=I_modes(1,i);

            I_min_n=i;        % number of mode that achieved min I

        end
    end

%%%%%%% storing optimal solutions in the results matrix, storing fitness of optimal
case in fitness matrix, %%%%%%%

    %%%%%%%
    jx=round(xx*10);

    if  I_min_n==1

        Results(jx,1)=Results_mode1(1,1);
        Results(jx,2)=Results_mode1(1,2);
        Results(jx,3)=Results_mode1(1,3);
        Results(jx,4)=Results_mode1(1,4);
        Results(jx,5)=Results_mode1(1,5);
        %%%% storing number of the optimal mode in the results matrix
        Results(jx,6)=1;

        for ix=1:1:iter_amount
            fitness_matrix(jx,ix)= fitnesses1(1,ix);
        end

    end
```

```
if  I_min_n==2

    Results(jx,1)=Results_mode2(1,1);
    Results(jx,2)=Results_mode2(1,2);
    Results(jx,3)=Results_mode2(1,3);
    Results(jx,4)=Results_mode2(1,4);
    Results(jx,5)=Results_mode2(1,5);
    %%%% storing number of the optimal mode in the results matrix
    Results(jx,6)=2;

    for ix=1:1:iter_amount
        fitness_matrix(jx,ix)= fitnesses2(1,ix);
    end

end

if  I_min_n==3

    Results(jx,1)=Results_mode3(1,1);
    Results(jx,2)=Results_mode3(1,2);
    Results(jx,3)=Results_mode3(1,3);
    Results(jx,4)=Results_mode3(1,4);
    Results(jx,5)=Results_mode3(1,5);
    %%%% storing number of the optimal mode in the results matrix
    Results(jx,6)=3;

    for ix=1:1:iter_amount
        fitness_matrix(jx,ix)= fitnesses3(1,ix);
    end

end

if  I_min_n==4

    Results(jx,1)=Results_mode4(1,1);
    Results(jx,2)=Results_mode4(1,2);
    Results(jx,3)=Results_mode4(1,3);
    Results(jx,4)=Results_mode4(1,4);
    Results(jx,5)=Results_mode4(1,5);
    %%%% storing number of the optimal mode in the results matrix
    Results(jx,6)=4;

    for ix=1:1:iter_amount
        fitness_matrix(jx,ix)= fitnesses4(1,ix);
    end
end

if  I_min_n==5
    Results(jx,1)=Results_mode5(1,1);
    Results(jx,2)=Results_mode5(1,2);
    Results(jx,3)=Results_mode5(1,3);
    Results(jx,4)=Results_mode5(1,4);
    Results(jx,5)=Results_mode5(1,5);
    %%%% storing number of the optimal mode in the results matrix
    Results(jx,6)=5;
    for ix=1:1:iter_amount
        fitness_matrix(jx,ix)= fitnesses5(1,ix);
    end

end


if I_min_n==6

    Results(jx,1)=Results_mode6(1,1);
    Results(jx,2)=Results_mode6(1,2);
    Results(jx,3)=Results_mode6(1,3);
    Results(jx,4)=Results_mode6(1,4);
```

```
        Results(jx,5)=Results_mode6(1,5);
        %%% storing number of the optimal mode in the results matrix
        Results(jx,6)=6;

        for ix=1:1:iter_amount
            fitness_matrix(jx,ix)= fitnesses6(1,ix);
        end

    end
    %%%storing optimal solutions of mode 11 (mode 1')
    if I_min_n==7

        Results(jx,1)=Results_mode11(1,1);
        Results(jx,2)=Results_mode11(1,2);
        Results(jx,3)=Results_mode11(1,3);
        Results(jx,4)=Results_mode11(1,4);
        Results(jx,5)=Results_mode11(1,5);
        %%%% storing number of the optimal mode in the results matrix
        Results(jx,6)=11;

        for ix=1:1:iter_amount
            fitness_matrix(jx,ix)= fitnesses11(1,ix);
        end

    end
    %%%storing optimal solutions of mode 22 (mode 2')
    if  I_min_n==8

        Results(jx,1)=Results_mode22(1,1);
        Results(jx,2)=Results_mode22(1,2);
        Results(jx,3)=Results_mode22(1,3);
        Results(jx,4)=Results_mode22(1,4);
        Results(jx,5)=Results_mode22(1,5);
        %%%% storing number of the optimal switching mode in the results matrix
        Results(jx,6)=22;

        for ix=1:1:iter_amount
            fitness_matrix(jx,ix)= fitnesses22(1,ix);
        end

    end

    Results(jx,7)=P_ref;

end
%*************************************************************************
```

C.2. MATLAB Code of DAB switching modes

This section includes the MATLAB program Code to calculate power and IRMS according to exact DAB model in chapter three. The code for only switching modes 1 and 1’ are shown here due to page constraints.

```
%****  Code to calculate P and IRMS in DAB at switching Modes (Exact Model) *******

%*****************************       Mode 1     ******************************
function y=Mode1(D1,D2,D12,K)

          t1=D12;
          t2=(D12+D2);
          t3=D1;
```

```
          %%%%%%%%%%%%%%
           A=  -2*(D1-K*D2)  ;     %iL(t0)
           B=  2*(-D1+2*D12+K*D2) ;   %iL(t1)
           C=  2*(-D1+2*D2+2*D12-K*D2)  ;   %iL(t2)
           D=  2*(D1-K*D2) ;   %iL(t3)
           %%%%%%%%%%%%%%%%%%

           X1= (A^2)*( t1+1-t3 );
           X2= (B^2)*( t2 ) ;
           X3= (C^2)*(-t1+t3 );
           X4= (D^2)*(-t2+1 );
           X5= (A*B)*( t1 );
           X6= (B*C)*( t2-t1 ) ;
           X7= (C*D)*( t3-t2 );
           X8= (A*D)*(-1+t3 );

           iL_rms=   (1/(3))*( X1 + X2 + X3 + X4 + X5 + X6 + X7 + X8 )    ;
           P= 2*K*( D2^2 - D1*D2 + 2*D2*D12 );

y=[P,iL_rms^0.5];

%**********************      Mode 1' (mode 11)   *************************

function y= Mode11(D1,D2,D12,K)

          t1=( D12+1) ;
          t2=((D12+1)+D2) ;
          t3=  D1;
          %%%%%%%%%%%%%%
           A=  -2*(D1+K*D2)  ;     %iL(t0)
           B=  2* (-D1+2*(D12+1)-K*D2) ;   %iL(t1)
           C=  2* (-D1+ 2*D2 + 2*(D12+1)+ K*D2)  ;   %iL(t2)
           D=  2* (D1+ K*D2) ;   %iL(t3)
           %%%%%%%%%%%%%%%%%%

           X1= (A^2)*( t1+1-t3 );
           X2= (B^2)*( t2 ) ;
           X3= (C^2)*(-t1+t3 );
           X4= (D^2)*(-t2+1 );
           X5= (A*B)*( t1 );
           X6= (B*C)*( t2-t1 ) ;
           X7= (C*D)*( t3-t2 );
           X8= (A*D)*(-1+t3 );

           iL_rms=  (1/(3))*( X1 + X2 + X3 + X4 + X5 + X6 + X7 + X8 )     ;
           P=-2*K*( D2^2 - D1*D2 + 2*D2*(D12+1) );

y=[P,iL_rms^0.5];
```